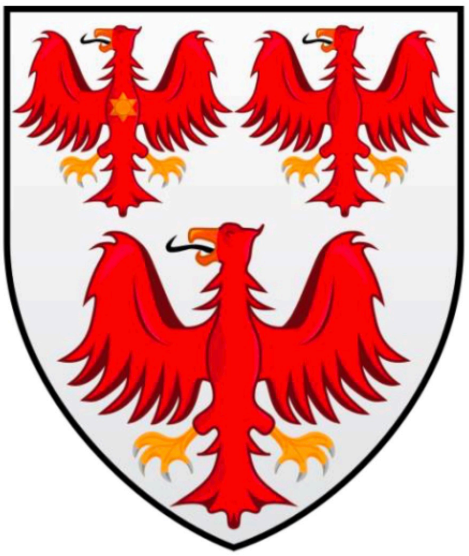
Experimental and Quantum Chemical Studies of Ligand Properties in Main Group Chemistry





Haoyu Niu

The Queen's College, Oxford

May 2019

A Thesis Submitted for the Degree of Doctor of Philosophy

Acknowledgements

First of all, I would like to thank Prof. Simon Aldridge for all his guidance during my degree. He is like a strategist, providing brilliant ideas in my battle with chemistry research; he is also like a therapist, providing confidence when the chemistry is not happy with me. He is a friend of students, being supportive and enthusiastic in their project and always willing to discuss chemistry. Having him as my supervisor is one of the best things that have happened in my life.

I extend my thanks to all the people who contributed to my research. Prof. John McGrady, Dr. Joe Abdalla and Dr. Petra Vasko have taught me the skills of computational chemistry and provided me with a lot of advice. Dr. Evgeny Kolychev has contributed countless hours of helpful discussion on synthetic work and processing X-ray crystal structures. Thanks also go out to other crystallographers: Dr. Maria Fuentes and Dr. Jamie Hicks. Valuable contributions to chapter 5 and 6 were also made by past Part II and summer students from the group: Mr. Thomas Hood, Miss. Molly Kemp and Mr. Paul Löwe.

Many thanks to the friendly members of the group who have been very helpful these years. Dr. Zhenbo Mo and Dr. Arnab Rit have been teaching me all the skills I need to conduct my experiments. Dr. Alexa Caise and Dr. Dinh Do Cao Huan have been very good fumehood neighbours, keeping each other safe from any fatal accidents. Sharing ligands with Dr. Lilja Kristinsdottir saves me a lot of time. While working late at night, I was very lucky to have Dr. Christian Sidlinger, Dr. Andrey Protchenko, Mr. Robert Mangan and Mr. Ying Kai Loh to be my companions, wiping out my depression in the evening and having informative chats with me. Last but not least, thanks to Lu Ying who helped me a lot with the THF distillation and bravely took up the duty after my departure.

Dr. Nick Rees has been very helpful these years with his advice and training on NMR spectroscopy. I wish one day there is an opportunity we play WoT together.

I am very grateful to the support from my parents, financially and mentally from a 12-hour flight away. Every weekend Skype chat was like a review of my life in Britain, sorting out my mind when it gets chaotic. Thanks a lot to Candice for listening to my complaints on anything, be in the lab in the evening when nobody is there and feeding me with very delicious food when I am unhappy.

I would also like to thank my friends outside the lab. Jasper, Tiger, Xiaoyu and Guma have been wonderful flatmates to have dinner and watch movies with. The Board Game Group has given me a lot of fun even though it burned my brain cells the most outside chemistry. Andy and Xuchen are the best mates to eat out together in Oxford, not to mention to chat with on sports, ranging from football to snowboarding. Also, thanks a lot to people in OURC and those whom we play badminton together. I enjoy the time we had competitions together, and I have learned a lot from them.

Abstract

This thesis examines the parameters that influence the electronic properties of different ligands including N-heterocyclic carbenes (NHCs), cyclic(alkyl)(amino)carbenes (CAACs) and N-heterocyclic imines (NHIs), and as a consequence, how their coordination chemistries with transition-metal or (predominantly) main group elements are influenced by these properties.

Chapter 3 reports on a theoretical investigation of factors that determine the σ-donor strength of a range of NHCs, and closely related analogues, including weakly-coordinating-anion functionalized NHCs (WCA-NHCs) and boryl anions. Geometry optimisation of the ligands themselves and fragment calculations on transition-metal systems, including Au(I) and Ni(II) complexes, have been conducted. These results reveal that heterocycle ring size is a dominant factor influencing σ-donor strength, and that the diazaborolyl systems are much stronger donors than their NHC counterparts.

Chapter 4 reports on investigations of the interaction between a CAAC ligand and the boron centre in two donor-stabilised organoboron(I) systems initially reported by Bertrand *et al.*, with a view to determining whether "a lone pair on boron" is an appropriate description. Theoretical studies including ellipticity and Natural Resonance Theory (NRT) analyses have been conducted on $LBNMe_2$ and L_2BH systems featuring a range of ligands with different π-acceptor strengths, including phosphines, NHCs, CAACs, cyclopentylidene and 9H-fluoren-9-ylidene. Results show significant π-back donation from boron to CAAC and related ligands, and that descriptions featuring a C=B double bond are more appropriate than localization of a lone pair at B. Related studies on heavier group 13 analogues, however, suggest that the

dominant resonance structures in these cases feature a lone pair at E. These findings are in line with classical understanding of the inert pair effect and s/p mixing for the heavier p-block elements.

Chapter 5 details investigations (both experimental and theoretical) of a family of N-heterocyclic iminato ligands (NHIs) formally derived from an NHC by the addition of an exocyclic N atom. Theoretical studies are consistent with a 2σ, 4π donor model, and with increasing donor strength with increasing heterocycle ring size. That the 7-membered NHI is a weaker donor than expected is explained on the basis of its unique geometric properties. Three different synthetic methods are reported for the protio-ligands, each of which has its advantages and disadvantages based on yield, time, toxicity and applicability.

Chapter 6 focuses on the coordination chemistry of NHIs with the heavier group 14 elements, tin and lead. Theoretical studies on the tin systems show that the HOMO energy depends not only on the N-Sn-N angle, but also more subtly on the torsional alignment of the ligand. Intramolecular C-H activation is observed in studies of the related lead systems, with a mechanism proposed on the basis of NMR data, kinetic measurements and theoretical studies.

Numbering Scheme and Abbreviations

Unless specified by the nomenclature scheme of the chapter, compounds are numbered sequentially **x** (*i.e.* **1**, **2**, **3**…) and self-contained in each chapter. Compounds with similar structures are numbered as **xa**, **xb** and **xc** etc. for the ease of comparison.

The following abbreviations will be used throughout this report:

Ad - Adamantyl

Ar – Aryl

ADF – Amsterdam Density Functional

BINAP – 2,2'-Bis(diphenylphosphino)-1,1' binaphthyl

^{n}Bu – n-Butyl

^{t}Bu – t-Butyl

ca. – Circa

calc. - Calculated

CAAC – Cyclic(alkyl)(Amino)Carbene

Cp – Cyclopentadienyl

Cp* - Pentamethylcyclopentadienyl

Cy – Cyclohexyl

d – day (time) / Doublet (NMR) / Distance (geometric data)

dd – Doublet of doublets

Dipp – 2,6-Diisopropylphenyl

DFT – Density Functional Theory

Et – Ethyl

Expt – Experimental

HOMO – Highest Occupied Molecular Orbital

IR – Infrared

J – Coupling constant

L – Ligand

LUMO – Lowest Unoccupied Molecular Orbital

m/m – *Meta*/Multiplet (NMR)

Me – Methyl

Mes – 2,4,6-Trimethylphenyl

min - Minutes

mol – Mole

NHC – N-heterocyclic Carbene

NHI – N-heterocyclic Imine

o – *Ortho*

p/p – *Para*/Pentet (NMR)

Ph – Phenyl

^{i}Pr – iso-Propyl

h – Hour

s – Singlet (NMR)

sept – Septet (NMR)

t – Triplet (NMR)

tol – Toluene

THF – Tetrahydrofuran

PTFE – Polytetrafluoroethylene

RT – Room temperature

TMEDA – *N,N,N',N'*-tetramethylethylenediamine

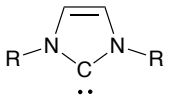
WCA-NHC – Weakly Coordinating Anion Functionalized N-heterocyclic Carbene

vs – Versus

ν – Frequency

Unless specified by the nomenclature scheme of the chapter, the following abbreviations are used for the carbenes shown below.

I^{t}Bu – R = ^{t}Bu
IMes – R = Mes
IDipp – R = Dipp



5-Mes – R = Mes, n = 1
5-Dipp – R = Dipp, n = 1
6-Mes – R = Mes, n = 2
6-Dipp – R = Dipp, n = 2
7-Mes – R = Mes, n = 3
7-Dipp – R = Dipp, n = 3
8-Mes – R = Mes, n = 4

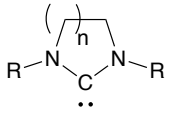


Table of Contents

CHAPTER 1 INTRODUTION **1**

1.1 LIGANDS 1

1.1.1 The Bonding of Dative Ligands *2*

1.2 PHOSPHINES 3

1.2.1 Electronic Properties of Phosphines *3*

1.2.2 Steric Properties of Phosphines *8*

1.3 CARBENES 10

1.3.1 N-heterocyclic Carbenes (NHCs) *14*

1.3.2 Cyclic (Alkyl)(Amino)Carbenes (CAACs) *27*

1.3.3 Diazaborolyl Ligands *29*

1.4 N-HETEROCYCLIC IMININATO (NHI) LIGANDS 31

1.5 APPLICATIONS OF LIGANDS WITH DIFFERENT ELECTRONIC PROPERTIES IN MAIN GROUP CHEMISTRY 35

1.5.1 NHCs in Compounds Featuring Multiple Bonds Between Heavier Main Group Elements *36*

1.5.2 Monomeric Low-valent Main-group Compounds *42*

1.6 RESEARCH PROPOSAL 50

1.7 REFERENCES 51

CHAPTER 2 EXPERIMENTAL METHODS **59**

2.1 INERT ATMOSPHERE TECHNIQUES 59

2.2 SPECTROSCOPIC TECHNIQUES 61

2.2.1 NMR spectroscopy *61*

2.2.2 Infrared Spectroscopy *61*

2.2.3 Elemental Analysis *61*

2.2.4 Photolysis *61*

2.2.5 X-ray Crystallography *62*

2.2.6 Synthesis of Starting Materials *62*

2.3 REFERENCES 67

CHAPTER 3 QUANTUM CHEMICAL STUDIES OF CYCLIC CARBENES AS σ-DONOR IN LATE TRANSITION METAL SYSTEMS **68**

3.1 INTRODUCTION 68

3.2 COMPUTATIONAL DETAILS 70

3.2.1 Density Functional Theory *70*

3.2.2 Amsterdam Density Functional *72*

3.2.3 XC Potential – Exchange-Correlated Potential *73*

3.2.4 Basis Set *74*

3.2.5 Frozen Core Approximation and Numerical Quality *78*

3.3 RESULTS AND DISCUSSION 78

3.3.1 The Selection and Geometry Optimisation of Ligands *78*

3.3.2 Fragment Calculations *86*

3.3.3 Quantum Chemical Studies of Gold Complexes *88*

3.3.4 Quantum Chemical Studies of Nickel Complexes *89*

3.4 SUMMARY 91

3.5 REFERENCES 92

CHAPTER 4 QUANTUM CHEMICAL STUDIES OF CYCLIC CARBENES AS π-ACCEPTORS IN MAIN GROUP SYSTEMS **95**

4.1 INTRODUCTION 95

4.2 COMPUTATIONAL DETAILS 97

4.2.1 Natural Bond Orbitals (NBOs) *97*

4.2.2 Natural Resonance Theory (NRT) *99*

4.2.3 Ellipticity *104*

4.3 RESULTS AND DISCUSSION 106

4.3.1 Selection of Ligands *106*

4.3.2 Analysis of π-Acceptor Behaviour in Organoboron Systems Isoelectronic with Carbenes *108*

4.3.3 Analysis of π-Acceptor Behaviour in Organoboron Systems Isoelectronic with Amines *122*

4.4 CONCLUSIONS 130

4.5 REFERENCES 131

CHAPTER 5 COMPUTATIONAL AND SYNTHETIC STUDIES OF BULKY RING-EXPANDED ANIONIC GUANIDINATO LIGANDS 133

5.1 INTRODUCTION 133

5.2 EXPERIMENTAL 136

5.3 PREPARATION AND CHARACTERIZATION OF LIGANDS 142

5.3.1 Theoretical Studies of the Ligands *142*

5.3.2 Syntheses of the Protio-ligands *148*

5.4 SUMMARY 164

5.5 REFERENCES 165

CHAPTER 6 COORDINATION CHEMISTRY AND REACTIVITY OF HEAVIER GROUP 14 ELEMENT COMPOUNDS FEATURING BULKY ANIONIC GUANIDINATO LIGANDS 167

6.1 INTRODUCTION 167

6.2 EXPERIMENTAL 168

6.3 SYNTHESIS OF GUANIDINATO COMPLEXES OF TIN AND GERMANIUM 176

6.3.1 Synthesis of systems of the type Sn{N(SiMe$_3$)$_2$}(Lg) *176*

6.3.2 ^{119}Sn NMR chemical shifts of compounds of the type Sn{N(SiMe$_3$)$_2$}(Lg) *179*

6.3.3 Carbonyl Stretching Frequencies of (Lg){(Me$_3$Si)$_2$N}SnMo(CO)$_5$ *184*

6.3.4 Attempted Syntheses of Sn(Ig)$_2$ and Ge(Ig)$_2$ *186*

6.3.5 Attempted Syntheses of Sn(5g)$_2$ and Ge(5g)$_2$ *188*

6.4 INTRAMOLECULAR C-H ACTIVATION AT LEAD 189

6.4.1 The Preparation and C-H Activation of Pb{N(SiMe$_3$)$_2$}(Lg) *189*

6.4.2 Mechanistic studies of the conversion of 13 to 15 *197*

6.5 SUMMARY 200

6.6 REFERENCES 202

Appendix: Copyright permission and Crystallographic data in DVD attached

Chapter 1

Introduction

1.1 Ligands

The word "ligand" stems from Latin "*ligare*" meaning to bind or tie. Indeed, ligands in a chemical context bind to central elements (typically metals from the *s*, *p*, *d* or *f*-blocks of the Periodic Table) and construct coordination complexes. The properties of a complex depend not only on the electronic configuration of its central element, but are also influenced by the electronic and steric properties of the ligands. In 1977 Tolman gave definitions to the two effects separately – the electronic effect brings changes in molecular properties as a result of transmission along the chemical bonds, while steric effects bring changes as a result of forces (usually nonbonding) between different parts of a complex molecule.[1] These two key properties will be discussed in detail in this introductory chapter.



Figure 1-1: The bonding of covalent (X) ligands (left) and dative (L) ligands (right) with the central element.

Ligands are generally classified into three groups,[2] namely the X-type (covalent), L-type (donor) and Z-type (acceptor) based on the charges assigned to them by oxidation state formalisms or the number of electrons that the ligand contributes to its bonding with

the central element. Among them, X-type (covalent ligands) share one electron and form a bond with the other electron formally being contributed by the central element (Figure 1-1(left)). L-type (dative ligands) donate a pair of electrons to form the bond with the central element. (Figure 1-1(right)).

1.1.1 The Bonding of Dative Ligands

By default, a dative ligand is a σ-donor as it donates a pair of electrons to the central element (the metal) in σ fashion to form a dative bond. However, in many cases, the ligand and metal can engage in π-symmetry interactions as well. Depending on its electronic properties, a ligand can be a π-acceptor or π-donor. A π-acceptor typically has an empty low-lying pπ orbital available to accept electron density from the metal; by contrast, a π-donor has a filled pπ orbital available to donate electron density.

π-Acceptors include carbonyls and Fischer carbenes, and tend to enlarge the HOMO-LUMO gap in transition metal complexes. The stabilization of the HOMO means that this type of ligand typically favours electron-rich metal centres, with electron density being delocalized onto the ligand framework. Typical π-donors include halide and allyl anions and more exotic ligands such as the guanidinato family, and exert the opposing influence – the HOMO-LUMO gap is typically narrowed. π-Donors therefore favour electron deficient central elements where electron density from the ligands can be donated via both the σ- and π-frameworks to stabilise the system.

1.2 Phosphines

Phosphines and related trivalent phosphorus ligands are among the most important ancillary ligands in homogeneous catalysis.[3] The parent compound of the phosphine family is phosphine (PH_3), which was first obtained by Philippe Gengembre in 1783, by heating phosphorus in an aqueous solution of potassium carbonate.[4-6] At first, phosphine was regarded as a gaseous form of phosphorus, but Lavoisier later recognised it as a combination of phosphorus with hydrogen.[7] The phosphine ligand family is well developed, following much research over the past two hundred years, and substituents at phosphorus range from alkyl groups to aryl groups and halides. Phosphines as ligands in coordination chemistry are most commonly (although not exclusively) tertiary phosphines, with three non-hydrogen substituents.

1.2.1 Electronic Properties of Phosphines

Phosphines are strong σ-donors, due to the lone pair located in the HOMO. Phosphines (and to a greater extent, phosphites) can potentially also act as π-acceptors by utilising the P-R (or P-OR) σ* orbitals (of local e symmetry), mixed to some degree with P-centred d-orbitals. However, this π-acceptor strength strongly depends on the electronic properties of the substituents.

Table 1-1: TEP values reported by Tolman

PR_3	TEP (cm^{-1})[1,8]	PR_3	TEP (cm^{-1})[1,8]
$(p\text{-}ClC_6H_4)_3P$	2072.8	$MePh_2P$	2067.0
$(p\text{-}FC_6H_4)_3P$	2071.3	Me_2PhP	2065.3
Ph_3P	2068.9	Me_3P	2064.1
$(o\text{-}MeC_6H_4)_3P$	2066.6	Cy_3P	2056.4
$(p\text{-}MeC_6H_4)_3P$	2066.7	Et_3P	2061.7
$(p\text{-}MeOC_6H_4)_3P$	2066.1	$^tBu_3P$	2056.1

The most common indicator of the electronic properties of a phosphine was introduced by Tolman in 1970, namely the Tolman Electronic Parameter (TEP).[8] The parameter is a measure of the frequency of the A_1 C-O vibrational mode of a (pseudo)-C_{3v} symmetric complex, $(R_3P)Ni(CO)_3$. In later developments this approach was extended to other donors such as NHCs[9] (as discussed below) to provide a consistent measure of the TEP for a range of ligands. In general, more electron density donated from the phosphine would be expected to reduce the CO stretching frequency, due to the presence of a more electron-rich metal centre which back-bonds more strongly to the CO π^* anti-bonding orbital and reduces the CO bond order. Hence, a smaller value would indicate stronger electron donation (Table 1-1). However, the TEP values measure not only the σ-donor strength, but an overall effect of both the donor and acceptor properties of the ligand. Therefore, different methods are needed to measure σ-donor strength and π-acceptor strength independently.

1.2.1.1 Phosphines as σ-Donors

The protic (Brønsted) basicities of phosphines have been investigated over many decades,[10-14] and are considered as a good indicator of σ-donor strength. Notably, the basicities of amines featuring identical substituents are similar to those of phosphines but the bonding between amines and transition metals is typically weaker. This is because most late transition metals are much softer acids than a proton and hence have a better interaction with the soft phosphorus in a phosphine than hard nitrogen in an amine.[15-17] Brønsted basicities are therefore regarded as suitable for comparing σ-donor strengths

within the same ligand family but not a good parameter to compare between different types of donor.

The pK_a values of selected phosphines alongside their enthalpies of protonation are summarized in Table 1-2[3]. The substituent (R) goes from slightly electron withdrawing at the top of the table to strongly electron donating at the bottom. The message delivered from these data is simple: the ability to donate a lone pair increases down the table in line with the inductive effects of the pendant substituents, and tri-(tert-butyl)-phosphine is the strongest σ-donor of those listed.

Table 1-2: Enthalpy of protonation and pK_a values of selected phosphines, summarised by Hartwig.[3] Numbers in parentheses are average deviations.

PR_3	Enthalpy of Protonation (kJ mol^{-1})[a]	pK_a
$(p\text{-}ClC_6H_4)_3P$	74.8(0.8)	1.03[11]
$(p\text{-}FC_6H_4)_3P$	81.9(0.8)	1.97[11]
Ph_3P	88.6(0.4)	2.73[13]
$(o\text{-}MeC_6H_4)_3P$	94.5(0.8)	3.08[11]
$(p\text{-}MeC_6H_4)_3P$	98.0(1.2)	3.84[11]
$(p\text{-}MeOC_6H_4)_3P$	100.7(0.8)	4.57[11]
$MePh_2P$	103.2(0.0)	4.59[18]
Me_2PhP	118.7(0.8)	6.50[13]
Me_3P	132.1(0.8)	8.65[13]
Cy_3P	138.8(1.6)	9.70[13]
Et_3P	140.9(1.2)	8.69[13]
$^tBu_3P$	153.0(1.2)	11.4[11]

a. For protonation with CF_3SO_3H in dichloroethane at 25°C.

1.2.1.2 Phosphines as π-Acceptors

The π-acceptor capabilities of phosphines also reflect the nature of the pendant substituents, as the electronegativity of R affects the energy of the P-R σ* orbitals. However, previous theoretical studies have shown that the relative π-acceptor strength of a phosphine is dependent on the metal complex used as the probe.[19] For example, in Pd

systems, PH_3 is a weaker π-acceptor than PPh_3, while it is the opposite in Cr and Mo systems. To unify the results from different complexes, and provide a single scale on which to compare different phosphines (as well as amines), Harvey and his co-workers introduced the concept of a "π-acceptor index".[20] The π-acceptor index combines the back-bonding interaction energies (E_{bb}) from a range of systems (including NH_3PdL, PdL, PH_3PdL, (CO)PdL, $Cr(CO)_5L$ and $Mo(CO)_5L$, with L denoting the ligand in interest) and normalised to 100 for the strongest acceptor on scale, CO, following equation 1.1:

$$\pi\text{-acceptor index} = [E_{bb}(\text{Total})/E_{bb}(\text{Total, CO})] \times 100 \qquad 1.1$$

with

$$E_{bb}(\text{Total}) = E_{bb}(NH_3PdL) + E_{bb}(PdL) + E_{bb}(PH_3PdL) + E_{bb}(COPdL) + 5 \times [E_{bb}(Cr(CO)_5L) + E_{bb}(Mo(CO)_5L)]$$

(E_{bb}(Total, CO) being the value of E_{bb} with L = CO). E_{bb}, the back-bonding interaction energy between the metal and the ligand in question, is estimated by second-order perturbative Natural Bond Orbital (NBO) analysis. The factor of 5 in the equation is used to give an overall comparable weight to $E_{bb}(Cr(CO)_5L)$ and $E_{bb}(Mo(CO)_5L)$, as their values are relatively smaller than those obtained for the Pd complexes.

The values of the π-acceptor index for various ligands are illustrated in Figure 1-2. Although the numbers are generated only from six systems based on three transition metals, the π-acceptor strength is clearly laid out on the scale. Taking phosphines as a starting point, the π-acceptor strength is very similar for triphenyl- and trimethylphosphines; as the alkyl/aryl substituents are replaced by more electronegative elements, the π-acceptor strength increases. A possible explanation is that the more

electronegative elements increase the p character in the LUMO of a phosphine and lower its energy, toward the region where a metal would bond more effectively.[21]

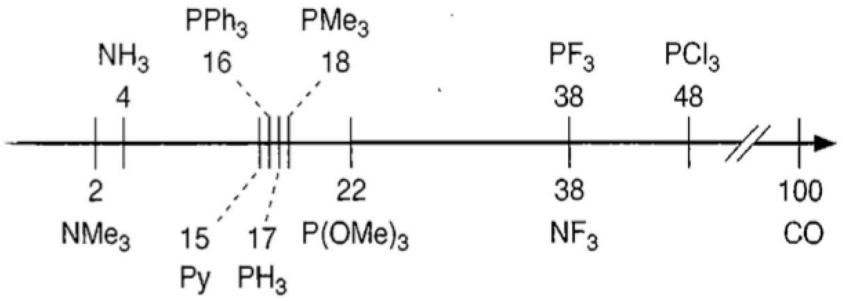


Figure 1-2: Calculated π-acceptor index for P- and N- based ligands, relative to carbon monoxide, determined by NBO analysis. Reprinted with permission from Harvey and his co-workers, Organometallics*, 2007, 26, 2637-2645. Copyright (2019) American Chemical Society.*[20]

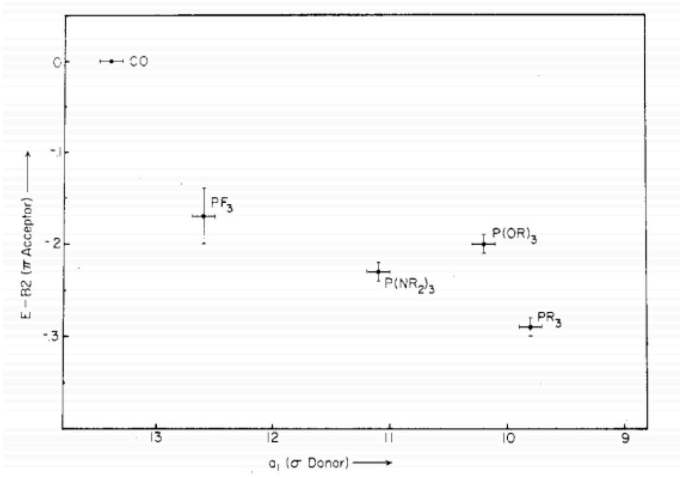


Figure 1-3: σ- π PES analysis. Reprinted with permission from Hall and his co-workers, Inorganic Chemistry*, 1978, 17, 2269-2275. Copyright (2019) American Chemical Society.* [22]

Generally speaking then, both the σ-donor and π-acceptor strengths of the phosphines depend on the electron-donating/withdrawing effects of their substituents. The two strengths often oppose one another (as shown in Figure 1-3) – trialkyl-phosphines are among the strongest σ-donors, but are not significant π-acceptors; trifluorophosphine

(and trihalophosphines in general), are among the weakest σ-donors but are very strong π-acceptors.

1.2.2 Steric Properties of Phosphines

The steric properties of phosphines have been studied extensively since the pioneering work of Tolman in 1970,[8,23] in which he proposed a structural parameter called the "cone angle" (later referred to as the "Tolman cone angle"). The angle is defined by the outer edges of the van der Waals spheres of the substituents at phosphorus and the metal centre of a space-filling model, as shown Figure 1-4 (left).[23]

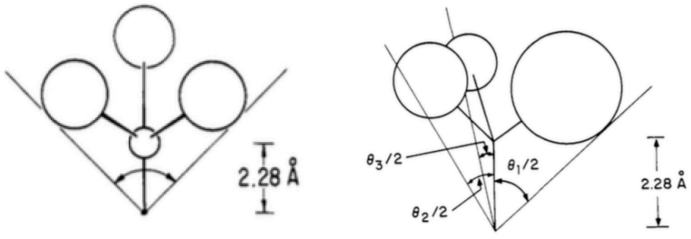


Figure 1-4: The cone angle for symmetric phosphines (left);[23] the cone angle for unsymmetrical phosphines (right). Reprinted with permission from Tolman, Chemical Reviews*, 1977, 77, 313-348. Copyright (2019) American Chemical Society.*[1]

In addition, the cone angle of unsymmetrical phosphine is slightly different – it is defined by a model that minimizes the sum of half-angles following the equation 1.2:

$$\theta = \frac{2}{3}\sum_{i=1}^{3}\frac{\theta_i}{2} \qquad 1.2$$

where each half-angle is defined as shown in Figure 1-4 (b).

Table 1-3: A summary of Tolman Cone Angle and solid angle data for various phosphines

PR_3	Cone Angle	Solid Angle[24-28]
PH_3	87	
PF_3	104	
$P(OMe)_3$	107	113
PMe_3	118	124
PMe_2Ph	122	126
$PHPh_2$	128	112
$P(OPh)_3$	128	135
PEt_3	132	143
PPh_3	145	129
$PPh_2{}^tBu$	157	149
PPh^tBu_2	170	168
PCy_3	170(163-181)[a]	181
P^tBu_3	182	
$P(o\text{-tol})_3$	194(183-196)[a]	142
P(mesityl)$_3$	212	

a. Cone angle range determined from X-ray diffraction studies of a series of metal complexes.

The Tolman cone angles of selected phosphines are summarised in Table 1-3. Clearly, as the pendant substituents get bigger the angle increases. However, there is a significant drawback with this steric parameter, in that it depends on the complex for which the geometric parameters are measured. Different complexes can feature different conformations of the same phosphine and therefore (as shown with PCy_3 and $P(o\text{-tol})_3$, for example, in Table 1-3) a range of cone angles can be determined.

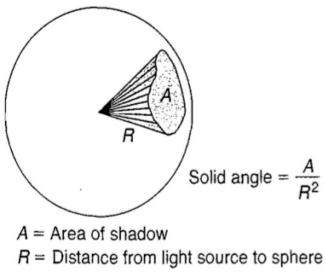


Figure 1-5: The definition of phosphine solid angle. Reprinted with permission from Hartwig, Organotransition Metal Chemistry - From Bonding to Catalysis, University Science Books, 2010, ch. 2, pp. 27-84. Copyright (2019) University Science Books.[3]

Therefore, a concept called “solid angle” based on a three-dimensional (rather than two-dimensional) angle, was subsequently proposed,[27] as defined in Figure 1-5. The corresponding values for this parameter for a range of phosphines are also listed in Table 1-3.

1.3 Carbenes

Carbenes are neutral compounds containing a divalent carbon centre with two non-bonding electrons, and therefore possessing six valence electrons.[29] The geometry of the carbenic carbon can be either linear or bent – a linear carbene system has formal sp-hybridization and degenerate pπ-orbitals, while in a bent carbene system one of the p-orbitals gains s-character to form a σ-orbital (at the expense of the C-X bonding orbitals), with the other p-orbital remaining unchanged (usually labelled pπ, as shown in Figure 1-6).

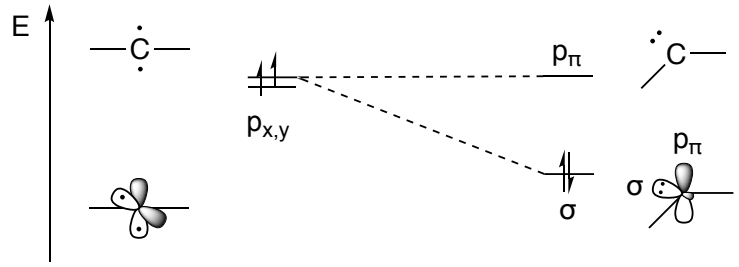


Figure 1-6：Change of ground spin-state upon the modification of carbene geometry.

The geometry of the carbene will affect its ground spin-state. Most carbenes have bent geometries, and depending on the energy gap between the σ and pπ orbitals, the molecule can adopt either a singlet or a triplet ground spin-state (Figure 1-7). A theoretical study by Hoffmann suggested that an energy gap of at least 2 eV is necessary to impose a

singlet group state, whereas an energy gap with less than 1.5 eV typically leads to a triplet state with one electron in each of the σ and pπ orbitals.

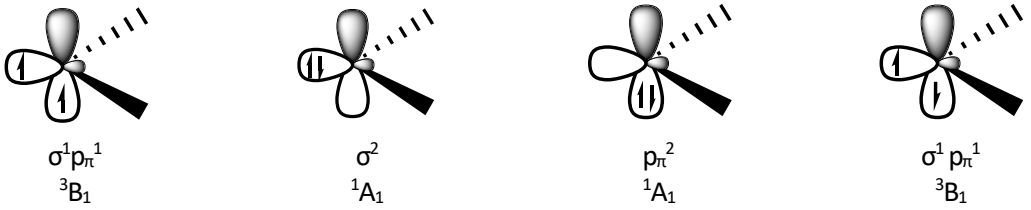


Figure 1-7: Potential orbital occupancies and electronic states arising for a bent carbene.

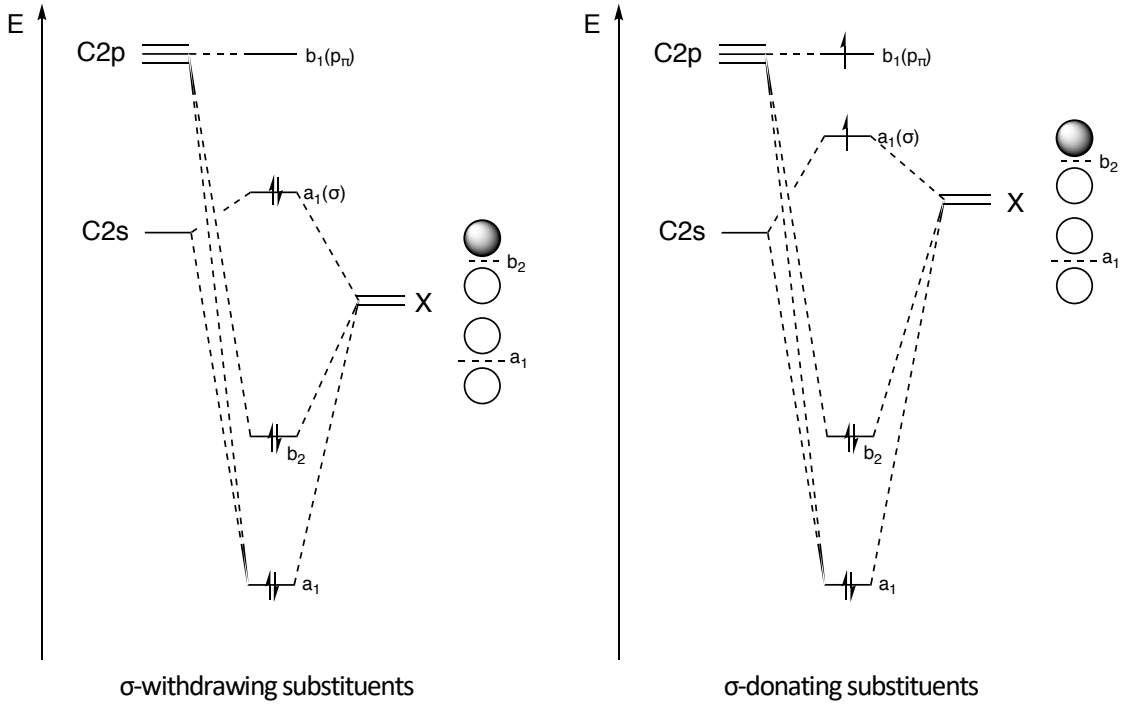


Figure 1-8: Orbital diagrams for a carbene, CX_2, when (a) X = σ-withdrawing substituent; (b) X = σ-donating substituent.

The spin-state of a generic carbene CX_2 depends on the donating or withdrawing effects (via both σ and π framework) of the X substituents. An inductively withdrawing substituent stabilises the σ orbital (which has C-X σ∗ character), thereby increasing the

energy gap and favouring a singlet ground state (Figure 1-8). By contrast, a σ-donating substituent decreases the energy gap and hence favours the triplet state.

The two spin states confer different modes of reactivity on the carbene due to spin conservation rules. The lone pair of a singlet carbene acts as σ-donor and its empty pπ orbital act as π-acceptor – such systems are known to insert into polar bonds such as N-H and O-H; triplet carbenes on the other hand, possess two unpaired electrons in two different orbitals and therefore behave as a diradicals – they can add across C-H and C=C bonds but with reduced stereoselectivity as the addition process is not concerted. In addition, carbenes (irrespective of spin state) have the tendency to dimerise to complete the octet valence at carbon. Based on the principles outlined above, carbenes form complexes with a wide range of metal systems, including main group metals,[30-36] and transition metals,[37-48] as well as the lanthanides and actinides.[49-52]

In 1964, Fischer and Maasböl reported the first stable transition-metal carbene complex.[53] Adding methyllithium to $W(CO)_6$ in diethyl ether under an inert atmosphere resulted in nucleophilic addition to the carbon of a CO ligand; the reaction was followed by protonation and then methylation with CH_2N_2 to eventually yield $W(CO)_5[C(OMe)Me]$ (Figure 1-9).

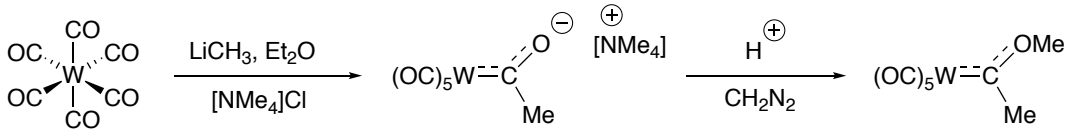


Figure 1-9: Synthesis of the first Fischer carbene complex.

These Fischer-type carbenes are singlet carbenes and rely on stabilisation of the carbon centre by π-donating substituents. They are σ-donor/π-acceptor ligands that usually coordinate to low oxidation state, mid- to late- transition metal centres.

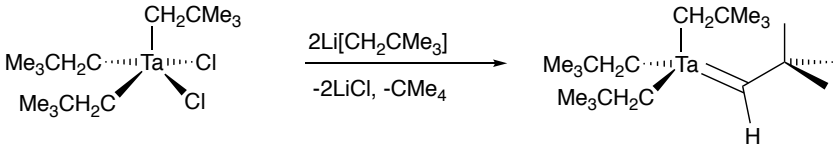


Figure 1-10: The synthesis of the first Schrock alkylidene complex.

In 1974, Schrock reported a second class of stable transition-metal carbene complexes, the first of which was obtained by treating $Ta[CH_2CMe_3]_3Cl_2$ with two equivalents of neopentyllithium.[54] The resulting complex $Ta[CH_2CMe_3]_3CHCMe_3$, often described as an alkylidene complex, bears a carbene featuring an alkyl substituent (Figure 1-10).

These alkylidene ligands (Schrock carbenes) formally possess a -2 charge, while Fischer carbenes are formally neutral. In a Schrock carbene, there is no π-donation from the (alkyl or H) substituents to the carbenic carbon and therefore the energy of the pπ orbital is lower, and the gap between the σ and pπ orbitals is narrowed. Hence, Schrock carbenes are regarded as possessing triplet configurations.

1.3.1 N-Heterocyclic Carbenes (NHCs)

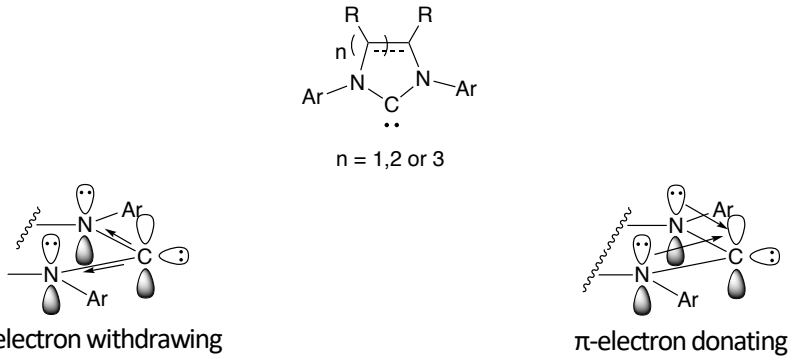


Figure 1-11: Generic structure of an N-heterocyclic carbene (upper) and depiction of the electronic effects induced by α-amino groups (lower).

As a sub-category of carbene, NHCs, are cyclic diaminocarbenes (upper row, Figure 1-11) which form Fischer-type complexes with transition metals.[48, 55] Importantly, NHCs are stabilised by the inductive and mesomeric effects of the α-nitrogen heteroatoms (lower row, Figure 1-11): the nitrogen atoms have higher electronegativity than carbon and therefore lower the energy of the HOMO σ orbital (σ-electron withdrawing, inductive effect) and enlarge the singlet-triplet gaps of the NHCs (reported to be 65 – 85 kcal mol^{-1} across the NHC class[56]). On the other hand, the planar geometry of NHCs allows the lone pairs of the α-nitrogens to be donated to the carbenic carbon via the π framework thereby elevating the energy of the LUMO (π-electron donating, mesomeric effect). As such, NHCs typically feature relatively wide HOMO-LUMO gaps and singlet ground states.

The first species with such structural features was identified by Wanzlick in 1962 (Figure 1-12).[57] However, this NHC (**1**) does not possess sufficient steric hindrance in the vicinity of the carbenic carbon, and therefore dimerizes at room temperature to give the tetraamino alkene **2**, with 50% dissociation observed at 170°C.

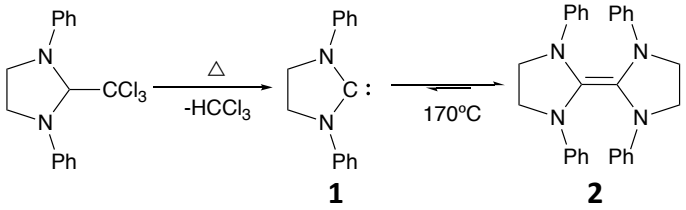


Figure 1-12: The Wanzlick equilibrium.

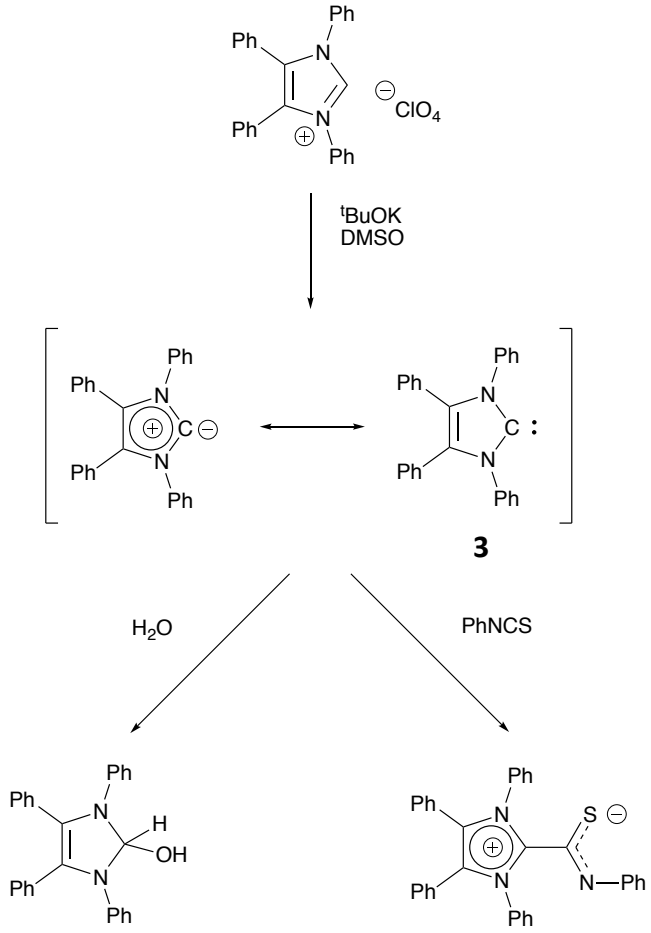


Figure 1-13: Products observed by Wanzlick and co-workers supporting the existence of a free NHC in solution.

A free monomeric NHC was not identified in solution until 1970, again by Wanzlick and his co-workers (**3**;Figure 1-13).[58] This was achieved by extending the π-framework of the heterocyclic ring with the unsaturated backbone, which increases the electron density in the pπ orbital of the carbenic carbon, preventing the NHC (**3**) from demerisation.

Reactions carried out with electrophilic species lead to nucleophilic addition of the NHC or deprotonation of an acidic proton (Figure 1-13). However, despite these reactivity studies, a free NHC was not isolated as a single substance until 1991.

Arduengo and his co-workers were the first group of researchers to isolate a crystalline free NHC in 1991 (Figure 1-14).[59] The use of extremely bulky adamantyl groups as N-substituents, delivered enough steric hindrance to prevent the NHC (**4a**) from dimerizing, and conferred sufficient kinetic inertness for isolation and characterisation by X-ray crystallography.

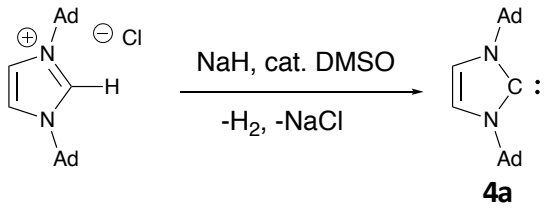


Figure 1-14: Synthesis of the first isolable crystalline NHC.

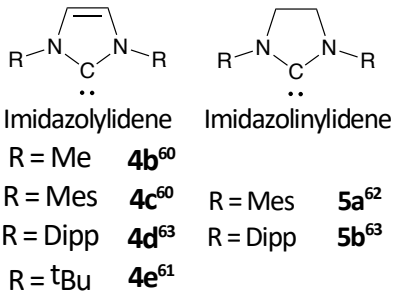


Figure 1-15: A selection of the NHCs developed by Arduengo and co-workers.

Following this path, Arduengo and his co-workers went on to synthesise NHCs featuring a range of substituents, some of which are among the most commonly applied in chemistry today (Figure 1-15).[60-63] Such systems typically employ modified N-substituents with different steric demands to tune the kinetic stabilization provided to the carbenic

centre, as well as (for example) a saturated backbone to further enhance the steric shielding (due to widening of the NCN angle).

These landmark studies opened up a range of possibilities to tune the structures of NHCs, with variation not restricted to the N-substituents and the bond order of the backbone. With reference to Figure 1-11, there are several other features that can be modified, including the size of heterocyclic ring and the substituents on the backbone itself. These peripheral features have the potential to influence the electronic and steric properties at the carbon centre.

1.3.1.1 Expanded Ring NHCs

Expanding the heterocyclic backbone of an NHC is considered to have three effects. Firstly, there is increased steric hindrance in the vicinity of the carbenic carbon, since the NCN angle becomes wider. Secondly, the σ-donation is strengthened due to increased p-character in the C-centred lone pair as a result of the increased NCN angle. Thirdly, the lack of aromaticity in saturated systems leads to decrease of energy of the pπ-orbital at the carbenic carbon and hence increased potential for back-bonding.[64, 65] Saturated NHCs have therefore been reported to be stronger σ-donors and π-acceptors than their unsaturated counterparts, leading to stronger metal-carbon bonds.[66]

The first example of an NHC based on a 6-membered heterocyclic ring was reported by Alder and his co-workers in 1999.[67] The synthetic method used is similar to that used for the synthesis of the first saturated, 5-membered NHCs (Figure 1-16). In contrast to its 5-membered analogue, however, the 6-membered NHC did not dimerize due to increased steric hindrance.

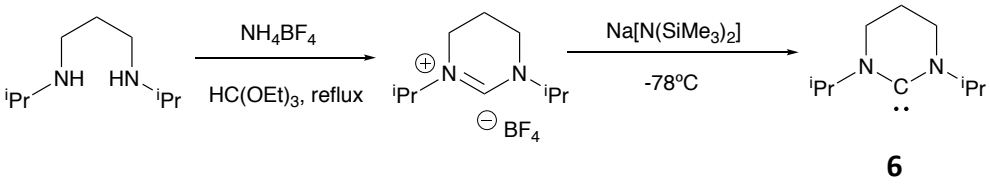


*Figure 1-16: Synthesis of the first 6-membered NHC (**6**).*

Notably, in the presence of an extra equivalent of base, such as $K[N(SiMe_3)_2]$, coordination of **6** to K^+ is observed; similar chemistry is observed in the presence of Na^+. These systems were the first examples of non-lithium, group 1 complexes of NHCs.

An unsaturated analogue featuring a 6-membered heterocycle was reported four years later, by Richeson and his co-workers, using a 1,8-naphthylenediyl backbone (**7**, Figure 1-17).[68] In this case the 6-membered heterocyclic ring is planar and the aromatic π-electrons can, in principle, conjugate with (and hence stablise) the carbenic carbon. However, the authors commented that the $N\text{-}C_{naphthyl}$ bond lengths (average = 1.414(6) Å) are relatively long, suggesting that the nitrogen lone pairs are predominantly involved with interaction with the carbenic carbon, and do not delocalize effectively into the naphthyl framework.

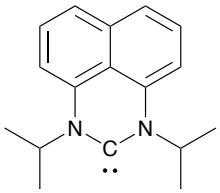


*Figure 1-17: The structure of **7**.*

The first example of NHC with a 7-membered heterocyclic ring was not reported until 2005, by Stahl and co-workers,[69] based on a diaminobiphenyl core (upper, Figure

1-18). The free NHC was not isolated, as deprotonation – even of the rigorously dried amidinium salt (**8**), with a variety of bases resulted into decomposition. Instead, deprotonation in a THF solution of $[PdCl(allyl)]_2$ allowed for the isolation of the NHC-Pd(II) complex **9**. Amidinium salt (**8**) could also be accessed in enantiomerically pure form by using a single enantiomer of the precursor diamino-BINAP.[70] Stahl and co-workers also attempted to synthesise other 7-membered NHCs featuring a range of different N-substituents.[69, 70] However, attempts to isolate systems featuring 2,6-diisopropylphenyl (Dipp) or mesityl (Mes) groups (two of the most commonly employed N-substituents) were unsuccessful, a finding which was thought to reflect the weak nucleophilicity of the diaryl-substituted nitrogen atoms.

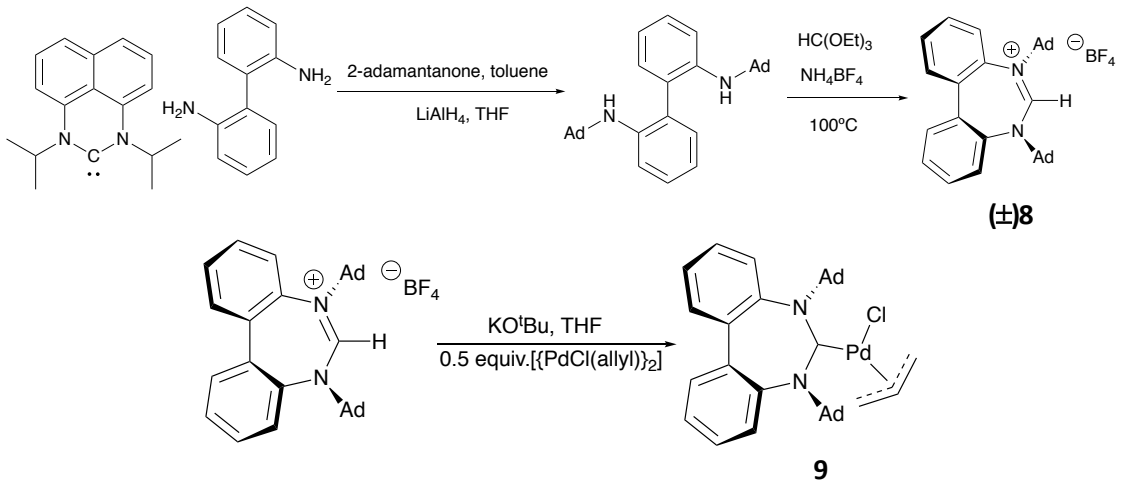


Figure 1-18: Synthesis of the first 7-membered biphenyl salt (upper); preparation of the corresponding Pd(II) NHC complex (lower).

These 7-membered NHCs were the first class of NHC to exhibit a non-zero torsion angle (α) between the N-substituents (Figure 1-19), as defined by Fallis and co-workers.[71] This distortion is due to the greater degree of freedom inherent in the backbone, and deviation from the ideal value of 120° for the C-N-C angles. As such, the backbone can twist

to reduce the strain energy at the sp^2 nitrogen atoms. In an analysis by Fallis, the average angles around the nitrogen atoms in a selection of 7-membered NHC complexes and salts were calculated. These average values sum to 359.3°, illustrating the planarity of the fragment at nitrogen even though the torsion angles between the N-substituents are not zero.

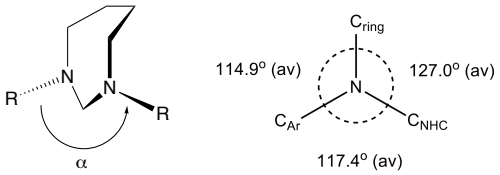


Figure 1-19: The torsion angle (α) between two N-R bonds (left), and depiction by Fallis showing the average angles around the nitrogen in 7-membered NHCs and their complexes (right.)

A variety of expanded ring NHCs have subsequently been reported;[72-74] a number of these are in a report from Fallis and co-workers describing the syntheses of N-aryl expanded ring NHCs.[71] A general synthetic route (Figure 1-20) suitable for the majority of N-aryl systems was developed, and the products are reported to be highly robust when stored in a dry atmosphere. An exception to this relates to the subset with a C=C double bond in the backbone (e.g. **11**).

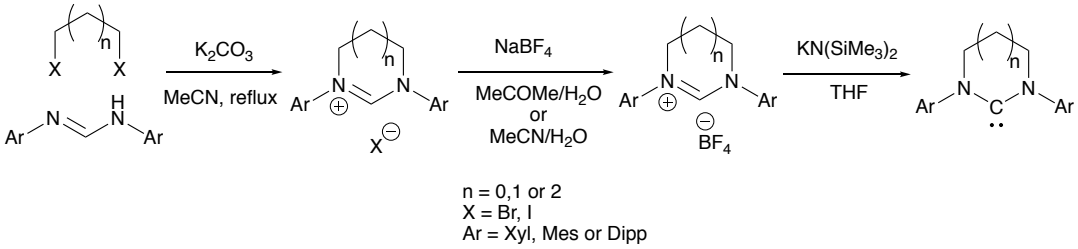
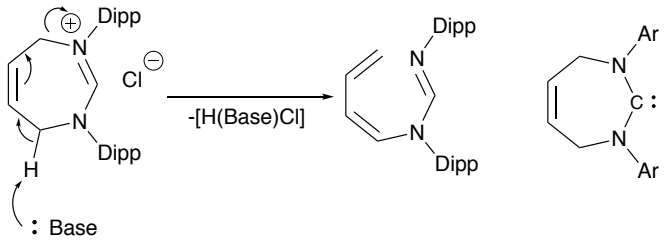


Figure 1-20: A general synthetic route for N-aryl expanded ring NHCs.[75]



10 **11**

*Figure 1-21: Backbone deprotonation of **10** (left); hypothetical carbene **11** derived from deprotonation at the amidinium position of **10** (right).*

11 has never been isolated as a free NHC due to cleavage of an N-$C_{backbone}$ bond by either a base or another equivalent of NHC,[75] rather than deprotonation at the desired amidinium function (Figure 1-21).

Heterocyclic rings in NHC systems were further expanded in 2011, when Cavell and co-workers reported a series of 8-membered NHCs.[76] This class of NHCs was found to have significant increase in steric hindrance, even for smaller aryl groups. The reaction times typically required to form the 8-membered heterocycle are, however, longer (10-14 d, cf. >7 d for smaller ring sizes[71]), but yields are reported to be greater than 75% (cf. 70%-90%[71] for smaller heterocycles). As these synthetic reactions require significant time investment, few examples of 8-membered NHC complexes have been reported in the literature.

1.3.1.2 Assessments of the Electronic Properties of NHCs

NHCs are considered to be strong σ-donors and to exhibit weakly π-accepting behaviour, based on a series of spectroscopic studies.[32, 39, 77] They have been described as behaving as phosphine (especially trialkylphosphine) mimics.[78] As Öfele concluded in 1993, "Both in terms of ligand properties and metal complex synthesis, they (NHCs) closely

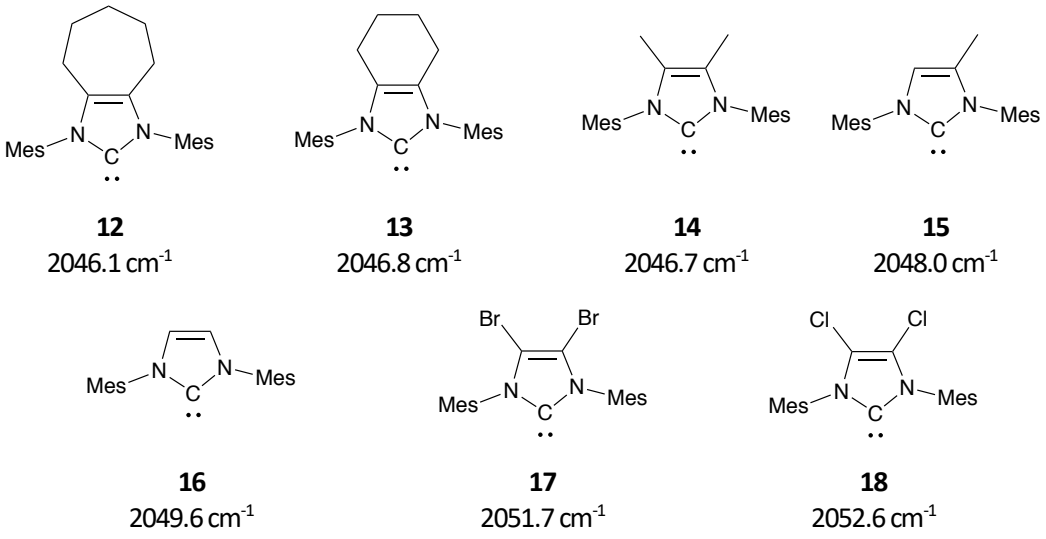
resemble electron-rich phosphines, e.g. trimethylphosphine."[79] However, it is now widely accepted that, in general, NHCs are better σ-donors than even the most σ-donating phosphines.[78]

In 1997, Green and co-workers investigated Pd/Pt NHC complexes using photoelectron spectroscopy (PES) and density functional theory (DFT). Interactions via the π framework were found to be very weak and the predominant binding between the metal and ligand fragments was reported to be via the σ framework.[80] Other than transition metal systems, a wide range of studies on NHC complexes of p-block elements,[30, 33, 34, 36] lanthanides,[49, 81, 82] alkaline earth[31, 77, 83] and even some alkali metals[67, 84] have been reported to provide evidence of strong σ-donation, thereby serving as circumstantial evidence of strong σ-donation and weak π-accepting capabilities.

In addition to PES and DFT methods, there are several spectroscopic techniques that have been used to analyse and quantify the electronic properties of NHCs. One of the most frequently used techniques exploits the CO stretching frequencies of carbonyl-containing carbene complexes,[9, 85-87] via the Tolman Electronic Parameter (TEP),[87] mentioned above. However, as mentioned in section 1.2.1, the TEP measures the overall effect of both the donor and acceptor characteristics of the ligand, not the σ-donor strength in isolation.

Alternatively, the chemical shift of carbenic carbon (free ligand) in ^{13}C NMR spectra has been advanced as a method for measuring the σ-donor strength.[88, 89] The shifts generally appear in the region δ_C = 200-260 ppm, due to the electron deficiency at the low-valent carbon centre.[88] A higher chemical shift has been reported to be associated with strong σ-donor properties; however, there are other important factors influencing the ^{13}C NMR chemical shift. A reduction of electron density in pπ-orbital would also increase the

^{13}C NMR chemical shift,[90, 91] and a change of angle at the carbenic carbon affects the chemical shift too.[88, 92] A smaller singlet-triplet gap also causes a downfield shift, as it allows mixing between the σ- and pπ-orbital which significantly affects the σ_p shielding parameter.[91] So, although a stronger σ-donating NHC would typically give a higher ^{13}C NMR chemical shift when compared to weaker donors, the chemical shift is not solely a function of the σ-donor strength as other factors play important roles. Therefore, the ^{13}C NMR chemical shift is an informative parameter of the electronic properties of NHCs, but needs to be used with caution in comparison, especially between carbenes that are significantly different in structure.



12 2046.1 cm^{-1} **13** 2046.8 cm^{-1} **14** 2046.7 cm^{-1} **15** 2048.0 cm^{-1}

16 2049.6 cm^{-1} **17** 2051.7 cm^{-1} **18** 2052.6 cm^{-1}

Figure 1-22: TEPs of NHCs featuring different backbone substituents.

As mentioned above, functional groups attached to the backbone of the heterocycle (i.e. the R groups in Figure 1-11) also influence the electronic properties of NHCs. Nolan and co-workers have summarised the TEPs of a wide variety of NHCs, including a selection featuring different backbone substituents.[87] As illustrated in Figure 1-22, the NHC with most electron-donating backbone substituents (**12**) has the lowest TEP

value, indicating the strongest donor strength; while the NHC with the most electron-withdrawing backbone substituent (**18**) has the highest TEP value, being the weakest donor in this selection. Notably, NHC **18** has such a weak donor strength that it can be handled with short exposure to moist air without decomposition.[63]

1.3.1.3 Steric Properties of NHCs

The size of the heterocyclic ring and the identity of the N-substituents are the two principal features that affect the steric properties of NHCs, which can conveniently be quantified by the "buried volume" parameter ($\%V_{bur}$) developed by Nolan, Cavallo and co-workers.[93-95] The $\%V_{bur}$ of an NHC refers to the percentage of a sphere occupied or "buried" by the ligand upon coordination to a metal at the centre of the sphere (Figure 1-23). The fixed parameters associated with this approach are a value of 2 Å for *d*, the metal-carbene bond distance and 3 Å (or sometimes 3.5 Å) for *r*, the sphere radius. The $\%V_{bur}$ values can be determined from X-ray crystallographic data or from theoretical calculations, with either the free NHC, an NHC metal complex or the protonated salt precursor being the data source. The data can now be processed with the SambVca (Salerno molecular buried volume calculation) software developed by Falivene and co-workers.[96]

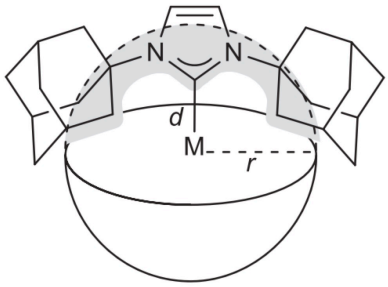


Figure 1-23: The demonstration of "buried volume" parameter (%V_{bur}) for NHCs bound to a metal. Reprinted with permission from Glorius and co-workers, Nature*, 2014, 510, 485-496. Copyright (2019) Springer Nature.*[97]

Steric bulk closer to the carbenic carbon (e.g. the ortho-substituents attached to aromatic groups), has the greatest effect on %V_{bur} values. Hence, for the complexes of the type (NHC)AuCl we observe the trend IMes < IDipp < I^{t}Bu. The limitations of this model are exemplified when square-planar systems are analysed, such as (NHC)IrCl(CO)$_2$. The %V_{bur} values are altered, and IDipp replaces I^{t}Bu as the largest ligand in the series, a finding which is thought to stem from the conformations adopted by the substituents and inherent ligand flexibility. Ligand flexibility has now been incorporated into the %V_{bur} model by dynamic DFT studies, as reported by Cavallo and co-workers.[98]

Table 1-4: %V_{bur} values for NHCs in (NHC)AgX complexes based on X-ray crystallographic data, with r = 3.5 Å, d = 2.0 Å and bond radii scaled by 1.17.[76]

Complex	Size of Ring	%V_{bur}
Ag(IMes)Cl	5	36.1
Ag(5-Mes)Cl	5	36.1
Ag(6-Mes)Cl	6	44.0
Ag(7-Mes)Br	7	44.7
Ag(8-Mes)Br	8	48.7

The size of the heterocyclic ring also contributes greatly to %V_{bur} values (Table 1-4). Based on studies of (NHC)AgX complexes, the %V_{bur} values increase as the ring expands, dramatically between 5-membered ring and 6-membered ring, and then between the 7-

membered and 8-membered ring systems. There is little difference between 6-membered and 7-membered ring due to the geometry flexibility of the backbone.

In a review by Nolan and co-workers, it was illustrated that the Tolman cone angle and $\%V_{bur}$ values for a wide range of phosphines have a good correlation with each other and therefore, $\%V_{bur}$ could be used as a useful comparison of the steric properties of phosphines and NHCs.[99] In this report, the $\%V_{bur}$ values for the most common NHC ligands, range from 26%-52%.

$\%V_{bur}$ values have also been found to have a good correlation with bond dissociation enthalpies (BDEs), in early studies based on Cp*Ru(NHC)Cl systems (Figure 1-24).[93, 95] These data highlight the influence of steric effects on the strength of the interaction between the NHC and the metal centre.

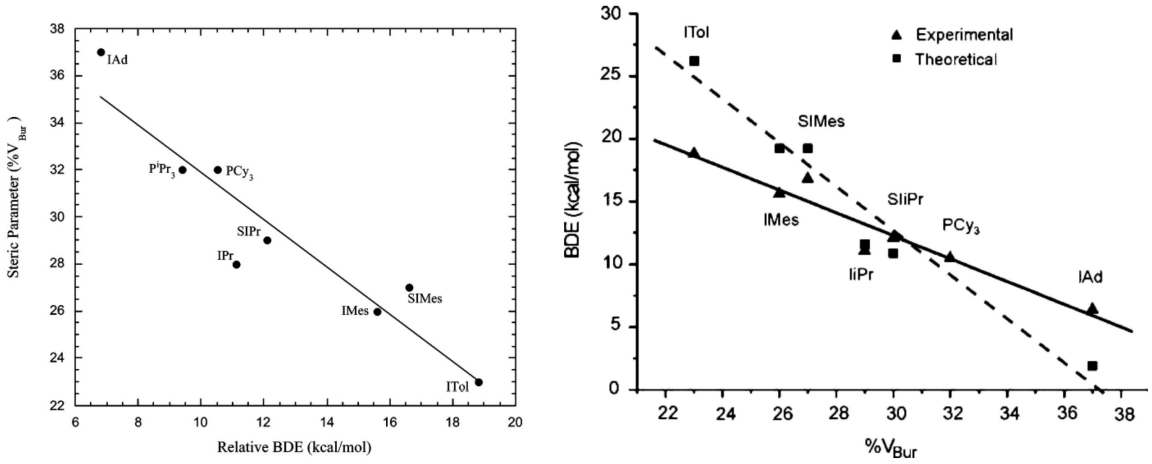
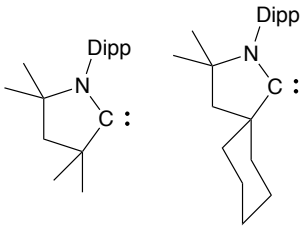


Figure 1-24: Plots showing the association of the $\%V_{bur}$ with BDE. Reprinted with permission from Nolan and co-workers, Organometallics*, 2003, **22**, 4322-4326. Copyright (2019) American Chemical Society (left),[93] and Cavallo and co-workers, Journal of Organometallic Chemistry, 2005, 690, 5407-5413. Copyright (2019) John Wiley and Sons (right).[95]*

1.3.2 Cyclic (Alkyl)(Amino)Carbenes (CAACs)



19 **20**

Figure 1-25: Selected CAACs reported by Bertrand and co-workers. [100]

CAACs (such as those shown in Figure 1-25), were first reported in 2005,[100] and represent another type of carbene finding widespread use in organometallic and main group chemistry; their properties are often compared with those of NHCs.[97, 101, 102] The main difference with CAACs is that they feature only one nitrogen atom in the heterocyclic ring. Thus, in comparison with NHCs, they feature only one α-nitrogen atom engaged in inductive electron withdrawal from the carbenic carbon via the σ framework, with the α-alkyl group donating electron density towards the carbon. In addition, the extent of electron donation to the carbenic pπ orbital is similarly reduced (Figure 1-26). Consequently, CAACs feature smaller HOMO-LUMO gaps and exhibit stronger σ-donating and π- accepting capabilities than NHCs.[101]

As CAACs exhibit both strong σ-donating and π-accepting capabilities, the experimental methods for quantifying the electronic properties of NHCs and phosphines, such as TEP values, do not provide enough detail to understand in depth the electronic properties of CAACs. To solve the problem, several methods have been developed to independently quantify the π-acceptor strengths of these ligands which, when combined with TEP values, allow the 'isolated' σ-donor strength to be assessed.

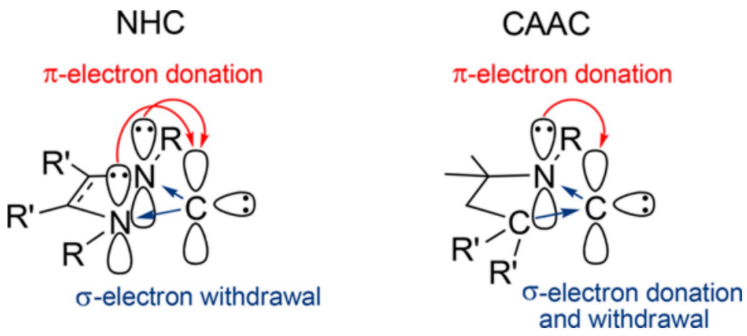


Figure 1-26: Schematic representation of electronic effects in imidazole(id)in-2-ylidenes and CAACs. Reprinted with permission from Inoue and co-workers, Chemical Reviews, 2018, 118, 9678-9842. Copyright (2019) American Chemical Society.[101]

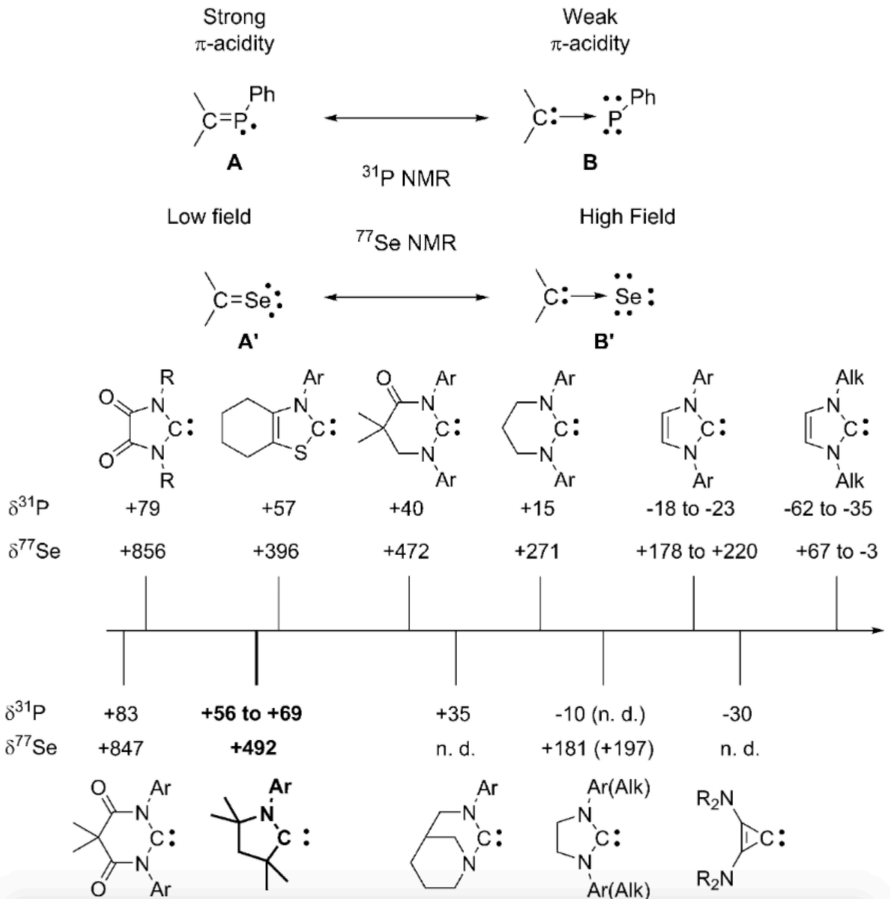


Figure 1-27: Resonance structures of the carbene-phosphinidene and carbene-selenium adducts (upper); The π- accepting properties of carbenes based on [31]*P and* [77]*Se NMR chemical shifts of these adducts (lower). "n.d." = not determined. Reprinted with permission from Bertrand, Angewandte Chemie-International Edition, 2017, 56, 10046-10068. Copyright (2019) John Wiley and Sons.*[102]

One of the methods developed, referred to as the "P-scale", utilizes the ^{31}P NMR chemical shifts of phenylphosphinidene-carbene adducts, and is based on the two resonance structures commonly associated with such species (Figure 1-27).[103, 104] Resonance structure A features a C=P double bond, and is most important for the strongest π-accepting carbenes (and gives rise to a downfield ^{31}P NMR chemical shift). Resonance structure B on the other hand reflects a relative lack of π-acceptor characteristics and gives rise to an upfield ^{31}P NMR chemical shift, with more electron density residing on the phosphorus atom. Within the family of carbenes (Figure 1-27), CAAC **19** (Figure 1-27) is one of the strongest π-acceptors, being weaker only in this respect than NHCs with very strongly electron withdrawing backbone substituents. This trend is further supported by the work of Ganter and co-workers, in which ^{77}Se NMR chemical shifts of carbene-selenium adducts were investigated, based on similar principles.[105, 106] Notably, unlike TEP values, the ^{31}P and ^{77}Se NMR chemical shifts for these phenylphosphinidene- and selenium-carbene adducts cover a wide spectral range. This feature allows clearer differentiation between carbenes.[103, 104, 107]

1.3.3 Diazaborolyl Ligands

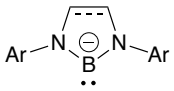


Figure 1-28: Anionic diazaborolyl ligand isoelectronic with an NHC.[123]

Diazaborolyl ligands are isoelectronic analogues of NHCs that feature a boron atom instead of the carbenic carbon in the heterocyclic ring (Figure 1-28). The diazaborolyl ligand family represents a subset of boryl ligands, which were first claimed in 1952 in the form of

alkali metal salts (albeit with no structural characterisation).[108, 109] There were several reports of transition metal complexes featuring boryl ligands dating back to the 1960s;[110, 111] however, the first structural characterization of such a compound was not published until the 1990s.[112, 113] Subsequently, many studies of the synthesis and reactivity of boryl-metal complexes have been reported.[114-122]

The development of nucleophilic sources of diazaborolyl ligands opened up a new phase of boryl ligand chemistry. Since 2006 and the availability of a boryllithium species of this type,[123-125] researchers have had another choice of synthetic methodology for preparing complexes containing the diazaborolyl ligand, i.e. by utilizing a nucleophilic boron reagent in metathesis processes.[118] The preparation of the boryllithium reagent reported by Yamashita and Nozaki requires only two steps: synthesis of the bromoborane precursor, followed by lithiation (Figure 1-29).[123]

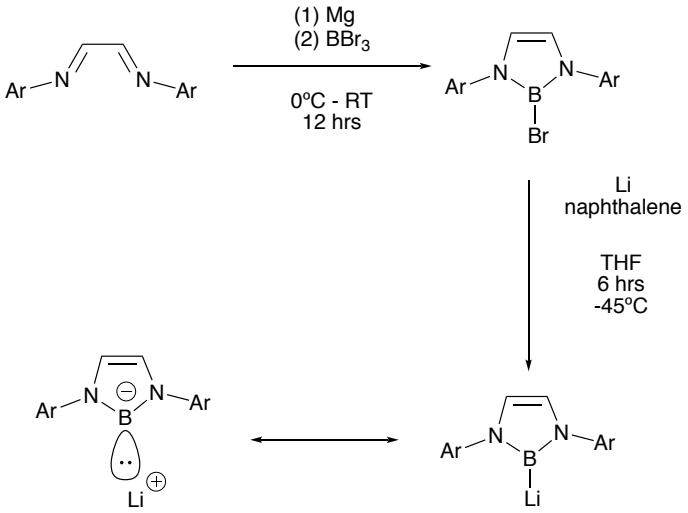
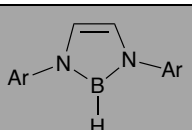
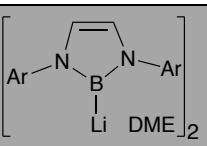
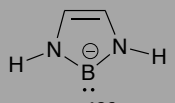
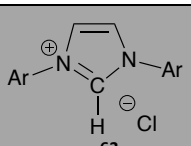
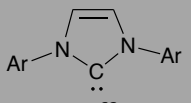


Figure 1-29: The synthesis of boryllithium.[123]

In terms of structural data (Table 1-5), boryllithium complex **22** closely resembles the results of theoretical studies on the naked boryl anion **23** reported in 1998.[126]

Comparison with the corresponding hydroborane (**21**) reveals that **22** has longer B-N bond lengths and a narrower N-B-N angle. These differences (0.02 Å) are similar to those between imidazolium salt **4d** and imidazolylidene **24**, and in the case of **21**/**22**, the difference stem from the highly polarised B-Li bond and anionic character of the boron centre.[123] The B-N bond lengths measured for **22** are longer than the corresponding C-N bond lengths in **4d** and the N-B-N angle is narrower (compared to the N-C-N angle in **4d**), presumably reflecting the larger size of boron compared to carbon.

*Table 1-5: Structural comparison of boryllithium **20** and related compounds. (Ar = Dipp)*

	 **21**[123]	 **22**[123]	 **23**[126]	 **24**[63]	 **4d**[63]
B/C – N (Å)	1.418(3)	1.465(4)	1.475	1.341(4)	1.364(3)
	1.423(3)	1.467(4)		1.338(5)	1.369(3)
N-B/C-N (°)	105.25(16)	99.2(2)	97.72	107.6(3)	101.5(2)

1.4 N-heterocyclic Iminato (NHI) Ligands

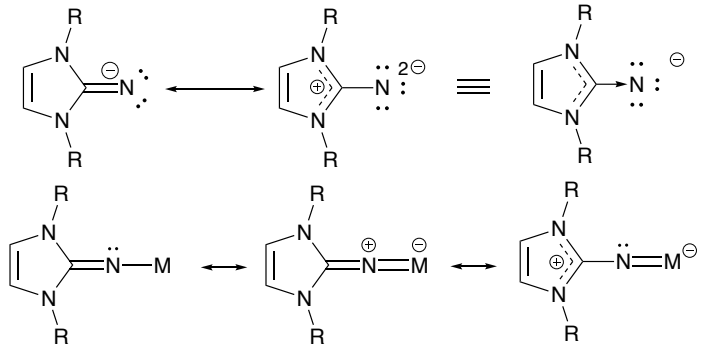


Figure 1-30: Selected resonance structures of an NHI ligand (upper) and of a generic complex with M^+(lower).[127]

NHI ligands, a subset of the class of η^1-guanidinates, are formally derived by attachment of an iminato group to the carbon centre of an NHC. They typically act as 2σ,

4π-electron donors (Figure 1-30) with the two π-molecular orbitals aligned orthogonal to each other and typically close in energy (Figure 1-31). Such systems are strong σ- and π-donors and offer significant potential in the stabilization of electron-deficient systems.[127] The donor strength of this ligand class benefits from its NHC derived core, (as summarised in previous section) which contributes significantly to the electron density localized on the exocyclic nitrogen. The donor strength is also attributed to negative charge on the imine group, with the charge separated (zwitterionic) resonance form emphasizing the electron richness at N. In addition, the N-heterocyclic ring can effectively stabilize the formal positive charge present in the same resonance structure (Figure 1-30) within its aromatic system.[128]

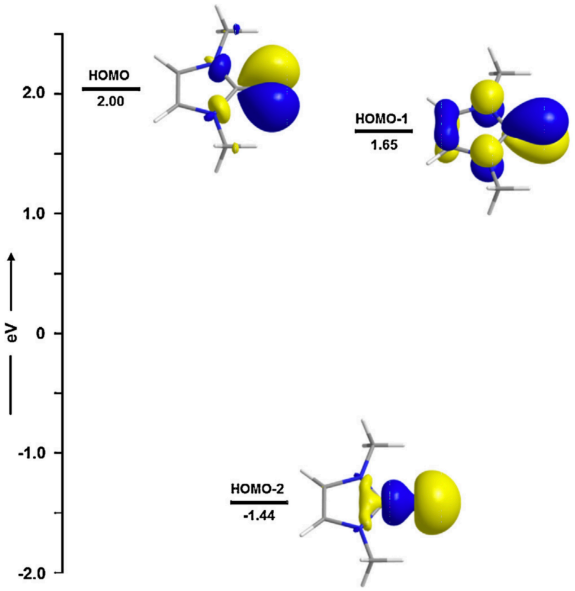


Figure 1-31: Contour plots and eigenvalues of the occupied frontier orbitals in the 1,3-dimethyllimidazolin-2-iminato anion, derived from a single-point DFT calculation. Reprinted with permission from Tamm and co-workers, Coordination Chemistry Reviews, 2014, 260, 116-138. Copyright (2019) John Wiley and Sons.[128]

The first NHI protio-ligand (**27a**) was synthesized by methylation of methylimidazolamine (**25**) followed by deprotonation of the 2-amino-1,3-dimethylimidazolium salt (**26**) with KH (upper row, Figure 1-32).[129] **27a** can be silylated to give **28a**, and **29** was also found to be accessible by reacting with a second equivalent of trimethylsilyl chloride (Figure 1-32).

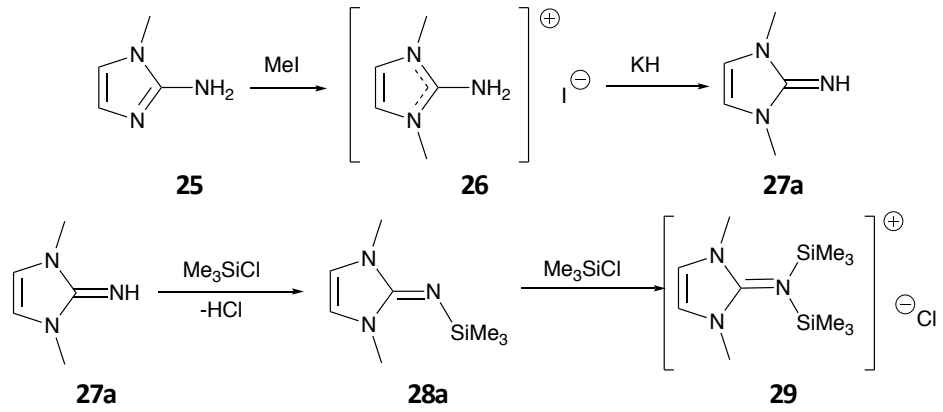
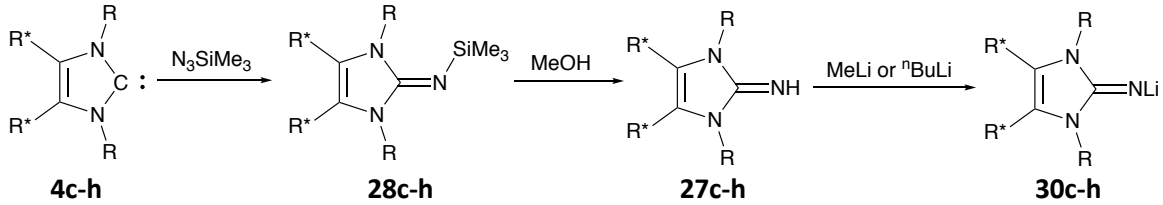


Figure 1-32: The synthesis of first NHI (upper) and its silylation (lower).



c: R = Mes, R* = H;
d: R = Dipp, R* = H;
e: R = ^{t}Bu, R* = H;
f: R = ^{i}Pr, R* = H;
g: R = ^{i}Pr, R* = Me;
h: R = Me, R* = Me

Figure 1-33: A general synthetic route to NHI protio-ligands and their lithiation.[128]

However, the synthetic method shown in Figure 1-32 was limited to **27a**, without application to other guanidinato (protio)-ligands. However, in 2004 and 2007 in two papers, Tamm *et al.* reported a synthetic route that is applicable to a range of guanidinato protio-ligands with different N- and backbone substituents (Figure 1-33).[128, 130, 131]

NHCs are the starting material in this synthetic route, with the initial step proceeding via a Staudinger-type reaction to form **28c-h** when treated with excess trimethylsilyl azide. Compounds **28c-h** can then be protonated by stirring in methanol to obtain **27c-h**, which can be converted to their corresponding lithium salts by deprotonation with an alkyllithium. In a different synthetic route reported by Bertrand in 2010, an analogue of **27d** was reported featuring a saturated backbone within the heterocyclic ring (Figure 1-34). The NHC is again the starting material for this process; instead of a subsequent reaction with an azide, however, **31** was synthesised via bromination and then treatment with ammonia.

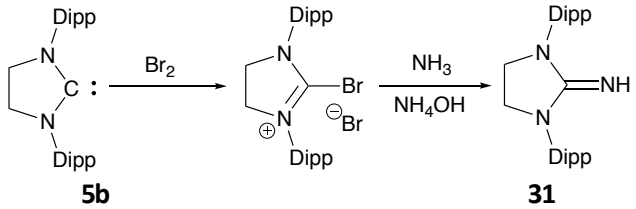


*Figure 1-34: The synthesis of backbone saturated analogue, **31**.*

1.5 Applications of Ligands with Different Electronic Properties in Main Group Chemistry

Table 1-6: Major differences between transition-metal and main-group compounds, as summarised by Power.[132]

Transition-metal compounds	Main-group compounds
Usually have partially occupied valence d orbitals that are often relatively close in energy	The valence s or p orbitals are either fully occupied or empty and are far apart energetically
Often coloured as a consequence of small orbital energy separations	Usually colourless
Often interact with small molecules such as CO, C_2H_4 or H_2	Generally do not interact strongly with CO, C_2H_4 or H_2
Often paramagnetic	Usually diamagnetic
Stereochemical electron pair character less pronounced	Have stereochemically active electron pairs which form the basis of VSEPR theory
Antiferromagnetic coupling is common	Antiferromagnetic coupling in stable compounds not common

In a review by Power in 2010, the chemistry of transition metals was compared to that of main-group elements (Table 1-6).[132] The greater range of reactivity of the former (especially in small molecule activation) was attributed in particular to the smaller HOMO-LUMO gap typically associated with d-block systems. To overcome the limitations imposed by much wider orbital separation, researchers have targeted several types of main-group compound that have similar behaviour to transition-metal complexes. Such species include:

(a) Compounds featuring multiple bonds between heavier main-group elements;[133-141]

(b) Stable (monomeric) low-valent derivatives with open coordination sites.[127, 142, 143]

Among systems of these types, ancillary ligand modification based on differing steric and electronic profiles (σ-donor strength, π-acceptor/donor behaviour) then offers a way to tune stability and reactivity.

1.5.1 NHCs in Compounds Featuring Multiple Bonds Between Heavier Main Group Elements

Since Lappert's synthesis of a Sn-Sn multiple-bond in 1976,[144] the chemistry of heavier main-group compounds featuring multiple bonds has been the subject of significant research effort,[133-141] including many different types of homo- and hetero-nuclear E-E bonds. Taking the heavier group 14 elements as examples, the structures are generally classified into three types (Figure 1-35).[138]

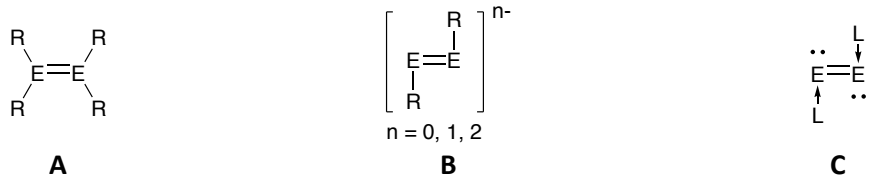


Figure 1-35: Types of dimeric group 14 compound featuring multiple bonds.

Among the three types of compounds, those of type **C** marked a milestone in the field, with its first example (E = Si) reported by Robinson and co-workers in 2008.[145] This compound (**34**) represents a rare example of a compound with dative coordination between a main group element and a ligand with the former in a formal oxidation state of zero - most such cases to have been reported involve transition metals. Compound **34** was obtained by the potassium graphite reduction of the neutral silicon tetrachloride carbene

complex, and depending on the reaction conditions, **33** could be produced as a side product (Figure 1-36).

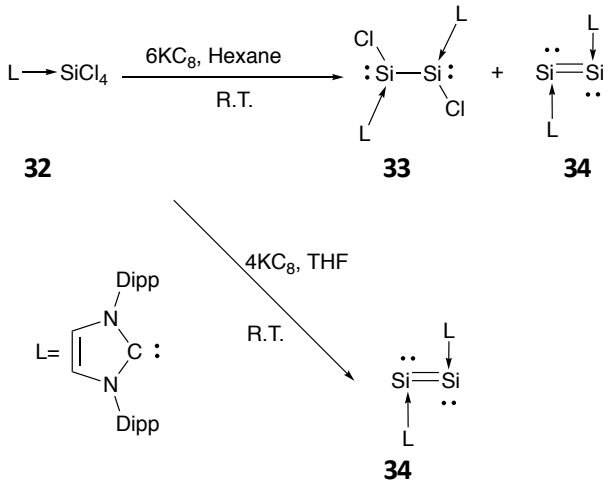
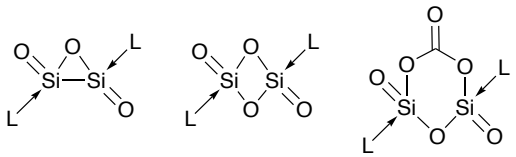


*Figure 1-36: The synthesis **33** and **34**.*

In **34**, the ancillary ligand L (the NHC **4d**) provides significant steric protection to the Si=Si double bond and prevents it from oligo-/polymerisation, while its strong σ-donor capabilities allow for stabilization of the electron deficient Si(0) system.

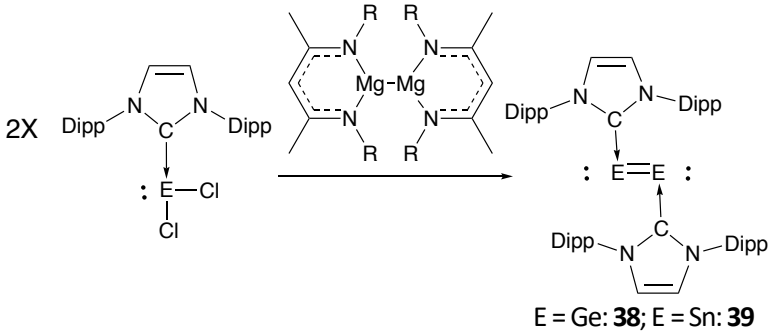
In further reactivity studies, **34** was shown to be a valuable precursor for oxidation and chalcogenation reactions. Its reactions with N_2O, O_2 and CO_2 result in the formation of derivatives **35**, **36** and **37**, respectively, in moderate yield (Figure 1-37).[146, 147] In this main-group system, the strongly electron donating NHC (**4d**) enhances the reactivity of the diatomic Si(0) system **34** toward small molecules by increasing the electron density at Si atoms, making it susceptible to oxidation.



35 **36** **37**

*Figure 1-37: Products of the reactions of **34** with N_2O, O_2 and CO_2, respectively.*

Following the path of Robinson, Jones and their co-workers synthesised the germanium and tin analogues of **34** (Figure 1-38).[148, 149] The starting materials in this case were slightly different – namely the NHC complexes of Ge(II) and Sn(II) dialides. Moreover a soluble magnesium(I) reductant was used in place of potassium graphite as a weaker (and more selective) reducing agent.



E = Ge: **38**; E = Sn: **39**

*Figure 1-38: Syntheses of NHC-stabilized diatomic germanium and tin complexes **38** and **39** (R = Mes).*

The E-E distances measured for **34**, **38** and **39** are within the range of E=E double bond lengths reported for compounds of type A (R_2EER_2). In addition, the allignment of the NHC donor with respect to the E=E fragment is very close to 90° (Table 1-7).

Table 1-7: Selected geometry data of NHC-stabilise diatomic E(0).[101]

	E-E distance (Å)	E-E distance of R_2EER_2 (Å)	NHC-E-E angle (°)
34	2.2294(11)	2.118-2.289	93.37(5)
38	2.3490(8)	2.206-2.285	89.87(8)
39	2.7225(5)	2.668-2.851	91.82(8)

The geometries of these NHC-stabilised diatomic E(0) systems can be rationalised by reference to the computational studies reported by Robison and Jones and their co-workers.[145, 149] As the lone pair has mainly s character (e.g. for **34**: 68.3% s, 31.6% p, 0.1% d character), the bonding between the two group 14 elements involves mainly orbitals of p-character. The NHC therefore interacts with a formally vacant p orbital at E, giving rise to an angle of ca. 90° with respect to the E=E fragment (Figure 1-39). Unfortunately, the NHC-stablised diatomic Pb(0) system could not be isolated.[148]

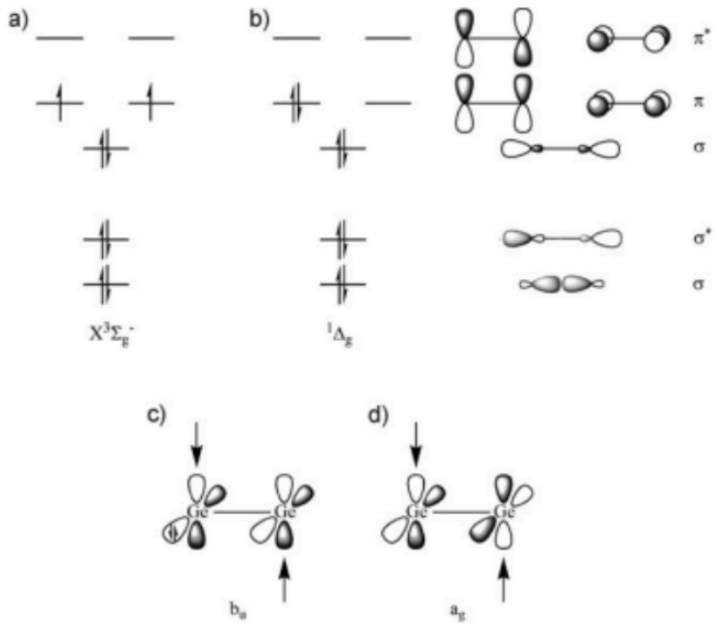


*Figure 1-39: Key molecular orbitals of **38-Me** (i.e. a model of **38** with the Dipp N-substituents replaced by Me) (a) in the ground state; and (b) first excited state. Reprinted with permission from Jones and co-workers, Angewandte Chemie-International Edition, 2009, 48, 9701-9704. Copyright (2019)} John Wiley and Sons.*[149]

Another landmark example of NHC-stabilised main-group multiple bonding is the diboryne (**40**) featuring a B≡B triple bond reported by Braunschweig and co-workers in 2012.[135] Subsequently, analogues featuring related carbene ligands (e.g. **43** and **46**, featuring saturated backbone NHC **5b** and CAAC **19**, respectively) were reported and their reactivity toward small molecules was compared (Figure 1-40).[151-154] From a geometric perspective, as the NHC **4d** is (formally) replaced by its saturated backbone counterpart **5b** and then by CAAC **19**, the B-B distance is lengthened, and the C-B distances are shortened (Table 1-8). This is an indication of electron density being withdrawn from B-B fragment via back-bonding to the ligand, implying that CAAC **19** has the greatest π acceptor strength, followed by NHC **5b**.

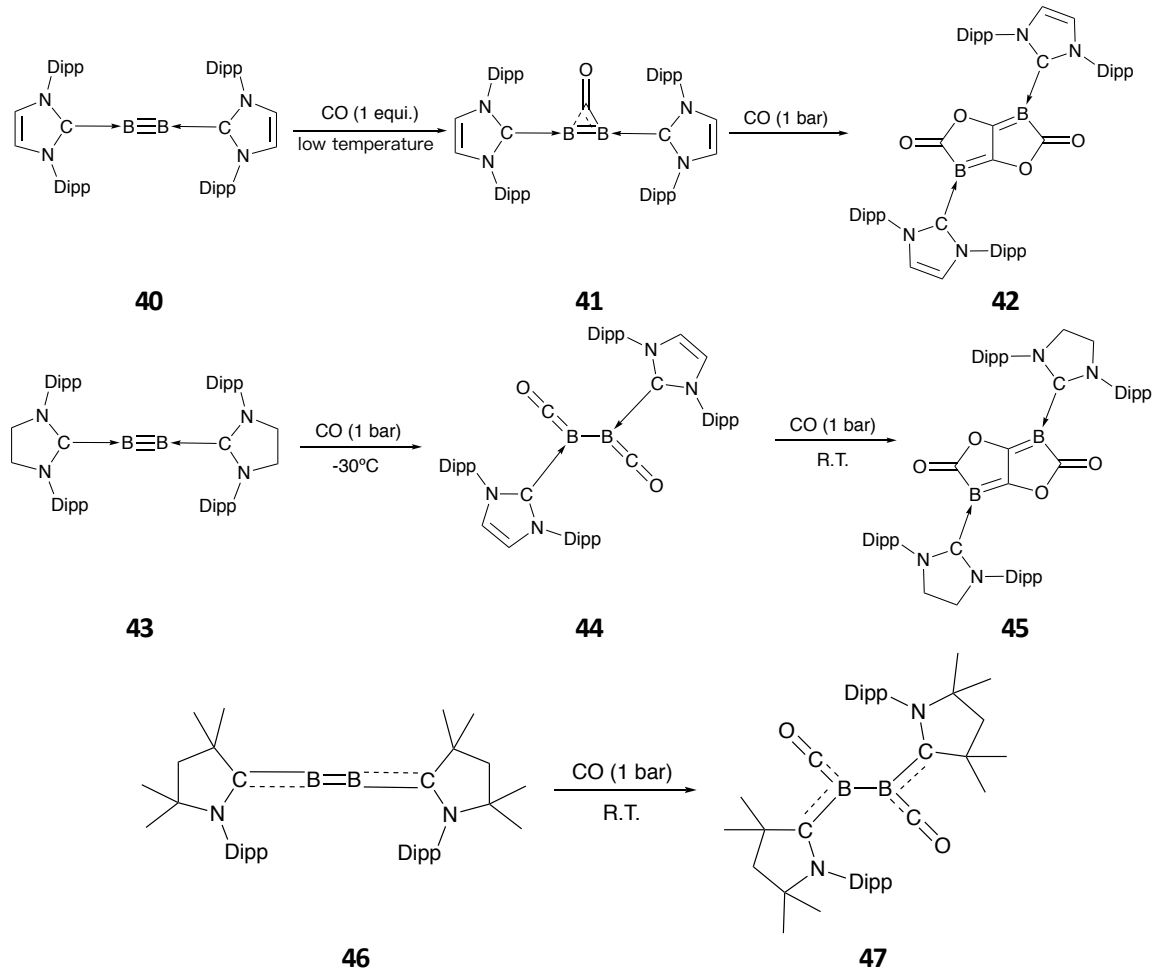


Figure 1-40: The reaction of diborynes and a diboracumulene with CO.[101]

*Table 1-8: Selected geometric data of **40**, **43** and **46**.*

	Ligand	B-B distance (Å)	C-B distance(s) (Å)
40	NHC **4d**	1.449(3)	1.487(3) 1.495(3)
43	NHC **5b**	1.465(2)	1.480(2) 1.482(2)
46	CAAC **19**	1.489(3)	1.459(2) 1.458(2)

In one of these reactivity studies, the activation of carbon monoxide was investigated (Figure 1-40).[151] The reactions of both diborynes **40** and **43** with CO lead to the ultimate formation of a planar, NHC-supported bicyclic bis(boralactone) (**42** and **45**, respectively); however, the pathways of the reactions are somewhat different. A further investigation of the reaction between **40** and CO revealed an intermediate (**41**) involving a bridging CO moiety.[136] **41** was isolated after stoichiometric control of CO at low temperature. Diboryne **43** on the other hand initially forms the bis(boraketene) **44**, which is slowly converted to the bis(boralactone) **45** on prolonged treatment with an excess of CO. Unlike the NHC-supported diborynes, however, the reaction of CAAC-supported diboryne **46** with CO stops at the corresponding bis(boraketene) (**47**), without further conversion to the corresponding bis(boralactone) even after the solution was heated at 150 °C.[151] The fact that **46** is less active toward CO in comparison to **40** and **43** can be rationalized by the electronic properties of the CAAC supporting ligand, which (being a better π acceptor) withdraws electron density from the diboryne fragment via the π-framework and deactivates it.[101] Such differences in electronic properties are consistent with the trend in geometric properties among **40**, **43** and **46** (Table 1-8).

1.5.2 Monomeric Low-valent Main Group Compounds

1.5.2.1 Electron-rich Systems

Featuring both σ-donor and π-acceptor properties, CAACs are able to provide stability to electron-rich systems featuring a low coordination number or low oxidation state by withdrawing electron density from central element(s) via the π framework.[102, 155] Examples of such applications include CAAC-supported organoboron species that are isoelectronic with amines[156] and singlet carbenes (Figure 1-41).[157]

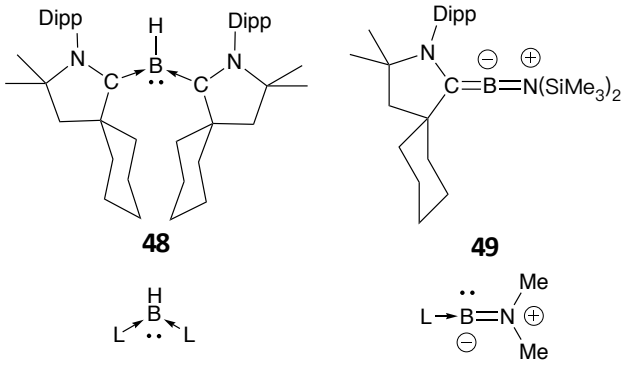


*Figure 1-41: Structures of organoborons compounds that are isoelectronic with amine (**48**) and singlet carbene systems (**49**).*

The CAAC-stabilized boron hydride **48** was reported by Bertrand and co-workers in 2011, being the first stable neutral, nucleophilic, tricoordinate boron derivative.[156] It was prepared by reduction of the corresponding CAAC adduct of BBr_3 (**50**) in the presence of an additional equivalent of the CAAC ligand (**20**) (Figure 1-42). In 2016, Braunschweig and co-workers reported a similar synthesis, this time reducing the CAAC adduct of $B(CN)Br_2$ (**51**) with potassium graphite in the presence of triethylphosphine to yield the cyanoborane **52**.[158] Notably, in the absence of additional phosphine the tetramer **53** was formed instead

of **52** and upon the addition of an NHC, the unsymmetrical bis(carbene) adduct **54** could be obtained.

A related organoboron compound (**49**) (that can potentially be described as being isoelectronic to singlet carbene) was reported in 2014. This system is reported to show similar reactivity to singlet carbenes in small molecule activation.[157] The synthesis of **49** was achieved by successive one-electron reduction steps from the CAAC adduct of an aminodichloroborane (**55**). Cp^*_2Co was used as the reducing agent for both steps and the aminoboryl radical **56** is proposed to be the product of first reduction process (Figure 1-43).

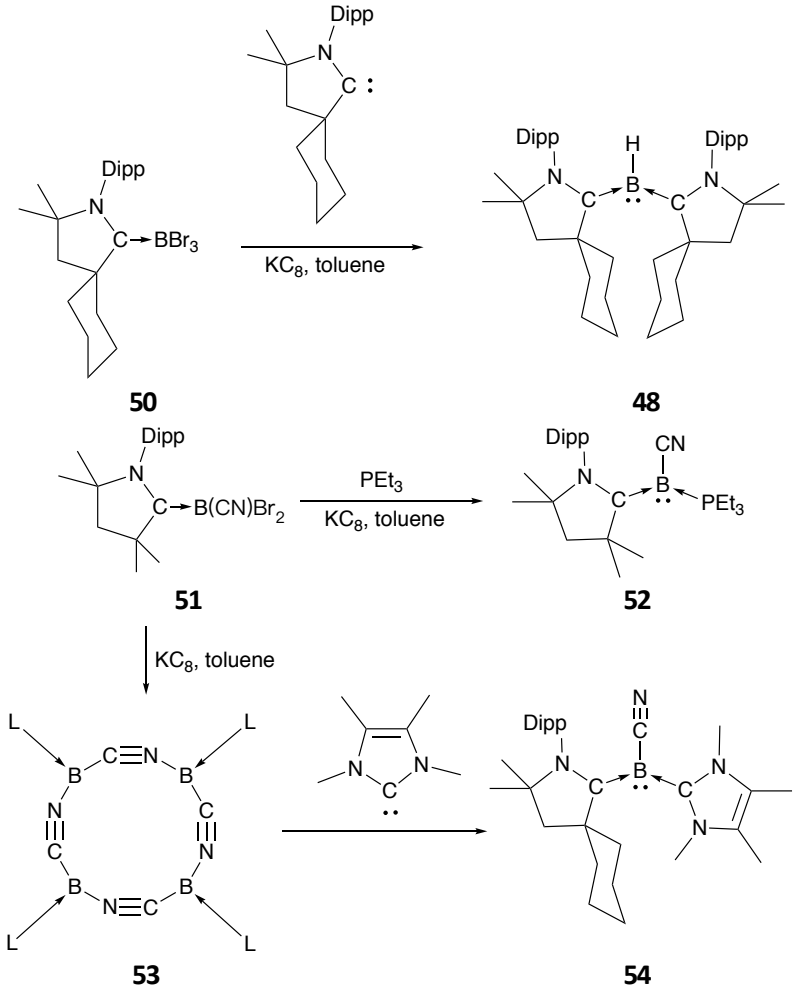
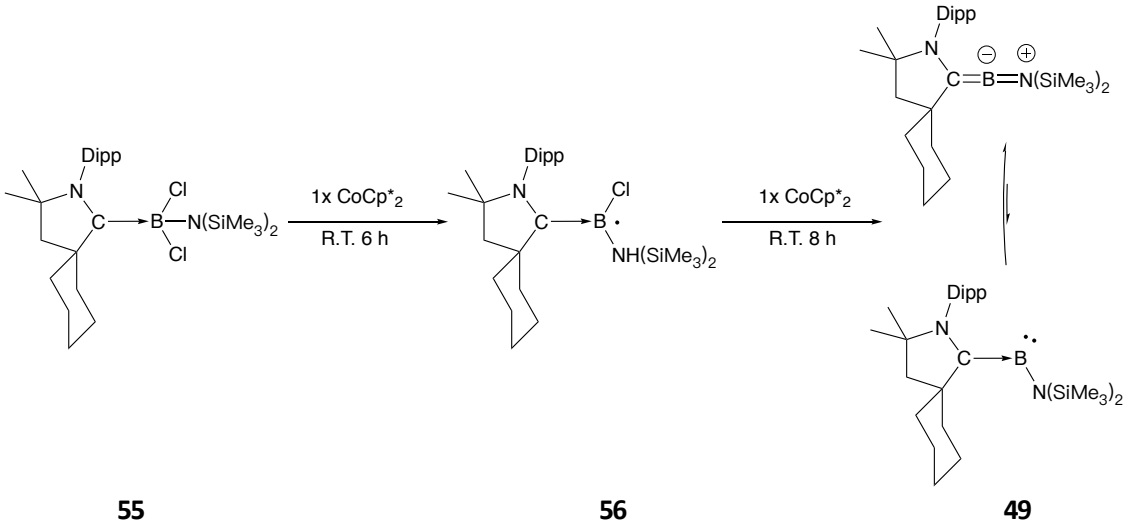
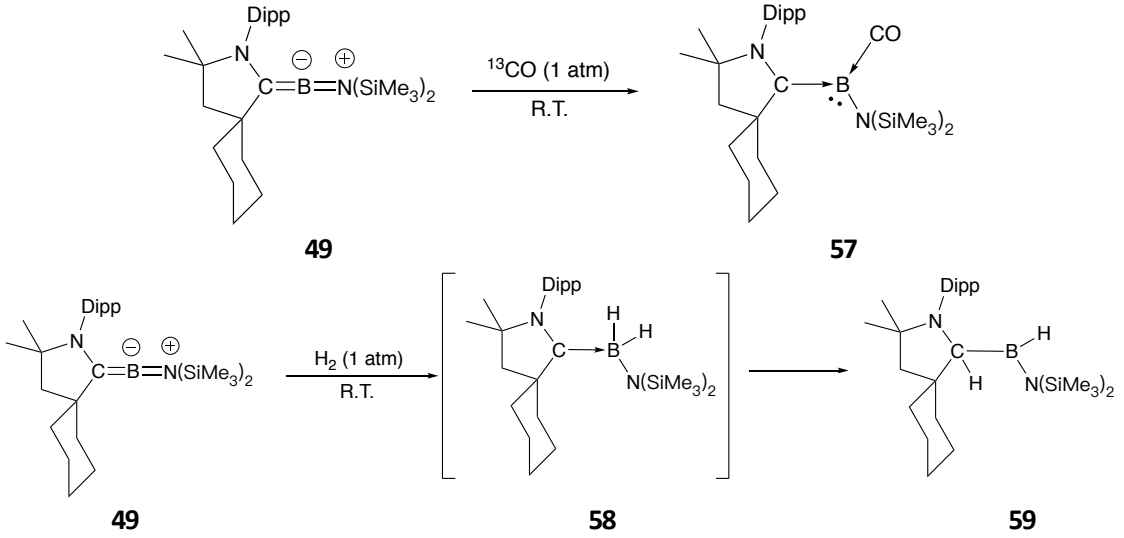


*Figure 1-42: Syntheses of CAAC-stablised neutral, nucleophilic, tricoordinate organoboron species (**48**, **52** and **54**)*



55 **56** **49**

*Figure 1-43: The synthesis of organoboron compound **49** which has been described as being isoelectronic to a singlet carbene.*



49 **57**

49 **58** **59**

*Figure 1-44: Small molecule activation by **49**: CO (upper) and dihydrogen (lower).*

Subsequent reactivity studies were conducted using **49**. The reaction with CO leads to the formation of the adduct **57** (Figure 1-44), resembling the reactivity of singlet carbenes that had previously been reported by Bertrand.[159-163] The formation of this adduct presumably benefits from the π-accepting properties of the CAAC donor. The

splitting of hydrogen by **49** also resembles the reactivity of some carbenes reported in previous literature,[164, 165] although the proposed four-coordinate borane **58** was not actually observed, and instead the 1,2 activation product **59** was isolated. A two-step process by which **49** is converted to **59** via **58** (Figure 1-44) was supported by DFT studies based on the previously reported 1,2-hydride migration of CAAC-borohydride.[166, 167]

1.5.2.2 Electron Deficient Systems

The cations of main-group elements and group 14 metallylenes are two of the major types of electron deficient systems in main-group chemistry that feature a low coordination number at the central element (Figure 1-45).[101, 142] Bulky ancillary ligands with strong donor capabilities, such as iminato (e.g. **60**), NHC (e.g. **62**), terphenyl (e.g. **61a-c**) and diazaborolyl (e.g. **63**) systems have been employed to stabilize the electron-deficient species of this sort.

Members of the η^1-guanidinato ligand family typically behave as 2σ, 4π electron donors, and therefore would be expected to be good candidates for stabilising electron-deficient systems. This series of ligands has been extensively used in transition metal chemistry[128, 130, 131, 172-183] as well as some rare earth metals systems,[184, 185] since the development of a general synthetic route by Tamm *et al.* It was not until 2012, however, that Inoue and co-workers applied the NHI series of ligands in main-group chemistry (Figure 1-46). [186] Initial reports focussed on silicon compounds which offer potential in bond activation processes.[187, 188]

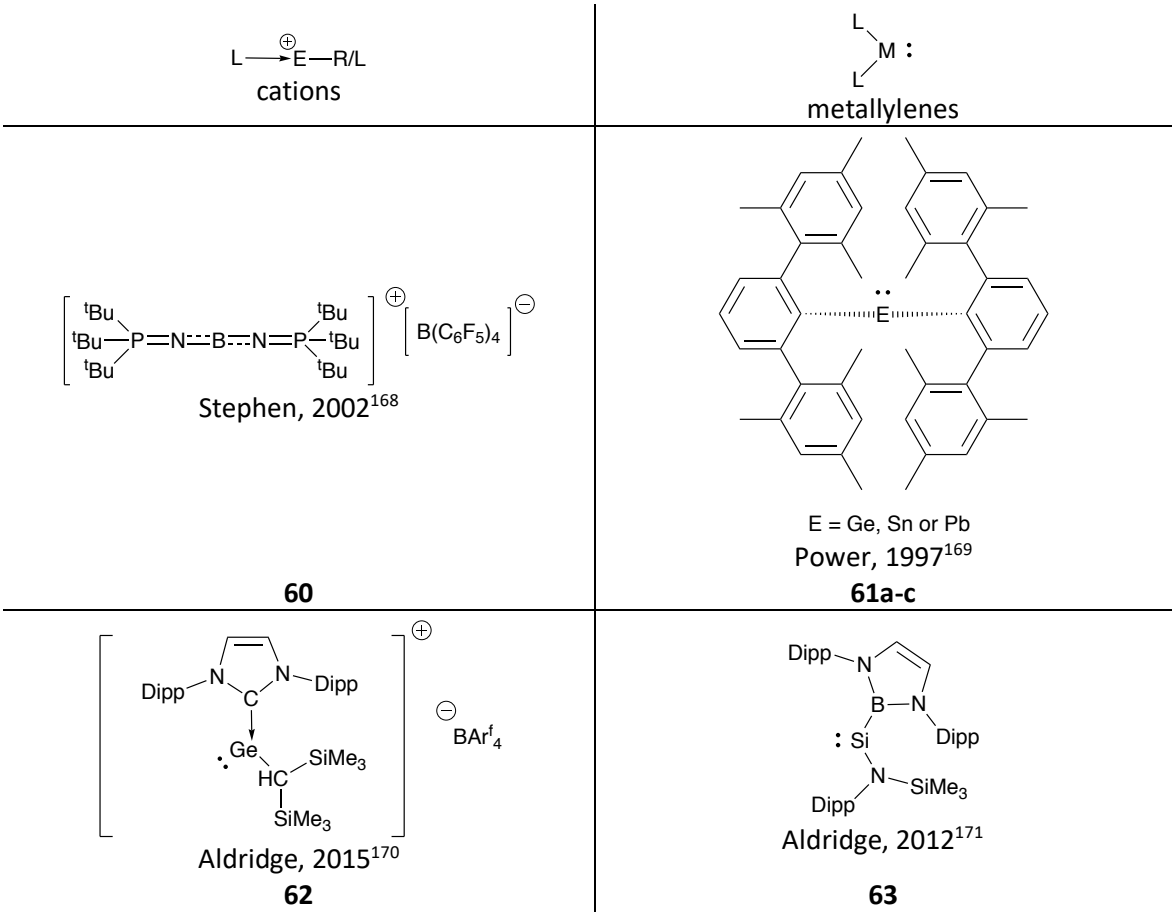


Figure 1-45: A selection of electron-deficient systems that are supported by strongly electron donating ligands.

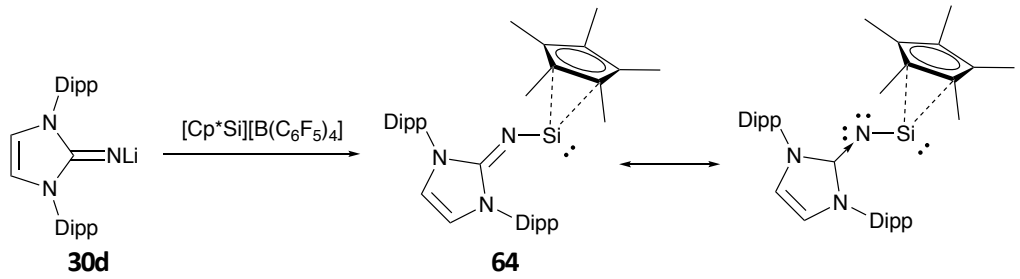


Figure 1-46: The synthesis of first main-group compound featuring an NHI ligand.

Thus, silylene **64** was isolated from the reaction between lithium salt of NHI ligand **30d** with Jutzi's [Cp*Si][$B(C_6F_5)_4$] at -78 °C. DFT studies on **64** show significant π-interaction between the lone pair of the NHI nitrogen donor and the formally unoccupied p-orbital at silicon.

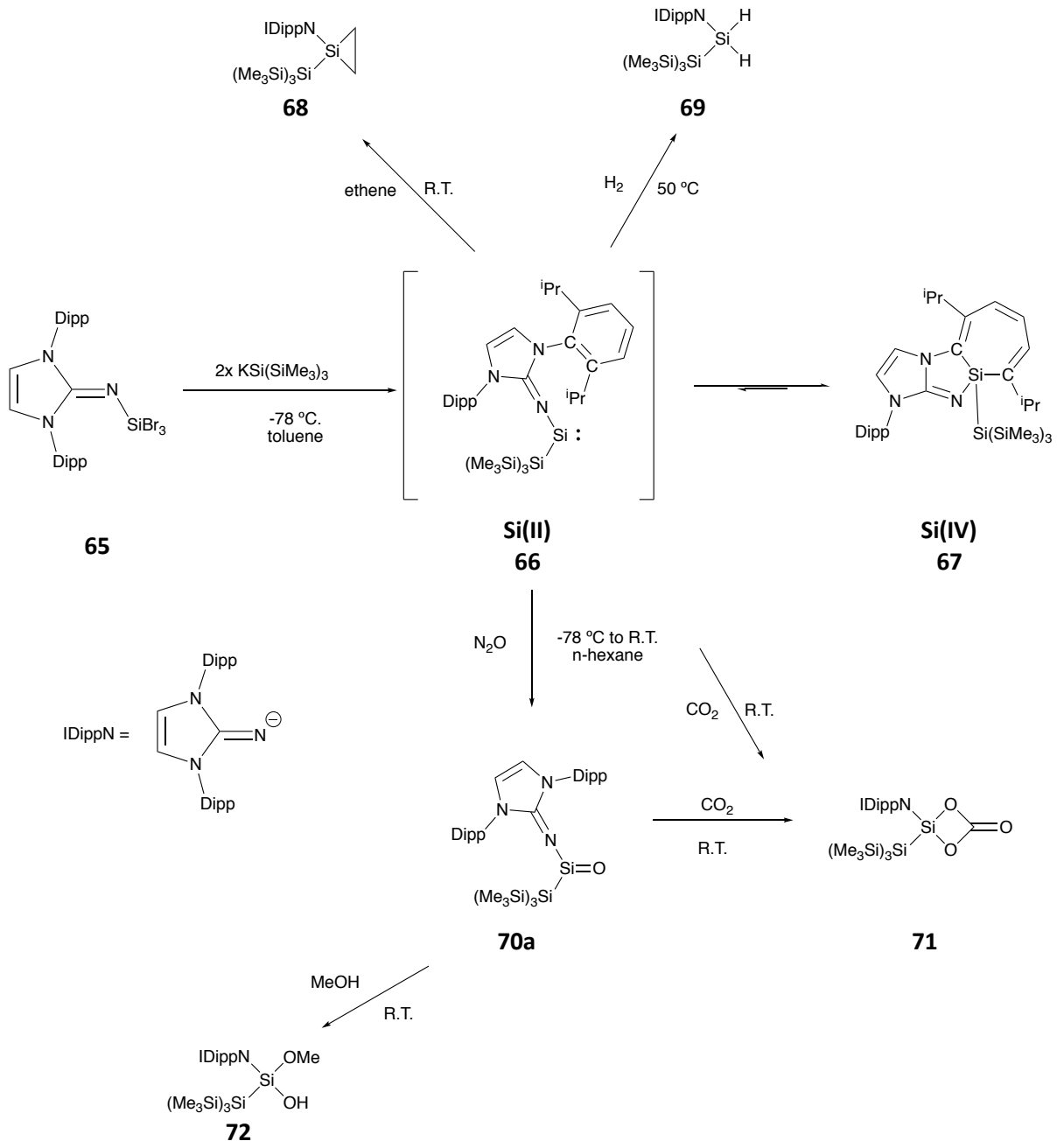


*Figure 1-47: The small molecule activations of **66** and the synthesis of silanone **70a** and its activation of small molecules.*

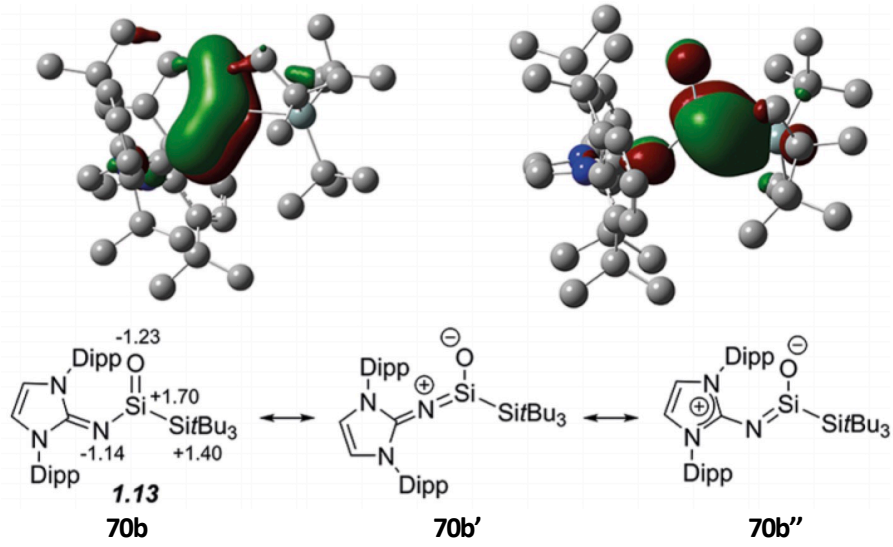


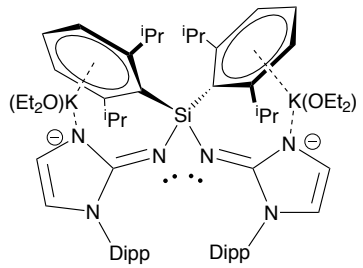
*Figure 1-48: DFT calculated HOMO-10 and LUMO+4 (upper); plausible resonance forms of **67b**, the analogue of **67a** with ($SiMe_3$) replaced by ^tBu groups. Reprinted with permission from Inoue and co-workers, Journal of the American Chemical Society, 2017, **139**, 17193-17198). Copyright (2019) American Chemical Society.*[189]

Further application of NHI ligands in silicon chemistry have subsequently been reported by Inoue and co-workers. In 2017, the group reported the synthesis of the first stable acyclic, charge-neutral silanone, together with a remarkable reversible intramolecular C-C bond activation process involving the silylene precursor (Figure 1-47).[189, 190] In the first step, the silylene **66** was obtained by reacting the (NHI)$SiBr_3$ complex **65** with two equivalents of $KSi(SiMe_3)_3$ at -78 °C. However, on warming to room temperature **66** undergoes intramolecular C-C bond activation to form **67**. The reactions of **67** with hydrogen, ethene and CO_2 reveal the reversibility of this C-C bond activation process, implying that **67** behaves as a 'dormant' form of silylene **66**.[190] This bond activation chemistry was considered to be an illustration of the powerful donor strength of the NHI ligand.

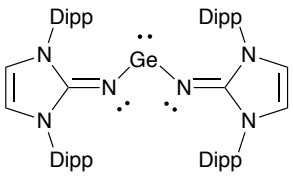
Subsequent oxidation of the silylene (**66**/**67**) afforded silanone **70a**, that is stable at room temperature, which gives the same product in activating carbon dioxide as the

activation by **66**/**67** (Figure 1-47).[189] The strongly donating NHI ligand is an important factor in stabilising **70a,b** by increasing the electron density in the π-framework, and in effect contributing electron density to the Si=O double bond (Figure 1-48).

Applications of NHI ligands have also been reported in metallylene chemistry involving heavier group 14 elements, Ge and Sn. The first germylene compound featuring the NHI ancillary ligand (**74**) was reported by Rivard and co-workers, being synthesised by dehalogenation of the corresponding bis(guanidinato)dichlorogermane (Figure 1-49).[191] DFT calculations show that **74** has a low singlet-triplet gap of 191.4 kJ mol^{-1}, implying potential for the germanium centre to insert into the element-element bonds of small molecules. However, the reaction of **74** with dihydrogen results in the formation of the protonated NHI ligand **28d** as the only soluble species, instead of the desired four-coordinate germane. This is believed to be caused by the higher proton affinity of the NHI ligand compared to the germanium centre. Interestingly, the synthesis of the silylene analogue of **74** was also attempted, but instead of the desired Si(II) product, the cleavage of N-aryl bonds was reported yielding a Si(IV) product **73** (Figure 1-49). The bond cleavage and substituent transfer processes may be accounted for by the highly reactive silicon centre associated with the strongly donating NHI ligand.



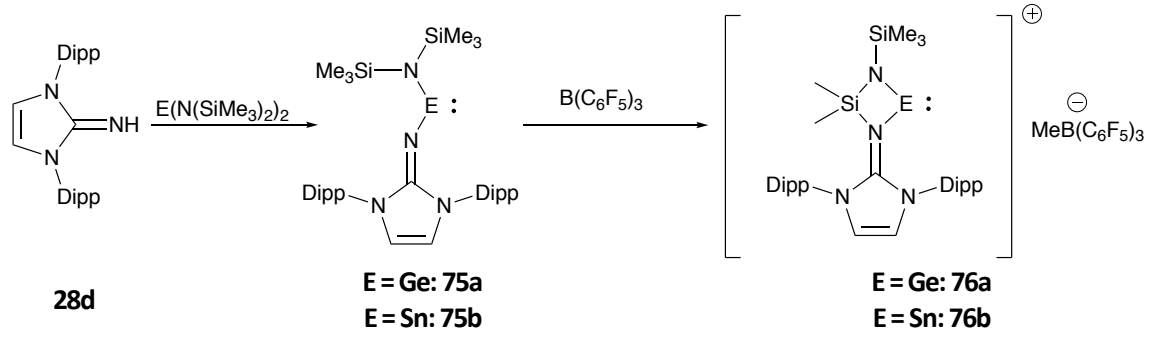
73



74

Figure 1-49: The products of Rivard's attempts to synthesize bis(NHI)-stabilized silylene and germylene compounds.

A related germylene compound featuring an NHI ligand (**75a**) was reported by Inoue and co-workers in 2015.[192] It was synthesised via acid/base chemistry by adding the protio-ligand **25d** to Lappert's germylene in toluene (Figure 1-50).



28d

E = Ge: 75a
E = Sn: 75b

E = Ge: 76a
E = Sn: 76b

Figure 1-50: The synthesis of germylene and stannylene by Inoue and the formation of corresponding cations.

The synthetic route can also be used to synthesize the tin analogue of **75a**.[193] Both germylene **75a** and stannylene **75b** can be shown to react with $B(C_6F_5)_3$ via abstraction of a methyl group from one of the trimethylsilyl groups to affords chelated E(II) compounds possessing a net positive charge.[192, 193] **76a,b** represent the first examples of main group cations stabilised by NHI-type ligands.

1.6 Research proposal

In the subsequent chapters of this thesis, a quantitative analysis of ligand electronic properties is presented (including σ-donor, π-acceptor and π-donor characteristics) via quantum chemical analysis with Amsterdam Density Functional, followed by exploration of factors that influence the electronic properties. All geometry of structures studies are optimized, with further analysis by fragment calculation and Natural Resonance Theory.

There is also experimental investigation of the properties of NHI as a π-donor in main group systems (Sn and Pb), as a comparison with the results from relevant quantum chemical studies. In the study of Pb system, intramolecular C-H activation is observed, which is rationalised with kinetic studies and mechanistic studies on Amsterdam Density Functional.

1.7 References

1. C. A. Tolman, *Chemical Reviews*, 1977, **77**, 313-348.
2. J. Hartwig, in *Organotransition Metal Chemistry: From Bonding to Catalysis*, University Science Books, 2010, ch. 1, pp. 1-26.
3. J. Hartwig, in *Organotransition Metal Chemistry - From Bonding to Catalysis*, University Science Books, 2010, ch. 2, pp. 27-84.
4. P. Gengembre, *Journal*, 1783, **10**, 651-658.
5. in *The Encyclopædia Britannica (1911 edition)*, 1911, vol. 21, p. 480.
6. T. Thomson, *A System of Chemistry*, 6 edn., 1820.
7. A. Lavoisier, in *Traité élémentaire de chimie*, Paris, France, 1789, vol. 1, p. 222.
8. C. A. Tolman, *Journal of the American Chemical Society*, 1970, **92**, 2953-2956.
9. R. Dorta, E. D. Stevens, N. M. Scott, C. Costabile, L. Cavallo, C. D. Hoff and S. P. Nolan, *Journal of the American Chemical Society*, 2005, **127**, 2485-2495.
10. R. C. Bush and R. J. Angelici, *Inorganic Chemistry*, 1988, **27**, 681-686.
11. T. Allman and R. G. Goel, *Canadian Journal of Chemistry-Revue Canadienne De Chimie*, 1982, **60**, 716-722.
12. W. A. Henderson and C. A. Streuli, *Journal of the American Chemical Society*, 1960, **82**, 5791-5794.
13. C. A. Streuli, *Analytical Chemistry*, 1960, **32**, 985-987.
14. A. Streitwieser, A. E. McKeown, F. Hasanayn and N. R. Davis, *Organic Letters*, 2005, **7**, 1259-1262.
15. R. G. Pearson, *Journal of Chemical Education*, 1968, **45**, 581.
16. R. G. Pearson, *Journal of Chemical Education*, 1968, **45**, 643.
17. R. G. Pearson, *Journal of the American Chemical Society*, 1963, **85**, 3533-&.
18. M. N. Golovin, M. Rahman, J. E. Belmonte and W. P. Giering, *Organometallics*, 1985, **4**, 1981-1991.
19. F. Weinhold and C. R. Landis, *Journal of chemical education*, 2007, **84**, 43.
20. T. Leyssens, D. Peeters, A. G. Orpen and J. N. Harvey, *Organometallics*, 2007, **26**, 2637-2645.
21. S. X. Xiao, W. C. Trogler, D. E. Ellis and Z. Berkovitchyellin, *Journal of the American Chemical Society*, 1983, **105**, 7033-7037.
22. L. W. Yarbrough and M. B. Hall, *Inorganic Chemistry*, 1978, **17**, 2269-2275.
23. C. A. Tolman, *Journal of the American Chemical Society*, 1970, **92**, 2956-2965.
24. D. White, B. C. Taverner, N. J. Coville and P. W. Wade, *Journal of Organometallic Chemistry*, 1995, **495**, 41-51.

25. D. White, B. C. Tavener, P. G. L. Leach and N. J. Coville, *Journal of Organometallic Chemistry*, 1994, **478**, 205-211.
26. D. White, B. C. Taverner, P. G. L. Leach and N. J. Coville, *Journal of Computational Chemistry*, 1993, **14**, 1042-1049.
27. N. J. Coville, M. S. Loonat, D. White and L. Carlton, *Organometallics*, 1992, **11**, 1082-1090.
28. T. L. Brown and K. J. Lee, *Coordination Chemistry Reviews*, 1993, **128**, 89-116.
29. W. Kirmse and P. P. Gaspar, *Carbene chemistry*, Academic Press, New York, 2nd edn., 1971.
30. A. J. Arduengo, H. V. R. Dias, J. C. Calabrese and F. Davidson, *Journal of the American Chemical Society*, 1992, **114**, 9724-9725.
31. A. J. Arduengo, H. V. R. Dias, F. Davidson and R. L. Harlow, *Journal of Organometallic Chemistry*, 1993, **462**, 13-18.
32. W. A. Herrmann, K. Ofele, M. Elison, F. E. Kuhn and P. W. Roesky, *Journal of Organometallic Chemistry*, 1994, **480**, C7-C9.
33. A. Schafer, M. Weidenbruch, W. Saak and S. Pohl, *Journal of the Chemical Society-Chemical Communications*, 1995, 1157-1158.
34. X. W. Li, J. R. Su and G. H. Robinson, *Chemical Communications*, 1996, 2683-2684.
35. H. Schumann, J. Gottfriedsen, M. Glanz, S. Dechert and J. Demtschuk, *Journal of Organometallic Chemistry*, 2001, **617**, 588-600.
36. N. Kuhn, G. Henkel, T. Kratz, J. Kreutzberg, R. Boese and A. H. Maulitz, *Chemische Berichte-Recueil*, 1993, **126**, 2041-2045.
37. K. Ofele, *Angewandte Chemie-International Edition*, 1968, **7**, 950.
38. K. Ofele, *Journal of Organometallic Chemistry*, 1968, **12**, P42-43.
39. K. Ofele, W. A. Herrmann, D. Mihalios, M. Elison, E. Herdtweck, T. Priermeier and P. Kiprof, *Journal of Organometallic Chemistry*, 1995, **498**, 1-14.
40. Schonher.Hj and H. W. Wanzlick, *Chemische Berichte-Recueil*, 1970, **103**, 1037-&.
41. W. A. Herrmann, M. Elison, J. Fischer, C. Kocher and G. R. J. Artus, *Chemistry-a European Journal*, 1996, **2**, 772-780.
42. W. A. Herrmann and C. Kocher, *Angewandte Chemie-International Edition*, 1997, **36**, 2162-2187.
43. D. J. Cardin, Cetinkay.B and M. F. Lappert, *Chemical Reviews*, 1972, **72**, 545-574.
44. D. J. Cardin, Cetinkay.B, M. F. Lappert, Manojlov.L and K. W. Muir, *Journal of the Chemical Society D-Chemical Communications*, 1971, 400-&.
45. C. M. Crudden and D. P. Allen, *Coordination Chemistry Reviews*, 2004, **248**, 2247-2273.
46. P. L. Arnold and S. Pearson, *Coordination Chemistry Reviews*, 2007, **251**, 596-609.
47. S. Diez-Gonzalez, N. Marion and S. P. Nolan, *Chemical Reviews*, 2009, **109**, 3612-3676.
48. P. de Fremont, N. Marion and S. P. Nolan, *Coordination Chemistry Reviews*, 2009, **253**, 862-892.
49. A. J. Arduengo, M. Tamm, S. J. McLain, J. C. Calabrese, F. Davidson and W. J. Marshall, *Journal of the American Chemical Society*, 1994, **116**, 7927-7928.
50. W. J. Oldham, S. M. Oldham, B. L. Scott, K. D. Abney, W. H. Smith and D. A. Costa, *Chemical Communications*, 2001, 1348-1349.
51. P. L. Arnold and I. J. Casely, *Chemical Reviews*, 2009, **109**, 3599-3611.

52. P. L. Arnold, Z. R. Turner, N. Kaltsoyannis, P. Pelekanaki, R. M. Bellabarba and R. P. Tooze, *Chemistry-a European Journal*, 2010, **16**, 9623-9629.
53. E. O. Fischer and A. Maasbol, *Angewandte Chemie-International Edition*, 1964, **3**, 580-&.
54. R. R. Schrock, *Journal of the American Chemical Society*, 1974, **96**, 6796-6797.
55. D. Bourissou, O. Guerret, F. P. Gabbai and G. Bertrand, *Chemical Reviews*, 2000, **100**, 39-91.
56. C. Heinemann and W. Thiel, *Chemical Physics Letters*, 1994, **217**, 11-16.
57. H. W. Wanzlick, *Angewandte Chemie-International Edition*, 1962, **74**, 129-134.
58. H. J. Schonherr and H. W. Wanzlick, *Annalen Der Chemie-Justus Liebig*, 1970, **731**, 176-+.
59. A. J. Arduengo, R. L. Harlow and M. Kline, *Journal of the American Chemical Society*, 1991, **113**, 361-363.
60. A. J. Arduengo, H. V. R. Dias, R. L. Harlow and M. Kline, *Journal of the American Chemical Society*, 1992, **114**, 5530-5534.
61. A. J. Arduengo, H. Bock, H. Chen, M. Denk, D. A. Dixon, J. C. Green, W. A. Herrmann, N. L. Jones, M. Wagner and R. West, *Journal of the American Chemical Society*, 1994, **116**, 6641-6649.
62. A. J. Arduengo, J. R. Goerlich and W. J. Marshall, *Journal of the American Chemical Society*, 1995, **117**, 11027-11028.
63. A. J. Arduengo, R. Krafczyk, R. Schmutzler, H. A. Craig, J. R. Goerlich, W. J. Marshall and M. Unverzagt, *Tetrahedron*, 1999, **55**, 14523-14534.
64. C. Heinemann, T. Muller, Y. Apeloig and H. Schwarz, *Journal of the American Chemical Society*, 1996, **118**, 2023-2038.
65. C. Boehme and G. Frenking, *Journal of the American Chemical Society*, 1996, **118**, 2039-2046.
66. S. Fantasia, J. L. Petersen, H. Jacobsen, L. Cavallo and S. P. Nolan, *Organometallics*, 2007, **26**, 5880-5889.
67. R. W. Alder, M. E. Blake, C. Bortolotti, S. Bufali, C. P. Butts, E. Linehan, J. M. Oliva, A. G. Orpen and M. J. Quayle, *Chemical Communications*, 1999, 241-242.
68. P. Bazinet, G. P. A. Yap and D. S. Richeson, *Journal of the American Chemical Society*, 2003, **125**, 13314-13315.
69. C. C. Scarborough, M. J. W. Grady, I. A. Guzei, B. A. Gandhi, E. E. Bunel and S. S. Stahl, *Angewandte Chemie-International Edition*, 2005, **44**, 5269-5272.
70. C. C. Scarborough, B. V. Popp, I. A. Guzei and S. S. Stahl, *Journal of Organometallic Chemistry*, 2005, **690**, 6143-6155.
71. M. Iglesias, D. J. Beetstra, J. C. Knight, L.-L. Ooi, A. Stasch, S. Coles, L. Male, M. B. Hursthouse, K. J. Cavell, A. Dervisi and I. A. Fallis, *Organometallics*, 2008, **27**, 3279-3289.
72. M. Iglesias, D. J. Beetstra, A. Stasch, P. N. Horton, M. B. Hursthouse, S. J. Coles, K. J. Cavell, A. Dervisi and I. A. Fallis, *Organometallics*, 2007, **26**, 4800-4809.
73. D. M. Khramov, E. L. Rosen, V. M. Lynch and C. W. Bielawski, *Angewandte Chemie-International Edition*, 2008, **47**, 2267-2270.
74. V. Cesar, N. Lugan and G. Lavigne, *Journal of the American Chemical Society*, 2008, **130**, 11286-11287.
75. E. L. Kolychev, I. A. Portnyagin, V. V. Shuntikov, V. N. Khrustalev and M. S. Nechaev, *Journal of Organometallic Chemistry*, 2009, **694**, 2454-2462.

76. W. Y. Lu, K. J. Cavell, J. S. Wixey and B. Kariuki, *Organometallics*, 2011, **30**, 5649-5655.
77. W. A. Herrmann, O. Runte and G. Artus, *Journal of Organometallic Chemistry*, 1995, **501**, C1-C4.
78. J. K. Huang, H. J. Schanz, E. D. Stevens and S. P. Nolan, *Organometallics*, 1999, **18**, 2370-2375.
79. K. Ofele, W. A. Herrmann, D. Mihalios, M. Elison, E. Herdtweck, W. Scherer and J. Mink, *Journal of Organometallic Chemistry*, 1993, **459**, 177-184.
80. J. C. Green, R. G. Scurr, P. L. Arnold and F. G. N. Cloke, *Chemical Communications*, 1997, 1963-1964.
81. R. D. Fischer, *Angewandte Chemie-International Edition in English*, 1994, **33**, 2165-2168.
82. H. Schumann, M. Glanz, J. Winterfeld, H. Hemling, N. Kuhn and T. Kratz, *Angewandte Chemie-International Edition in English*, 1994, **33**, 1733-1734.
83. A. J. Arduengo, F. Davidson, R. Krafczyk, W. J. Marshall and M. Tamm, *Organometallics*, 1998, **17**, 3375-3382.
84. G. Boche, C. Hilf, K. Harms, M. Marsch and J. C. W. Lohrenz, *Angewandte Chemie-International Edition in English*, 1995, **34**, 487-489.
85. A. R. Chianese, X. W. Li, M. C. Janzen, J. W. Faller and R. H. Crabtree, *Organometallics*, 2003, **22**, 1663-1667.
86. R. A. Kelly, H. Clavier, S. Giudice, N. M. Scott, E. D. Stevens, J. Bordner, I. Samardjiev, C. D. Hoff, L. Cavallo and S. P. Nolan, *Organometallics*, 2008, **27**, 202-210.
87. D. J. Nelson and S. P. Nolan, *Chemical Society Reviews*, 2013, **42**, 6723-6753.
88. D. Tapu, D. A. Dixon and C. Roe, *Chemical Reviews*, 2009, **109**, 3385-3407.
89. H. V. Huynh, Y. Han, R. Jothibasu and J. A. Yang, *Organometallics*, 2009, **28**, 5395-5404.
90. A. J. Arduengo, *Accounts of Chemical Research*, 1999, **32**, 913-921.
91. R. W. Alder, M. E. Blake and J. M. Oliva, *Journal of Physical Chemistry A*, 1999, **103**, 11200-11211.
92. M. Nonnenmacher, D. Kunz, F. Rominger and T. Oeser, *Chemical Communications*, 2006, 1378-1380.
93. A. C. Hillier, W. J. Sommer, B. S. Yong, J. L. Petersen, L. Cavallo and S. P. Nolan, *Organometallics*, 2003, **22**, 4322-4326.
94. A. Poater, B. Cosenza, A. Correa, S. Giudice, F. Ragone, V. Scarano and L. Cavallo, *European Journal of Inorganic Chemistry*, 2009, 1759-1766.
95. L. Cavallo, A. Correa, C. Costabile and H. Jacobsen, *Journal of Organometallic Chemistry*, 2005, **690**, 5407-5413.
96. L. Falivene, R. Credendino, A. Poater, A. Petta, L. Serra, R. Oliva, V. Scarano and L. Cavallo, *Organometallics*, 2016, **35**, 2286-2293.
97. M. N. Hopkinson, C. Richter, M. Schedler and F. Glorius, *Nature*, 2014, **510**, 485-496.
98. F. Ragone, A. Poater and L. Cavallo, *Journal of the American Chemical Society*, 2010, **132**, 4249-4258.
99. H. Clavier and S. P. Nolan, *Chemical Communications*, 2010, **46**, 841-861.
100. V. Lavallo, Y. Canac, C. Prasang, B. Donnadieu and G. Bertrand, *Angewandte Chemie-International Edition*, 2005, **44**, 5705-5709.

101. V. Nesterov, D. Reiter, P. Bag, P. Frisch, R. Holzner, A. Porzelt and S. Inoue, *Chemical Reviews*, 2018, **118**, 9678-9842.
102. M. Melaimi, R. Jazzar, M. Soleilhavoup and G. Bertrand, *Angewandte Chemie-International Edition*, 2017, **56**, 10046-10068.
103. O. Back, M. Henry-Ellinger, C. D. Martin, D. Martin and G. Bertrand, *Angewandte Chemie-International Edition*, 2013, **52**, 2939-2943.
104. R. R. Rodrigues, C. L. Dorsey, C. A. Arceneaux and T. W. Hudnall, *Chemical Communications*, 2014, **50**, 162-164.
105. K. Verlinden, H. Buhl, W. Frank and C. Ganter, *European Journal of Inorganic Chemistry*, 2015, 2416-2425.
106. A. Liske, K. Verlinden, H. Buhl, K. Schaper and C. Ganter, *Organometallics*, 2013, **32**, 5269-5272.
107. U. S. D. Paul, C. Sieck, M. Haehnel, K. Hammond, T. B. Marder and U. Radius, *Chemistry-a European Journal*, 2016, **22**, 11005-11014.
108. R. W. Auten and C. A. Kraus, *Journal of the American Chemical Society*, 1952, **74**, 3398-3401.
109. Y. Segawa, Y. Suzuki, M. Yamashita and K. Nozaki, *Journal of the American Chemical Society*, 2008, **130**, 16069-16079.
110. H. Nöth and G. Schmid, *Angewandte Chemie International Edition in English*, 1963, **2**, 623-623.
111. G. Schmid, *Angewandte Chemie International Edition in English*, 1970, **9**, 819-830.
112. J. R. Knorr and J. S. Merola, *Organometallics*, 1990, **9**, 3008-3010.
113. R. T. Baker, D. W. Ovenall, J. C. Calabrese, S. A. Westcott, N. J. Taylor, I. D. Williams and T. B. Marder, *Journal of the American Chemical Society*, 1990, **112**, 9399-9400.
114. S. Onozawa, Y. Hatanaka, T. Sakakura, S. Shimada and M. Tanaka, *Organometallics*, 1996, **15**, 5450-5452.
115. G. J. Irvine, M. J. G. Lesley, T. B. Marder, N. C. Norman, C. R. Rice, E. G. Robins, W. R. Roper, G. R. Whittell and L. J. Wright, *Chemical Reviews*, 1998, **98**, 2685-2722.
116. S. Aldridge and D. L. Coombs, *Coordination Chemistry Reviews*, 2004, **248**, 535-559.
117. D. L. Kays and S. Aldridge, *Contemporary Metal Boron Chemistry I: Borylenes, Boryls, Borane (Sigma)-Complexes, and Borohydrides*, 2008, **130**, 29-122.
118. H. Braunschweig, R. D. Dewhurst and A. Schneider, *Chemical Reviews*, 2010, **110**, 3924-3957.
119. L. Dang, Z. Y. Lin and T. B. Marder, *Chemical Communications*, 2009, 3987-3995.
120. H. Braunschweig, C. Kollann and D. Rais, *Angewandte Chemie-International Edition*, 2006, **45**, 5254-5274.
121. H. Braunschweig, *Angewandte Chemie-International Edition*, 1998, **37**, 1786-1801.
122. H. Braunschweig and M. Colling, *Coordination Chemistry Reviews*, 2001, **223**, 1-51.
123. Y. Segawa, M. Yamashita and K. Nozaki, *Science*, 2006, **314**, 113-115.
124. M. Yamashita, Y. Suzuki, Y. Segawa and K. Nozaki, *Journal of the American Chemical Society*, 2007, **129**, 9570-+.
125. M. Yamashita, Y. Suzuki, Y. Segawa and K. Nozaki, *Chemistry Letters*, 2008, **37**, 802-803.
126. N. Metzler-Nolte, *New Journal of Chemistry*, 1998, **22**, 793-795.
127. T. Ochiai, D. Franz and S. Inoue, *Chemical Society Reviews*, 2016, **45**, 6327-6344.
128. X. Wu and M. Tamm, *Coordination Chemistry Reviews*, 2014, **260**, 116-138.

129. N. Kuhn, R. Fawzi, M. Steimann, J. Wiethoff, D. Blaser and R. Boese, *Zeitschrift Fur Naturforschung Section B-a Journal of Chemical Sciences*, 1995, **50**, 1779-1784.
130. M. Tamm, S. Randoll, T. Bannenberg and E. Herdtweck, *Chemical Communications*, 2004, 876-877.
131. M. Tamm, D. Petrovic, S. Randoll, S. Beer, T. Bannenberg, P. G. Jones and O. Grunenberg, *Organic & Biomolecular Chemistry*, 2007, **5**, 523-530.
132. P. P. Power, *Nature*, 2010, **463**, 171-177.
133. P. P. Power, *Chemical Reviews*, 1999, **99**, 3463-3503.
134. R. C. Fischer and P. P. Power, *Chemical Reviews*, 2010, **110**, 3877-3923.
135. H. Braunschweig, R. D. Dewhurst, K. Hammond, J. Mies, K. Radacki and A. Vargas, *Science*, 2012, **336**, 1420-1422.
136. H. Braunschweig, T. Dellermann, R. D. Dewhurst, W. C. Ewing, K. Hammond, J. O. C. Jimenez-Halla, T. Kramer, I. Krummenacher, J. Mies, A. K. Phukan and A. Vargas, *Nature Chemistry*, 2013, **5**, 1025-1028.
137. H. Braunschweig, T. Dellermann, W. C. Ewing, T. Kramer, C. Schneider and S. Ullrich, *Angewandte Chemie (International ed. in English)*, 2015, **54**, 10271-10275.
138. Y. Z. Wang and G. H. Robinson, *Chemical Communications*, 2009, 5201-5213.
139. Y. Z. Wang and G. H. Robinson, *Inorganic Chemistry*, 2014, **53**, 11815-11832.
140. Y. Z. Wang and G. H. Robinson, *Dalton Transactions*, 2012, **41**, 337-345.
141. Y. Z. Wang and G. H. Robinson, *Inorganic Chemistry*, 2011, **50**, 12326-12337.
142. Y. Mizuhata, T. Sasamori and N. Tokitoh, *Chemical Reviews*, 2009, **109**, 3479-3511.
143. G. Linti and H. Schnockel, *Coordination Chemistry Reviews*, 2000, **206**, 285-319.
144. D. E. Goldberg, D. H. Harris, M. F. Lappert and K. M. Thomas, *Journal of the Chemical Society-Chemical Communications*, 1976, 261-262.
145. Y. Z. Wang, Y. M. Xie, P. R. Wei, R. B. King, H. F. Schaefer, P. V. Schleyer and G. H. Robinson, *Science*, 2008, **321**, 1069-1071.
146. Y. Z. Wang, M. W. Chen, Y. M. Xie, P. R. Wei, H. F. Schaefer, P. V. Schleyer and G. H. Robinson, *Nature Chemistry*, 2015, **7**, 509-513.
147. Y. Z. Wang, M. W. Chen, Y. M. Xie, P. R. Wei, H. F. Schaefer and G. H. Robinson, *Journal of the American Chemical Society*, 2015, **137**, 8396-8399.
148. C. Jones, A. Sidiropoulos, N. Holzmann, G. Frenking and A. Stasch, *Chemical Communications*, 2012, **48**, 9855-9857.
149. A. Sidiropoulos, C. Jones, A. Stasch, S. Klein and G. Frenking, *Angewandte Chemie-International Edition*, 2009, **48**, 9701-9704.
150. W. Kutzelnigg, *Angewandte Chemie-International Edition in English*, 1984, **23**, 272-295.
151. J. Bohnke, H. Braunschweig, T. Dellermann, W. C. Ewing, K. Hammond, J. O. C. Jimenez-Halla, T. Kramer and J. Mies, *Angewandte Chemie-International Edition*, 2015, **54**, 13801-13805.
152. J. Boehnke, H. Braunschweig, P. Constantinidis, T. Dellermann, W. C. Ewing, I. Fischer, K. Hammond, F. Hupp, J. Mies, H.-C. Schmitt and A. Vargas, *Journal of the American Chemical Society*, 2015, **137**, 1766-1769.
153. J. Bohnke, H. Braunschweig, W. C. Ewing, C. Horl, T. Kramer, I. Krummenacher, J. Mies and A. Vargas, *Angewandte Chemie-International Edition*, 2014, **53**, 9082-9085.
154. M. Arrowsmith, J. Bohnke, H. Braunschweig, M. A. Celik, T. Dellermann and K. Hammond, *Chemistry-a European Journal*, 2016, **22**, 17169-17172.

155. M. Soleilhavoup and G. Bertrand, *Accounts of Chemical Research*, 2015, **48**, 256-266.
156. R. Kinjo, B. Donnadieu, M. A. Celik, G. Frenking and G. Bertrand, *Science*, 2011, **333**, 610-613.
157. F. Dahcheh, D. Martin, D. W. Stephan and G. Bertrand, *Angewandte Chemie-International Edition*, 2014, **53**, 13159-13163.
158. M. Arrowsmith, D. Auerhammer, R. Bertermann, H. Braunschweig, G. Bringmann, M. A. Celik, R. D. Dewhurst, M. Finze, M. Grune, M. Hailmann, T. Hertle and I. Krummenacher, *Angewandte Chemie-International Edition*, 2016, **55**, 14462-14466.
159. T. W. Hudnall, J. P. Moerdyk and C. W. Bielawski, *Chemical Communications*, 2010, **46**, 4288-4290.
160. T. W. Hudnall and C. W. Bielawski, *Journal of the American Chemical Society*, 2009, **131**, 16039-16041.
161. G. D. Frey, V. Lavallo, B. Donnadieu, W. W. Schoeller and G. Bertrand, *Science*, 2007, **316**, 439-441.
162. V. Lavallo, Y. Canac, B. Donnadieu, W. W. Schoeller and G. Bertrand, *Angewandte Chemie-International Edition*, 2006, **45**, 3488-3491.
163. D. Martin, M. Soleilhavoup and G. Bertrand, *Chemical Science*, 2011, **2**, 389-399.
164. M. R. Hoffmann and K. Kuhler, *Journal of Chemical Physics*, 1991, **94**, 8029-8039.
165. L. Nyulaszi, D. Szieberth, J. Reffy and T. Veszpremi, *Journal of Molecular Structure-Theochem*, 1998, **453**, 91-95.
166. M. R. Momeni, E. Rivard and A. Brown, *Organometallics*, 2013, **32**, 6201-6208.
167. G. D. Frey, J. D. Masuda, B. Donnadieu and G. Bertrand, *Angewandte Chemie-International Edition*, 2010, **49**, 9444-9447.
168. S. Courtenay, J. Y. Mutus, R. W. Schurko and D. W. Stephan, *Angewandte Chemie-International Edition*, 2002, **41**, 498-501.
169. R. S. Simons, L. H. Pu, M. M. Olmstead and P. P. Power, *Organometallics*, 1997, **16**, 1920-1925.
170. A. Rit, R. Tirfoin and S. Aldridge, *Angewandte Chemie-International Edition*, 2016, **55**, 378-382.
171. A. V. Protchenko, K. H. Birjkumar, D. Dange, A. D. Schwarz, D. Vidovic, C. Jones, N. Kaltsoyannis, P. Mountford and S. Aldridge, *Journal of the American Chemical Society*, 2012, **134**, 6500-6503.
172. S. Beer, C. G. Hrib, P. G. Jones, K. Brandhorst, J. Grunenberg and M. Tamm, *Angewandte Chemie-International Edition*, 2007, **46**, 8890-8894.
173. M. Tamm, S. Randoll, E. Herdtweck, N. Kleigrewe, G. Kehr, G. Erker and B. Rieger, *Dalton Transactions*, 2006, 459-467.
174. S. Beer, K. Brandhorst, J. Grunenberg, C. G. Hrib, P. G. Jones and M. Tamm, *Organic Letters*, 2008, **10**, 981-984.
175. S. H. Stelzig, M. Tamm and R. M. Waymouth, *Journal of Polymer Science Part a-Polymer Chemistry*, 2008, **46**, 6064-6070.
176. S. Beer, K. Brandhorst, C. G. Hrib, X. Wu, B. Haberlag, J. Grunenberg, P. G. Jones and M. Tamm, *Organometallics*, 2009, **28**, 1534-1545.
177. D. Shoken, M. Sharma, M. Botoshansky, M. Tamm and M. S. Eisen, *Journal of the American Chemical Society*, 2013, **135**, 12592-12595.

178. S. Lysenko, C. G. Daniliuc, P. G. Jones and M. Tamm, *Journal of Organometallic Chemistry*, 2013, **744**, 7-14.
179. K. Nomura, B. K. Bahuleyan, S. Zhang, P. M. V. Sharma, S. Katao, A. Igarashi, A. Inagaki and M. Tamm, *Inorganic Chemistry*, 2014, **53**, 607-623.
180. K. Nomura, B. K. Bahuleyan, K. Tsutsumi and A. Igarashi, *Organometallics*, 2014, **33**, 6682-6691.
181. I. S. R. Karmel, N. Fridman, M. Tamm and M. S. Eisen, *Organometallics*, 2015, **34**, 2933-2942.
182. A. Igarashi, E. L. Kolychev, M. Tamm and K. Nomura, *Organometallics*, 2016, **35**, 1778-1784.
183. D. Shoken, L. J. W. Shimon, M. Tamm and M. S. Eisen, *Organometallics*, 2016, **35**, 1125-1131.
184. A. G. Trambitas, T. K. Panda and M. Tamm, *Zeitschrift Fur Anorganische Und Allgemeine Chemie*, 2010, **636**, 2156-2171.
185. T. K. Panda, A. G. Trambitas, T. Bannenberg, C. G. Hrib, S. Randoll, P. G. Jones and M. Tamm, *Inorganic Chemistry*, 2009, **48**, 5462-5472.
186. S. Inoue and K. Leszczynska, *Angewandte Chemie-International Edition*, 2012, **51**, 8589-8593.
187. M. Asay, C. Jones and M. Driess, *Chemical Reviews*, 2011, **111**, 354-396.
188. G. H. Lee, R. West and T. Muller, *Journal of the American Chemical Society*, 2003, **125**, 8114-8115.
189. D. Wendel, D. Reiter, A. Porzelt, P. J. Altmann, S. Inoue and B. Rieger, *Journal of the American Chemical Society*, 2017, **139**, 17193-17198.
190. D. Wendel, A. Porzelt, F. A. D. Herz, D. Sarkar, C. Jandl, S. Inoue and B. Rieger, *Journal of the American Chemical Society*, 2017, **139**, 8134-8137.
191. M. W. Lui, C. Merten, M. J. Ferguson, R. McDonald, Y. J. Xu and E. Rivard, *Inorganic Chemistry*, 2015, **54**, 2040-2049.
192. T. Ochiai, D. Franz, X. N. Wu and S. Inoue, *Dalton Transactions*, 2015, **44**, 10952-10956.
193. T. Ochiai, D. Franz, E. Irran and S. Inoue, *Chemistry-a European Journal*, 2015, **21**, 6704-6707.

Chapter 2

Experimental Methods

2.1 Inert Atmosphere Techniques

The majority of the experimental work described in this thesis involved compounds that are highly sensitive to air and moisture. Therefore, it was necessary to carry out transformations in inert environments, as opposed to using traditional bench-top methods. There are two common techniques employed to provide the inert environment: a Schlenk line with an argon atmosphere for solution-phase manipulations, and a glove box with a nitrogen atmosphere for the manipulation of solids.[1, 2]

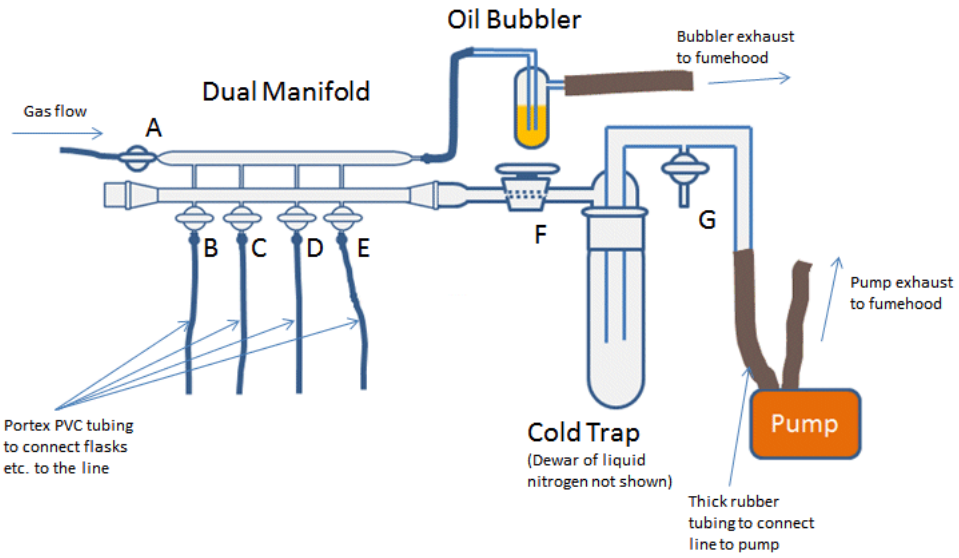


Figure 2-1: A Schlenk line.

Schlenk line techniques have been shown to be effective and efficient methods for carrying out solution-phase reactions of air- and moisture-sensitive compounds, with low risk of oxidation or hydrolysis.[3] A typical line (Figure 2-1) consists of a dual Pyrex glass manifold connected to a high vacuum pump and to a source of purified inert gas (argon in this case). This allows access to a positive pressure of argon gas and a vacuum down to ca. 10^{-3} mbar via two different manifolds. Several two-way taps are installed for switching between the two environments when connected to reaction vessels.

In order to create an environment that is almost free from oxygen and moisture, a "pump and purge" cycle, of alternating vacuum and gas, was carried out three times before any further action. The vacuum manifold was fitted with a liquid nitrogen cold trap to prevent volatile solvents and reactants from contaminating the pump, and excess pressure in the argon manifold was vented through a mercury bubbler. All ground glass joints and taps were lubricated with high vacuum grease to ensure an air-tight seal. Transfer of liquids and solutions between reaction vessels was achieved by the use of cannulae (made from either stain steel or PTFE) and syringes to avoid exposure to air.

Air-sensitive solids were handled and stored in a nitrogen atmosphere glove box. The atmosphere was purified by passing through activated copper metal and molecular sieves to remove oxygen and water, respectively. Neoprene gloves were built in to the side of the box to allow access to the sealed system. Materials and apparatus entered the box via a side port to which the standard "pump and purge" method was applied.

2.2 Spectroscopic Techniques

2.2.1 NMR spectroscopy

^{1}H and ^{13}C NMR spectra were measured using a Bruker Avance III HD Nanobay 400 MHz spectrometer; ^{29}Si, ^{119}Sn and ^{207}Pb NMR spectra were measured on a Bruker Avance III 500MHz spectrometer. ^{1}H and ^{13}C spectra were referenced to the residual peaks of deuterated solvents, while other nuclei were referenced to external (^{29}Si, $SiMe_4$; ^{119}Sn, $SnMe_4$; ^{207}Pb, $PbMe_4$). Samples of air and moisture sensitive compounds were prepared under an inert atmosphere using NMR tubes fitted with a J. Young's valve.

2.2.2 Infrared Spectroscopy

Infrared spectra were measured on a Nicolet 500 FT-IR spectrometer using air-tight cells. The solvent used was pentane and a background scan of the solvent was acquired before measurements were carried out on the compounds of interest.

2.2.3 Elemental Analysis

Elemental analyses were carried out at London Metropolitan University.

2.2.4 Photolysis

Photolysis experiments were carried out using a mercury arc lamp (1 kW). Samples were contained within sealed NMR tubes fitted with a J. Young's valve.

2.2.5 X-ray Crystallography

Measurements were carried out at 150 K on an Enraf-Nonius Kappa CCD diffractometer using MoKα radiation or on an Oxford Diffraction SuperNova using CuKα radiation. Data reduction was carried out using DENZO or CrysAlis Pro.[4] Crystallographic studies were carried out by Dr Evgeny Kolychev or Dr Jamie Hicks and the structures were solved by Superflip.[5] Structure refinement was performed using either the SHELX[6] or CRYSTALS software.[7, 8]

2.2.6 Synthesis of Starting Materials

Previously reported chemicals which are not readily available from commercial sources needed to be synthesised using literature procedures. These are briefly outlined below.

Preparation of glyoxal-bis-(2,6-diisopropylphenyl)imine

The method employed followed that reported by Arduengo *et al*.[9] An aqueous solution of glyoxal (40 w.t. %, 27.0 ml, 0.22 mol) was added with vigorous stirring to a warmed (50 °C) solution of 2,6-diisopropylphenylamine (94.3 mL, 0.45 mol) and acetic acid (1.0 mL, 0.16 mol). A slightly exothermic reaction commenced and the product started to crystallise after 15 min. The mixture was stirred for a further 10 h at room temperature, after which the suspension was filtered, and the solid product washed with methanol (20 mL) until the washings remained bright yellow. The product was pre-dried by suction then dried to constant weight in *in vacuo*. ^{1}H NMR data agrees with that reported in literature.[9]

Preparation of N,N'-(bis-2,6-diisopropylphenyl)-1,2-diaminoethane

The method employed followed that reported by Arduengo *et al*.[9] Glyoxal-bis-(2,6-diisopropylphenyl)imine (10.0 g, 0.027 mol) was suspended in ethanol (500 mL) and 10 equivalents of sodium borohydride (16.0 g, 0.27 mol) added. The reaction mixture was heated to reflux until gas evolution ceased. After quenching at room temperature by the addition of water and removal of ethanol *in vacuo*, the product was extracted into chloroform (200 mL). The chloroform phase was then washed with water (2 x 100 mL) and dried over anhydrous magnesium sulphate. A white solid was obtained upon drying *in vacuo* for which ^{1}H NMR data agrees with that reported in literature.[9]

Preparation of N,N'-(Bis-2,6-diisopropylphenyl)-1,3-diaminopropane

Distilled 2,6-diisopropylphenylamine (10.4 mL, 0.056 mol) was dissolved in dry, degassed THF (100 mL) and cooled to -78 °C, whereupon ^{n}BuLi (35.5 mL of a 1.6 M solution in hexane, 0.056 mol) was added dropwise. After the addition, the reaction mixture was allowed to warm to room temperature. The solution was then cooled to 0 °C, and TMEDA (8.44 mL, 0.056 mol) added dropwise. The resulting solution was then added to a solution of 1,3-dibromopropane (2.86 mL, 0.028 mol) in THF (20 ml) at 0 °C. The reaction mixture was allowed to stir overnight, and then poured into water (100 mL). The product was extracted into dichloromethane (3 x 100 mL), the organic layer separated and dried over anhydrous sodium sulphate, and solvent then removed *in vacuo*. The resulting yellow oil was dissolved in diethyl ether and excess concentrated HCl (25 mL) then added. The resulting salt was removed by filtration, washed with diethyl ether and dissolved again in dichloromethane. The solution was poured into saturated aqueous sodium hydrocarbonate (100 mL) and stirred for 30 min. The organic layer was separated and dried

over anhydrous sodium sulphate. Removal of the solvent yielded the product as a viscous yellow oil. ^{1}H NMR data agrees with that reported in literature.[10]

Preparation of 1,3-bis-(2,6-diisopropylphenyl)imidazolium chloride

The method employed followed that reported by Arduengo *et al*.[9] Glyoxal-bis-(2,6-diisopropylphenyl)imine (22.2 g, 0.059 mol) was dissolved in ethyl acetate (450 mL) and the solution was heated to 70 °C. Paraformaldehyde (1.8 g, 0.059 mol of monomer unit) was added during the heating. A solution of trimethylsilyl chloride (7.5 mL, 0.059 mol) in ethyl acetate (50 mL) was added dropwise over a period of 45 min with vigorous stirring, and the resulting yellow suspension was allowed to stir for 2 h at 70 °C. After cooling the solution to 10 °C in an ice bath, the suspension was filtered and the resulting solid washed with ethyl acetate (50 mL). ^{1}H NMR data agrees with that reported in literature.[9]

General procedure for synthesis of N,N'-diarylformamidines (Ar = Mes, Dipp).

The method employed followed that reported by Nechaev *et al*.[11] A round-bottomed flask containing $ArNH_2$ (0.130 mol), $HC(OEt)_3$ (0.065 mol) and acetic acid (0.007 mol) was fitted with a short path distillation head. The mixture was stirred and heated to 180 °C over a period of 2 h resulting in the removal (by distillation) of EtOH. On cooling to room temperature, a colourless crystalline mass formed which was washed with hexanes (200 mL) and dried *in vacuo*. ^{1}H NMR data agrees with that reported in literature.[11]

General Procedure for synthesis of expanded-ring N-heterocyclic carbene salts ([5-DippH]Br, [6-MesH]Br, [6-DippH]Br, [7-DippH]Br).

The method employed followed that reported by Fallis *et al*.[12] The respective *N,N'*-diarylformamidine (0.036 mol), dibromoalkane (1,2-dibromoethane, 1,3-dibromopropane or 1,4-dibromobutane) (0.040 mol) and K_2CO_3 (0.019 mol) were combined in acetonitrile (200 mL) and heated to reflux for 16 h (Ar = Mes) or 96 h (Ar = Dipp). After cooling, the solvent was removed *in vacuo* and the residue dissolved in dichloromethane (50 mL). This solution was filtered through 0.5 cm of silica and solvent removed *in vacuo* to give an off-white solid. The solid was dried at 200 °C overnight. ^{1}H NMR data agrees with that reported in literature.[12]

General Procedure for synthesis of N-heterocyclic carbene silver complexes, (5-Dipp)AgBr and (7-Dipp)AgBr

The method employed followed that reported by Fallis *et al*.[12] The amidinium salt ([5-DippH]Br or [7-DippH]Br) (0.01 mol) was mixed with Ag_2O (0.01 mol) and NaBr (0.05 mol) in dichloromethane (200 mL) and stirred in the dark for 3 d. The resulting off-white precipitate was filtered and washed with dichloromethane (3 x 50 mL). The combined filtrates were collected, and the solvent was reduced in volume until the solution became cloudy. Subsequently hexane was added to afford, after crystallisation, colourless crystals of the product. ^{1}H NMR data agrees with that reported in literature.[12]

General Procedure for synthesis of bromoamidinium salts. ([5-DippBr]Br, [7-DippBr]Br)

The method employed followed that reported by Nechaev *et al*.[13] To a solution of silver complex ((5-Dipp)AgBr or (7-Dipp)AgBr) in dichloromethane (approx. 0.02 M), was

added a solution containing three equivalents of bromine in dichloromethane (1 M). The colour of the mixture turned to yellow, and AgBr precipitated. The reaction mixture was allowed to stir for a further 2 d in the dark. The mixture became colourless, and an additional amount of AgBr precipitated. The mixture was then filtered through a short pad of Celite and evaporated to dryness to give the pure product. ^{1}H NMR data agrees with that reported in literature.[13]

General Procedure for the deprotonation of N-heterocyclic carbene salts

The method employed followed that reported by Fallis *et al*.[12] A flame dried Schlenk tube was charged with the N-heterocyclic carbene salts ([5-DippH]Br, [6-MesH]Br, [6-DippH]Br, [7-DippH]Br) (0.01 mol) and was further dried using three 'pump and purge' cycles followed by continuous vacuum for 30 min. The salt was then suspended in THF (20 mL) and a solution of K[N(SiMe$_3$)$_2$] (0.011 mol) in THF (30 mL) was added via cannula. After stirring for 30 min, the salt dissolved; filtration and removal of the volatiles *in vacuo* gave a yellow residue. The free N-heterocyclic carbene was extracted into diethyl ether (3 x 30 ml) and the resulting solution concentrated until cloudy. Storage overnight at -30 °C yielded the white crystalline N-heterocyclic carbene. ^{1}H NMR data agrees with that reported in literature.[12]

General Procedure for synthesis of E[N(SiMe$_3$)$_2$] (E = Sn, Pb)

The method employed followed that reported by Lappert *et al*.[14] ECl$_2$ (0.025 mol) was suspended in diethyl ether (100 ml), and a solution of Li[N(SiMe$_3$)$_2$] (0.05 mol) in diethyl ether (100 mL) added by cannula. The reaction mixture was stirred overnight. After stopping the stirring, the LiCl precipitate was allowed to settle and the supernatent

separated by filtration. Upon removing the solvent *in vacuo*, the residual oil was frozen with liquid nitrogen, affording a spectroscopically pure solid material (orange when E = Sn; yellow when E = Pb). ^{119}Sn and ^{207}Pb NMR data, respectively, agree with that reported in literature.[15] ^{1}H NMR (400 MHz, benzene-d_6) δ = 0.30 (E = Sn); δ = 0.29 (E = Pb).

2.3 References

1. R. E. Dodd and P. L. Robinson, *Experimental inorganic chemistry : a guide to laboratory practice*, Elsevier Pub. Co, Amsterdam, 1954.
2. R. J. Errington, *Advanced practical inorganic and metalorganic chemistry*, Blackie Academic & Professional, London, 1997.
3. D. F. Shriver and M. A. Drezdzon, *The manipulation of air-sensitive compounds*, Wiley, New York, 2nd edn., 1986.
4. Z. Otwinowski and W. Minor, *Macromolecular Crystallography, Pt A*, 1997, **276**, 307-326.
5. L. Palatinus and G. Chapuis, *Journal of Applied Crystallography*, 2007, **40**, 786-790.
6. G. M. Sheldrick, *Acta Crystallographica a-Foundation and Advances*, 2008, **64**, 112-122.
7. A. L. Thompson and D. J. Watkin, *Journal of Applied Crystallography*, 2011, **44**, 1017-1022.
8. R. I. Cooper, A. L. Thompson and D. J. Watkin, *Journal of Applied Crystallography*, 2010, **43**, 1100-1107.
9. A. J. Arduengo, R. Krafczyk, R. Schmutzler, H. A. Craig, J. R. Goerlich, W. J. Marshall and M. Unverzagt, *Tetrahedron*, 1999, **55**, 14523-14534.
10. J. D. Scollard, D. H. McConville, J. J. Vittal and N. C. Payne, *Journal of Molecular Catalysis a-Chemical*, 1998, **128**, 201-214.
11. E. L. Kolychev, I. A. Portnyagin, V. V. Shuntikov, V. N. Khrustalev and M. S. Nechaev, *Journal of Organometallic Chemistry*, 2009, **694**, 2454-2462.
12. M. Iglesias, D. J. Beetstra, J. C. Knight, L.-L. Ooi, A. Stasch, S. Coles, L. Male, M. B. Hursthouse, K. J. Cavell, A. Dervisi and I. A. Fallis, *Organometallics*, 2008, **27**, 3279-3289.
13. E. L. Kolychev, V. V. Shuntikov, V. N. Khrustalev, A. A. Bush and M. S. Nechaev, *Dalton Transactions*, 2011, **40**, 3074-3076.
14. D. H. Harris and M. F. Lappert, *Journal of the Chemical Society-Chemical Communications*, 1974, 895-896.
15. B. Wrackmeyer, *Journal of Magnetic Resonance*, 1985, **61**, 536-539.

Chapter 3

Quantum Chemical Studies of Cyclic Carbenes as σ-Donors in Late Transition Metal Systems

---

3.1 Introduction

N-heterocyclic carbenes (NHCs; e.g. **1**, Figure 3-1) are neutral, carbon-donor ligands which have been widely exploited in the stabilization of cationic metal species implicated in homogenous catalysis.[1-11] They are known to be very strong σ-donors, and the strong metal-ligand bonds formed with late transition metal centres underpin the longevity of many 'noble' metal NHC catalysts.[7-11]

For the isolation of free (i.e. uncomplexed) NHCs, so-called 'push-pull' electronic stabilization is known to be a significant enabling factor; inductive stabilization of the HOMO and mesomeric destabilization of the LUMO by the electronegative and π-donor α-nitrogen substituents typically contribute to a relatively wide HOMO-LUMO separation.[12] More recently, expanded ring NHC systems (**2,** where n = 1-3) and cyclic amino alkyl carbenes (CAACs, **3**, Figure 3-1) have been explored,[13-18] demonstrating how the HOMO and LUMO energies (and consequently ligand properties) can be tuned by heterocycle design.

Anionic variants of NHCs featuring a pendant weakly-coordinating anion component tethered to the heterocycle backbone (WCA-NHCs) have recently emerged (e.g. **4**, Figure 3-1), in part driven by a desire to generate zwitterionic metal complexes with

improved solubility in apolar media.[19-22] Such systems have been shown to be effective, for example, in bringing about catalytic hydrogenation chemistry in pure hydrocarbon media.[20] The Aldridge group has been interested in expanding the scope of such systems, by developing versatile synthetic routes to a range of WCA-NHC complexes offering systematic variation in the size of the heterocyclic backbone (e.g. Figure 3-1, **5**, where *m* = 1-3).[23] For systems of this type, it was hypothesized that the remote CH_2-mediated tethering of the WCA component (*cf.* direct bonding to the ligand heterocycle in systems of type **4**, Figure 3-1)[19-22] should give rise to relatively unperturbed ligand properties closely aligned with those of the corresponding "simple" NHCs.

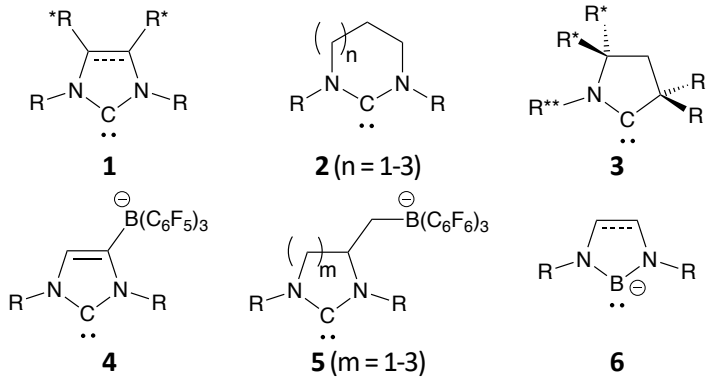


Figure 3-1: Neutral NHC and isoelectronic (anionic) boryl ligands.

A related class of complex are those containing diazaborolyl ligands (**6**), based on an isoelectronic B-containing heterocycle with the anionic charge formally localized at boron. Compounds containing such ligands have been known since the 1990s,[24-29] but recent syntheses owe much to the development of nucleophilic boryllithium reagents by Yamashita, Nozaki and co-workers in 2006.[30-33] Superficially, diazaborolyl ligands have a similar frontier orbital make up to NHCs, i.e. a boron lone-pair type HOMO, and a LUMO potentially featuring a significant contribution from the perpendicular boron pπ orbital.[34]

Observations made from structural studies of p and d-block systems, however, imply that these B-donor ligands present an even higher degree of σ electron donation than do NHCs.[35-38]

Given ongoing interests in the Aldridge group in both of these families of anionic ligands,[23, 39-47] and their relationships to the widely-used NHC donor class, it was perceived that there was a need for a systematic study – involving both structural and quantum chemical input – of their comparative ligand properties. Quantum chemical studies to this end are summarized in this chapter.

3.2 Computational Details

3.2.1 Density Functional Theory

Researchers have been trying to describe multiple-electron systems via wavefunctions since the early development of quantum mechanics. These wavefunctions grant us access to information concerning a specific state of the target system; however, the number of variables in the wavefunction increases dramatically as the size of the system expands – there being three spatial and one spin variables for each of the electrons in the system. The size of the system will soon become unmanageable if we are studying, for example a biological molecule with thousands of atoms. Therefore, we need a simpler method: Density Functional Theory has become the solution of choice in many cases for this problem.

The core of Density Functional Theory is the replacement of the N-electron wavefunction with its dependence on 3N spatial plus N spin variables, by a simpler quantity, the electron density of the target system, which depends only on three spatial

variables.[48] There were several attempts since 1927 to tackle this problem, including the Thomas-Fermi Model and the Hartree-Fock-Slater model,[48] but the birth of Density Functional Theory did not come until 1964 when Hohenberg and Kohn published their landmark paper in *Physical Review*.[48, 49]

In this paper, the authors set out the First and Second Hohenberg-Kohn Theorems which have become the cornerstone of Density Functional Theory. The First Theorem states that "the external potential $V_{ext}(\vec{r})$ is (to within a constant) a unique fuction of election density $\rho(\vec{r})$; Since, in turn $V_{ext}(\vec{r})$ fixes $\widehat{H}$ we see that the full many particle ground state is a unique functional of $\rho(\vec{r})$."[49] The First Hohenberg-Kohn Theorem is a proof for the existence of Density Functional Theory – we can actually replace the wavefunction with the electron density of the target system, since the electron density itself is unique for a specific energy state. In addition, the Second Theorem states that $F_{HK}[\rho]$, the functional that delivers the ground state energy of the system, delivers the lowest energy if and only if, the input density is the ground state density, ρ_0.[50] Based on these two theorems we can actually calculate the ground state energy with electron density instead of the wavefunctions.

The Kohn-Sham Model of Density Functional Theory was reported a year after the two basic theorems, and describes the approach of calculating energy from electron density.[50] The Kohn-Sham Equation described in this paper is as shown in equation 3.1:

$$\mathrm{E}[\rho(\vec{r})] = T_s[\rho] + J[\rho] + E_{xc}[\rho] + E_{Ne}[\rho] \qquad 3.1$$

In which $\mathrm{E}[\rho(\vec{r})]$ is the total energy of the system, $T_s[\rho]$ the non-interacting kinetic energy, $J[\rho]$ the Coulomb Energy, $E_{Ne}[\rho]$ the energy of the electron-nuclear interaction

and $E_{xc}[\rho]$ the exchange-correlation energy, which can be further described as shown in equation 3.2:

$$E_{XC} = T_C[\rho] + E_{ncl}[\rho] \qquad 3.2$$

$T_C[\rho]$ is the residual part of true kinetic energy that is not covered by $T_s[\rho]$, and $E_{ncl}[\rho]$ the non-classical electrostatic contribution. The exchange-correlation energy functional contains everything that is unknown,[48] and many approximations on it have been published and I will describe our choice on this term in the next section.

3.2.2 Amsterdam Density Functional

Amsterdam Density Functional (ADF) is so far the only DFT program based on Slater-Type-Orbitals (STOs). STOs were first introduced by John C. Slater in 1930 with the form as shown in equation 3.3: [51]

$$\mathrm{f(r)} = Y_{lm}(\theta, \phi) r^{n-1} e^{-\left(\frac{Z_{eff}}{n}\right) r} \qquad 3.3$$

$Y_{lm}(\theta, \phi)$ is a spherical harmonic, r the distance between electrons and the nucleus, and the exponential factor determines the long-range decay of the function. Compared to Gaussian-type-orbitals (GTOs), which are used in most other quantum-chemical codes, STOs have the advantage of possessing the required cusp behaviour as well as the appropriate long-range decay.[52] High-quality basis sets with relatively small numbers of functions can then be achieved in this case, which saves computational time, or in other words we can have more accurate computational results.

The calculations featured in this thesis were obtained using the packages ADF2013.01, ADF2014.02 and ADF 2014.05. Specific details of the calculation setup will be described in the next section.

3.2.3 XC Potential – Exchange-Correlated Potential

As described at the end of section 3.2.1, the exchange-correlated term accumulates everything unknown in Density Functional Theory. To complete the Kohn-Sham Equation we therefore need an approximation for this term. ADF has implemented many approximations that have been developed over many years, which consist of LDA (Local Density Approximation), a GGA part (Generalized Gradient Approximation), a Hartree-Fock exchange part and a meta-GGA part. LDA is the basis of all the approximations implemented in ADF, in which the XC potential in each point of space depends only on the (spin) density at that same point. Either one of the GGA part, the Hartree-Fock exchange part, the meta-GGA part or the combinations thereof are the additives to LDA for more precise approximation.

Many calculations in organometallic chemistry[53-57] are performed using the Vosko-Willk-Nusair Local Density Approximation, with exchange from Becke,[58] and correlation correction from Perdew,[59] which is under the GGA catalogue. In recent years ADF has implemented a series of exchange-correlated functionals with the dispersion term contained within it. The dispersion term which accounts for dispersion forces inside or between molecules, can increase the accuracy of calculated energies, especially in the presence of weak interactions.[60] Our targets include weakly-coordinated-anions N-heterocyclic carbenes (WCA-NHCs) and therefore the introduction of dispersion force in

our calculations is necessary. In conclusion, BP86-D3 has been chosen as the exchange-correlated potential functional.

3.2.4 Basis Set

In the sense of theoretical and computational chemistry, the basis set consists of functions describing atomic orbitals and the linear combinations of these functions are used to create molecular orbitals. As mentioned in section 3.2.2, ADF exploits Slater-Type-Orbitals (STO) as basis set elements, with the general formula as shown in equation 3.3.

The ADF program is currently equipped with different sizes of basis set, from single zeta (SZ), double zeta (DZ), valence triple zeta with one polarization function (TZP) all the way to valence quadruple zeta with four polarization function, relativistically optimized. The accuracy of calculations depends on the size of basis set – typically the bigger the basis set, the more accurate the calculation will be.[61] The choice on basis set therefore will be a balance between the accuracy demanded and the CPU time affordable.

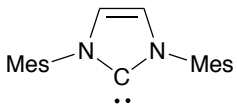


*Figure 3-2: The structure of (**I-c**)^{Mes}.*

To determine out the most suitable basis set in our case, (**I-c**)^{Mes} were chosen for a series of test calculations, as displayed in Figure 3-2. In these tests, the XC potential was fixed to GGA:BP86-D3, all electrons in atoms were considered and the numerical quality was set to Becke Good. (The setup on frozen core and numerical quality is rationalised in the next section). An affordable but accurate basis set, ET/ET-pVQZ (even-tempered

valence quadruple zeta with polarization), was chosen at first for accuracy reference calculations. The choice of basis set was then varied and HOMO/LUMO energies were calculated, together with total elapsed CPU time, as shown in Table 3-1.

Table 3-1: A summary of HOMO/LUMO energies and CPU time against the choice of basis set The first basis set ET/ET-pVQZ is a reference and the theoretical accuracy then decreases on going down the table.

Basis Set	HOMO Energy(kJ mol^{-1})	LUMO Energy(kJ mol^{-1})	CPU Time(min)
ET/ET-pVQZ	-475.73	-125.13	424
TZ2P	-474.31	-125.37	231
TZP(ZORA)	-475.68	-124.95	444
TZP	-474.91	-125.24	153
DZ	-483.27	-144.62	93
SZ	-206.81	106.07	72

As can be seen from Table 3-1 the accuracy increases significantly from SZ to TZP with a consequent doubling of the CPU time; employing a larger basis set will increase the accuracy further but only by expanding the amount of CPU time significantly for relatively modest improvements. The trend is easier to understand if we plot the difference between HOMO/LUMO energies of each basis set and the reference, against CPU time consumed, as in Figure 3-3.

In addition, a TZP basis set with relativistic correlation (ZORA) was additionally employed in the test as well. The consequent ZORA/TZP provides similar accuracy to 'normal' TZP but consumes more CPU time. Therefore, the use of ZORA/TZP was not thought necessary unless heavy atoms, such as gold form part of the system.

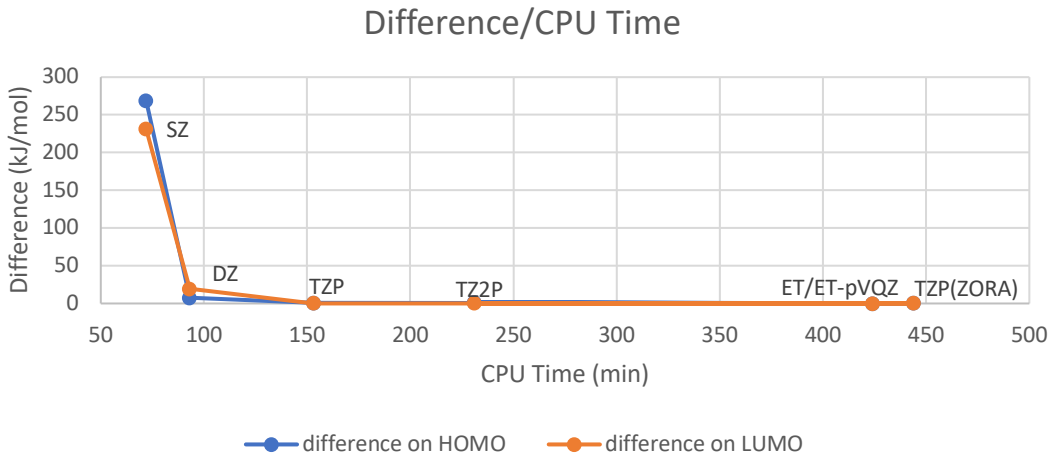
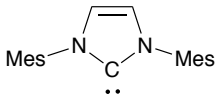
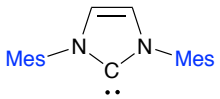
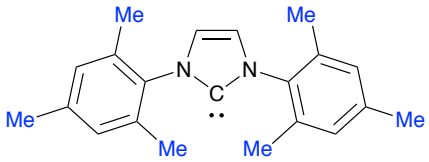


Figure 3-3: Plot of difference between the HOMO-LUMO energy gap calculated for a given basis set vs. the reference basis set, against CPU time consumed.

Calculations were also carried out using a smaller basis set for the minor part of the molecule (i.e. that which seemed more peripheral to the donor atom), which might save CPU time while preserving the accuracy of the calculations. The reference basis set for this series of calculations was TZP, with a small modification to the XC potential function (from BP86-D3 to BP86-D in order to save time). The results of these comparative calculations are summarised in Table 3-2. From this analysis it is clear that most of the basis sets alter the HOMO/LUMO energies to a significant degree, and some of them may even take a longer CPU time. The final set-up, which separates the methyl group from the rest of the structure, results in a very high accuracy, but does not save much time (~7%). In conclusion, TZP for the whole molecule is the best choice of basis set, achieving balance between accuracy and CPU time.

Table 3-2: Results of applying different basis set to different parts of a reference carbene.

Structure	Basis Set	HOMO (kJ mol^{-1})	LUMO (kJ mol^{-1})	CPU (min)
	TZP on whole molecule	-478.00	-122.54	126
	N:TZP C:TZP H:SZ	-466.90	-115.10	153
 **a**	Mes-H:SZ Mes-C:SZ Ring-H:SZ Ring-N:TZP Ring-C:TZP	-389.93	46.04	107
	Mes-H:SZ Mes-C:DZ Ring-H:SZ Ring-N:TZP Ring-C:TZP	-493.63	-147.31	99
	Mes-H:SZ Mes-C:DZ Ring-H:TZP Ring-N:TZP Ring-C:TZP	-495.36	-146.66	84
	Mes-H:SZ Mes-C:TZP Ring-H:TZP Ring-N:TZP Ring-C:TZP	-468.35	-114.34	158
 **b**	Me-H:SZ Me-C:DZ Main-H:TZP Main-C:TZP Main-N:TZP	-478.10	-119.55	117

a. The structure is separated into two parts: the N-heterocyclic ring, denoted “Ring” and the mesityl, denoted “Mes”, displayed in blue;
b. The structure is separated into two parts: the methyl groups of the mesityl substituents, denoted “Me”, displayed in blue and the rest of the molecule, denoted “Main”.

3.2.5 Frozen Core Approximation and Numerical Quality

The use of the frozen core approximation reduces the number of functions involved in the calculation.[48] However, for some of the later calculations, for example, involving gold complexes, the use of a frozen core may cause lower accuracy, so all-electron basis sets were used instead, to preserve the consistency for publication. In our case, 'Becke Good' was used.

3.3 Results and Discussion

3.3.1 The Selection and Geometry Optimisation of Ligands

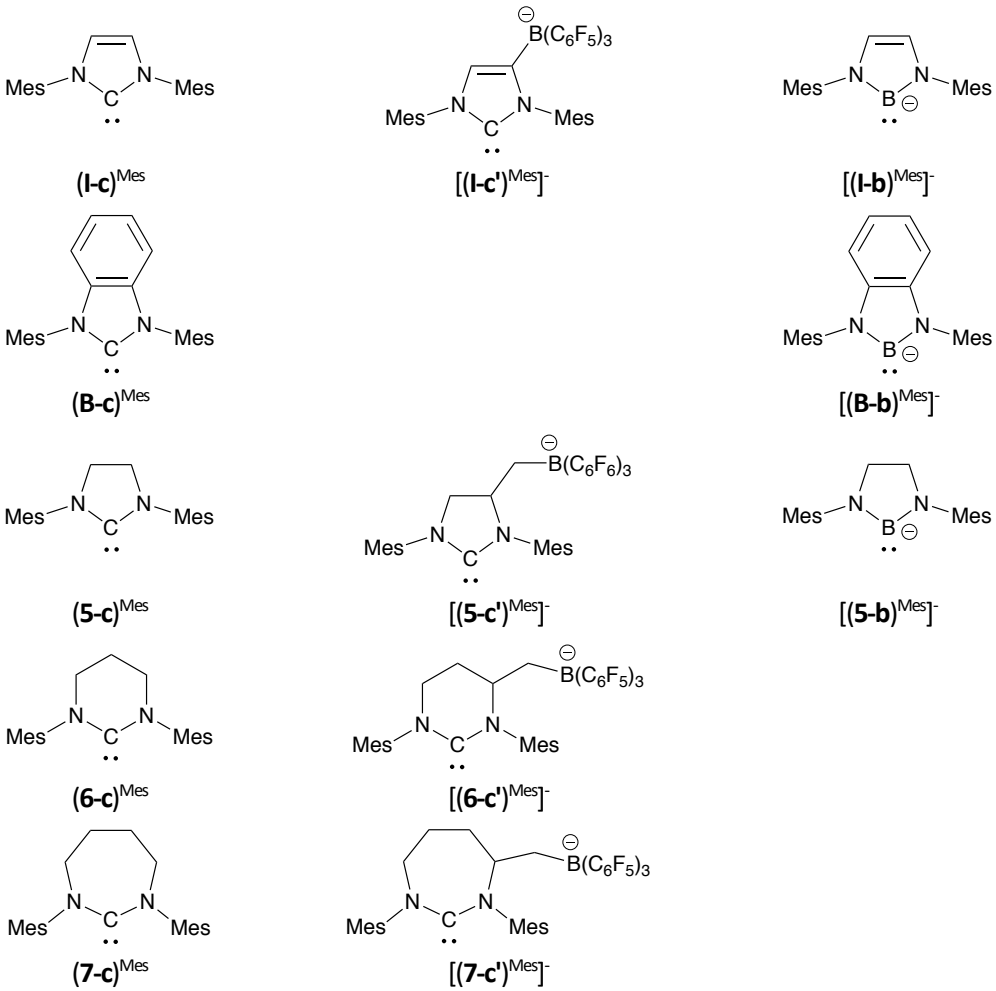


Figure 3-4: NHC, WCA-NHC and boryl ligands examined in the current study.

Figure 3-4 shows the carbene and diazaborolyl ligands which have been probed in the current study. These can be subdivided into neutral N-heterocyclic carbenes (NHCs) (Figure 3-4, left column, denoted by the label c), N-heterocyclic carbenes incorporating a pendant weakly coordinating anion component (WCA-NHCs) (centre, labelled c'), and formally anionic diazaborolyl ligands (right, labelled b). In each case the prefix denotes the nature of the central heterocycle, be it imidazole (I-) or benzimidazole-derived (B-), or based on a saturated 5-, 6- or 7-membered core (5-, 6-, 7-); the nature of the N-bound aryl group is indicated by the superscript tag.

Isolable NHCs, of course, have been known for many years, as outlined above,[1-6] and their experimental properties are well understood. We therefore sought to use these systems as a computational baseline for our subsequent analyses of the electronic structure in less familiar WCA-NHC and diazaborolyl systems.[12] As such, the perturbation brought about by introducing a pendant borate functionality, or by formally replacing the carbene carbon with boron, could readily be assessed for a range of heterocyclic systems. In all cases, calculations were carried out on systems featuring mesityl groups as the N-aryl substituents (although some experimental studies rely on bulkier Dipp groups). This regime was employed in order to provide uniform like-for-like comparison between the different classes of ligand, without unduly expanding the computational timeframe of the study.

*Table 3-3: Key geometric parameters for (**I-c**)^{Mes}, (**5-c**)^{Mes}, (**6-c**)^{Mes}, (**7-c**)^{Mes}, [(**5-c'**)^{Mes}]-, [(**5-b**)^{Mes}]- and [(**I-b**)^{Mes}]- derived from X-ray crystallography and DFT calculations.*

Ligand	Ref	Experimental			Calculated		
		N-C(B)-N bond angle (°)	N-C(B) bond length (Å)	C-C 'backbone' separation (Å) [a]	N-C(B)-N bond angle (°)	N-C(B) bond length (Å)	C-C backbone distance (Å)[a]
(I-c)^{Mes}	62	101.4(2)	1.371(4)	1.333(5)	101.2	1.375	1.361
(5-c)^{Mes}	63	104.7(3)	1.352(5)	1.505(6)	105.8	1.350	1.531
(6-c)^{Mes}	13	114.7(1)	1.346(1)	2.453(2)	115.3	1.350	2.485
(7-c)^{Mes}	13	116.6(4)	1.346(5)	2.787(6)	117.5	1.351	2.836
[(I-c')^{Mes}]$^{-}$	19	102.8(1)	1.355(2), 1.371(2)	1.358(2)	101.3	1.371, 1.378	1.364
[(5-c')^{Mes}]$^{-}$ [b]	23	104.7(2)	1.353(3), 1.353(4)	1.514(4)	105.5	1.350, 1.354	1.537
[(I-b)^{Mes}]$^{-}$ [b]	32	98.6(2)	1.474(4), 1.481(4)	1.338(4)	97.7	1.483	1.363
[(5-b)^{Mes}]$^{-}$ [c]	31	101.9(2)	1.455(2)	1.524(2)	101.5	1.459	1.534

a. Defined as the distance between the two backbone carbon atoms attached to nitrogen;
b. Experimental data for the N-Dipp analogue, as $[Li(THF)_2]^+$ derivative; calculated data for N-Mes, $[Li(THF)_2]^+$ system;
c. Experimental data for the N-Dipp analogue, as $[K(18\text{-crown-}6)]^+$ derivative; calculated data for $[K(THF)_3]^+$ system.

Geometry optimisations were first carried out on ligands for which experimental crystallographic data were available, with the key results being displayed in Table 3-3. In general, the agreement between the calculated and measured metrical parameters is very good. Thus, for example, differences in the key N-C-N bond angle are small: the calculated value for (**5-c**)^{Mes} diverges by 1.1˚,[16] but the remainder all have discrepancies of less than 1˚. In the case of the WCA-NHC and boryl systems, the most convenient experimentally

determined solid-state metrical data for the "isolated" anions are derived from adducts featuring Group 1 metal cations. Thus, the complexes of [(**5-c'**)^{Mes}]$^-$ (or strictly its N-Dipp substituted analogue) with [Li(η^6-toluene)]$^+$ and K[18-crown-6]$^+$ have been crystallographically characterized,[23] as have [Li(THF)$_2$]$^+$ complexes of [(**I-b**)^{Dipp}]$^-$ and [(**5-b**)^{Dipp}]$^-$.[31, 32] Thus, model systems featuring [(**5-c'**)^{Mes}]$^-$ and [(**I-b**)^{Mes}]$^-$ complexed to [Li(THF)$_2$]$^+$ and [K(THF)$_3$]$^+$ were optimized computationally and the metrical parameters compared to the available experimental data (Table 3-3). Here too, agreement between the two sets of data was very good.

From a geometric perspective, a key parameter relating to the σ-donor properties of all three classes of ligand is the N-E-N angle (E = C, B),[1-6, 12] and this metric is very well modelled computationally. In general, both N-C-N and N-B-N angles increase as the heterocyclic backbone increases in size: for saturated NHCs and WCA-NHCs the N-C-N angle widens with increasing length of the hydrocarbon linker between the two nitrogen atoms (i.e. from 5- to 6- to 7-membered heterocycles). More subtly, N-E-N angles also widen on going from systems featuring unsaturated backbones (e.g. (**I-c**)^{Mes}) to saturated linkers (e.g. (**5-c**)^{Mes}); this reflects the increase in the backbone C-C bond length as the formal bond order changes from two to one. Boryl systems typically feature narrower N-E-N angles than their NHC analogues, reflecting the larger covalent radius of boron within otherwise similar heterocycle frameworks.[63]

Table 3-4: Key orbital energies (in kJ mol^{-1}) and compositions (in vacuum and thf dielectric) for the NHCs, WCA-NHCs and boryl ligands depicted in Figure 3-4.

Ligand	Calc. N-E-N angle (°)	E(σ) vacuum (thf)	E(pπ) vacuum (thf)	ΔE vacuum (thf)	s/p ratio for HOMO (thf)
(I-c)^{Mes}	101.2	-475 (-538)	-33 (-41)	442 (482)	0.71 (0.60)
(B-c)^{Mes}	102.7	-489 (-549)	-15 (-39)	474 (510)	0.68 (0.58)
(5-c)^{Mes}	105.8	-463 (-517)	-33 (-56)	430 (461)	0.60 (0.49)
(6-c)^{Mes}	115.3	-421 (-473)	-42 (-55)	379 (418)	0.56 (0.46)
(7-c)^{Mes}	117.5	-403 (-446)	-52 (-63)	351 (383)	0.54 (0.44)
[(I-b)^{Mes}]$^-$	97.7	93 (-266)	415 (51)	322 (317)	0.75 (0.66)
[(B-b)^{Mes}]$^-$	98.1	66 (-283)	393 (60)	327 (343)	0.84 (0.71)
[(5-b)^{Mes}]$^-$	101.5	94 (-254)	422 (45)	328 (299)	0.61 (0.53)
[(I-c')^{Mes}]$^-$	101.3	-231 (-482)	205 (-1)	436 (481)	0.64 (0.48)
[(5-c')^{Mes}]$^-$	105.5	-242 (-471)	186 (-6)	428 (465)	0.55 (0.47)
[(6-c')^{Mes}]$^-$	114.9	-209 (-429)	182 (-2)	391 (427)	0.52 (0.44)
[(7-c')^{Mes}]$^-$	118.4	-194 (-392)	165 (-14)	359 (378)	0.52 (0.43)

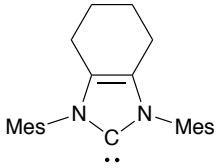
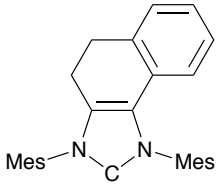
Table 3-4 lists the calculated energies of the σ and pπ orbitals for each of the ligands, both in the gas phase and with allowance made for the THF dielectric effect using the COSMO approach. With the exception of the benzannulated systems (i.e. (**B-c**)^{Mes} and [(**B-b**)^{Mes}]$^-$), the calculated data for NHC, WCA-NHC and boryl ligands follow a common trend: widening of the N-C-N bond angle (e.g. by expanding the heterocycle), leads to a reduction in the s:p ratio (greater p character) and a consequent increase in the energy of the σ orbital (HOMO).[2] The energy of the pπ orbital is less sensitive to these geometric changes, with the effect that the σ-pπ energy separation systematically falls. With respect to the NHC and WCA-NHC systems, the change is most marked between the saturated five-

membered systems (**5-c**)^{Mes}/[(**5-c'**)^{Mes}]$^{-}$ and their six-membered analogues (**6-c**)^{Mes}/[(**6-c'**)^{Mes}]$^{-}$, with the smaller change on further ring expansion to (**7-c**)^{Mes}/[(**7-c'**)^{Mes}]$^{-}$, reflecting the puckered nature of the seven-membered heterocycle and the consequently smaller effect on the N-C-N angle brought about by the inclusion of the additional backbone methylene spacer.[13] The relative effect of the THF dielectric is minimal for the NHC systems, but understandably more pronounced for the negatively charged WCA-NHC and boryl systems, particularly for the latter class of compound in which the negative charge is localized on the low-valent boron centre.

Benzannulated systems (**B-c**)^{Mes} and [(**B-b**)^{Mes}]$^{-}$[31] do not appear to fit easily into the simple trend identified for other NHC/boryl ligands based on the variation in the respective N-E-N angles. Consideration of the bond order (and hence length) of the backbone C-C linker, accounts for the N-C-N and N-B-N angles for these benzannulated ligands, which are found to be intermediate between (**I-c**)^{Mes}/[(**I-b**)^{Mes}]$^{-}$ (C=C backbone) and (**5-c**)^{Mes}/[(**5-b**)^{Mes}]$^{-}$ (C-C backbone). On this basis, it might be expected that the σ orbital energies for both (**B-c**)^{Mes} and [(**B-b**)^{Mes}]$^{-}$ would lie between those for the respective saturated/unsaturated systems. However, both ligands feature HOMO (σ) orbitals which are significantly more stabilized (and higher in s-character) than would be expected on the basis of these simple geometric considerations. The additional factor underlying these data is the electron-withdrawing effect of the benzene backbone function in (**B-c**)^{Mes}/[(**B-b**)^{Mes}]$^{-}$ - a factor which has been demonstrated elegantly for a range of (poly)aromatic backbone functionalized NHCs by Peris and co-workers.[64] This effect is not limited to directly benzannulated heterocycles. Studies of NHC ligands **1** and **2** show that – despite possessing essentially identical (calculated) N-C-N angles (101.2 and 101.7°, respectively; Table 3-5)[65] – these ligands have Tolman Electronic Parameters (TEPs) of 2046.8 and 2048.0 cm^{-1} [65]

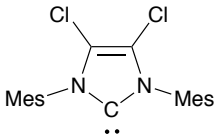
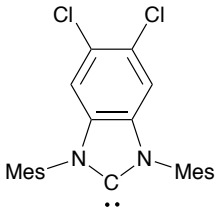
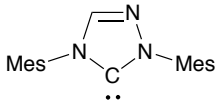
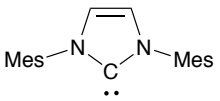
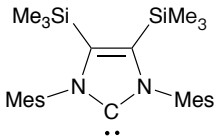
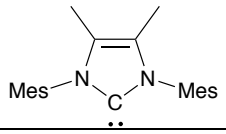
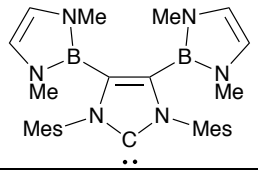
which implies that **2** is a less strongly donating NHC than **1**. The mild electron withdrawing capabilities of the pendant benzene ring in **2** are also consistent with HOMO energies for **1** and **2** (calculated using our method) of -455 and -474 kJ mol^{-1}, respectively.

Table 3-5: Comparison between the two carbenes studied for trans-influence.

Carbene Cl—Ir—CO CO **Carbene**	**Backbone Length (Å)**	**N-C-N Angle**	**E(σ) in gas phase (kJ mol^{-1})**	**TEPs (cm^{-1})**	**Reported average CO stretching Frequency (cm^{-1})**
 **1**	1.36	101.2	-455	2046.8	2019.8
 **2**	1.37	101.7	-474	2048.0	2021.3

In a broader sense, examination of the electronic effects of a range of backbone substituents shows (not unexpectedly) that the HOMO energy correlates well with the respective Hammett parameter σ_p (Table 3-6)[20]. Without a large variation in N-C-N angle, the σ orbital energy level increases as the ligand become a weaker electron-withdrawing group or a stronger electron-releasing group.

Table 3-6: The backbone length, N-C-N angle and the σ energy levels of carbene in the study of backbone induction effect.

Carbene	N-C-N Angle	Hammett Parameter[66]	E(σ) in gas phase (kJ mol^{-1})
	102.3	+0.23	-511
	103.0	N/A	-502
	100.2	N/A	-493
	101.2	0.00	-489
	101.6	-0.07	-441
	101.3	-0.17	-401
	101.6	N/A	-401

However, while these initial calculations allow some trends to be identified within a given ligand class, the desired comparison between NHCs on the one hand, and WCA-NHC/boryl donors on the other (e.g. between (**I-c**)^{Mes} and [(**I-c'**)^{Mes}]$^{-}$ or [(**I-b**)^{Mes}]$^{-}$), is more difficult to achieve for the ligands in isolation owing to the differences in net charge.

With this in mind, we wanted to compare the properties of the different ligands within a family of (otherwise identical) transition metal complexes. Linear Au(I) complexes

of the type $[LAuCl]^{n-}$ (NHC: $n = 0$; WCA-NHC, boryl: $n = 1$) were thought to be good potential model systems, given (i) their geometric simplicity (and the lack of potential complicating effects associated, for example, with the presence of *cis* ligands), and (ii) the large pool of available structural data associated with complexes of this type reported in the literature featuring L = NHC.[67] Computational efforts were therefore moved on to focus on the $[LAuCl]^{n-}$ model. (Experimental efforts were separately carried out by my colleague Dr. Andrey Protchenko, focused on the synthesis and structural characterization of a range of related compounds featuring L = WCA-NHC or boryl ligand, in order to allow for direct structural comparisons.)

3.3.2 Fragment Calculations

A second part of this comparative ligand analysis involves investigating computationally the trans influence of the NHCs, WCA-NHCs and boryl anions. The trans influence, also known as 'thermodynamic trans effect', is the destabilization of ligands that are trans to the donor in question. The σ-donor L will donate electron density to the anti-bonding orbital of M-X (metal-halide) and therefore weaken the M-X bond. As the σ-donor strength of L (Ligand) gets stronger, the M-X bond will be further destabilised.

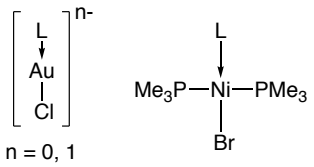


Figure 3-5: The generic structures of Au (left) and Ni complexes (right) investigated in this study.

Destabilization of the M-X bond will lead to a longer bond length to the metal centre. In this section NHCs, WCA-NHCs and boryl anions are all examined as component ligands of linear Au(I) complexes of the type $[LAuCl]^{n-}$ (with the structures shown in Figure 3-5 (left)) mentioned in the last section, as well as nickel complexes (with the structures shown in Figure 3-5(right), for comparison with work done by Lin, Marder *et al.*[35]). At first geometry optimizations for each of the complexes were carried out, and both the M-L and M-Br (M being Au or Ni) bond lengths were used as the indications of the trans influence. However, both σ orbital energies and trans bond lengths are indirect indicators of σ-donor strength. A fragment calculation which shows the interaction between σ-donor and metal would be a more direct quantum chemical method to investigate the σ-donor strength of the target systems. An in-depth investigation of the L-M(Au/Ni) bond using ETS-NOCV was then employed to provide a further basis for comparison of NHC, WCA-NHC and (anionic) boryl ligands. Extended Transition State – Natural Orbitals for Chemical Valence (ETS-NOCV) analysis, offers a compact quantitative picture of the chemical bond. With the ETS-NOCV charge and energy decomposition scheme, the deformation density is partitioned into the different components of the chemical bond σ, π and δ. The energy contributions to the total bond energy are calculated for each specific orbital interaction between fragments, giving insight into the various potential orbital interactions. In our case, we are looking at the interaction between the carbenes or boryl anions, and the metal centre. Therefore, the complex molecule is separated into two fragments – the neutral carbene or anionic boryl, then the rest of the complex, as depicted in Figure 3-5.

3.3.3 Quantum Chemical Studies of Gold Complexes

Key data relating to the geometry optimizations (with comparison to corresponding crystallographic data of compounds synthesised by colleague Dr. Andrey Protchenko or reported in previous literatures) and ETS-NOCV analyses for the $[LAuCl]^{n-}$ systems are summarized in Table 3-7.

Table 3-7: Geometric parameters obtained from X-ray crystallography comparing with calculated results, and (ETS-NOCV determined) interaction energies for gold complexes of the type $[LAuCl]^{n-}$.

Ligand	Expt. Au-L bond length (Å)[a]	Calc. Au-L bond length (Å)	Expt. Au-Cl bond length (Å)[a]	Calc. Au-Cl bond length (Å)	$E_{int}(\sigma)$ (kJ mol^{-1})[e]	$E_{int}(\pi)$ (kJ mol^{-1})[e]
(I-c)^{Mes}	1.942(3)[68]	1.981	2.270(1)[68]	2.296	-174	-51
(5-c)^{Mes}	1.979(3)[69]	1.985	2.276(1)[69]	2.296	-178	-53
(6-c)^{Mes}	2.004(8)[16]	2.008	2.281(12)[16]	2.301	-179	-49
(7-c)^{Mes}	2.012(6)[17]	2.011	2.305(1)[17]	2.302	-180	-51
[(I-b)^{Mes}]$^-$	2.026(3)[b, 70]	2.022	2.405(1)[b, 70]	2.423	-267	-35
[(5-b)^{Mes}]$^-$	c	2.028	c	2.426	-274	-37
[(5-c')^{Mes}]$^-$	2.006(5)[d, 70]	1.992	2.276(2)[d, 70]	2.313	-187	-49
[(6-c')^{Mes}]$^-$	2.011(2)[d, 70]	2.013	2.286(1)[d, 70]	2.318	-188	-45
[(7-c')^{Mes}]$^-$	c	2.019	c	2.318	-189	-46

a. The N-substituents being Dipp for the parameters obtained from X-ray crystallography, i.e. data for (**I-c**)^{Dipp} instead of (**I-c**)^{Mes};
b. [K(18-crown)$_6$(η^2-toluene)] salt;
c. Data not available;
d. [Li(thf)$_4$] salt;
e. Interaction energy between two fragments, cauculated by ETS-NOCV.

As shown in the table, the trend in geometric parameters from quantum chemical studies and X-ray crystallography are in good agreement with each other. Descending Table 3-7 it can be seen that the trans Au-Cl bond lengths of the NHC and WCA-NHC systems ((**5-c**)^{Mes} vs. [(**5-c'**)^{Mes}]$^-$, (**6-c**)^{Mes} vs. [(**6-c'**)^{Mes}]$^-$) are statistically identical, suggesting that the

anionic component on WCA-NHC is effectively isolated from the heterocycle via the saturated CH_2 linker. The trend in Au-Cl bond length is more obvious when associated with the change from NHC/WCA-NHC donors to boryl ligands. In agreement with the experimental data, like-for-like comparison shows that the Au-Cl distance is >0.1 Å longer for the boron-centred donors. This in turn can be related to the enhanced donor capabilities of the anionic boryl ligand class, with the much higher energy of the σ-symmetry frontier orbital (Table 3-4) leading to a significantly larger σ component to the overall interaction energy (Table 3-7).

On the other hand, especially for NHCs and WCA-NHCs, the Au-C bond length increases together with the Au-Cl bond length. A similar trend was also reported by Lin and Marder,[35] who rationalized the trend as stemming from the greater p orbital contribution to the σ donor orbital of the ligand as that ligand becomes a stronger donor. Hence the Au-C bond lengthens, as greater p orbital character leads to expanded radial extension.

Last but not least, the π-acceptor properties of the diazaborolyl ligands are shown to be smaller even than those of NHCs, presumably reflecting the much higher energy of the respective pπ orbital in a ligand system bearing a formal negative charge. Differences between the NHC and WCA-NHC systems, as with the experimental data outlined above, are very minor.

3.3.4 Quantum Chemical Studies of Nickel Complexes

Fragment calculations were repeated on the Ni complexes of the selected ligands, and the results of geometry optimisations on the Ni complexes are displayed in Table 3-8.

Table 3-8: The summary of Ni bond length and Ni-Br bond length of Ni complex with NHCs, WCA-NHCs and boryl anions trans to Br.

Ligand	Calc. Ni-L bond length (Å)	Calc. Ni-Cl bond length (Å)	$E_{int}(\sigma)$ (kJ mol^{-1})	$E_{int}(\pi)$ (kJ mol^{-1})
(I-c)^{Mes}	1.905	2.383	-171	-48
(B-c)^{Mes}	1.910	2.384	-167	-54
(5-c)^{Mes}	1.901	2.391	-176	-52
(6-c)^{Mes}	1.930	2.416	-182	-48
(7-c)^{Mes}	1.972	2.419	-179	-43
[(I-b)^{Mes}]$^{-}$	1.958	2.455	-391	-36
[(B-b)^{Mes}]$^{-}$	1.959	2.442	-365	-39
[(5-b)^{Mes}]$^{-}$	1.953	2.475	-411	-36
[(5-c')^{Mes}]$^{-}$	1.900	2.420	-199	-48
[(6-c')^{Mes}]$^{-}$	1.938	2.433	-197	-42
[(7-c')^{Mes}]$^{-}$	1.964	2.441	-192	-41

Analogous to the results for the Au complexes, for each class of ligand, both the Ni-L and the Ni-Br bond length increase as the size of the ring expands. In terms of the trend in Ni-Br bond length, it is aligned with the conclusions drawn in the section 1.3.1, where the σ donating capabilities become stronger as the ring expands and hence these systems display a stronger trans influence. Between different categories of ligand, the trans influence follows the trend: boryls > WCA-NHCs > NHCs, as concluded on the trend of σ-donor strength at the end of section 1.3.1.

The results of ETS-NOCV analyses of Ni complexes are also summarized in Table 3-8. In general, the trends for both σ donation and π acceptor behaviour match the trends delineated for the electronic properties of NHCs and boryl anions from the studies of Au complexes, in that the σ donor contribution to the bond energy increases as the ring

expands, with (**B-c**)^{Mes} and its boryl analogue being exceptions. The boryl anions are consistently the strongest σ-donors as they have highest σ energy overall, follow by WCA-NHCs and then NHCs. Notably, the values of $E_{int}(\sigma)$ are very close for each of the NHC/WCA-NHC systems (comparing between Table 3-7 and Table 3-8), but the value of $E_{int}(\sigma)$ is much larger in the case of the Ni complexes featuring the anionic boryl ligand (vs their Au counterparts with the same ligand). The stronger interaction may be caused by the more positively charged Ni centre (Ni^{2+} vs. Au^{+}) which is – as a consequence – a stronger Lewis acid.

3.4 Summary

Comparisons of $E_{int}(\sigma)$ values within a given ligand class reflect the greater carbon p orbital character in the HOMO as a function of increasing heterocycle ring size (cf. Table 3-4), which results in (i) higher σ orbital energies and (slightly) longer trans M-hal bonds; and (ii) longer M-L distances associated with the metal-carbene/boryl bond itself.[35] The electronic properties of backbone substituents also play an important role in the σ orbital energy. An electron withdrawing backbone substituent decreases the σ orbital energy and an electron donating substituent would increase it. Finally, comparison of the complexes featuring the saturated backbone NHC (**5-c**)^{Mes} with its unsaturated counterpart (**I-c**)^{Mes} show small differences between the two ligands. (**5-c**)^{Mes} is predicted to be both a (marginally) stronger σ donor and π acceptor than (**I-c**)^{Mes}, in line with analyses made by Nolan and co-workers to rationalize the similar TEPs for these two ligands (TEP values being 1-2 cm^{-1} lower in the unsaturated counterpart).[71]

3.5 References

1. A. J. Arduengo, *Accounts of Chemical Research*, 1999, **32**, 913-921.
2. D. Bourissou, O. Guerret, F. P. Gabbai and G. Bertrand, *Chemical Reviews*, 2000, **100**, 39-91.
3. F. E. Hahn and M. C. Jahnke, *Angewandte Chemie-International Edition*, 2008, **47**, 3122-3172.
4. T. Droge and F. Glorius, *Angewandte Chemie-International Edition*, 2010, **49**, 6940-6952.
5. D. Martin, M. Melaimi, M. Soleilhavoup and G. Bertrand, *Organometallics*, 2011, **30**, 5304-5313.
6. M. N. Hopkinson, C. Richter, M. Schedler and F. Glorius, *Nature*, 2014, **510**, 485-496.
7. W. A. Herrmann, *Angewandte Chemie-International Edition*, 2002, **41**, 1290-1309.
8. S. Wurtz and F. Glorius, *Accounts of Chemical Research*, 2008, **41**, 1523-1533.
9. R. Corberan, E. Mas-Marza and E. Peris, *European Journal of Inorganic Chemistry*, 2009, 1700-1716.
10. J. C. Y. Lin, R. T. W. Huang, C. S. Lee, A. Bhattacharyya, W. S. Hwang and I. J. B. Lin, *Chemical Reviews*, 2009, **109**, 3561-3598.
11. S. Diez-Gonzalez, N. Marion and S. P. Nolan, *Chemical Reviews*, 2009, **109**, 3612-3676.
12. D. Munz, *Organometallics*, 2018, **37**, 275-289.
13. M. Iglesias, D. J. Beetstra, J. C. Knight, L.-L. Ooi, A. Stasch, S. Coles, L. Male, M. B. Hursthouse, K. J. Cavell, A. Dervisi and I. A. Fallis, *Organometallics*, 2008, **27**, 3279-3289.
14. E. L. Kolychev, I. A. Portnyagin, V. V. Shuntikov, V. N. Khrustalev and M. S. Nechaev, *Journal of Organometallic Chemistry*, 2009, **694**, 2454-2462.
15. M. Iglesias, D. J. Beetstra, B. Kariuki, K. J. Cavell, A. Dervisi and I. A. Fallis, *European Journal of Inorganic Chemistry*, 2009, 1913-1919.
16. S. Flugge, A. Anoop, R. Goddard, W. Thiel and A. Furstner, *Chemistry-a European Journal*, 2009, **15**, 8558-8565.
17. J. J. Dunsford, K. J. Cavell and B. M. Kariuki, *Organometallics*, 2012, **31**, 4118-4121.
18. M. Melaimi, R. Jazzar, M. Soleilhavoup and G. Bertrand, *Angewandte Chemie-International Edition*, 2017, **56**, 10046-10068.
19. S. Kronig, E. Theuergarten, C. G. Daniliuc, P. G. Jones and M. Tamm, *Angewandte Chemie-International Edition*, 2012, **51**, 3240-3244.
20. E. L. Kolychev, S. Kronig, K. Brandhorst, M. Freytag, P. G. Jones and M. Tamm, *Journal of the American Chemical Society*, 2013, **135**, 12448-12459.
21. A. Winkler, K. Brandhorst, M. Freytag, P. G. Jones and M. Tamm, *Organometallics*, 2016, **35**, 1160-1169.
22. A. Igarashi, E. L. Kolychev, M. Tamm and K. Nomura, *Organometallics*, 2016, **35**, 1778-1784.
23. N. Phillips, R. Tirfoin and S. Aldridge, *Dalton transactions (Cambridge, England : 2003)*, 2014, **43**, 15279-15282.
24. S. Onozawa, Y. Hatanaka, T. Sakakura, S. Shimada and M. Tanaka, *Organometallics*, 1996, **15**, 5450-5452.

25. G. J. Irvine, M. J. G. Lesley, T. B. Marder, N. C. Norman, C. R. Rice, E. G. Robins, W. R. Roper, G. R. Whittell and L. J. Wright, *Chemical Reviews*, 1998, **98**, 2685-2722.
26. S. Aldridge and D. L. Coombs, *Coordination Chemistry Reviews*, 2004, **248**, 535-559.
27. D. L. Kays and S. Aldridge, *Contemporary Metal Boron Chemistry I: Borylenes, Boryls, Borane (Sigma)-Complexes, and Borohydrides*, 2008, **130**, 29-122.
28. H. Braunschweig, R. D. Dewhurst and A. Schneider, *Chemical Reviews*, 2010, **110**, 3924-3957.
29. L. Dang, Z. Y. Lin and T. B. Marder, *Chemical Communications*, 2009, 3987-3995.
30. Y. Segawa, M. Yamashita and K. Nozaki, *Science*, 2006, **314**, 113-115.
31. Y. Segawa, Y. Suzuki, M. Yamashita and K. Nozaki, *Journal of the American Chemical Society*, 2008, **130**, 16069-16079.
32. M. Yamashita, Y. Suzuki, Y. Segawa and K. Nozaki, *Chemistry Letters*, 2008, **37**, 802-803.
33. L. Weber, *European Journal of Inorganic Chemistry*, 2017, 3461-3488.
34. A. Sundermann, M. Reiher and W. W. Schoeller, *European Journal of Inorganic Chemistry*, 1998, 305-310.
35. J. Zhu, Z. Y. Lin and T. B. Marder, *Inorganic Chemistry*, 2005, **44**, 9384-9390.
36. A. A. Dickinson, D. J. Willock, R. J. Calder and S. Aldridge, *Organometallics*, 2002, **21**, 1146-1157.
37. K. C. Lam, W. H. Lam, Z. Y. Lin, T. B. Marder and N. C. Norman, *Inorganic Chemistry*, 2004, **43**, 2541-2547.
38. H. Braunschweig, K. Radacki, D. Rais and D. Scheschkewitz, *Angewandte Chemie-International Edition*, 2005, **44**, 5651-5654.
39. A. V. Protchenko, J. Urbano, J. A. B. Abdalla, J. Campos, D. Vidovic, A. D. Schwarz, M. P. Blake, P. Mountford, C. Jones and S. Aldridge, *Angewandte Chemie-International Edition*, 2017, **56**, 15098-15102.
40. A. V. Protchenko, M. P. Blake, A. D. Schwarz, C. Jones, P. Mountford and S. Aldridge, *Organometallics*, 2015, **34**, 2126-2129.
41. A. V. Protchenko, D. Dange, M. P. Blake, A. D. Schwarz, C. Jones, P. Mountford and S. Aldridge, *Journal of the American Chemical Society*, 2014, **136**, 10902-10905.
42. A. V. Protchenko, D. Dange, J. R. Harmer, C. Y. Tang, A. D. Schwarz, M. J. Kelly, N. Phillips, R. Tirfoin, K. H. Birjkumar, C. Jones, N. Kaltsoyannis, P. Mountford and S. Aldridge, *Nature Chemistry*, 2014, **6**, 315-319.
43. A. V. Protchenko, D. Dange, A. D. Schwarz, C. Y. Tang, N. Phillips, P. Mountford, C. Jones and S. Aldridge, *Chemical Communications*, 2014, **50**, 3841-3844.
44. A. V. Protchenko, K. H. Birjkumar, D. Dange, A. D. Schwarz, D. Vidovic, C. Jones, N. Kaltsoyannis, P. Mountford and S. Aldridge, *Journal of the American Chemical Society*, 2012, **134**, 6500-6503.
45. L. M. A. Saleh, K. H. Birjkumar, A. V. Protchenko, A. D. Schwarz, S. Aldridge, C. Jones, N. Kaltsoyannis and P. Mountford, *Journal of the American Chemical Society*, 2011, **133**, 3836-3839.
46. A. V. Protchenko, J. I. Bates, L. M. A. Saleh, M. P. Blake, A. D. Schwarz, E. L. Kolychev, A. L. Thompson, C. Jones, P. Mountford and S. Aldridge, *Journal of the American Chemical Society*, 2016, **138**, 4555-4564.
47. A. Rit, J. Campos, H. Y. Niu and S. Aldridge, *Nature Chemistry*, 2016, **8**, 1022-1026.
48. W. Koch and M. C. Holthausen, *A chemist's guide to density functional theory*, Wiley-VCH, Weinheim ; Chichester, 2000.

49. P. Hohenberg and W. Kohn, *Physical Review B*, 1964, **136**, B864-+.
50. W. Kohn and L. J. Sham, *Physical Review*, 1965, **140**, 1133-&.
51. J. C. Slater, *Physical Review*, 1930, **36**, 57-64.
52. G. te Velde, F. M. Bickelhaupt, E. J. Baerends, C. F. Guerra, S. J. A. Van Gisbergen, J. G. Snijders and T. Ziegler, *Journal of Computational Chemistry*, 2001, **22**, 931-967.
53. J. M. Younker and K. D. Dobbs, *Journal of Physical Chemistry C*, 2013, **117**, 25714-25723.
54. K. Y. Monakhov and C. Gourlaouen, *Organometallics*, 2012, **31**, 4415-4428.
55. M. P. Mitoraj, M. Parafiniuk, M. Srebro, M. Handzlik, A. Buczek and A. Michalak, *Journal of Molecular Modeling*, 2011, **17**, 2337-2352.
56. J. A. B. Abdalla, I. M. Riddlestone, R. Tirfoin and S. Aldridge, *Angewandte Chemie-International Edition*, 2015, **54**, 5098-5102.
57. J. Turner, J. A. B. Abdalla, J. I. Bates, R. Tirfoin, M. J. Kelly, N. Phillips and S. Aldridge, *Chemical Science*, 2013, **4**, 4245-4250.
58. A. D. Becke, *Physical Review A*, 1988, **38**, 3098-3100.
59. J. P. Perdew, *Physical Review B*, 1986, **33**, 8822-8824.
60. S. Grimme, J. Antony, S. Ehrlich and H. Krieg, *Journal of Chemical Physics*, 2010, **132**.
61. E. Van Lenthe and E. J. Baerends, *Journal of Computational Chemistry*, 2003, **24**, 1142-1156.
62. A. J. Arduengo, H. V. R. Dias, R. L. Harlow and M. Kline, *Journal of the American Chemical Society*, 1992, **114**, 5530-5534.
63. A. J. Arduengo, J. R. Goerlich and W. J. Marshall, *Journal of the American Chemical Society*, 1995, **117**, 11027-11028.
64. H. Valdes, M. Poyatos and E. Peris, *Inorganic Chemistry*, 2015, **54**, 3654-3659.
65. S. Urban, M. Tursky, R. Froehlich and F. Glorius, *Dalton Transactions*, 2009, 6934-6940.
66. C. Hansch, A. Leo and R. W. Taft, *Chemical Reviews*, 1991, **91**, 165-195.
67. S. P. Nolan, *Accounts of Chemical Research*, 2011, **44**, 91-100.
68. M. R. Fructos, T. R. Belderrain, P. de Fremont, N. M. Scott, S. P. Nolan, M. M. Diaz-Requejo and P. J. Perez, *Angewandte Chemie-International Edition*, 2005, **44**, 5284-5288.
69. P. de Fremont, N. M. Scott, E. D. Stevens and S. P. Nolan, *Organometallics*, 2005, **24**, 2411-2418.
70. H. Niu, R. J. Mangan, A. V. Protchenko, N. Phillips, W. Unkrig, C. Friedmann, E. L. Kolychev, R. Tirfoin, J. Hicks and S. Aldridge, *Dalton Transactions*, 2018, **47**, 7445-7455.
71. R. A. Kelly, H. Clavier, S. Giudice, N. M. Scott, E. D. Stevens, J. Bordner, I. Samardjiev, C. D. Hoff, L. Cavallo and S. P. Nolan, *Organometallics*, 2008, **27**, 202-210.

Chapter 4
Quantum Chemical Studies of Cyclic Carbenes as π-Acceptors in Main Group Systems

---

4.1 Introduction

As examined in chapter 3, N-heterocylic carbenes are known to be strong σ-donors, but also have some potential for π-acceptor behaviour, with the latter stemming from the presence of amplitude from the C-N pπ anti-bonding orbital at carbon. However, their π-acceptor strength is typically weak, as this orbital is relatively high lying in carbenes featuring two α-nitrogen substituents. Since 2005, in addition to N-heterocyclic carbenes, researchers have had access to a related family of cyclic (alkyl)(amino)carbenes (CAACs).[1] In CAACs, a strong σ-donor alkyl group replaces one of the α-amino groups of the NHC framework, reducing π donation from the α-nitrogen atoms to the central carbon (leading to greater π-acceptor capabilities), while at the same time enhancing the σ-donor strength of the ligand.[1]

As a family of ligands featuring both strong σ-donation and enhanced π-acceptor strength, CAACs would be expected to be valuable in the stabilization of electron-rich systems. Strong π-acceptor properties provide a sink to delocalise π electrons from the metal centre and thereby stabilize compounds of this nature. Previously reported applications of these ligands in this regard include low-coordinate, low oxidation state rhodium, palladium and gold complexes. Such complexes have been shown to be efficient catalysts for a number of synthetic protocols, including the α-arylation of propiophenone

and isobutanal with aryl chloride (Pd)[1] and alkyne/allene hydroamination (Au).[2-6] In addition, certain ruthenium CAAC complexes have been reported to be among the most active olefin metathesis catalysts.[7-9] More recently, in addition to their use in transition metal organometallics, CAACs have also been shown to be important ligands in main group chemistry, e.g. in stabilising group 14 and 15 systems capable of small molecule activation.[10]

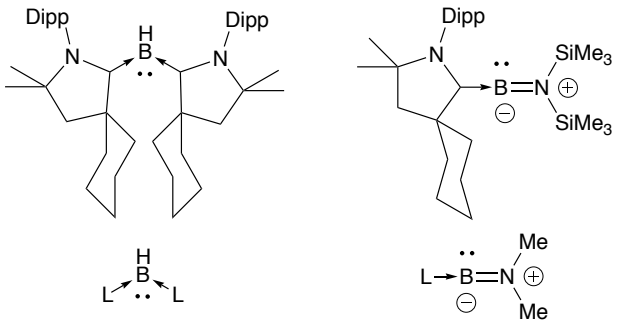


Figure 4-1: (upper) Structures of Bertrand's organoboron systems isoelectronic with amine and singlet carbene systems, and (lower) generic structures of their analogues investigated in this chapter. ($SiMe_3$ groups are replaced by Me to simplify the calculations).

In 2011 and 2014 Bertrand *et al.* published two papers describing organoboron derivatives isoelectronic with amine[11] and singlet carbene species,[12] respectively (Figure 4-1). These compounds represent landmark examples of the application of CAACs in group 13 chemistry, since boron is usually considered to be electron-deficient. However, in these compounds boron adopts a formal oxidation state of +1, and the role of the CAAC ligand is thus thought to be critical in stabilising a system based on a relatively electron-rich (yet relatively electropositive) element. Such systems have been described in some publications as featuring a lone pair on boron (despite a lack of corroborating stereochemical evidence),

and given the use of CAAC substituents, we were interested to investigate factors influencing ligand π-acceptor strength, and related issues concerning the validity of descriptions involving the localisation of significant electron density at boron.

In this chapter, quantum chemical studies are described of neutral-donor-stabilized B(I) systems as a basis to investigate the π-acceptor strengths of a series of ancillary ligands in main group compounds (lower row, Figure 4-1). The relevance of alternative descriptions involving multiple bonds to boron will be discussed, as will the effect of changing the central group 13 atom.

4.2 Computational Details

4.2.1 Natural Bond Orbitals (NBOs)

Natural Bond Orbitals (NBOs), together with Natural Atomic Orbitals (NAOs) Natural Hybrid Orbitals (NHOs) and Natural Localised Molecular Orbitals (NLMOs) are examples of the concept Natural Orbitals (NOs) – an optimal description of the wavefunction and defined as the eigen-orbitals of the first-order reduced density operator Γ, as shown equation 4.1:

$$\Gamma\theta_k = p_k\theta_k \qquad 4.1$$

in which p_k represents the occupancy of the orbitals. Since its first version in 1980,[13] NBO as a program[14, 15] has been used to analyse the multi-electron molecular wavefunction in terms of localised electron-pairs, determining the Natural Orbitals. All these orbitals can

be considered as sequential transformations of the input atomic orbital basis set in the following order:

Input basis AOs – NAOs – NHOs – NBOs – NLMOs-Molecular orbitals[16]

The atomic orbitals (AOs) are transformed into NAOs $\{\Theta_k^{(A)}\}$ by optimising the spatial diffuseness for the effective atomic charge in the molecular environment; the optimized linear combination of NAOs $\{\Theta_k^{(A)}\}$ on the given centre become NHOs $\{h_A\}$ following equation 4.2[13]:

$$h_A = \Sigma_k \, a_k \Theta_k^{(A)} \qquad 4.2$$

in which a_k represents the weight of NAOs $\{\Theta_k^{(A)}\}$ in the linear combination. In the next level, NBOs are constructed from NHOs $\{h_A\}$, in three different situations. Core NBOs (labelled "CR" in the NBO output file) are typically composed of pure NAO character; lone pair NBOs $\{\sigma_A\}$ are each composed of a single normalised NHO ($\sigma_A = h_A$); the 2-centre bonding NBOs $\{\sigma_{AB}\}$, unlike the others, are normalised linear combinations of two NHOs, h_A and h_B following equation 4.3[16]:

$$\sigma_{AB} = a_A h_A + a_B h_B \qquad 4.3$$

in which a_A and a_B are "polarization coefficients" that satisfy $a_A^2 + a_B^2 = 1$. Based on the values of these coefficients, a 2-centre bonding NBO $\{\sigma_{AB}\}$ may be described as covalent ($a_A = a_B$) or ionic ($a_A >> a_B$). Antibonding NBOs $\{\sigma^*_{AB}\}$ are defined as in equation 4.4[16]:

$$\sigma^*_{AB} = a_A h_A - a_B h_B \qquad 4.4$$

The information inherent in these orbitals can further be used to perform tasks pertaining to localised analyses of wavefunction properties, such as natural resonance theory (NRT), as discussed with more detail in the next section.

The NBO analysis used in this chapter is utilises the NBO 6.0 protocol[14, 15] embedded within the ADF software.[17]

4.2.2 Natural Resonance Theory (NRT)

The fundamental hypothesis of Natural Resonance Theory (NRT) is "resonance averaging",[18] which describes the optimised structure of certain compounds as the average of all of its possible resonance structures ("reference" structures), each with a different weighting. NRT analysis is a module of NBO 6.0,[14] and all the resonance structures considered in the analysis are obtained from the NBO analysis.

Based on this hypothesis, the one-electron reduced density operator, Γ, is expressed as an optimized hybridization of Γ_α, according to equation 4.4:

$$\Gamma \cong \sum_\alpha w_\alpha \Gamma_\alpha \qquad 4.4$$

in which Γ_α represents a set of candidates reduced density operators for idealized resonance structures determined by NBO analysis. The NRT resonance weights $\{w_\alpha\}$ are constrained to satisfy $[w_\alpha \geq 0, \sum_\alpha w_\alpha = 1]$ in order to preserve the normalization, hermiticity,

and positivity of the true Γ.[19] Any irreducible error along with the hypothesis described by equation 4.4 is measured by a least-squares variational functional of the unknown weight, as shown in equation 4.5:

$$\delta_w = min(w_\alpha) \left|\left| \Gamma - \sum_\alpha w_\alpha \Gamma_\alpha \right|\right| \quad 4.5$$

where

$$\left|\left| A \right|\right| = [\sum_{i \leqslant j} a_{ij}^2]^{1/2}$$

denotes the matrix norm in a matrix representation $\{a_{ij}\}$ of operator A.

Given that there is a quantity, δ_{ref}, denoting the irreducible error for an expansion (i.e. optimised structure expanded into the "reference" structures) in which Γ is approximated by the leading "reference" structure (i.e. the one with highest weight) Γ_{ref} and defined as equation 4.6:

$$\delta_{ref} = \left|\left| \Gamma - \Gamma_{ref} \right|\right| \quad 4.6$$

In addition to the above equation, the accuracy of the resonance expansion can be expressed by the fractional improvement f_w following equation 4.7:

$$f_w = (\delta_{ref} - \delta_w)/\delta_{ref} \quad 4.7$$

with $0 \leq f_w \leq 1$.

Towards the limit of $f_w = 1$ and $\delta_w = 0$, the error of the expansion is minimised, while the other limit, $f_w = 0$ and $\delta_w = \delta_{ref}$, the resonance weighting gives no improvement over a single-term localised representation.

There are two limits of the analysis, ranging from weak to strong delocalisation. Compounds with weak delocalisation mainly have a single dominant "reference" structure. In such a case, the reduced density operator Γ is strongly dominated by its diagonal elements (i.e. the NBO populations) and the deviations from locality can be conveniently expressed in terms of the diagonal NBO population shifts alone.

Given that the set of NBOs is represented by $\{\sigma_i\}$ (with i=1,2…n), the populations of NBOs can be described as in equation 4.8:

$$p_i = \langle \sigma_i | \Gamma | \sigma_i \rangle \qquad 4.8$$

In terms of localised resonance-weighted populations, equation 4.4 can be inserted into equation 4.8 to give equation 4.9:

$$p_i\,(NRT) = \sum_\alpha w_\alpha \langle \sigma_i | \Gamma_\alpha | \sigma_i \rangle \qquad 4.9$$

Since the reduced density operator Γ, and hence the secondary operators Γ_α, are strongly dominated by the NBO populations, the variational functional shown as equation 4.5 can be simplified into equation 4.10:

$$d(w) = min\,[n^{-1} \sum_i (\, q_i\,(NRT) - q_i)^{\,2}\,]^{\,1/2} \qquad 4.10$$

in which single "reference" NRT resonance weights are chosen such that the resonance-weighted NBO populations $[q_i\,(NRT)]$ most nearly resemble the exact NBO populations $[q_i]$ of the full molecular wavefunction. Analogous to equation 4.7, the accuracy of the single

"reference" NRT expansion is assessed by evaluation of the fractional improvement, f(w), according to equation 4.11:

$$f(w) = [d(0) - d(w)]/d(0) \qquad 4.11$$

in which d(0) replaces δ_{ref} of equation 4.7, being the value of the variational functional for the single term expansion [$w_1 = 1$, $w_2 = w_3 = ... = 0$].

In cases of strong delocalization, when two or more resonance structures contribute comparably to the optimised structure, the NRT program will adopt multi-reference analysis,[18] in which the off-diagonal density matrix elements (as well as diagonal populations) must be taken into account. Practically, the program adopts a "composite NRT algorithm" which combines aspects of both weak and strong delocalisation limits, including the following steps.

The first step of multi-reference NRT is to perform single-reference NRT analysis for each reference manifold r. As described with the weak delocalisation limit, this leads to a set of resonance structures (with associated density matrices $\Gamma_\alpha(r)$ and optimized composite weights $w_\alpha(r)$) within each reference manifold.

In the second step, the program proceeds to the strong delocalisation aspect, calculating an optimised set of reference weights W(r) satisfying [$W(r) \geq 0$, $\sum_r W(r) = 1$], to give the relative weighting of each reference manifold. These weights are chosen to minimize the corresponding variational functional according to equation 4.12:

$$D(W) = min\ (W(r))\ ||\ \Gamma - \sum_r W(r)\ \Gamma(r)\ || \qquad 4.12$$

Analogous to equation 4.11, the accuracy of the variational functional is assessed by equation 4.13:

$$F(W) = [D(0) - D(W)]/D(0) \qquad 4.13$$

In the final step, the optimized weights [W(r)] for each reference manifold are combined with the composite weightings [$w_\alpha(r)$] within each manifold following equation 4.14:

$$w_\alpha = \sum_r w_\alpha (r)\, W(r) \qquad 4.14$$

in which w_α is the final weighting of each resonance structure α. Before the termination of calculation, it will scan the list of structures for any of them with w_α higher than a preset threshold, appending each to the list of reference structures and deleting those with w_α lower than the preset threshold.

After working out the list of reference structures, the bond orders and valencies[20] of each of the reference structures are evaluated from the final optimized resonance weights w_α. The natural bond order is evaluated as equation 4.15:

$$b_{AB} = \sum_\alpha w_\alpha b_{AB}(\alpha) \qquad 4.15$$

In which $b_{AB}(\alpha)$ is the integer number (0,1,2…) of bonds A-B in the structural formula for the αth natural Lewis structure. The program also calculates the ionic (b_{AB}(ion)) and covalent (b_{AB}(cov)) contributions to the bond order according to equations 4.16 and 4.17:

$$b_{AB}(ion) = b_{AB}i_{AB} \quad 4.16$$

$$b_{AB}(cov) = b_{AB}(1 - i_{AB}) \quad 4.17$$

where the (average) ionic character i_{AB} of each bond A-B is defined as equation 4.18:

$$i_{AB} = \sum_{\alpha} w_{\alpha} i_{AB}(\alpha) / b_{AB} \quad 4.18$$

in which $i_{AB}(\alpha)$ denotes the ionicity of the bonds A-B in the structural fomula, as determined from NBO polarization coefficients c_A, c_B with equation 4.19:

$$i_{AB}(\alpha) = |(c_A^2 - c_B^2)/(c_A^2 + c_B^2)| \quad 4.19$$

(averaged, if necessary, over multiple bonds)

Finally, the program evaluates the natural atomic valency $V_A = \sum_{B \neq A} b_{AB}$ and its electrovalent (V_A (ion)) and covalent (V_A (cov)) contributions according to equations 4.20 and 4.21:

$$V_A \text{ (ion)} = \sum_{B \neq A} b_{AB}(ion) \quad 4.20$$

$$V_A \text{ (cov)} = \sum_{B \neq A} b_{AB}(cov) \quad 4.21$$

4.2.3 Ellipticity

Ellipticity is one of the most convenient ways to distinguish double bonds from single bonds and triple bonds, based on the quantum topology of molecular charge distributions developed by Bader et al. Ellipticity is defined by equation 4.22:[21]

$$\varepsilon = (\lambda_1/\lambda_2) - 1 \qquad 4.22$$

where λ_1 and λ_2 are eigenvalues of the Hessian of electron density at the bond critical point. The two eigenvalues summarize the curvature of the electron density near the bond critical point, telling us how steep is the change in the electron density. In addition, since $\lambda_1 \leq \lambda_2 < 0$ for a bond critical point ($\lambda_1 \geq \lambda_2 > 0$ in the case of ring critical points), the first term of the equation is always positive and is manifestly larger than or equal to 1, in order to retrieve a zero ellipticity quotient.

If the π character is increasingly accumulated in one of the eigenplanes on the bond critical point, λ_1 by default will be more negative than λ_2, indicating stronger double bond character; however, the accumulation of π character in a second eigenplane results in a smaller gap between λ_1 and λ_2, indicating the formation of a triple bond. For example, Table 4-1[21] lists the eigenvalues and ellipticities reported by Bader previously for a series of reference CC bonded compounds. In this analysis, the ellipticity increases from 0 when bond order is equal to 1, to 0.74 when bond order equal to 2, and then falls to 0 again when the bond order rises to 3.

Table 4-1: Bond critical point data of various types of CC bond, calculated in Gaussian 09 using a STO-3G basis set

molecule	λ_1	λ_2	Bond Order	Ellipticity
Ethane	-9.75	-9.75	1.00	0.00
Benzene	-12.36	-9.19	1.58	0.34
Ethylene	-13.85	-7.95	2.08	0.74
Acetylene	-6.82	-6.82	2.88	0.00

In this section, the eigenvalues λ_1 and λ_2 are obtained from Bader Analysis, a function of the ADF program, and the ellipticity values are calculated via equation 4.20.

4.3 Results and Discussion

4.3.1 Selection of Ligands

Figure 4-2 shows the ligands that have been probed in the studies outlined in this chapter. They can be subdivided into phosphine (Figure 4-2, labelled **P-Me**), N-heterocyclic carbene (denoted **I-c** and **5-c**), cyclic(alkyl)(amino)carbene (**CAAC-5** and **CAAC-R**), 9H-fluoren-9-ylidene (**C-9**) and cyclopentylidene (**C-P**) systems, with each of the carbene examples featuring a 5-membered heterocyclic core.

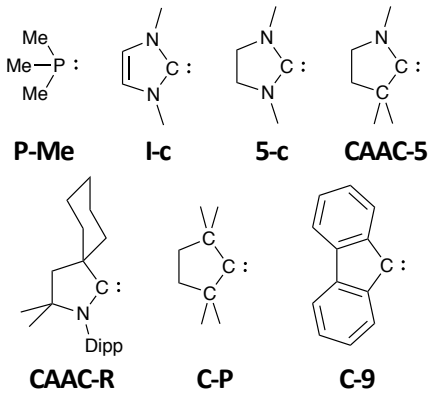


Figure 4-2: The structures of ligands analysed in this chapter.

Trialkylphosphines have been recognized for a long time in transition metal chemistry as strong σ-donors,[22] being applied in many different systems, including, for example, the first generation of Grubbs' catalyst.[23] As a purported 'pure' σ-donor with weak π-accepting capabilities, trialkylphosphines such as PMe_3 (**P-Me**), offer a good baseline for the investigation of other ligands outlined in this chapter.

As shown in chapter 3, N-heterocyclic carbenes are strong σ-donors, but are usually considered to be weak π-acceptors. The comparison of the π-acceptor strength between

imidazolylidene **I-c** and its saturated counterpart **5-c** provides potential understanding of the effect of the backbone within the π system in the context of main group compounds. Cyclic(alkyl)(amino)carbenes, on the other hand, are thought to be not only strong σ-donors but also strong π-acceptors. In this study, we have chosen **CAAC-5**, which represents a ligand framework similar to **5-c** and is hence convenient for comparison. **CAAC-R** is the actual ligand exploited in Bertrand's systems and analysis of its properties is therefore of direct relevance to the sorts of novel main group compounds outlined in the introduction to this chapter. We have also extended this carbene series to include 2,2,5,5-tetramethyl-cyclopentylidene (**C-P**), in which a further amino group within the heterocycle is replaced by an alkyl substituent. This ligand has not been reported experimentally as an isolable compound but has been studied theoretically.[24] **C-P** is expected to have an essentially non-donor stabilised pπ orbital and to behave as a stronger π-acceptor than CAAC ligands. Finally, we have also included 9H-fluoren-9-ylidene (**C-9**) in this selection. **C-9** is also a strong π-acceptor: in addition to factors similar to those expected for **C-P** , the possibility for **C-9** to obtain aromatic character[25] through fulfilment of Hückel's rule (4n+2 π electrons) also drives its potential behaviour as a π acceptor. Moreover, low-coordinate boron species stabilized by ligands similar to **C-9** have also been realised experimentally.[26,27]

4.3.2 Analysis of π-Acceptor Behaviour in Organoboron Systems Isoelectronic with Carbenes

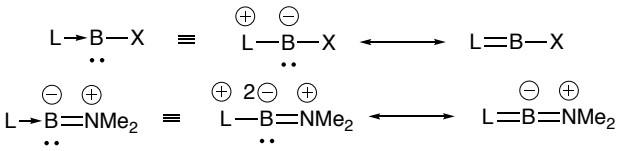


Figure 4-3: Generic structures of organoboron compounds isoelectronic with a carbene.

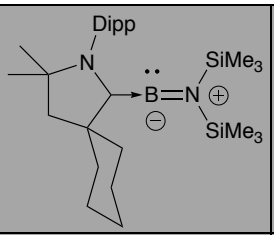
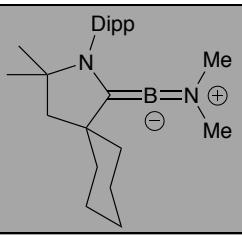
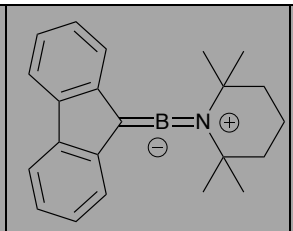
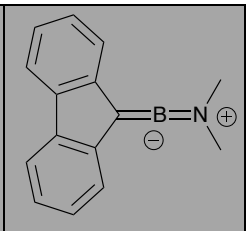
Initial studies focused on isoelectronic organoboron analogues of carbenes (Figure 4-3), with a particular focus on investigating the influence of the ligand on the nature of the ligand-boron bond (and especially single bond vs. double bond character). Geometry optimization with ADF was carried out in the initial step (XC correlation: BP86-D3; Basis set: TZP; Frozen core: all electron; numerical quality: good; this represents an identical set-up to those calculations carried out in chapter 3 for consistency), followed by NRT and ellipticity analyses to provide information on ligand-boron bond order.

4.3.2.1 Geometry Optimisation and Bond Orders

Upon geometry optimization, all structures converged with no restraints. As a probe of the reliability of these calculations, key geometric parameters were compared between crystallographic and calculated data for two (known) compounds synthesized by Bertrand and Nöth.[12,16] As shown in Table 4-2, the C-N-B angles are (almost) linear for all four structures. In addition, the C-B and B-N distances are very close (for each compound) in the calculated and experimentally determined structures. The similarity of key structural

parameters for these two systems therefore gives confidence in the computational set-up used for subsequent analyses.

*Table 4-2: Comparison of key structural information between that calculated for (**C-9**)$BNMe_2$, (**CAAC-R**)$BNMe_2$ and crystallographic data of their analogue, (**C-9**)B(TMP) and (**CAAC-R**)$BN(SiMe_3)_2$ reported by Nöth[26] and Bertrand,[12] respectively.*

				
	(CAAC-R)$BN(SiMe_3)_2$	(**CAAC-R**)$BNMe_2$	(**C-9**)B(TMP)	(**C-9**)$BNMe_2$
C-B-N angle	174.8(3)	172	175.1(2)	180
C-B distance (Å)	1.401(5)	1.42	1.424(3)	1.42
B-N distance (Å)	1.382(5)	1.39	1.354(3)	1.36

The geometric information for all $LBNMe_2$ is summarised in Table 4-3. In general, the L-B-N angle widens on going from L = **P-Me** to the various carbene donors, with the system for which L = **C-9** (which is thought to have the greatest propensity for π acceptor behaviour), featuring a linear L-B-N fragment. This, alongside a shortening of the L-B bond distances (for the carbenes) is consistent with a greater degree of π donation from the boron centre to the ligand.

Table 4-3: The L-B-N angle and HOMO energies of selected $LBNMe_2$ compounds, together with the relative probabilities of resonance structures having a double bond or a single bond between the ligand and the $BNMe_2$ fragment (from NRT studies).

Ligand	L-B-N angle (°)	L-B distance (Å)	HOMO energy (kJ mol^{-1})	Ellipticity of L-B bond	Probability (NRT)[a]	
					Double Bond[b]	Single Bond[b]
P-Me	123	1.94	-295	0.25	23%	55%
I-c	131	1.50	-281	0.54	42%	16%
5-c	143	1.46	-300	0.61	48%	14%
CAAC-5	167	1.42	-340	0.65	55%	5%
CAAC-R	172	1.42	-289	0.69	c	c
C-P	179	1.40	-411	0.57	60%	2%
C-9	180	1.42	-453	0.35	c	c

a. Only NRT reference structures with a weight >1% are considered;
b. The structures with a double bond or single bond between the ligand and $BNMe_2$ are defined in Figure 4-3;
c. Analysis by NRT is difficult due to the presence of numerous resonance structures that stem from the aryl groups in the ligand.

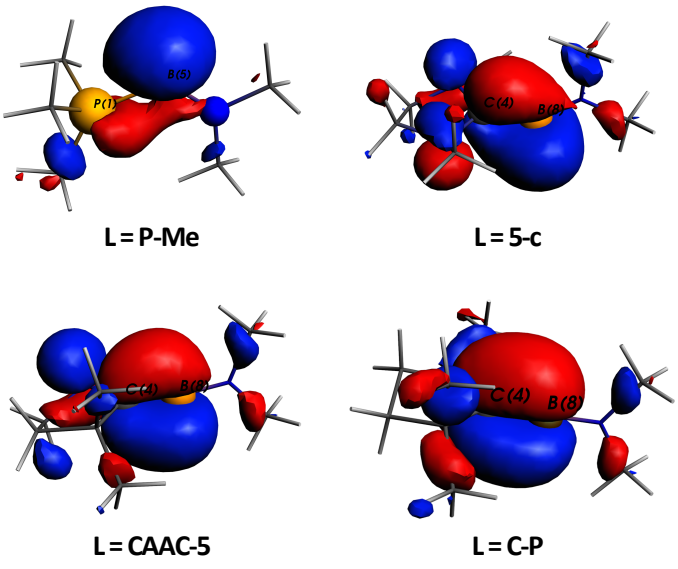


Figure 4-4 ：Depictions of the HOMO of selected systems of the type $LBNMe_2$. Iso-surface parameter = 0.03.

Alongside the widening L-B-N angle and shortening L-B distances, the HOMO energy also shows a consistent lowering as Table 4-4 is descended. As shown in Figure 4-4, the HOMO has significant boron-centred lone pair character when L = **P-Me**, but this starts to be delocalized onto the ligand fragment on going to from L = **5-c** and ultimately to L = **C-P** and **C-9**. The stabilisation of the HOMO for the carbene ligands lower down in Table 4-3 is caused by delocalisation of electron density from the electropositive boron centre onto the ligand. Moreover, this delocalisation of electron density via the π-framework is consistent with the calculated ellipticities of the respective L-B bonds. As introduced in section 4.2.3, the ellipticity of a bond increases (from 0 to 1) as the bond order increases from 1 to 2, due to the presence of the non-cylindrical π component. The trend of increasing ellipticity shown in Table 4-3 implies that both the widening of the L-B-N angles and the shortening of the L-B bond lengths (of carbenes donors, L) are caused by strengthening of the π interaction between the ligand and boron. Interestingly, the ellipticity of the case L = **C-9** (0.35) is significantly lower than those of other carbene-ligated systems (which range from 0.54 to 0.69), despite the expected strong π-acceptor capabilities of this ligand. In fact, this figure resembles quite closely the ellipticity determined for benzene (0.34), and is consistent with the idea that the (**C-9**)-B π interaction forms part of the extended aromatic system, as shown in Figure 4-5. The addition of two π electrons to **C-9** (a twelve-electron π system) would then fulfil Hückel's rule ($4n+2\pi$) criterion mentioned in Section 4.3.1.

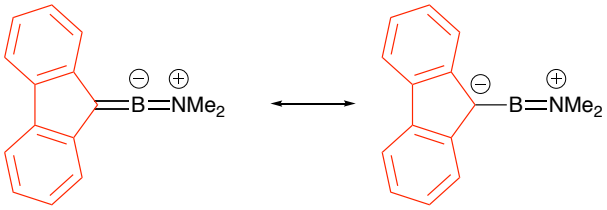
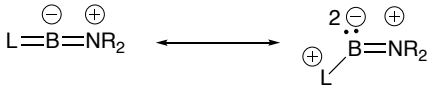
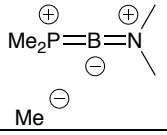
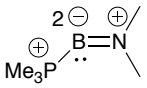
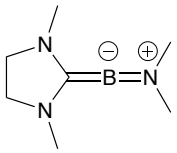
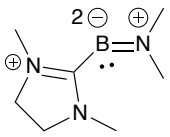
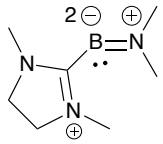
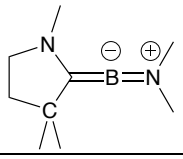
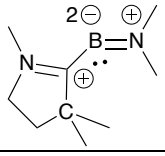


*Figure 4-5: Illustration of the aromatic system (red) in (**C-9**)BNMe₂.*

Table 4-4: Key resonance structures (reference structures) featuring L-B double and single bonds, and their respective probabilities.[a]

Ligand		
	L=B double bond	**L-B single bond**
P-Me		
	23%	55%
5-c		 
	48%	14%
CAAC-5		
	55%	5%

a. Only dominant resonance structures (i.e. those with weights larger than 1% as reported in the NRT output files) are considered in this table and therefore the probability of "L=B double bond" and "L-B single bond" does not add up to 100%

A further part of the analysis of compounds of the type $LBNMe_2$ involves calculating the contributions from resonance structures having a double bond or a single bond between the ligand and boron using Natural Resonance Theory (NRT) (Table 4-4). Natural Resonance Theory is a good method for studying the nature of the L-B bond as it has been widely used to study the bonding nature in simple molecules, ranging from CO_2 and

benzene[27] to mesoionic compounds,[28] and even those in reaction pathways[29], specialising in systems involving lighter p-block elements.

As shown in Table 4-4, a single-bonded resonance structure, featuring a lone pair at boron is the most dominant structure in the case of L = **P-Me**, although the probability of a resonance structure featuring a P=B double-bond given by the NRT method is not negligible, despite involving formal heterolytic cleavage of a P-C bond to generate a methyl anion. As we go down both Table 4-3 and Table 4-4, the double-bonded resonance structure becomes more dominant, giving extra support to the argument that there is a stronger π interaction between the ligand and the boron centre. Thus, in the case of the model CAAC ligand, **CAAC-5**, the heteroallene resonance structure is dominant and the corresponding structure featuring a B-centred lone pair is a very minor contributor.

Geometrically, the widening of L-B-N angle and the shortening of the L-B bonds is closely related to the double bond character of the L-B bonds that stems from π donation from the boron centre to the ligand. Such a difference resembles the reported interactions of CO with NHCs and CAACs, since CO is isolobal with the $BNMe_2$ fragment. An attempt to form a ketene by reacting NHC with CO was reported by Arduengo in 1995. However, the putative ketene was not isolated and theoretical studies showed instead that a weak van der Waals interaction between the NHC and CO was at an energetic minimum (about 1 kcal mol^{-1}), featuring a bent C-C-O fragment (114.1°).[30] Later in 2006, Bertrand reported a ketene formed by reacting CAAC with CO, featuring a linear C-C-O fragment (168.3(4)°). The difference in geometry and reactivity toward CO also stem from the π donation from CO to the ligand (NHC vs. CAAC).

In our studies of $LBNMe_2$, the change in geometry can be rationalized by visualizing the way that the ligand and $BNMe_2$ fragments interact with each other.

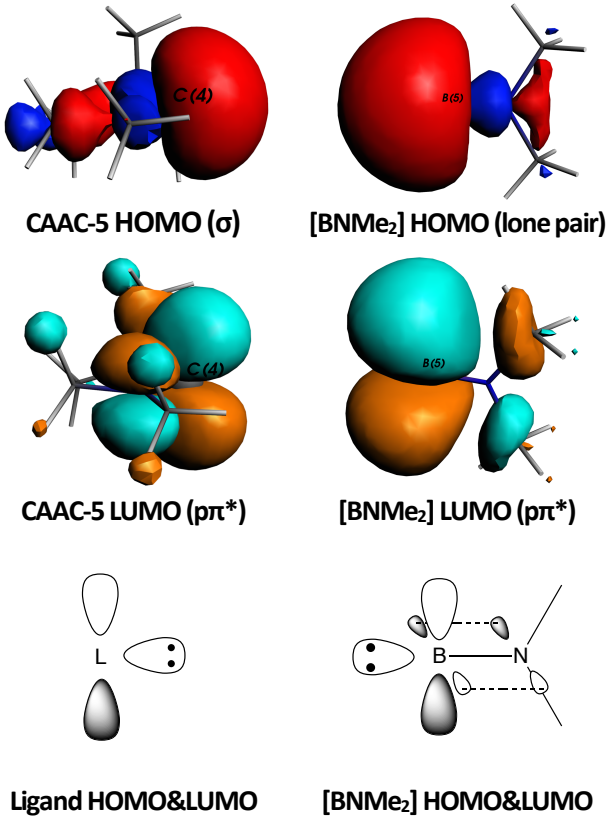


*Figure 4-6: The HOMO and LUMO of [$BNMe_2$] fragment and selected ligand (L = **CAAC-5**). Iso-surface parameter = 0.03.*

By optimizing the geometries of the ligands and the [$BNMe_2$] fragment independently, the respective frontier orbitals can be investigated, as illustrated in Figure 4-6. All of the ligands have a lone-pair-like HOMO, and most of them (with the exception of **P-Me**) have a pπ orbital as the LUMO. The [$BNMe_2$] fragment is similar in some respect to the ligands, with a description as a lone pair characterizing the HOMO and a vacant pπ orbital being the LUMO.

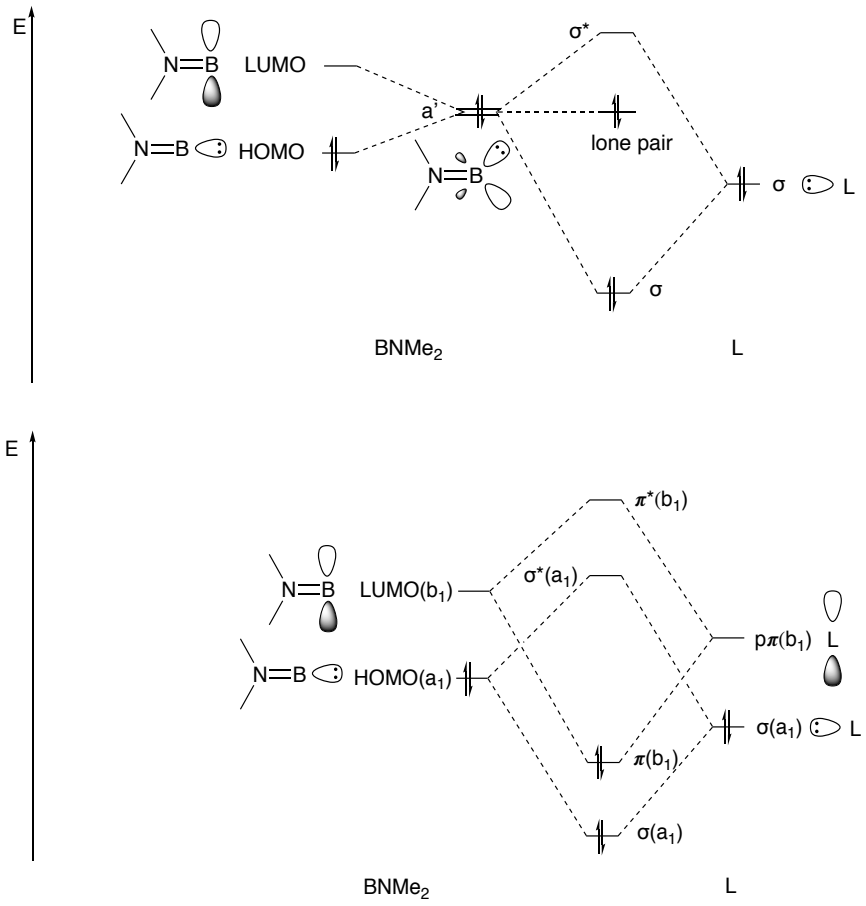
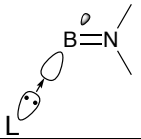
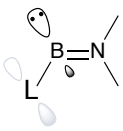
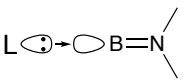
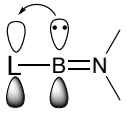


Figure 4-7: Simplified molecular orbital diagrams showing the interaction(s) between the ligand and the $BNMe_2$ fragment when the ligand is a "pure" σ donor (upper, C_s symmetry) and a σ donor/π acceptor (lower, C_{2v} symmetry).

Table 4-5: The interaction between different types of ligand and boron centre.

	σ interaction	π interaction
L being σ donor only		
L being strong π acceptor		

The potential modes of interaction of L with [$BNMe_2$] (and the geometry of the resulting $LBNMe_2$ system) depend on the electronic properties of the ligand – and critically

on its ability to act as a π-acceptor. In the case of the ligand L being essentially only a σ donor, as with **P-Me**, an L-B-N angle of ca. 120° is calculated for the minimum energy geometry. This presumably reflects both steric and electronic factors, and could be envisaged through mixing of the HOMO (lone pair) and the LUMO (vacant pπ orbital) of the [$BNMe_2$] fragment facilitated by the lower symmetry of the $LBNMe_2$ (C_s, Figure 4-7, upper). The two resulting orbitals (labelled a') can then be exploited – one to accept the electron density from the ligand and the other to accommodate the 'lone pair' located on the boron centre (Table 4-5, first row). A bent geometry for the $LBNMe_2$ molecule and a formal lone pair at boron would be expected.

In the case of L being a stronger π acceptor (and the complex $LBNMe_2$ then possessing an overall C_{2v} geometry), the fragment orbitals with the same symmetry (the LUMO of $BNMe_2$ and the pπ orbital of L; and the HOMO of $BNMe_2$ and the σ orbital of L, as shown in Figure 4-7, lower) can interact with each other to form two bonding orbitals (π(b_1) and σ(a_1)). Each is filled with a pair of electrons, resulting in a formal bond order of two (Table 4-5, second row) in a manner similar to the linear ketene shown by Bertrand and co-workers to result form the reaction of a CAAC with CO.

The transition in L from being exclusively a σ donor to a progressively stronger π acceptor (Table 4-5) would explain the trend in Table 4-3 – as the π interaction strengthens on descending Table 4-3 and an increased degree of L=B double bond character is presented between ligand and boron, the L-B-N angle shifts from around 120° to 180°. At the same time, the delocalisation of electron density from the boron to the vacant ligand pπ orbital lowers down the HOMO energy of the molecule as a whole. The strength of π interaction in these systems appears to be dominated by the ligand's π acceptor

capabilities, which can in turn be probed by an analysis of the energies of the respective (vacant) pπ orbitals (Table 4-6).

Table 4-6: Energies of σ and π orbitals for each ligand. (All the ligands are compared in singlet state).*

(kJ mol^{-1})	P-Me	I-c	5-c	CAAC-5	CAAC-R	C-P	C-9	**$BNMe_2$**
σ	-523	-469	-453	-430	-405	-439	-432	-485
pπ*	>100[a]	-6	-28	-107	-109	-253	-407	-202

a. Not observed within the range of LUMO to LUMO+50

As the table is crossed from the left to the right, the pπ* orbital energy becomes more negative, implying greater π acceptor character. On this basis, the π-acceptor strength of the ligands, L, follows the order:

C-9 > **C-P** > **CAAC-5** > **CAAC-R** > **5-c** > **I-c** > **P-Me**

which matches with the trend of greater electron density delocalisation on descending Table 4-3, meaning that this trend is indeed highly dependent on the strength of the ligand π acceptor capabilities.

4.3.2.2 Fragment Calculations



Figure 4-8: The two possible definitions of fragment.

Unlike the study in σ-donor strength in chapter 3, a fragment calculation for the system of $LBNMe_2$ is not unambiguous, as either one of the fragment would have been

defined as excited state in the fragment calculation (Figure 4-8), and the interaction energy from fragment calculation would depend on which fragmentation route we choose.

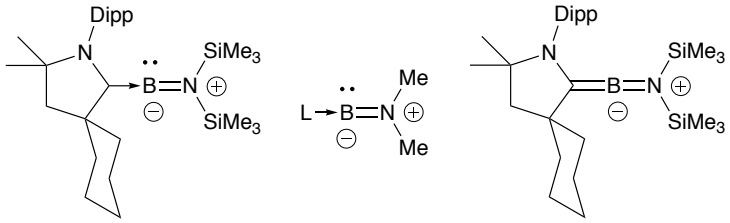


Figure 4-9: Structural descriptions of Bertrand's organoboron compounds isoelectronic with carbenes and the framework of investigation in this chapter.

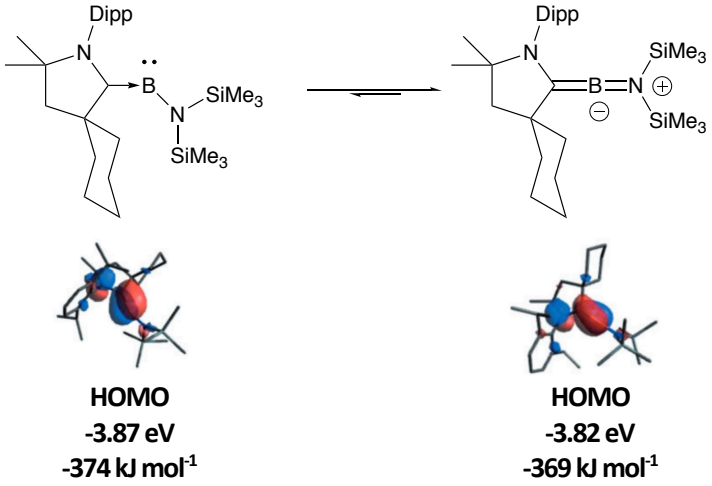


*Figure 4-10: DFT-calculated orbital energies for (**CAAC-R**)BN(SiMe$_3$)$_2$,comparing the HOMO energy between bent C-B-N angle (155°, left) and almost linear C-B-N moieties (175°, right), reported by Bertrand et al. Reprinted with permission from Bertrand et al.,* Angewandte Chemie-International Edition*, 2014, **53**, 13159-13163. Copyright (2019) John Wiley and Sons.*[12]

Based on the results from section 4.3.2.1, the description as a heteroallene (Figure 4-9, right) is almost certainly more appropriate for Bertrand's system. In fact, the computational study reported in Bertrand's paper shows little difference in the HOMO energies of the two limiting geometries (Figure 4-10); meanwhile, the energetic cost of bending the C-B-N angle from 175° to 155° is negligible (~24 kJ mol^{-1}). Bending the C-B-N

fragment by 20° makes little difference to the electronic properties, as there is "strong bonding interaction between the vacant π* molecular orbital of the CAAC and the occupied p orbital of the boron atom", concluded in the computational section of the paper.[12]

The preceding analysis suggests that resonance structures involving a B-centred lone pair are minor contributors when the ligands are π acceptors; however, the tenets of the inert pair effect and the reduced efficiency of π bond overlap as group 13 is descended mean that such descriptions might be more valid for the heavier group 13 elements. As such, analyses of analogous complexes featuring the heavier group 13 elements form the basis of the next section.

4.3.2.3 Heavier Group 13 Element Systems Isoelectronic with Carbenes

To further extend the study, we have looked at the role of selected ligands in related systems of the type $LENMe_2$, featuring the heavier elements (E) of group 13 (Al, Ga, In and Tl). The geometry of each compound was freely optimised, and the L-B-N angles are summarised in Figure 4-11.

In general, as group 13 is descended, there is a narrowing of the L-E-N angle (with an exception when L = **C-P** and **C-9**, which are strong π acceptors). This is presumably caused by the weakening of π interaction as group 13 descended, and is consistent with the results of NRT studies summarised in Figure 4-12.

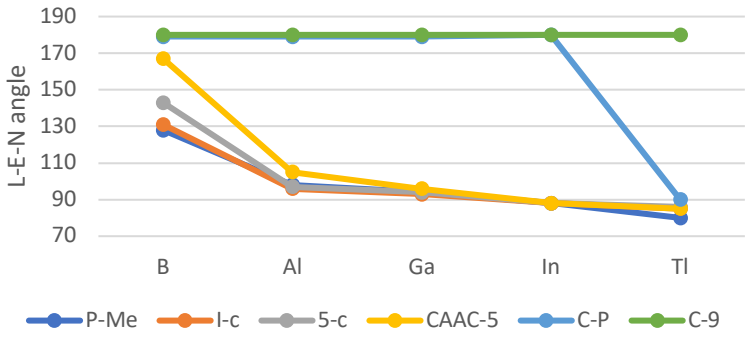


Figure 4-11: Calculated L-E-N angles for a range of systems of the type $LENMe_2$ as a function of L and E.

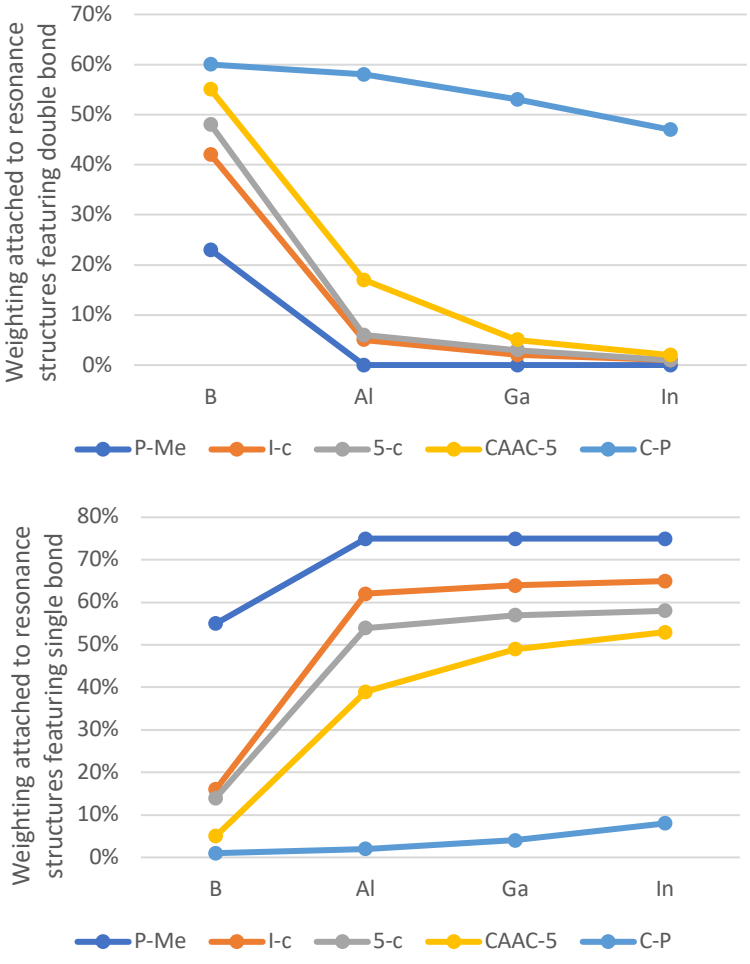


Figure 4-12: Relative probabilities of resonance structures featuring L-E double (upper) and single bonds (lower) calculated by NRT. The data with E = Tl is not available due to limitations of the NRT program within ADF; the data with L = C-9 gives an unmanageable number of resonance structures stemming from the presence of the N-bound aromatic substituent.

Table 4-7: Covalent radii of group 13 elements.[31]

	B	Al	Ga	In	Tl
Covalent radii (Å))	0.84(3)	1.21(4)	1.22(3)	1.42(5)	1.45(7)

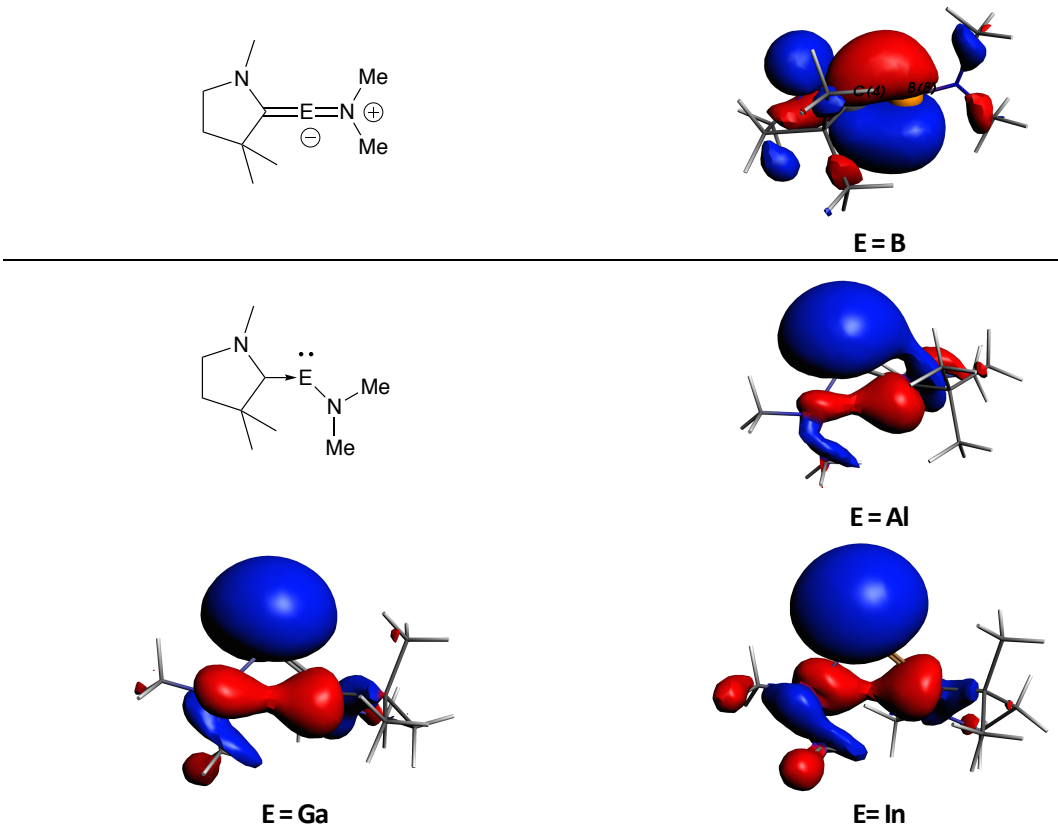


*Figure 4-13: Depiction of the HOMOs of the type (**CAAC-5**)ENMe$_2$ and their corresponding structural description. Iso-surface parameter = 0.03.*

As shown in Figure 4-12, the double bond character in the L-E bond decreases and the single bond character increases as we go down group 13 – most of the ligands, including **P-Me**, **I-c**, **5-c** and **CAAC-5** give rise to essentially single bonds with E when E = Al, Ga and In. A logical reason for this observation is poorer π overlap between L and E which is caused by the larger covalent radius of E on going down group 13 (Table 4-7). In addition, poorer valence s/p mixing would be expected to result in more p character in L-E bonding orbitals and to contribute to the narrowing of L-E-N angles. As an exceptionally strong π acceptor,

C-P appears still to favour L=E double bond formation, even with the heavier group 13 elements.

As noted at the end of preceding section, descriptions featuring a lone pair at E are more appropriate when E is a heavier group 13 element. As shown in Figure 4-13, for the case where L = **CAAC-5**, the boron system is decidedly different from the complexes featuring E = Al, Ga or In. In the latter cases the electron density in the HOMO becomes progressively more localized at E, with little delocalisation onto the **CAAC-5** framework.

4.3.3 Analysis of π-Acceptor Behaviour in Organoboron Systems Isoelectronic with Amines

Given the results outlined above for systems of the type $LBNMe_2$, we wanted to examine whether similar conclusions could be drawn for related low-oxidation state main group systems. In particular, given a recent high profile report of an organoboron system, L_2BH, isoelectronic with amines (Figure 4-14),[11] we wanted to investigate the influence of the ligand on the validity of resonance descriptions featuring a lone pair at boron, or multiple bond character within the L-B-L fragment (i.e. single bond vs. double bond character). As utilized for the related compounds discussed above, geometry optimization with Amsterdam Density Functional (ADF) was carried out in the initial step, followed by NRT analyses to provide information on the L-B-L fragment.

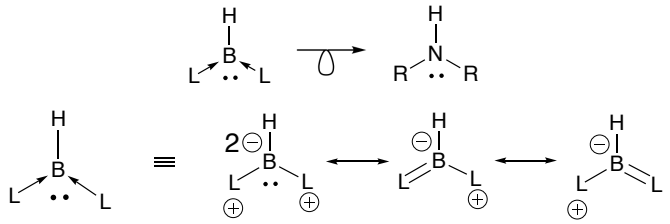
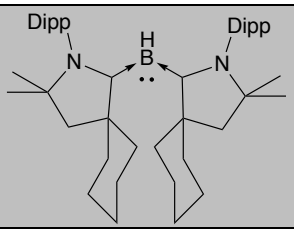


Figure 4-14: Generic structure of organoboron compounds isoelectronic with amines.

4.3.3.1 Geometry Optimisation and Bond Order

The results of our geometry optimization closely resemble both the experimental and computational results reported by Bertrand *et al*. (Table 4-8). All other structures also converged without restraints, and key geometric information is summarized in Table 4-9.

Table 4-8: Comparison between our computational study with ADF and both the experimental and computational results reported by Bertrand et al.[11]

	**C-B-C angle**	**C-B distance (Å)**	**Sum angle of central trigonal plane**	**HOMO (kJ mol^{-1})**
Our calculation	138	1.50	360	-303
Bertrand's report (expt.)	138.85(10)	1.5175(15)	359.94	N/A
Bertrand's report (calc.)	140	1.54	360	-322

In general, the L-B-L angles increase on going down the table; however, the L-B distance for the series of carbene-ligated compounds remains almost invariant. The sum of the angles at boron (i.e. the sum of the two L-B-H and the L-B-L angles) is the same throughout the table except for L = **P-Me**, which is marginally lower than 360°. Since **P-Me** is a very weak π acceptor (according to the previous section) while the carbenes possess (to a

greater or lesser extent) significant π acceptor properties, it is believed that steric effects must be important in driving these systems to planarity.

Table 4-9: The L-B-L angle and HOMO energies of selected compounds of the type L_2BH, together with the weightings attached to resonance structures featuring double and single bonds between L and B, as obtained from NRT studies.

Ligand	L-B-L angle	L-B distance (Å)	Sum of angles at boron	HOMO (kJ mol^{-1})	Probalibity (NRT)[a]	
					Double Bond[b]	Single Bond[b]
P-Me	125	1.82	357	-266	28%	52%
I-c	122	1.51	360	-258	21%	7%
5-c	126	1.50	360	-302	28%	11%
CAAC-5	130	1.50	359	-324	24%	7%
CAAC-R	138	1.50	360	-303	c	c
C-P	141	1.50	360	-465	27%	3%
C-9	128	1.50	360	-488	c	c

a. Only reference structures with weight higher than 1% are considered;
b. The resonance structures featuring a double bond or a single bond between the ligand and BH fragment are defined in Figure 4-14;
c. There are very many resonance structures that stem from the aryl groups in the ligand, each of which has very low probability.

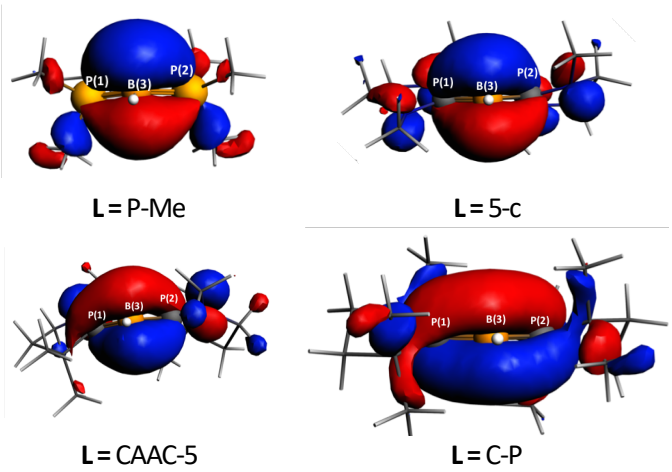
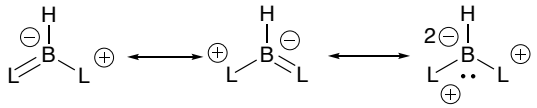
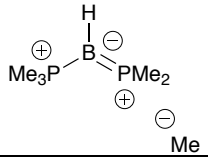
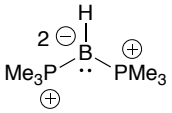
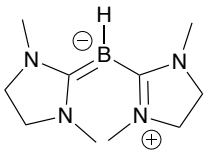
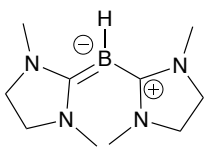
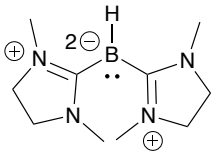
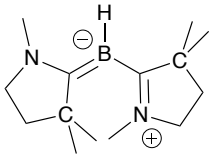
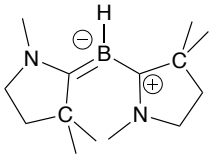
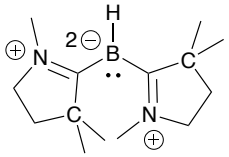


Figure 4-15: Depictions of the HOMO of selected systems of the type L_2BH. Iso-surface parameter = 0.03.

Analogous to the data provided for systems of the type $LBNMe_2$ in Table 4-3, the HOMO energy decreases on descending Table 4-9. Moreover, as shown in Figure 4-15, the HOMO has significant boron-centred lone pair character at boron when L = **P-Me**, and shows increasing delocalization onto the ligands on going to from L = **5-c** and ultimately to L = **C-P**. Notably, however, the change in delocalisation of the L_2BH systems shown in Figure 4-15 appears to be less pronounced than the with the $LBNMe_2$ systems shown in Figure 4-4. We used the NRT program to determine the weighting attached to various resonance structures for L = **P-Me**, **I-c**, **5-c**, **CAAC-5** and **C-P**; the compounds with L = **CAAC-R** and **C-9** result in an unmanageably large number of resonance structures in the NRT analysis due to the presence of the pendant aryl groups, and therefore their results were not analysed in depth.

Table 4-10: The resonance structures (reference structures) featuring L-B double and single bonds, and their associated probabilities with selected ligands. Only resonance structures with weighting greater than 1% are considered.

Ligand			
	double bond		**single bond**
P-Me			
	28%		52%
5-c			
	12%	16%	11%
CAAC-5			
	8%	16%	7%

Key results are summarised in Table 4-9 and 4-11. Since the concept of electron delocalisation is not included in the NRT method, there is only one L-B double bond in a single resonance structure. However, the electron density is clearly delocalised in a symmetrical fashion onto both ligands according to Figure 4-15; therefore, the total weight of the double bond resonance structure (shown in both Table 4-9 and Table 4-10) is the sum of the weights attached to resonance structures with either one L-B double bond.

According to Table 4-10, the single-bonded resonance structure featuring a lone pair at boron is again the dominant structure in the case of L = **P-Me** (analogous to the results outlined in Table 4-4 for (**P-Me**)$BNMe_2$); the doubly-bonded resonance structure in this case also involves releasing the methyl anion by breaking a P-C bond. As we go down both Table 4-9 and Table 4-10, the double-bonded resonance structure is not as dominant as for the $LBNMe_2$ systems shown in Table 4-4, but they still represent a higher probability than the resonance structure featuring an L-B single bond.

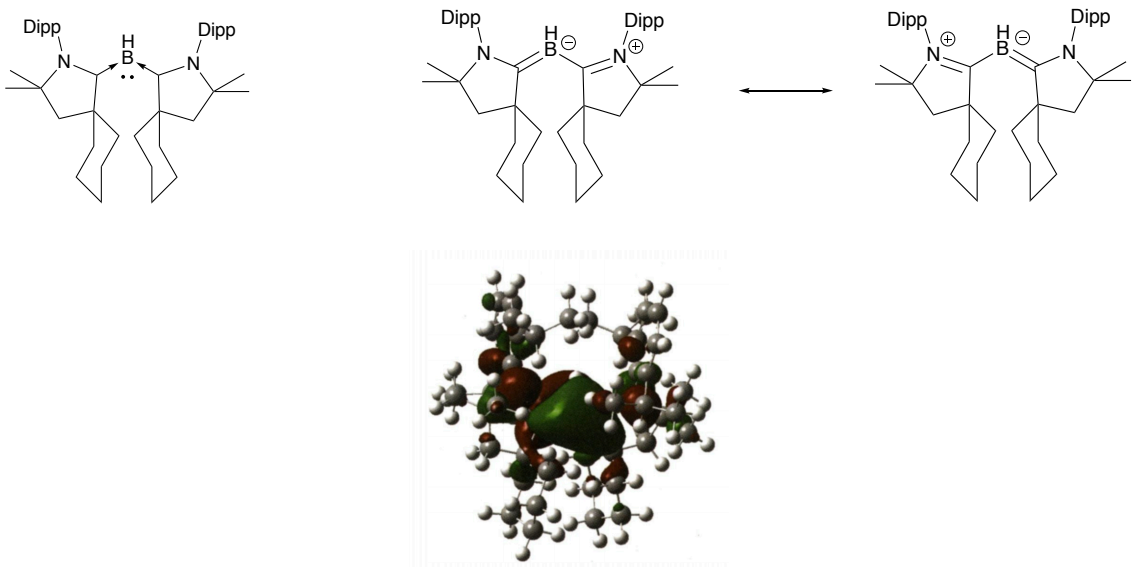


*Figure 4-16: Description of (**CAAC-R**)$_2$BH with a lone pair localized on boron (top left), description with C=B double bonded resonance structure(top right) and depiction of the HOMO, reprinted with permission from Bertrand et al.,* Science*, 2011, **333**, 610-613. Copyright (2019) American Association for the Advancement of Science (bottom).*[11]

The results of calculations on the HOMO energy, taken together with NRT studies lead to broadly similar conclusions similar to those drawn at the end of section 4.3.2, in that the case of the ligand L being a π acceptor, C=B double bonded resonance structures (Figure 4-16, top right) are more appropriate descriptions than those having a lone pair localised on the boron centre (Figure 4-16, top left). The 3-D depiction of the HOMO reported by Bertrand *et al.* also appears to be consistent with such a description (Figure 4-16, bottom).

4.3.3.2 Heavier Group 13 Elements Systems Isoelectronic with Amines

Analogous to the studies of $LBNMe_2$, resonance descriptions of L_2BH that feature a lone pair at the boron centre are clearly not as appropriate as those featuring C=B double bond character; however, a description incorporating a lone pair localized on the central element E, might be expected to be a more suitable description when E is a heavier group 13 element due to poorer π overlap between ligand and E. Therefore, we conducted an investigation of the influence of the heavier central elements within an L_2EH framework.

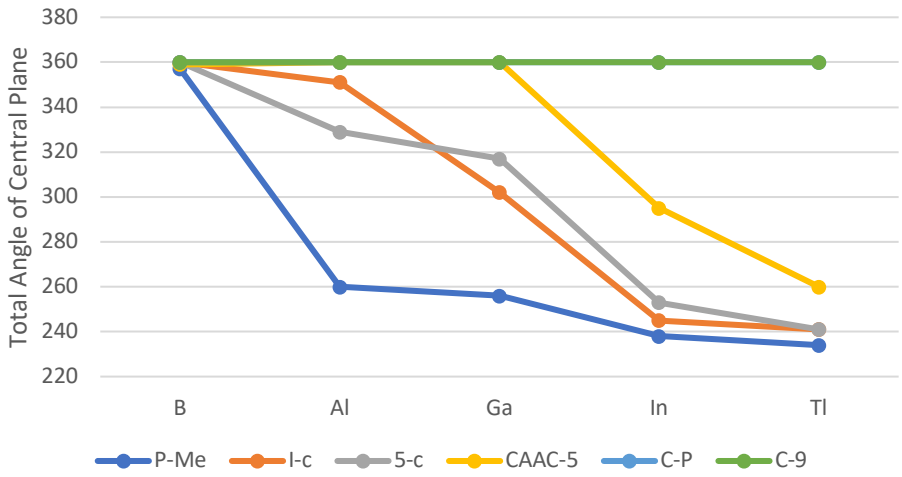


Figure 4-17: Sum of the three angles at E (the L-E-L and two L-E-H bond angles) of group 13 complexes of the type L_2EH featuring various ligands, L.

As shown in Figure 4-17, the shape at the central element E becomes increasingly pyramidalized as group 13 is descended (i.e. the total angle around the centre element falls significantly below 360°), except in the case of L = **C-9**, for which the complexes retain planarity. As noted in section 4.4.3, this presumably reflects the fact that **C-9** is a very strong π acceptor on the basis of Hückel's rule of aromaticity. In fact, electron density in the π framework is withdrawn to **C-9** to fulfil the ($4n+2\pi$) Hückel's rule, leaving a E(2+) centre instead of E centre with lone pair (Figure 4-18).

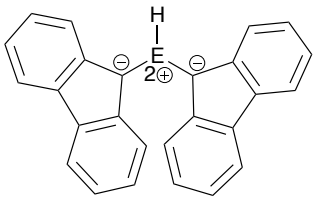


*Figure 4-18: Dominant resonance structure of (**C-9**)$_2$EH.*

The more general pattern of increased pyramidalization is very similar to that which was observed in the previous section, indicating a much weaker π interaction and poorer s/p mixing towards the bottom of group 13.

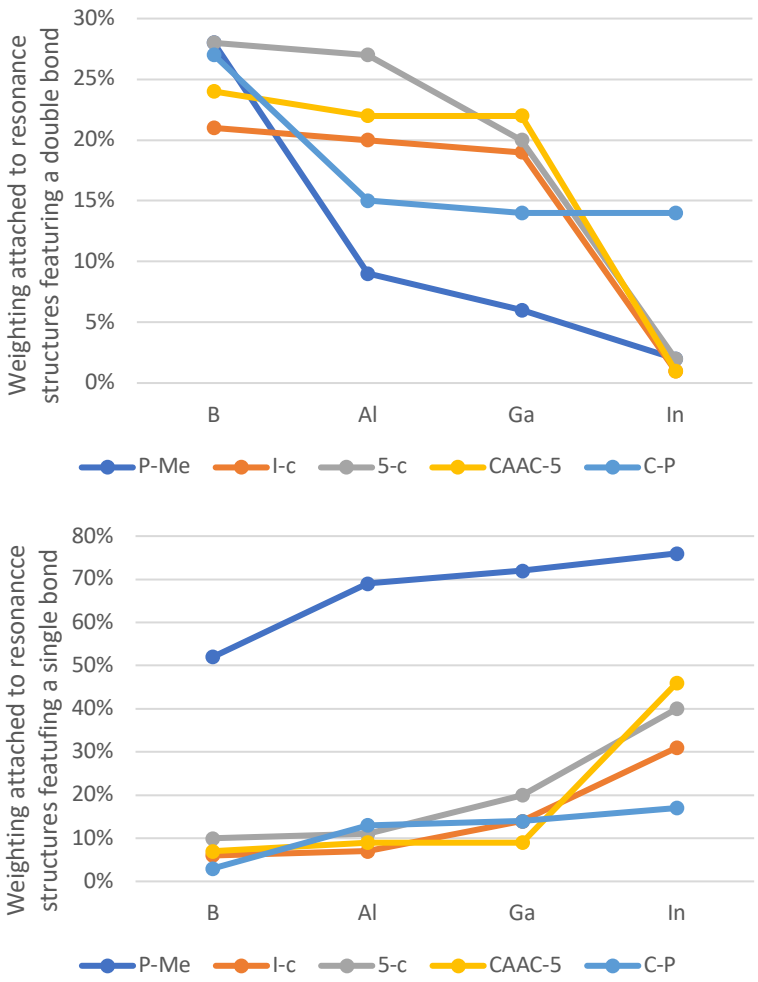


Figure 4-19: Probability of double bond (upper) and single bond (lower) of L-E bond calculated from results of NRT.

The results delivered by the NRT method (Figure 4-19) are consistent with this idea, i.e. that there is weaker π interaction between L and E towards the bottom of group 13. The weightings associated with resonance structures featuring L=E double bonds decrease and those associated with single-bonded structures increase by going from B to In. This provides further support for the conclusion that the idea of localization of a lone pair at E is only really an appropriate description for the heavier group 13 elements. This is further illustrated in Figure 4-20, which shows the HOMOs of systems of the type (**5-c**)$_2$EH: electron

density is progressively more concentrated at the E centre as one moves from B to Al, Ga and ultimately In.

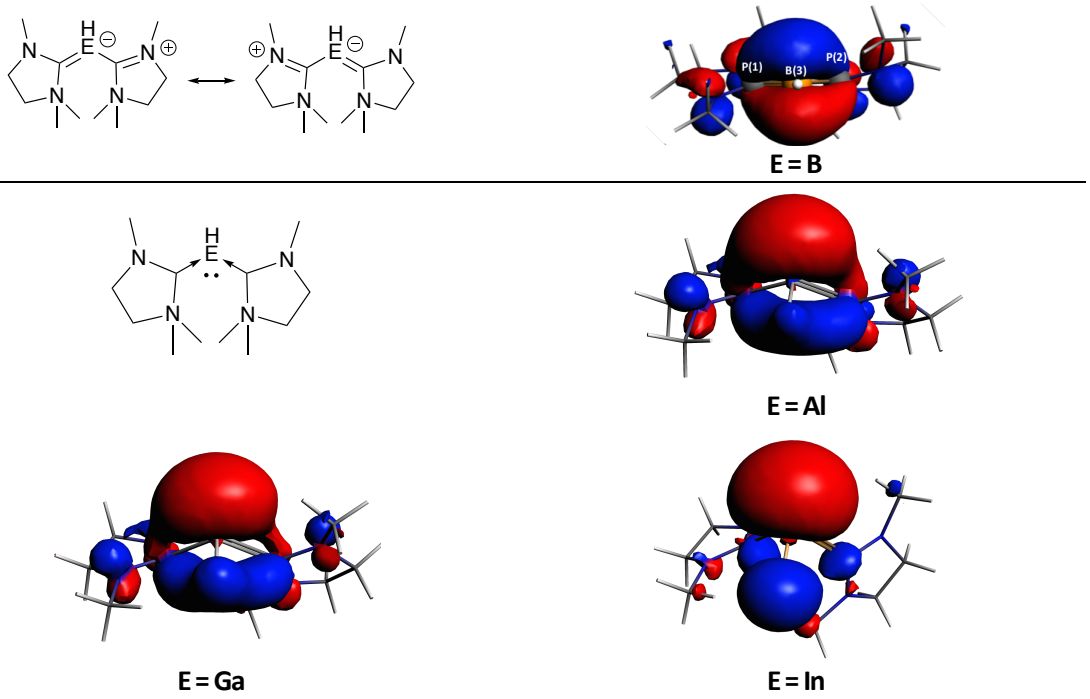


*Figure 4-20: Depiction of the HOMOs of compounds the type (**5-c**)$_2$EH and their corresponding structural description. Iso-surface parameter = 0.03.*

4.4 Conclusions

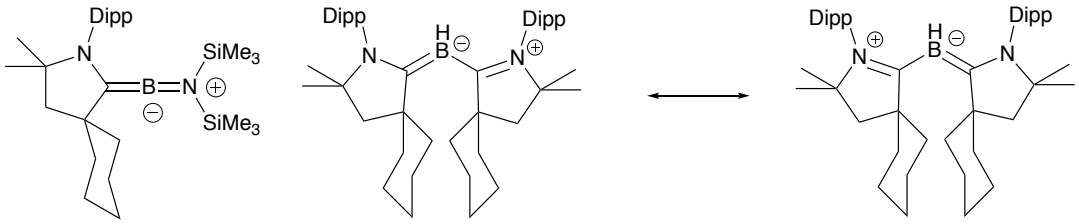


Figure 4-21: More appropriate description of Bertrand's organoboron compounds.

DFT methods have been used to analyse bonding in complexes of the type $LBNMe_2$ and L_2BH, with results mainly analysed by NRT. Electron density is delocalised from the boron centre to the ancillary π accepting ligand(s) in the organoboron compounds reported by Bertrand *et al.*, a finding which is supported by a range of methods, ranging from geometric data and orbital energies to ellipticity of the L-B bond and the results of NRT studies. Therefore, the description illustrated in Figure 4-21 would be more appropriate for these organoboron compounds.

Descriptions featuring a lone pair localized on boron are more appropriate if the ligand is a very weak π acceptor (as there is no low-lying orbital for the electron density to be delocalised into); such a description would also be valid if the boron centre were replaced by a heavier group 13 element, as there is poorer π orbital overlap between the ligand(s) and the central element.

4.5 References

1. V. Lavallo, Y. Canac, C. Prasang, B. Donnadieu and G. Bertrand, *Angewandte Chemie-International Edition*, 2005, **44**, 5705-5709.
2. V. Lavallo, G. D. Frey, B. Donnadieu, M. Soleilhavoup and G. Bertrand, *Angewandte Chemie-International Edition*, 2008, **47**, 5224-5228.
3. R. Kinjo, B. Donnadieu and G. Bertrand, *Angewandte Chemie-International Edition*, 2011, **50**, 5560-5563.
4. X. M. Zeng, G. D. Frey, S. Kousar and G. Bertrand, *Chemistry-a European Journal*, 2009, **15**, 3056-3060.
5. X. M. Zeng, M. Soleilhavoup and G. Bertrand, *Organic Letters*, 2009, **11**, 3166-3169.
6. X. M. Zeng, R. Kinjo, B. Donnadieu and G. Bertrand, *Angewandte Chemie-International Edition*, 2010, **49**, 942-945.
7. V. M. Marx, A. H. Sullivan, M. Melaimi, S. C. Virgil, B. K. Keitz, D. S. Weinberger, G. Bertrand and R. H. Grubbs, *Angewandte Chemie-International Edition*, 2015, **54**, 1919-1923.
8. D. R. Anderson, V. Lavallo, D. J. O'Leary, G. Bertrand and R. H. Grubbs, *Angewandte Chemie-International Edition*, 2007, **46**, 7262-7265.
9. D. R. Anderson, T. Ung, G. Mkrtumyan, G. Bertrand, R. H. Grubbs and Y. Schrodi, *Organometallics*, 2008, **27**, 563-566.

10. M. Melaimi, R. Jazzar, M. Soleilhavoup and G. Bertrand, *Angewandte Chemie-International Edition*, 2017, **56**, 10046-10068.
11. R. Kinjo, B. Donnadieu, M. A. Celik, G. Frenking and G. Bertrand, *Science*, 2011, **333**, 610-613.
12. F. Dahcheh, D. Martin, D. W. Stephan and G. Bertrand, *Angewandte Chemie-International Edition*, 2014, **53**, 13159-13163.
13. J. P. Foster and F. Weinhold, *Journal of the American Chemical Society*, 1980, **102**, 7211-7218.
14. E. D. Glendening, C. R. Landis and F. Weinhold, *Journal of Computational Chemistry*, 2013, **34**, 1429-1437.
15. E. D. Glendening, J. Badenhoop, K., A. E. Reed, J. E. Carpenter, J. A. Bohmann, C. M. Morales, C. R. Landis and F. Weinhold, *Journal*, 2013.
16. F. Weinhold, C. R. Landis and E. D. Glendening, *International Reviews in Physical Chemistry*, 2016, **35**, 399-440.
17. SCM, *ADF Manual 2014*, 2014.
18. E. D. Glendening and F. Weinhold, *Journal of Computational Chemistry*, 1998, **19**, 593-609.
19. P. O. Lowdin, *Physical Review*, 1955, **97**, 1474-1489.
20. E. D. Glendening and F. Weinhold, *Journal of Computational Chemistry*, 1998, **19**, 610-627.
21. R. F. W. Bader, T. S. Slee, D. Cremer and E. Kraka, *Journal of the American Chemical Society*, 1983, **105**, 5061-5068.
22. R. H. Crabtree, in *Organometallic Chemistry of the Transition Metals, 4th Edition*, Blackwell Science Publ, Oxford, 2005, pp. 87-124.
23. P. Schwab, M. B. France, J. W. Ziller and R. H. Grubbs, *Angewandte Chemie-International Edition*, 1995, **34**, 2039-2041.
24. M. Z. Kassaee, F. A. Shakib, M. R. Momeni, M. Ghambarian and S. M. Musavi, *Journal of Organic Chemistry*, 2010, **75**, 2539-2545.
25. C. Goedecke, M. Leibold, U. Siemeling and G. Frenking, *Journal of the American Chemical Society*, 2011, **133**, 3557-3569.
26. B. Glaser and H. Noth, *Angewandte Chemie-International Edition in English*, 1985, **24**, 416-417.
27. E. D. Glendening, J. K. Badenhoop and F. Weinhold, *Journal of Computational Chemistry*, 1998, **19**, 628-646.
28. I. C. Anjos, M. Vasconcellos and G. B. Rocha, *Theoretical Chemistry Accounts*, 2012, **131**.
29. E. D. Glendening and F. Weinhold, *Tetrahedron*, 2018, **74**, 4799-4804.
30. D. A. Dixon, A. J. Arduengo, K. D. Dobbs and D. V. Khasnis, *Tetrahedron Letters*, 1995, **36**, 645-648.
31. B. Cordero, V. Gomez, A. E. Platero-Prats, M. Reves, J. Echeverria, E. Cremades, F. Barragan and S. Alvarez, *Dalton Transactions*, 2008, 2832-2838.

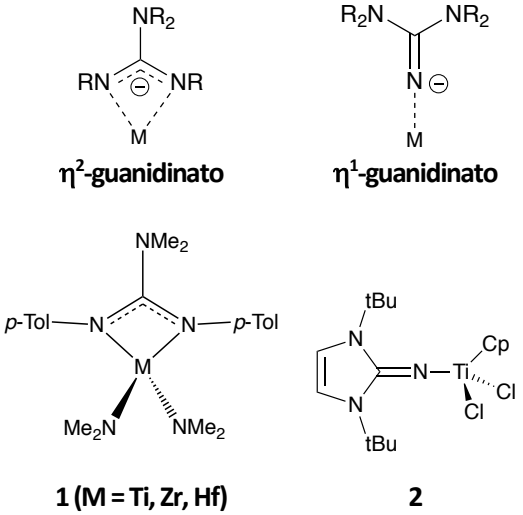
Chapter 5

Computational and Synthetic Studies of Bulky Ring-Expanded Anionic Guanidinato Ligands

---

5.1 Introduction

The guanidinato ligand family has been a significant presence in coordination chemistry since the first reported synthesis of such a complex in 1970, by Lappert and co-workers (**1**; Figure 5-1).[1] The particular ligand in these systems behaves as a bidentate donor (η^2-guanidinato system); however, related analogues have been shown to exhibit numerous coordination modes in numerous complexes involving metals from across the Periodic Table.[2-5]



η^2-guanidinato **η^1-guanidinato**

1 (M = Ti, Zr, Hf) **2**

Figure 5-1: The two common types of coordination observed for guanidinato ligands (upper) and their first examples (lower).

Isomeric systems have also been reported in which the guanidinato ligand behaves as a monodentate ligand (η^1-guanidinato), including the N-heterocyclic iminato (NHI) family. The first examples of transition metal complexes featuring an NHI donor, to the best of our knowledge, were first reported by Tamm *et al.* in 2004[6] (**2**; Figure 5-1). This type of ligand is recognised as a strong donor, involving both the σ- and π- systems of the electron-rich iminato fragment (Figure 5-2).

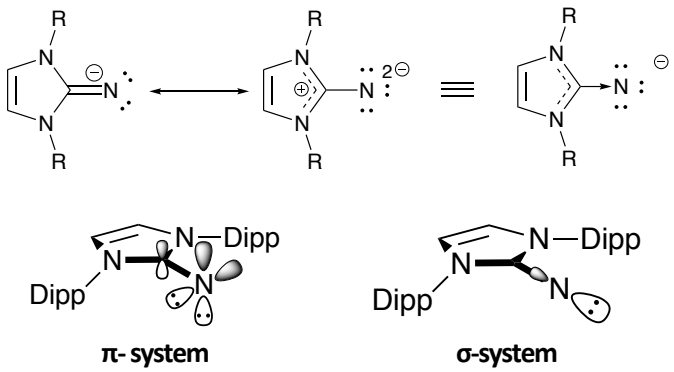


Figure 5-2: The resonances structure of an NHI ligand and the σ- and π- systems of its iminato sub-unit.

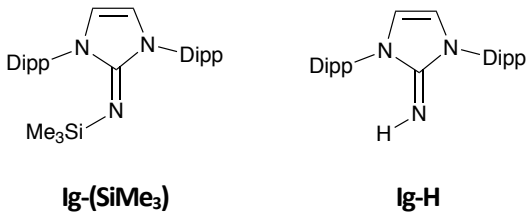
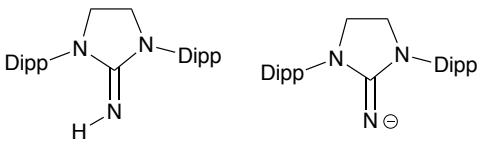


*Figure 5-3: The structures of **Ig-(SiMe$_3$)** and **Ig-H**.*

At the same time as titanium complex **2** was reported, Tamm and co-workers also reported the preparation of **Ig-(SiMe$_3$)** (Figure 5-3).[6] This compound can be synthesized from the corresponding N-heterocyclic carbene via a Staudinger-type reaction, and **Ig-H**

can then be obtained easily via the reaction of **Ig-(SiMe$_3$)** with methanol.[7] With these syntheses in hand, Tamm *et al.* moved forward to the application of cyclic guanidinato ligands in transition metal catalysis, including the use of titanium complexes for ethylene polymerization[6, 8-11] and tungsten complexes for alkyne metathesis;[12-15] the same group also reported the coordination chemistry of guanidinato ligands with rare earth elements.[16, 17]



5g-H **[5g]$^-$**

*Figure 5-4: Protio-ligand **5g-H** and the corresponding anionic ligand **[5g]$^-$**.*

Most of the research to date (across a wide range of metals) has focused on the imidazolium-derived ligand **[Ig]$^-$**, a situation which mimics the early stages of NHC research in the 1990s. The saturated backbone analogue **5g-H** (Figure 5-4) has been used only in a relatively small number of applications by Bertrand,[18, 19] Nomura,[20, 21] and Tamm.[22] Bearing in mind the conclusions reached in chapter 3, that expanding the heterocyclic ring enhances the electron donating capabilities of a carbene ligand, it was also thought profitable to investigate whether a similar effect might apply to guanidinato systems. With these thoughts in mind, the work outlined in this chapter aims to develop ring-expanded analogues of **[5g]$^-$**, namely **[6g]$^-$** and **[7g]$^-$**. (**[Lg]$^-$** is used to represent the family of guanidinato ligands **[Ig]$^-$**, **[5g]$^-$**, **[6g]$^-$** and **[7g]$^-$**).

5.2 Experimental

*General Preparation of **Lg-(SiMe$_3$)** (where **Lg** = **5g**, **6g** or **7g**):*

To a solution of 5-Dipp, 6-Dipp or 7-Dipp (10 mmol) in mesitylene (250 mL) at room temperature was added 1.4 equivalents of trimethylsilyl azide (14 mmol). The solution was heated under reflux (at 166°C) for 12 h, and then cooled and filtered. The solution was concentrated *in vacuo* and the product crystallised on cooling to room temperature. Crystals suitable for X-ray crystallography were obtained by recrystallisation from hot hexane. Yields: **5g-(SiMe$_3$)**: 3.20 g, 67%; **6g-(SiMe$_3$)**: 2.50 g, 51%; **7g-(SiMe$_3$)**: 2.23 g, 44%.

*Spectroscopic data for **5g-(SiMe$_3$)**:*

^{1}H NMR (400 MHz, benzene-d_6) δ 7.23 (dd, $^3J_{HH}$ = 7.2, 8.4 Hz, 2H, *p*-C<u>H</u>), 7.04 (d, $^3J_{HH}$ = 7.1 Hz, 4H, *m*-C<u>H</u>), 3.50 (s, 4H, backbone C<u>H$_2$</u>N), 3.35 (sept, $^3J_{HH}$ = 6.9 Hz, 4H, C<u>H</u>Me$_2$), 1.43 (d, $^3J_{HH}$ = 6.8 Hz, 12H, C<u>H$_3$</u>), 1.28 (d, $^3J_{HH}$ = 6.8 Hz, 12H, C<u>H$_3$</u>), -0.23 (s, 9H, SiMe$_3$). **^{13}C NMR{^{1}H}** (101 MHz, benzene-d_6) δ 148.9 (*o*-<u>C</u>), 147.1 (N<u>C</u>N), 136.8 (*ipso*-<u>C</u>), 128.6 (*p*-<u>C</u>), 124.2 (*m*-<u>C</u>), 47.4 (backbone <u>C</u>H$_2$), 28.9 (<u>C</u>HMe$_2$), 25.0 (<u>C</u>H$_3$), 24.4 (<u>C</u>H$_3$), 3.4(Si<u>C</u>H$_3$). **^{29}Si NMR** (99 MHz, benzene-d_6) δ -21.5. Elemental Analysis does not meet standard, with percentage of C lower than expected after a few attempts.

*Crystallographic data for **5g-(SiMe$_3$)**:*

$C_{30}H_{47}N_3Si$, M_r = 477.80, triclinic, *P-1*, a = 9.6508(3), b = 12.5687(3), c = 24.9982(7) Å, α = 88.317(2)°, β = 83.394(2)°, γ = 80.163(2)°, V = 2967.67(14) Å^3, Z = 4, ρ_c = 1.069 Mg m^{-3}, T = 150 K, λ = 1.54184 Å, 43077 reflections collected, 12289 independent [R(int) = 0.0433], which were used in all calculations. R_1 = 0.0418, wR_2 = 0.1082 for observed unique reflections [I > 2σ(I)] and R_1 = 0.0532, wR_2 = 0.1168 for all unique reflections. Max. and min. residual electron densities 0.405 and -0.315 e Å^{-3}.

*Spectroscopic data for **6g-(SiMe$_3$)**:*

^{1}H NMR (400 MHz, benzene-d_6) δ 7.23 (dd, $^3J_{HH}$ = 6.6, 6.7 Hz, 2H, *p*-C<u>H</u>), 7.15 (d, $^3J_{HH}$ = 7.7 Hz, 4H, *m*-C<u>H</u>), 3.38 (t, $^3J_{HH}$ = 5.6 Hz, 4H, backbone C<u>H$_2$</u>N), 3.34 (sept, $^3J_{HH}$ = 6.9 Hz, 4H, C<u>H</u>Me$_2$), 1.76 (p, $^3J_{HH}$ = 5.9 Hz, 2H, backbone C<u>H$_2$</u>), 1.45 (d, $^3J_{HH}$ = 7.0 Hz, 12H, C<u>H$_3$</u>), 1.26 (d, $^3J_{HH}$ = 6.8 Hz, 12H, C<u>H$_3$</u>), -0.34 (s, 9H, *SiMe$_3$*). **^{13}C NMR{^{1}H}** (101 MHz, benzene-d_6) δ 147.1 (*o*-<u>C</u>), 142.1 (*ipso*-<u>C</u>), 141.6 (N<u>C</u>N), 127.9 (*p*-<u>C</u>), 124.1 (*m*-<u>C</u>), 51.0 (backbone N<u>C</u>H$_2$), 28.7 (<u>C</u>HMe$_2$), 25.0 (<u>C</u>H$_3$), 24.4 (<u>C</u>H$_3$), 23.0 (backbone <u>C</u>H$_2$), 3.6 (Si<u>C</u>H$_3$). **^{29}Si NMR** (99 MHz, benzene-d_6) δ -26.4. Elemental Analysis does not meet standard with percentage of C lower than expected after a few attempts.

*Crystallographic data for **6g-(SiMe$_3$)**:*

$C_{31}H_{49}N_3Si$, M_r = 491.82, monoclinic, *P 2$_1$/c*, a = 19.0434(5), b = 9.9053(2), c = 17.9664(4) Å, α = 90°, β = 95.434(2)°, γ = 90°, V = 3033.18 (13) Å^3, Z = 4, ρ_c = 1.077 Mg m^{-3}, T = 150 K, λ = 1.54180 Å, 35268 reflections collected, 6301 independent [R(int) = 0.029], which were used in all calculations. R_1 = 0.0498, wR_2 = 0.1241 for observed unique reflections [I > 2σ(I)] and R_1 = 0.0562, wR_2 = 0.1302 for all unique reflections. Max. and min. residual electron densities 0.86 and -0.35 e Å^{-3}.

*Spectroscopic data for **7g-(SiMe$_3$)**:*

^{1}H NMR (400 MHz, benzene-d_6) δ 7.21 (dd, $^3J_{HH}$ = 8.1, 6.0 Hz, 2H, *p*-C<u>H</u>), 7.15 (d, $^3J_{HH}$ = 7.6 Hz, 4H, *m*-C<u>H</u>), 3.65 (p, $^3J_{HH}$ = 5.1 Hz, 4H, backbone C<u>H$_2$</u>N), 3.39 (sept, $^3J_{HH}$ = 6.7 Hz, 4H, C<u>H</u>Me$_2$), 1.68 (p, $^3J_{HH}$ = 5.0 Hz, 4H, backbone C<u>H$_2$</u>), 1.45 (d, $^3J_{HH}$ = 6.8 Hz, 12H, C<u>H$_3$</u>), 1.29 (d, $^3J_{HH}$ = 6.8 Hz, 12H, C<u>H$_3$</u>), -0.34 (s, 9H, *SiMe$_3$*). **^{13}C NMR{^{1}H}** (101 MHz, benzene-d_6) δ 146.9 (N<u>C</u>N), 146.5 (*o*-<u>C</u>), 144.8 (*ipso*-<u>C</u>), 127.3 (*p*-<u>C</u>), 124.5 (*m*-<u>C</u>), 53.1 (backbone N<u>C</u>H$_2$), 28.9 (<u>C</u>HMe$_2$), 27.0 (backbone <u>C</u>H$_2$), 25.7 (<u>C</u>H$_3$), 24.3 (<u>C</u>H$_3$), 3.7 (Si<u>C</u>H$_3$). **^{29}Si NMR** (99 MHz,

benzene-d_6) δ -25.3. Elemental Analysis does not meet standard with percentage of C lower than expected after a few attempts.

*Crystallographic data for **7g-(SiMe$_3$)**:*

$C_{32}H_{51}N_3Si$, M_r = 505.85, monoclinic, *P 2$_1$/c*, a = 10.4251(2), b = 15.9774(3), c = 19.1353(3) Å, α = 90°, β = 103.614(2)°, γ = 90°, V = 3097.74(10) Å^3, Z = 4, ρ_c = 1.085 Mg m^{-3}, T = 150 K, λ = 1.54180 Å, 32060 reflections collected, 6419 independent [R(int) = 0.029], which were used in all calculations. R_1 = 0.0364, wR_2 = 0.0913 for observed unique reflections [I > 2σ(I)] and R_1 = 0.0422, wR_2 = 0.0955 for all unique reflections. Max. and min. residual electron densities 0.49 and -0.33 e Å^{-3}.

*General Procedures for the Synthesis of **Lg-H***

*Procedure A (**Lg** = **5g** or **7g**)*

In the case of **5g-H**, **[5-DippBr]Br** (0.75 g, 1.36 mmol) was dissolved in THF (50 mL) and ammonia bubbled through the solution for 30 min. A colour change from orange to a pale yellow was observed, together with the formation of a precipitate. The reaction mixture was quenched with aqueous ammonia (12 mL, 25% solution), and 100 mL of diethyl ether was then added. The solution was then washed with a saturated potassium carbonate solution (2 x 10 mL). The organic layer was collected and stirred over magnesium sulphate before drying *in vacuo* to yield the product as a spectroscopically pure colourless solid. Yield: 0.49 g, 89%.

In the case of **7g-H**, **[7-DippBr]Br** (0.75 g, 1.32 mmol) was dissolved in THF (50 mL) and ammonia (which had been pre-dried by passing through a potassium hydroxide column) was bubbled through the solution for 2 h. A colour change from red to a pale yellow was observed, together with the formation of a precipitate. The reaction mixture was then

filtered, and the solvent removed from the filtrate *in vacuo*. At this stage the crude **[7-DippNH$_2$]$^+$** salt was purified by recrystallization from a hot 1:1 mixture of hexane and chloroform, yielding colourless crystals. These crystals were then dissolved in dichloromethane and washed with saturated sodium hydroxide solution (2 x 10 mL); the organic layer was collected and stirred over magnesium sulphate before drying *in vacuo* to yield the product as a spectroscopically pure colourless solid. Yield: 0.39 g, 70 %.

*Procedure B (**Lg = Ig, 5g, 6g** or **7g**)*

In the case of **Ig**, **5g** or **7g**, the trimethylsilyl derivative **Lg-(SiMe$_3$)** (1.05 mmol) was added to methanol (*ca.* 15 equiv.) and the reaction mixture stirred for 3 h, after which time volatiles were removed *in vacuo* to yield the product as a spectroscopically pure colourless solid. Yields: **Ig-H** 0.37 g, 87%; **5g-H**: 0.35 g, 81%; **7g-H**, 0.37 g, 80%.

In the case of **6g-H**, **6g-(SiMe$_3$)** (0.61 g, 1.24 mmol) was added to methanol (ca. 15 equiv.) and the reaction mixture stirred for 2 h, after which time volatiles were removed *in vacuo* and the crude product extracted into boiling diethyl ether. After drying *in vacuo*, the residue was extracted into *n*-heptane, and a solution of 0.1 mL acetic acid in 10 mL *n*-heptane (molarity: 1.75 M) was then added dropwise, causing **[6g-H$_2$][OAc]** to precipitate out of solution. The emulsion was left to stand overnight, then filtered and the precipitate extracted into diethyl ether. After washing with saturated sodium hydroxide solution (2 x 10 mL), the organic layer was separated, stirred over magnesium sulphate, filtered and then dried *in vacuo* to yield the product as a spectroscopically pure colourless solid. Yield: 0.275 g, 53%.

*Procedure C (**Lg = 5g** or **6g**)*

A solution of cyanogen bromide (14 mmol) in toluene (100 mL) was added dropwise to a stirred solution of *N*,*N*'-(bis-diisopropylphenyl)-1,2-diaminoethane (for **5g-H**) or *N*,*N*'-(bis-diisopropylphenyl)-1,2-diaminopropane (for **6g-H**) (10 mmol) in toluene (100 mL) at 100°C. During the course of the addition a white solid started to precipitate (in the case of **6g-H**, the precipitation does not start until ca. 110°C). After complete addition, the mixture was allowed to stir at 110°C for 3 h (or overnight in the case of **6g-H**). The mixture was then cooled to room temperature and filtered, and the precipitate washed with toluene (50 mL) and diethyl ether (3 x 50 mL). Drying *in* vacuo yielded a white, crystalline solid, **[Lg-H$_2$]Br**. To a suspension of **[Lg-H$_2$]Br** in diethyl ether (100 mL) was then added saturated potassium hydroxide solution (100 mL) and the reaction mixture stirred vigorously for 2 h at room temperature. Brine (25 mL) was then added to the resulting mixture; the two layers were separated, and additional product extracted from the aqueous layer with diethyl ether. After drying over magnesium sulphate, volatiles were removed *in vacuo* to yield a spectroscopically pure colourless solid. Yield: **5g-H**: 2.64 g, 65%; **6g-H**: 3.73 g, 89%.

*Spectroscopic data for **5g-H**:*

^{1}H NMR (400 MHz, chloroform-*d*) δ 7.37 (dd, $^3J_{HH}$ = 7.2, 7.8 Hz, 2H, *p*-C<u>H</u>), 7.25 (d, $^3J_{HH}$ = 7.5 Hz, 4H, *m*-C<u>H</u>), 3.82 (s, $^3J_{HH}$ = 5.8 Hz, 4H, backbone C<u>H$_2$</u>N), 3.22 (sept, $^3J_{HH}$ = 6.9 Hz, 4H, C<u>H</u>Me$_2$), 1.35 (d, $^3J_{HH}$ = 6.9 Hz, 12H, C<u>H$_3$</u>), 1.29 (d, $^3J_{HH}$ = 6.9 Hz, 12H, C<u>H$_3$</u>), N<u>H</u> was not observed. **^{13}C NMR{^{1}H}** (101 MHz, chloroform-*d*) δ 160.0 (N<u>C</u>N), 149.0 (*o*-<u>C</u>), 134.2 (*ipso*-<u>C</u>), 128.9 (*p*-<u>C</u>), 124.4 (*m*-<u>C</u>), 48.5 (backbone <u>C</u>H$_2$), 28.9 (<u>C</u>HMe$_2$), 24.7 (<u>C</u>H$_3$), 24.5 (<u>C</u>H$_3$).

*Crystallographic data for **5g-H**:*

Crystals suitable for X-ray crystallography were obtained by slow evaporation from a benzene solution. However, the single crystal suffered phase change at T = 150 K and

therefore, the data collected was not suitable for publication. $C_{27}H_{40}N_3$, M_r = 405.63, monoclinic, *Cc*, a = 39.288(5), b = 13.3790(8), c = 23.935(3) Å, α =90°, β = 124.062(18)°, γ = 90°, V=10423(3) Å^3, Z=8, ρ_c = 1.069 Mg m^{-3}, T = 150 K, λ = 1.54180 Å, 31588 reflections collected, 13115 independent [R(int) = 0.060], which were used in all calculations. R_1 = 0.6934, wR_2 = 1.1572 for observed unique reflections [I > 2σ(I)] and R_1 = 0.7856, wR_2 = 3.8964 for all unique reflections. Max. and min. residual electron densities 4.79 and -1.92 e Å^{-3}.

*Spectroscopic data for **6g-H**:*

^{1}H NMR (400 MHz, chloroform-*d*) δ 7.30 (dd, $^3J_{HH}$ = 8.3, 7.1 Hz, 2H, *p*-C<u>H</u>), 7.18 (d, $^3J_{HH}$ = 7.7 Hz, 4H, *m*-C<u>H</u>), 3.56 (t, $^3J_{HH}$ = 5.8 Hz, 4H, backbone C<u>H$_2$</u>N), 3.19 (sept, $^3J_{HH}$ = 7.0 Hz, 4H, C<u>H</u>Me$_2$), 2.28 (p, $^3J_{HH}$ = 5.9 Hz, 2H, backbone C<u>H$_2$</u>), 1.29 (d, $^3J_{HH}$ = 7.0 Hz, 12H, C<u>H$_3$</u>), 1.23 (d, $^3J_{HH}$ = 6.8 Hz, 12H, C<u>H$_3$</u>), N<u>H</u> was not observed. **^{13}C NMR{^{1}H}** (101 MHz, chloroform-*d*) δ 155.0 (N<u>C</u>N), 147.8 (*ipso*-<u>C</u>), 138.9 (*o*-<u>C</u>), 128.4 (*p*-<u>C</u>), 124.5 (*m*-<u>C</u>), 49.7 (backbone <u>C</u>H$_2$N), 28.8 (<u>C</u>HMe$_2$), 24.7 (<u>C</u>H$_3$), 24.5 (<u>C</u>H$_3$), 23.4 (backbone <u>C</u>H$_2$). **ESI-MS (cation):** [6-DippH$_2$]$^+$: calc.: 420.3373; meas.: 420.3369.

*Crystallographic data for **6g-H**:*

Crystals suitable for X-ray crystallography were obtained by slow diffusion of hexane into a solution of the product in diethyl ether. $C_{28}H_{41}N_3$, M_r = 419.64, monoclinic, *P 2$_1$/c*, a = 19.6059(5), b = 6.9304(1), c = 19.9946(5) Å, α = 90°, β = 105.125(3)°, γ = 90°, V = 2622.69(11) Å^3, Z = 4, ρ_c = 1.063 Mg m^{-3}, T = 150 K, λ = 1.54180 Å, 15772 reflections collected, 5390 independent [R(int) = 0.017], which were used in all calculations. R_1 = 0.492, wR_2 = 0.1268 for observed unique reflections [I > 2σ(I)] and R_1 = 0.0546, wR_2 = 0.1319 for all unique reflections. Max. and min. residual electron densities 0.34 and -0.29 e Å^{-3}.

*Spectroscopic data for **7g-H**:*

^{1}H NMR: ^{1}H NMR (400 MHz, chloroform-*d*) δ 7.27 (dd, $^{3}J_{HH}$ = 8.4, 6.8 Hz, 2H, *p*-C<u>H</u>), 7.18 (d, $^{3}J_{HH}$ = 7.3 Hz, 4H, *o*-C<u>H</u>), 3.75 (t, $^{3}J_{HH}$ = 5.0 Hz, 4H, backbone C<u>H$_2$</u>N), 3.34 (sept, $^{3}J_{HH}$ = 6.9, 6.1 Hz, 4H, C<u>H</u>Me$_2$), 1.87 (t, $^{3}J_{HH}$ = 5.0 Hz, 4H, backbone C<u>H$_2$</u>C<u>H$_2$</u>), 1.29 (d, $^{3}J_{HH}$ = 6.9 Hz, 12H, C<u>H$_3$</u>), 1.19 (d, $^{3}J_{HH}$ = 6.8 Hz, 12H, C<u>H$_3$</u>), N<u>H</u> was not observed. **^{13}C NMR{^{1}H}** (101 MHz, Chloroform-*d*) δ 155.1 (N<u>C</u>N), 147.1 (*ipso*-<u>C</u>), 146.9 (*o*-<u>C</u>), 127.9 (*p*-<u>C</u>), 124.7 (*m*-<u>C</u>), 55.2 (*backbone* <u>C</u>H$_2$), 29.0 (<u>C</u>HMe$_2$), 28.5 (*backbone* <u>C</u>H$_2$<u>C</u>H$_2$), 24.6 (<u>C</u>H$_3$), 24.3 (<u>C</u>H$_3$). **ESI-MS (cation):** [7-DippNH$_2$]$^{+}$: calc.: 434.3530; meas.: 434.3525.

*Crystallographic data for **7g-H**:*

Crystals suitable for X-ray crystallography were obtained by recrystallization from hot cyclohexane. $C_{29}H_{43}N_3$, M_r = 433.66, triclinic, *P-1*, a = 8.7502(1), b = 9.4858(1), c = 17.5850) Å, α = 87.3073(5)°, β = 90.0027(6)°, γ = 62.5304(7)°, V = 1293.22(3) Å^3, Z = 2, ρ_c = 1.114 Mg m^{-3}, T = 150 K, λ = 0.71073 Å, 83733 reflections collected, 5874 independent [R(int) = 0.027], which were used in all calculations. R_1 = 0.0540, wR_2 = 0.1167 for observed unique reflections [I > 2σ(I)] and R_1 = 0.0878, wR_2 = 0.1465 for all unique reflections. Max. and min. residual electron densities 0.45 and -0.38 e Å^{-3}.

5.3 Preparation and characterization of Ligands

5.3.1 Theoretical Studies of the Ligands

DFT studies of the anionic ligands **[Lg]**$^{-}$ (Figure 5-5) were carried out at the outset with a view to understanding key influences on donor properties; important results are displayed inTable 5-1. From the DFT studies, three key frontier orbitals can be identified for each ligand, namely the HOMO, HOMO-1 and HOMO-3, which are centred on the

exocyclic N-atom. In the case of **[6g]**$^-$, these orbitals are depicted in Figure 5-6, and consist of a pair of effectively perpendicular π type frontier orbitals (the HOMO and HOMO-1), together with the lower lying σ-symmetry HOMO-3.

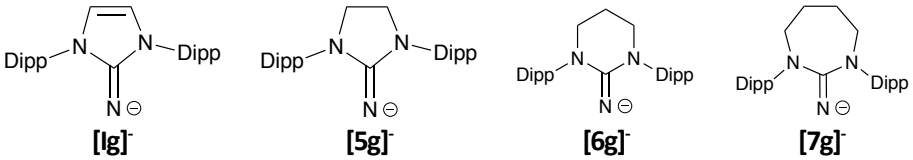


Figure 5-5: The ligands investigated in this chapter.

*Table 5-1: Internal N-C-N bond angles and key orbital energies calculated for **[Ig]**$^-$, **[5g]**$^-$, **[6g]**$^-$ and **[7g]**$^-$ by DFT methods.*

	[Ig]$^-$	[5g]$^-$	[6g]$^-$	[7g]$^-$
NCN angle	97.0	99.2	107.9	107.5
HOMO (kJ mol^{-1})	21.3	48.4	70.0	58.6
HOMO-1 (kJ mol^{-1})	9.3	-62.9	-44.7	-58.7
HOMO-3 (kJ mol^{-1})	-253.6	-228.6	-214.5	-230.0

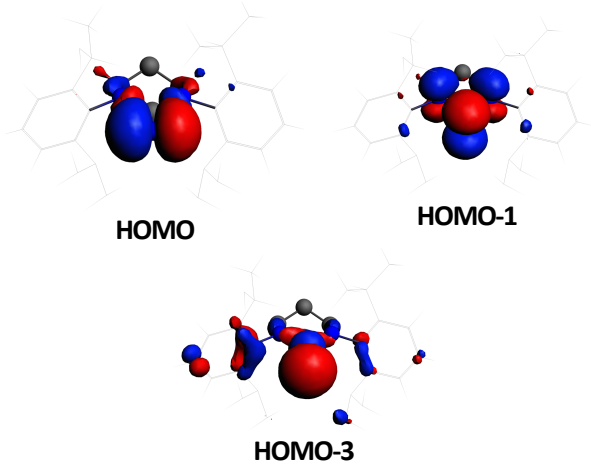


Figure 5-6: Depictions of the HOMO, HOMO-1 and HOMO-3 for [6g]-.

We expect the energies of all three N-centred orbitals increase with increasing ring size, reflecting trends elucidated for N-heterocyclic carbenes discussed in chapter 3. However, there are two data that stand out of the trend. First, the HOMO-1 of **[Ig]**$^-$ is found at much higher energy than for the corresponding saturated backbone systems. This is readily rationalized on the basis that the unsaturated backbone gives rise to a π-symmetry C=C component which destabilises the LUMO of the NHC fragment (due to the additional anti-bonding phase relationship; Figure 5-7).

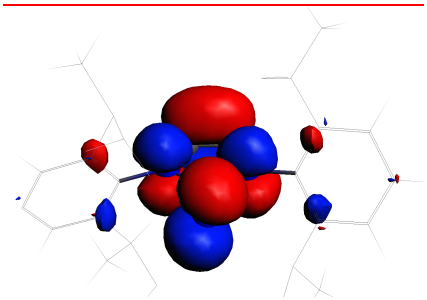


*Figure 5-7: The calculated HOMO-1 orbital of **[Ig]**$^-$, showing the out-of-phase interaction.*

The energies of all three N-centred orbitals of **[7g]**$^-$ represent another exception: its orbital energies are actually marginally lower than those of **[6g]**$^-$, despite the increased ring size. This can be explained (for the HOMO and HOMO-1, at least) by considering the orbital correlation diagram between p orbitals on the exocyclic nitrogen and those on N-heterocyclic carbene fragment (Figure 5-8).

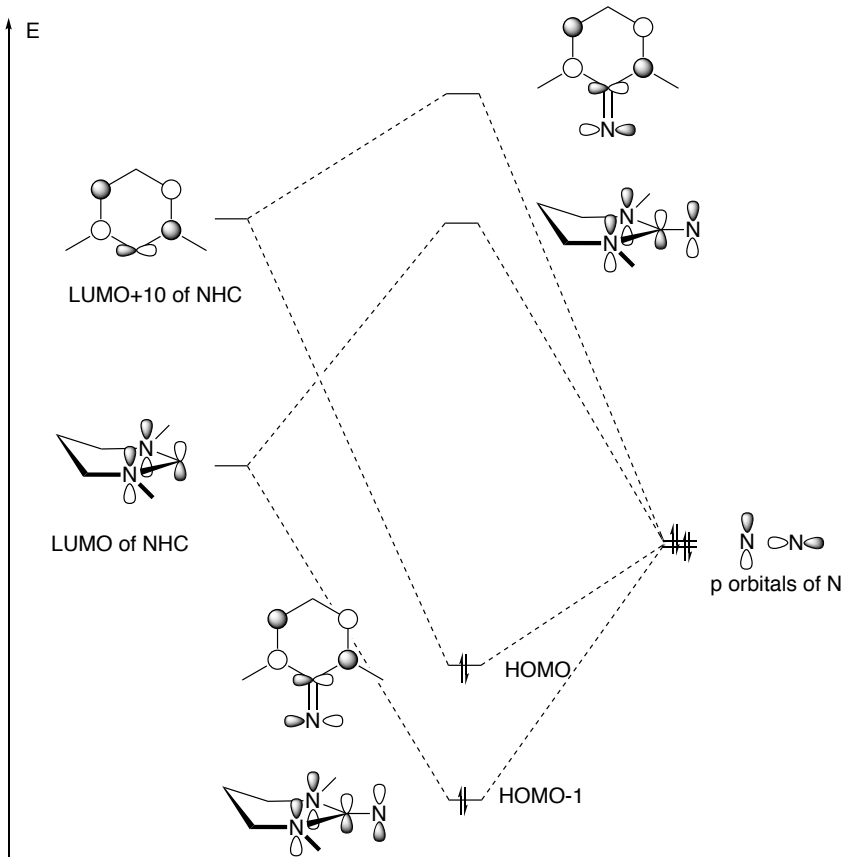


*Figure 5-8: Qualitative molecular orbital interaction diagram showing the construction of the HOMO and HOMO-1 of **[6g]**$^-$ from 6-Dipp and N fragments*

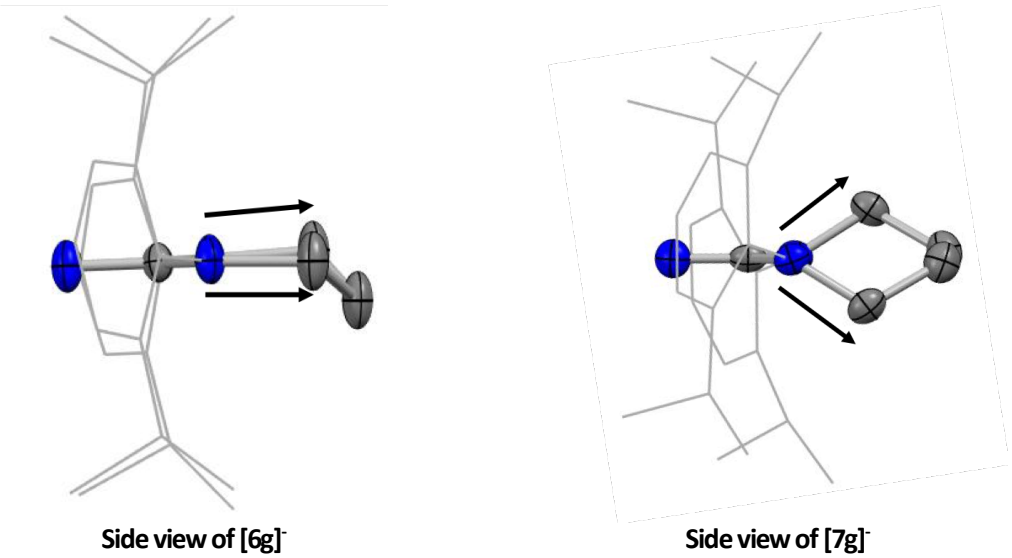
As illustrated in Figure 5-8, the energies of both the HOMO and HOMO-1 depend on two factors. The first is the energies of the (anti-bonding) fragment orbitals (in-plane and out-of-plane π orbitals) of the NHC (given that the energy levels of the nitrogen p orbitals are the same in all cases). The second factor is the contribution of these orbitals to the HOMO or HOMO-1. Based on DFT analyses involving fragmentation of each **[Lg]**$^-$ system into neutral NHC and anionic N^- fragments, the seemingly anomalous behaviour of **[7g]**$^-$ – in terms of HOMO and HOMO-1 orbital energies – can be rationalized.

*Table 5-2: Results of fragment orbital calculations for the HOMO of **[Lg]**$^-$.*

HOMO	**[Ig]**$^-$	**[5g]**$^-$	**[6g]**$^-$	**[7g]**$^-$
HOMO (kJ mol^{-1})	21.3	48.4	70.0	58.6
N-p orbital contribution	66.5%	68.4%	69.9%	66.5%
Energy of LUMO+n[a] of NHC (kJ mol^{-1})	194	211	283	195
NHC LUMO+n[a] orbital contribution	13.8%	15.1%	10.7%	6.0%

a. n being 6 for **[Ig]**$^-$, 4 for **[5g]**$^-$, 10 for **[6g]**$^-$ and 9 for **[7g]**$^-$.

Table 5-2 displays the results of the fragment orbital calculations, describing the factors on which the energy of the HOMO of the respective **[Lg]**$^-$ systems depend. All four rows of data reveal an exception in the case of **[7g]**$^-$: the contribution from the nitrogen p orbital increases marginally from **[Ig]**$^-$ to **[6g]**$^-$ but decreases from **[6g]**$^-$ to **[7g]**$^-$; the energy of the in-plane LUMO+n orbital of the respective NHC fragment increases across the table, but again decreases from **[6g]**$^-$ to **[7g]**$^-$; the contribution from the LUMO+n orbital of the NHC fragment is exceptionally low in the case of **[7g]**$^-$. All of these data are consistent with the fact that that the HOMO energy of **[7g]**$^-$ is lower than that of **[6g]**$^-$. Differences in geometry between **[7g]**$^-$ and the other **[Lg]**$^-$ systems offer a potential explanation of the data in Table 5-2. As shown in Figure 5-9, the endocyclic C-N bonds of the heterocyclic backbone are orientated differently in **[7g]**$^-$; in the other ligands (such as **[6g]**$^-$) the C-N bonds are essentially co-planar. The non-planarity of the backbone of **[7g]**$^-$ leads to a significantly lower energy for the in-plane π fragment orbital of the NHC fragment (LUMO+9 for the 7-Dipp fragment in **[7g]**$^-$: +195 kJ mol^{-1} vs +283 kJ mol^{-1} for LUMO+10 of the 6-Dipp fragment in **[6g]**$^-$). As the energy of the LUMO+n fragment orbital decreases, so the energy of the HOMO (which is constituted from this NHC fragment orbital together with the in-plane p orbital of the exocyclic nitrogen) is also lowered. The HOMO is therefore lower in energy in the case of **[7g]**$^-$.



Side view of [6g]$^-$ **Side view of [7g]$^-$**

Figure 5-9: The side view of two selected ligands.

The backbone distortion out of planarity also leads to a change in the energy of the LUMO of the NHC fragment and hence explains the stabilization of the HOMO-1 of **[7g]**$^-$. With the p orbitals on the endocyclic nitrogen in the seven-membered ring no longer aligned so close to parallel with that on the carbene carbon, the LUMO of the NHC fragment in **[7g]**$^-$ is rendered less anti-bonding. Since the contributions from the p-orbital from the exocyclic N and the LUMO of the NHC fragment are similar among **[5g]**$^-$, **[6g]**$^-$ and **[7g]**$^-$, the energy of NHC LUMO becomes a major factor in lowering the energy of the HOMO-1 in **[7g]**$^-$ (Table 5-3).

Table 5-3: results of fragment calculation for HOMO-1.

HOMO-1	[Ig]$^-$	[5g]$^-$	[6g]$^-$	[7g]$^-$
N-p orbital contribution	26.1%	38.8%	38.9%	37.1%
Energy of LUMO of NHC (kJ mol^{-1})	-141	-172	-160	-173
NHC LUMO orbital contribution	31.8%	41.0%	40.6%	39.7%

5.3.2 Syntheses of the Protio-ligands

Three complementary routes have been developed for the syntheses of the target ligands (Figures 5.10-5.12 and Table 5-4). The ligands, **[Lg]**$^-$, are negatively charged and therefore are conveniently accessed via the corresponding (easily stored) protio-ligands, **Ig-H**, **5g-H**, **6g-H** and **7g-H**. These protio-ligands can be synthesised via more than one route. In the case of route A (Figure 5-11), which involves the reaction of the corresponding silver NHC complex with ammonia, the synthesis of **5g-H** can be carried out in air, while the last step in the case of **7g-H** must be carried out under argon to prevent the formation of the (oxidized) cyclic urea (7-Dipp)=O. Overall synthesis via route A takes a longer time to complete than the other two routes, as the formation of silver complexes and the subsequent reaction with Br_2 constitute additional synthetic steps. Route B (Figure 5-12) is the only methodology which is suitable for all protio-ligands in the series, but it is also hampered by a relatively long duration, and every step in the synthetic route needs to be carried out under the exclusion of air/moisture. Route C (Figure 5-13) has fewer steps and each takes only a short time. Its disadvantage is potential toxicity – the second step involves a reflux with cyanogen bromide, for which the LD_{50} (orally) in rats is reported to be 25–50 mg kg^{-1}.

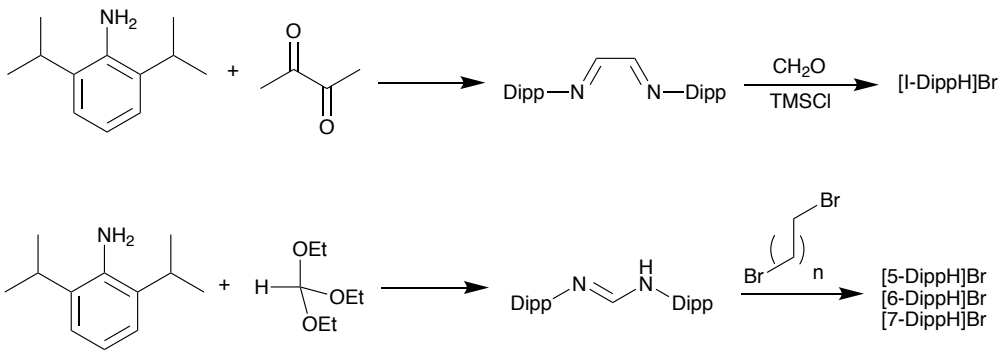


Figure 5-10: Syntheses of precursors for routes A and B.

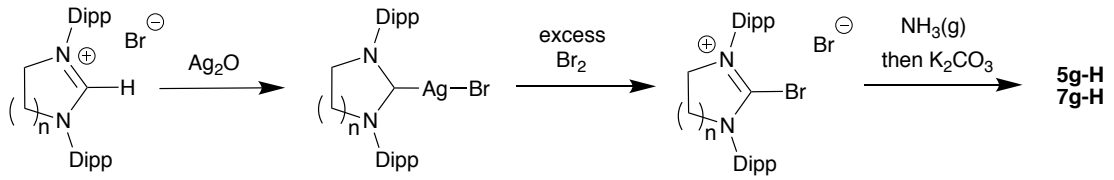


Figure 5-11: Route A.

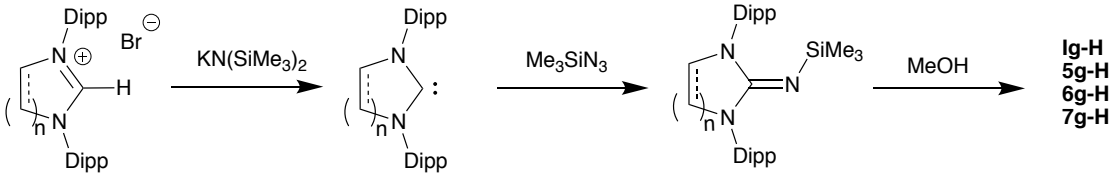


Figure 5-12: Route B.

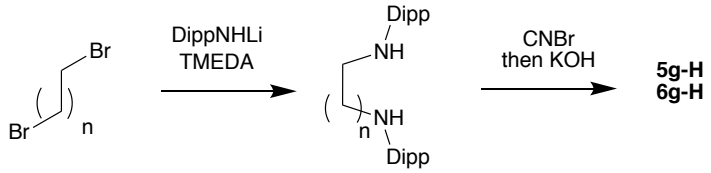


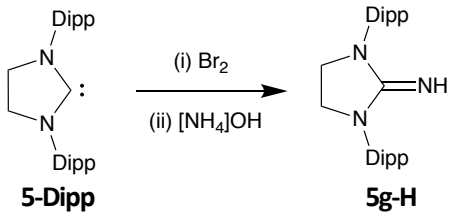
Figure 5-13: Route C.

Table 5-4: Applicabilities of the three routes for synthesising each protio-ligand.

	A	B	C
Ig-H	NO	YES	NO
5g-H	YES	YES	YES
6g-H	NO	YES	YES
7g-H	YES	YES	NO

5.3.2.1 Synthesis via Route A

As mentioned in the introduction to this chapter, only **Ig-H** and **5g-H** have been reported in the literature prior to the start of this research. **Ig-H** was synthesized via route B by Tamm in 2007; **5g-H** on the other hand, was synthesized via a methodology similar to route A by Bertrand in 2010 (Figure 5-14) [18]. The synthesis that Bertrand reported has a relatively poor overall yield (61% for the precursor **5-Dipp**, and then 24% for its conversion to **5g-H**, representing a 15% overall yield). This poor yield is largely due to the difficulty associated with the direct bromination of the N-heterocyclic carbene, **5-Dipp**.



5-Dipp **5g-H**

*Figure 5-14: The original synthetic route to **5g-H** reported by Bertrand et al.*

In order to increase the yield, especially of the bromination step, we employed the corresponding NHC silver complexes, **(5-Dipp)AgBr** and **(7-Dipp)AgBr**, in the first step, rather than the free carbene. The silver complexes of both **5-Dipp** and **7-Dipp** are known to behave as carbene transfer reagents, and their use in the bromination step increases the overall yield to 42% (i.e. ca. three times higher than the previous literature yield). The silver complexes are themselves synthesized from the respective amidinates and Ag_2O, and are then added to an excess of bromine to yield **[5-DippBr]Br** and **[7-DippBr]Br**. In the final step ammonia gas is bubbled through a solution of the dibromide for one hour, and the protio-ligands **5g-H** and **7g-H** can then be isolated after deprotonation by K_2CO_3.

In the case of **5g-H**, the reaction of **[5-DippBr]Br** with ammonia can be performed in air, and all manipulations were performed at room temperature. This contrasts favourably with previously reported procedures involving the free carbene as an intermediate, which require anaerobic conditions. By contrast, carrying out the synthesis of **7g-H** in air leads to the formation of the corresponding urea, (7-Dipp)=O. Hence, in this case, the reaction must be performed under the exclusion of air, and the ammonia pre-dried using a potassium hydroxide column.[23] Interestingly, the increased basicity of **7g-H** (over **5g-H**) is evident in the purification procedure, in that a K_2CO_3 work up is unable to deprotonate its conjugate acid, **[7-DippNH$_2$]$^+$** while this deprotonation occurs readily for **[5-DippNH$_2$]$^+$**. Potassium hydroxide must be employed instead to deprotonate **[7-DippNH$_2$]$^+$**.

Crystallisation of **5g-H** via slow evaporation of pentane yielded single crystals that undergo a phase change at 150 K (the default temperature for X-ray crystallographic measurements). Therefore, diffraction experiments were carried out at 200 K, at which temperature the crystals are stable, but the data are not of sufficient quality for publication. Unlike **5g-H**, crystallisation of **7g-H** from hot cyclohexane at 4°C yielded crystals of X-ray diffraction quality that are stable at 150 K.

The structures obtained for **5g-H** and **7g-H** are shown in Figure 5-15 and are consistent in geometric terms with the DFT calculations carried out on the same neutral protio-ligand species. Thus, the experimentally determined NCN angles are 105.1(9)° and 113.9(2)° for **5g-H** and **7g-H**, respectively, compared to values of 106.4° and 116.5° obtained computationally.

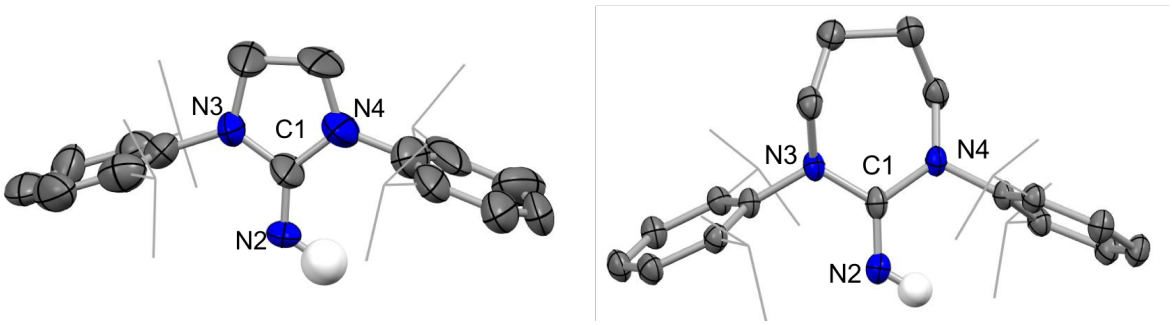


*Figure 5-15: Crystal structures of **5g-H** (left) and **7g-H** (right). H atoms omitted (except NH) and isopropyl groups shown in wireframe format for clarity. Thermal ellipsoids set at the 50% probability level. Key bond lengths and angles: **5g-H:** d(C1=N2) = 1.30(1) Å, ∠ N3C1N4 = 105.1(9)°; **7g-H:** d(C1=N2) = 1.250(3) Å, ∠N3C1N4=113.9(2)°.*

5.3.2.2 The Synthesis of 6g-H – General Application of Route B

Initial plans also involved synthesizing **6g-H** via route A. However, bubbling ammonia through a solution of **[6-DippBr]Br** (Route A) proved ineffective for the preparation of **6g-H**. Inspection of the ^{1}H NMR spectrum of the reaction mixture shows little-to-no product formation, and the corresponding mass spectrum shows mainly starting material (*m*/*z* = 483.3) and very little product (*m*/*z*= 420.4). The reaction was repeated in various solvents (including THF, dichloromethane, chloroform and acetonitrile) and at different temperatures, all of which led to very low degrees of product formation, essentially independent of the amount of time ammonia gas was bubbled through the solution. Given the superficially similar nature of **5-**, **6-** and **[7-DippBr]Br**, this lack of reactivity appeared anomalous.

Inspection of the previously reported crystal structure of **[6-DippBr]Br** reveals a short Br---Br contact, and it was hypothesized that the bromide counter-ion might hinder the approach of ammonia and inhibit the reaction. Anion exchange for tetrafluoroborate might then be expected to circumvent the problem.[24] However, as with **[6-DippBr]Br**,

bubbling of ammonia through a solution of **[6-DippBr][BF_4]** yielded only a trace amount of product, with the reaction mixture predominantly being comprised of starting material. It is, therefore, reasonable to conclude that the counter-ion is not the impeding factor of the reaction. Additionally, the use of more forcing conditions, including the treatment of **[6-DippBr]X** (X^- = Br^- or BF_4^-) with sodium amide and increased reaction times, also yielded only trace amounts of product.

Attempts to synthesise the mesityl analogue of **6g-H** (**6-MesNH**), so as to probe the importance of sterics on reactivity, also proved fruitless. Due to the reduced steric demand of the mesityl- substituent, reaction of **[6-MesH]Br** with Ag_2O leads to the formation of a mixture of **(6-Mes)AgBr** and **[(6-Mes)$_2$Ag][AgBr$_2$]**, the latter of which is unreactive towards Br_2, resulting in a very low yield for the formation of **[6-MesBr]Br**.[25] Even then, subsequent attempts to react **[6-MesBr]Br** with ammonia yielded results analogous to that of the Dipp system, i.e. essentially no reaction was observed.

Consequently, other synthetic pathways towards the elusive protio-ligand **6g-H** were explored, proceeding via the free carbene. As a starting point, a directly analogous procedure to that used in the synthesis of **Ig-H** was considered (i.e. from the free carbene and Me_3SiN_3).[26] A longer reflux time was envisaged due to the increased steric profile of **6-Dipp** compared to **IDipp**. However, even after an 11 day reflux in toluene, the ^{1}H NMR spectrum showed a mixture of **6-Dipp**, **6g-(SiMe$_3$)**, and **[6-DippH]X** (where presumably X^- = N_3^-). This low level of conversion was attributed to both steric factors and the poor solubility of **6-Dipp** in toluene.

In order to reduce the reaction time, the reaction was repeated in mesitylene, due to its higher boiling point (163-166°C). After allowing the reaction mixture to reflux

overnight, the colourless suspension became bright yellow and no starting material was observed to be retained in solution (Figure 5-16)

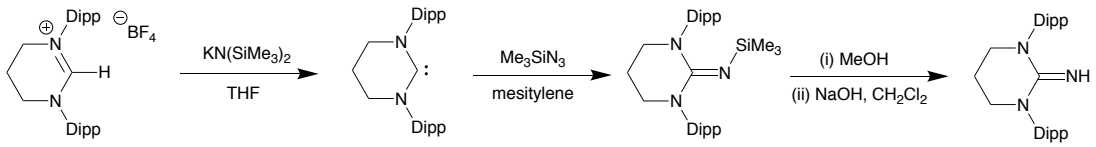


*Figure 5-16: Synthesis of **6g-H** via route B.*

However, even under these conditions, a mixture of products was formed: the target compound, **6g-(SiMe$_3$)**, together with **[6-DippH][N$_3$]**. Attempts were made to separate the products by fractional crystallization from hexane, acetonitrile and $Me_3SiOSiMe_3$. However, in each case the products co-crystallised. Thus, the imine was de-protected by stirring in methanol, and the crude product extracted with boiling diethyl ether. The mixture at this point still consisted of **6g-H** and **[6-DippH][N$_3$]**; however both products are highly soluble in most solvent systems. Hypothesizing that **[6g-H$_2$]$^+$** would likely be as insoluble as its 7-membered analogue, the mixture was treated with a solution of acetic acid in heptane, thereby causing **[6g-H$_2$][OAc]** to precipitate out of solution, as an oil. After allowing the emulsion to stand overnight, the suspension could be separated by filtration. Once separated, the salt could be deprotonated by washing with NaOH solution to yield the pure product, **6g-H** in 53% overall yield. Slow diffusion between ether and hexane led to the formation of crystals suitable for X-ray diffraction (Figure 5-17).

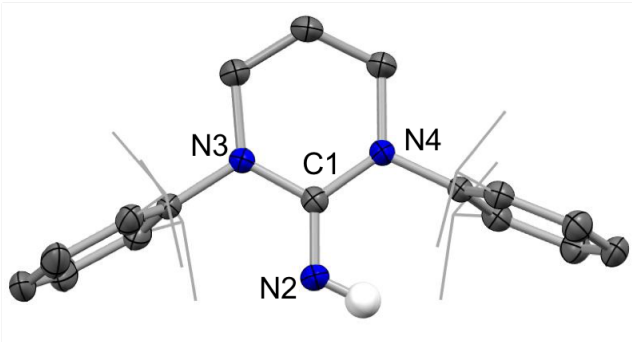


*Figure 5-17: Crystal structure of **6g-H**. H atoms omitted (except NH) and isopropyl groups shown in wireframe format for clarity. Thermal Ellipsoids set at 50% probability level. Key bond lengths and angles: d(C1=N2) = 1.288(2) Å and ∠N3C1N4= 115.8(1)°.*

The isolation of **[6-DippH]X** (i.e. the protonated carbene) under air- and moisture-free conditions is difficult to rationalize, given the lack of an obvious proton source; however, comparison with Tamm's procedure for the synthesis of **Ig-H** offers precedent. In the synthesis of **Ig-H** it is found that the precipitate formed during that reaction can also be attributed to the imidazolium species, **[IDippH]X**, again presumably where X = N_3. However, in the case of **[IDippH][N_3]**, the imidazolium salt is insoluble in non-polar solvents and thus is easily separated. **[6-DippH][N_3]**, somewhat surprisingly, appears to be soluble in both polar and non-polar solvents. We hypothesise that this is due to the fact that while **[IDippH][N_3]** remains ionic, **[6-DippH][N_3]** exists in an equilibrium between the ionic salt and the addition product (Figure 5-18).

Thus it is conceivable that, in the case of **[6-DippH][N_3]**, the equilibrium position can shift to the left or right in the presence of polar and non-polar solvents, respectively. This type of equilibrium is known for related systems, for example in cases in which the counter anion is cyanide.[27,28] This phenomenon is presumably not observed in the case of

[IDippH][N₃] as addition of the azide anion is disfavoured, due to the disruption of the π-system of the imidazolium salt.

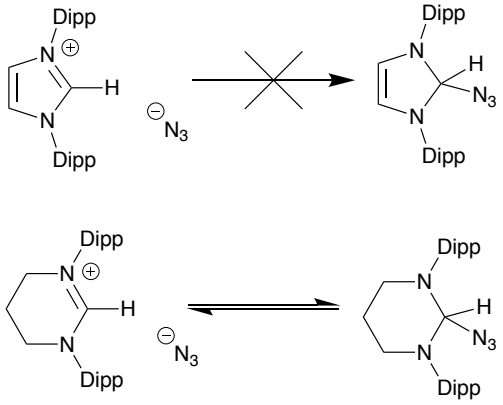


*Figure 5-18: Proposed differences between the **[IDippH][N₃]** and **[6-DippH][N₃]** systems.*

It is known that some organic azides can be converted into the corresponding imine by treatment with a catalytic amount of base or by photolysis, via the formation of a nitrene.[29, 30] However, preliminary results from the treatment of **[7-DippH][N₃]** with K[O^{t}Bu] and from the irradiation of **[6-DippH][N₃]** give no indication of the formation of **7g-H** and **6g-H** respectively.

5.3.2.3 Synthesis using Cyanogen Bromide (Route C)

A good synthetic route is cost efficient – taking into account the cost of materials used in the synthesis such as starting materials, solvents and catalysts – as well as the conversion cost, which includes factors such as atom economy, yield, time taken to synthesise the product and environmental factors.[31]

Route B has shown its capability for the synthesis of all of the target ligands. However, the syntheses of the respective (protonated carbene) precursors take a very long time. For example, **[5-DippH]Br** requires 4 days in synthesis and work-up, as well as another 4 days for deprotonation, reflux with trimethylsilyl azide and work-up before isolating **5g-H** (and the overall yield is only 29%). The syntheses of **[6-DippH]Br** and **[7-DippH]Br** require 6 days and 10 days, respectively, not to mention the additional time required to isolate before isolating **6g-H** and **7g-H**. Synthesizing **5g-H** via route A is more time consuming – taking 11 days to complete, although the overall yield is higher (42%), and air-sensitive techniques are not required. Furthermore, the final step of route A is often complicated by contamination with traces of bromine (excess of bromine is used), which means that reactions using ligands derived from route A are typically not so clean.

In order to shorten the period of time required for ligand synthesis, to increase the yield and avoid contamination from excess bromine, route C was investigated as a potential alternative. On the face of it, this approach is quite straightforward – the heterocycle backbone can be synthesized from the respective α,ω-dibromide in the first step, and the ring is closed by refluxing with cyanogen bromide in toluene. The synthesis of **5g-H** via route C yields a clean, uncontaminated product and is much more time efficient – taking a total of 3 days to complete. At the same time, the yield is increased significantly compared to that achieved via either route A and B. (Table 5-5)

*Table 5-5: Time, atom economy and overall yields of the different routes applied to the synthesis of **5g-H**.*

	Route A	Route B	Route C
Time (d)	11	8	3
Overall Yield (%)	42	29	50
Atom Economy (%)	31	40	47

In addition, as fewer steps were used in the synthesis, less waste is created and the atom economy of route C is the highest among the three routes. However, one problem with this synthetic route is the use of cyanogen bromide. **CNBr is highly toxic**. It can be deactivated with aqueous alkali hydroxide, which instantly hydrolyses it to alkaline cyanide and bromide. Following this, the cyanide is oxidised with sodium hypochlorite to give the cyanate ion, which is significantly less toxic.[32] However, the deactivation process produces a lot of waste, which must be disposed of. Thus, this synthetic route does not have a favourable environmental impact.

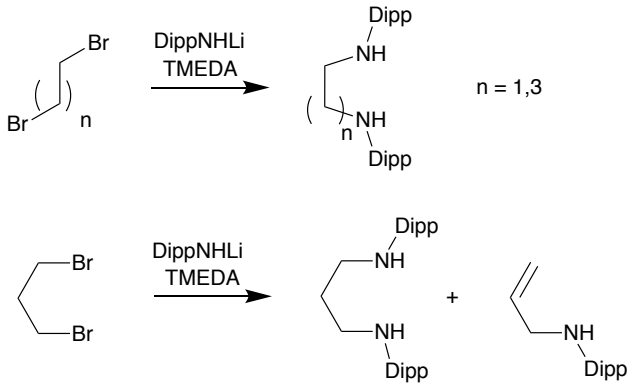


Figure 5-19: The syntheses of the backbone diamines for the 5-membered ring [N,N'-bis(diisopropylphenyl)-1,2-diaminoethane] or 7-membered ring [N,N'-bis(diisopropylphenyl)-1,4-diaminobutane] result mainly the desired product (upper), while the attempted synthesis of the corresponding backbone for the 6-membered ring [N,N'-bis(diisopropylphenyl)-1,3-diaminopropane] results in desired product and side product in a ca. 1:1 ratio (lower).

In addition to **5g-H**, **6g-H** can also be synthesized via route C. The ring closure step with cyanogen bromide takes longer (3 days) in the case of **6g-H** compared to **5g-H** (overnight). In addition, the synthesis of the acyclic backbone precursor, *N*,*N*'-

bis(diisopropylphenyl)-1,3-diaminopropane, has a much lower yield compared to its two-carbon bridged analogue.

The reason for this lower yield is outlined in Figure 5-19. In the case of 1,2-diaminoethane and 1,4-diaminobutane, substitution occurs almost exclusively, while in the case of 1,3-diaminopropane, elimination and substitution processes compete, resulting in two products.[33]

Finally, we attempted to synthesize **7g-H** via route C. However, an unidentified brown oil is the only product obtained by refluxing 1,4-daminobutane with cyanogen bromide. Longer reflux times were investigated, as well as the use of solvents with higher boiling points (*e.g.* mesitylene), but no clean generation of the desired product could be achieved. Presumably this reflects the well-known entropic problems associated in synthesizing larger heterocycles via ring closure, as mentioned in section 1.3.1.1.

5.3.2.4 Syntheses of Trimethylsilyl Derivatives

The protio-ligands **Lg-H** provide a variety of potential donors for use in both main group and transition metal chemistry. While these systems can be applied to the synthesis of guanidinato complexes via acid/base chemistry, the development of related trimethylsilyl-substituted systems would offer further synthetic versatility. With this in mind, these silylated systems were also prepared.

Thus the N-silyl derivatives **Lg-(SiMe$_3$)** (upper row, Figure 5-20) have been synthesized via route B utilizing trimethylsilyl azide (but without methanolysis in the last step), and single crystals obtained, thereby enabling the respective solid-state structures to be determined by X-ray crystallography (lower row, Figure 5-20). Each of **5g-(SiMe$_3$)**, **6g-(SiMe$_3$)** and **7g-(SiMe$_3$)** features the expected molecular connectivity, featuring an

exocyclic =N(SiMe$_3$) function derived from the azide reagent. However, while **5g-(SiMe$_3$)** and **7g-(SiMe$_3$)** feature a bent geometry at N2, that of **6g-(SiMe$_3$)** features a C-N-Si unit which is very close to linear, with an angle of 174.0(1)°. To understand this apparent anomaly a series of computational studies of the **Lg-(SiMe$_3$)** (and related) systems was carried out in order to explain the structural differences in the C-N-Si units.

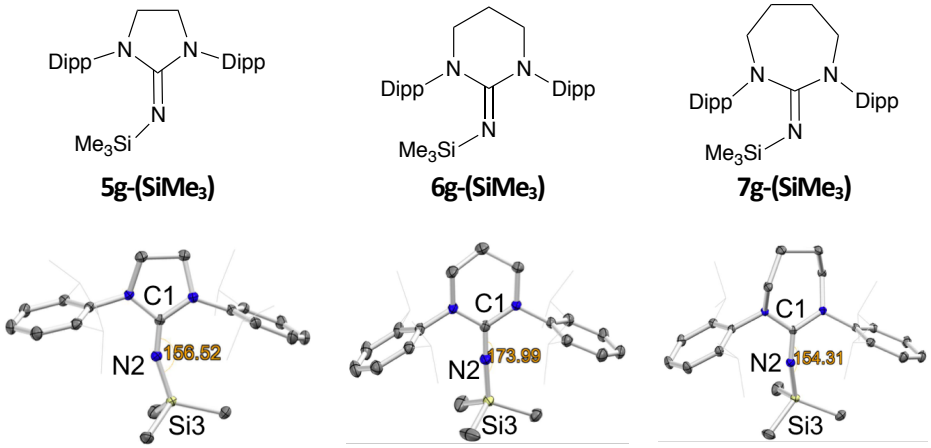


*Figure 5-20: (upper) Trimethylsilyl derivatives of each guanidinato ligand: **5g-(SiMe$_3$)** (left), **6g-(SiMe$_3$)** (centre) and **7g-(SiMe$_3$)** (right). (Lower) Molecular structures, as determined in the solid state by X-ray crystallography; H atoms omitted and isopropyl groups shown in wireframe format for clarity and thermal ellipsoids set at 50% probability level. Key bond lengths and angles: 5g-(SiMe3): d(C-N) = 1.258(2) Å and d(N-Si) = 1.684(1) Å, ∠CNSi=156.5(2), ∠NCN= 105.2(1)°; 6g-(SiMe3): d(C-N) = 1.258(2) Å and d(N-Si) = 1.685(1) Å, ∠CNSi=174.0(1), ∠NCN= 115.4(1)°; 7g-(SiMe3): d(C-N) = 1.261(2) Å and d(N-Si) = 1.678(1) Å, ∠CNSi=154.3(1), ∠NCN= 113.9(1)°.*

*Table 5-6: Geometric information relating to **Lg-(SiMe$_3$)** systems obtained from both experimental and computational studies.*

	∠C-N-Si (expt.)/°	∠C-N-Si (calc.)/°
Ig-(SiMe$_3$)	155.4(1)[2]	157
5g-(SiMe$_3$)	156.5(2)	156
6g-(SiMe$_3$)	174.0(1)	169
7g-(SiMe$_3$)	154.3(1)	156

In Table 5-6, the key C-N-Si bond angles are listed - both those derived from experiment and those from DFT calculations - for all four **Lg-(SiMe$_3$)** compounds. It can be seen that while most of these systems feature a bent C-N-Si moiety, that of **6g-(SiMe$_3$)** is much closer to linearity. The difference in the experimentally determined angle for **6g-(SiMe$_3$)** compared to the other systems is of the order of 20^o. While there is always the possibility of the molecular geometry being perturbed by crystal packing forces in the solid state, it should be noted that the C-N-Si angles determined computationally (for the isolated gas-phase molecules) agree with the solid-state trend (albeit with a slightly more bent structure in the case of **6g-(SiMe$_3$)**). In order to understand the apparently anomalous behaviour of **6g-(SiMe$_3$)**, fragment orbital calculations were undertaken to probe the interaction between the guanidinato and Me_3Si groups.

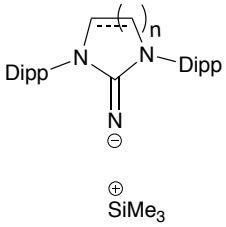


*Figure 5-21: The two fragments defined for fragment orbital calculations on **Lg-(SiMe$_3$).***

Within the optimised structure, two fragments were defined, namely a guanidinato ligand (set to -1.0 charge) and the Me_3Si group (set to +1.0 charge) (Figure 5-21). ETS-NOCV analyses were applied to investigate the interaction between the two fragments for each **Lg-(SiMe$_3$)** system. The interaction, as expected, is mainly comprised of σ-bonding

between N and Si, with two weaker π-bonding interactions (Table 5-7). The interaction energies are summarised in Table 5-8.

*Table 5-7: Interactions between the anionic guanidinato and cationic silicon fragments in systems of the type **Lg-(SiMe₃)**.*

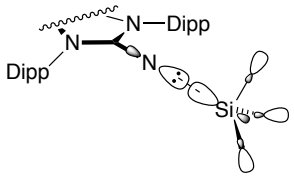
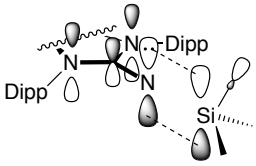
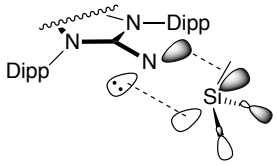
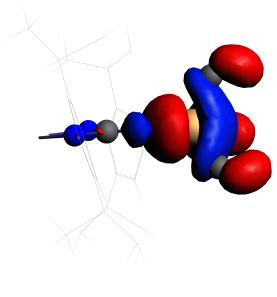
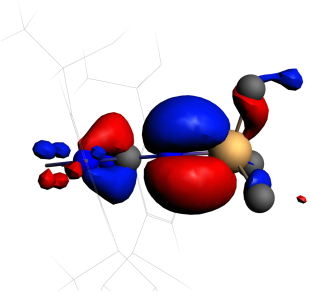
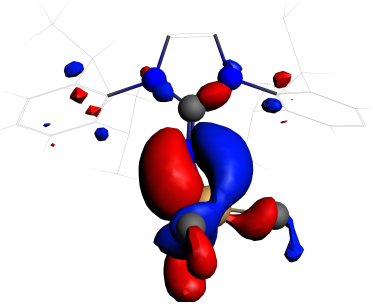
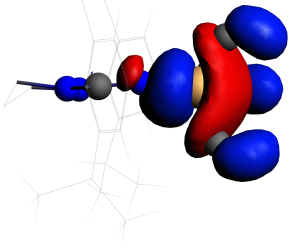
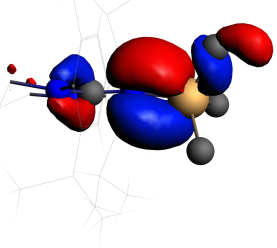
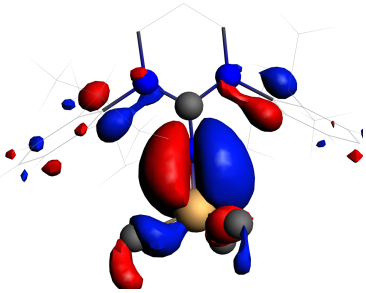
	σ-bonding	out-of-plane π-bonding	in-plane π-bonding
Interaction between two fragments			
Depiction for **Ig-(SiMe₃)**			
Depiction for **6g-(SiMe₃)**			

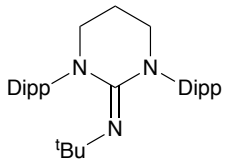
*Table 5-8: Interaction energies between the anionic guanidinato and cationic silicon fragments in systems of the type **Lg-(SiMe₃)**.*

ligand	σ-bonding (kJ mol^{-1})	π-bonding (out-of-plane) (kJ mol^{-1})	π-bonding (in-plane) (kJ mol^{-1})
[Ig]$^-$	-397	-125	-108
[5g]$^-$	-397	-117	-109
[6g]$^-$	-388	-121	**-138**
[7g]$^-$	-397	-120	-112

As can be seen in Table 5-8, both σ-bonding and out-of-plane π-bonding energies are similar for all the trimethylsilyl systems, while the in-plane π-bonding for **6g-(SiMe₃)**

stands out as being significantly more negative than those determined for the other systems. This finding is in line with the results of previous calculations on the **[6g]**$^-$ anion (Section 5.3.1), which show that the in-plane π donor orbital (the HOMO of **[6g]**$^-$) is found at significantly higher energy than the corresponding orbital for the other **[Lg]**$^-$ systems. More effective π donation from this orbital to the Si-C σ* orbital therefore results, and a more linear C-N-Si geometry is observed.

To further investigate the role of electronic factors in determining the geometry of the C-N-Si unit in the **6g-(SiMe$_3$)** system, similar fragment orbital calculations were carried out on **6g-(tBu)** (Figure 5-22).



6g-(tBu)

*Figure 5-22: The structure of **6g-(tBu)**.*

The replacement of the $SiMe_3$ fragment by ^{t}Bu has a significant effect on the C-N-E angle (E = C, Si), being somewhat narrower for **6g-(tBu)** (145^o) when compared to **6g-(SiMe$_3$)** (169 ^{o}). When Si is replaced with a C, the C-N-E angle becomes narrower, as the in-plane π-bonding component becomes much weaker (Table 5-9), presumably reflecting the higher energy of the C-based acceptor orbitals.

Table 5-9 ：The interaction energies between guanidinatos and ($SiMe_3$) /tBu group.

	C-N-Si(C) angle (calc.)	σ-bonding (kJ/mol)	π-bonding (out-of-plane) (kJ/mol)	π-bonding (in-plane) (kJ/mol)
6g-($SiMe_3$)	169	388	-121	-138
6g-tBu	145	-928	-75	-84

5.4 Summary

In summary, we have developed three different synthetic routes to four guanidinato ligands featuring different heterocycle ring sizes. Route B that installs imino groups onto NHCs via a Staudinger reaction is the most general synthetic route, capable of accessing all four ligands; route A involving ammonia gas in forming the imino groups is a more convenient route in some respects, being tolerant of air in the most part, but long in duration; route C involving cyanogen bromide is the quickest route and results in both the highest overall yield and atom economy, but it can only be used to synthesize **5g-H** and **6g-H** and has obvious issues regarding reagent toxicity. In addition to **Lg-H**, we have also synthesized the **Lg-($SiMe_3$)** analogues which offer additional synthetic versatility.

Theoretical studies have revealed that **[6g]**$^-$ is the strongest donor among the **[Lg]**$^-$ systems (via both σ and π framework) with the corresponding orbitals for **[7g]**$^-$ having lower energies than expected. This results from a distortion of backbone in **[7g]**$^-$ which leads to less effective (repulsive) overlap between the exocyclic C=N π system and the lone pairs of the ring nitrogens. The strong π-donor strength of **[6g]**$^-$ is shown to play an important role in supporting a near linear C-N-Si fragment in **6g-($SiMe_3$)**.

5.5 References

1. G. Chandra, A. D. Jenkins, M. F. Lappert and Srivasta.Rc, *Journal of the Chemical Society a -Inorganic Physical Theoretical*, 1970, 2550-&.
2. C. Jones, *Coordination Chemistry Reviews*, 2010, **254**, 1273-1289.
3. F. T. Edelmann, *Advances in Organometallic Chemistry, Vol 57*, 2008, **57**, 183-352.
4. M. P. Coles, *Dalton Transactions*, 2006, 985-1001.
5. P. J. Bailey and S. Pace, *Coordination Chemistry Reviews*, 2001, **214**, 91-141.
6. M. Tamm, S. Randoll, T. Bannenberg and E. Herdtweck, *Chemical Communications*, 2004, 876-877.
7. M. Tamm, D. Petrovic, S. Randoll, S. Beer, T. Bannenberg, P. G. Jones and O. Grunenberg, *Organic & Biomolecular Chemistry*, 2007, **5**, 523-530.
8. M. Tamm, S. Randoll, E. Herdtweck, N. Kleigrewe, G. Kehr, G. Erker and B. Rieger, *Dalton Transactions*, 2006, 459-467.
9. S. H. Stelzig, M. Tamm and R. M. Waymouth, *Journal of Polymer Science Part a-Polymer Chemistry*, 2008, **46**, 6064-6070.
10. D. Shoken, L. J. W. Shimon, M. Tamm and M. S. Eisen, *Organometallics*, 2016, **35**, 1125-1131.
11. D. Shoken, M. Sharma, M. Botoshansky, M. Tamm and M. S. Eisen, *Journal of the American Chemical Society*, 2013, **135**, 12592-12595.
12. S. Beer, K. Brandhorst, C. G. Hrib, X. Wu, B. Haberlag, J. Grunenberg, P. G. Jones and M. Tamm, *Organometallics*, 2009, **28**, 1534-1545.
13. S. Beer, K. Brandhorst, J. Grunenberg, C. G. Hrib, P. G. Jones and M. Tamm, *Organic Letters*, 2008, **10**, 981-984.
14. S. Beer, C. G. Hrib, P. G. Jones, K. Brandhorst, J. Grunenberg and M. Tamm, *Angewandte Chemie-International Edition*, 2007, **46**, 8890-8894.
15. S. Lysenko, C. G. Daniliuc, P. G. Jones and M. Tamm, *Journal of Organometallic Chemistry*, 2013, **744**, 7-14.
16. A. G. Trambitas, T. K. Panda and M. Tamm, *Zeitschrift Fur Anorganische Und Allgemeine Chemie*, 2010, **636**, 2156-2171.
17. T. K. Panda, A. G. Trambitas, T. Bannenberg, C. G. Hrib, S. Randoll, P. G. Jones and M. Tamm, *Inorganic Chemistry*, 2009, **48**, 5462-5472.
18. R. Kinjo, B. Donnadieu and G. Bertrand, *Angewandte Chemie-International Edition*, 2010, **49**, 5930-5933.
19. O. Back, B. Donnadieu, M. von Hopffgarten, S. Klein, R. Tonner, G. Frenking and G. Bertrand, *Chemical Science*, 2011, **2**, 858-861.
20. K. Nomura, B. K. Bahuleyan, K. Tsutsumi and A. Igarashi, *Organometallics*, 2014, **33**, 6682-6691.
21. K. Nomura, S. Patamma, H. Matsuda, S. Katao, K. Tsutsumi and H. Fukuda, *Rsc Advances*, 2015, **5**, 64503-64513.
22. K. Nomura, B. K. Bahuleyan, S. Zhang, P. M. V. Sharma, S. Katao, A. Igarashi, A. Inagaki and M. Tamm, *Inorganic Chemistry*, 2014, **53**, 607-623.
23. D. A. Dixon and A. J. Arduengo, *Journal of Physical Chemistry*, 1991, **95**, 4180-4182.
24. D. J. Cardin, Cetinkay.B and M. F. Lappert, *Chemical Reviews*, 1972, **72**, 545-+.
25. K. Ofele, W. A. Herrmann, D. Mihalios, M. Elison, E. Herdtweck, T. Priermeier and P. Kiprof, *Journal of Organometallic Chemistry*, 1995, **498**, 1-14.

26. Y. Xiong, S. L. Yao and M. Driess, *Chemistry-an Asian Journal*, 2012, **7**, 2145-2150.
27. P. H. Mueller, N. G. Rondan, K. N. Houk, J. F. Harrison, D. Hooper, B. H. Willen and J. F. Liebman, *Journal of the American Chemical Society*, 1981, **103**, 5049-5052.
28. C. Buron, H. Gornitzka, V. Romanenko and G. Bertrand, *Science*, 2000, **288**, 834-836.
29. R. W. Alder, M. E. Blake, C. Bortolotti, S. Bufali, C. P. Butts, E. Linehan, J. M. Oliva, A. G. Orpen and M. J. Quayle, *Chemical Communications*, 1999, 1049-1049.
30. P. Bazinet, G. P. A. Yap and D. S. Richeson, *Journal of the American Chemical Society*, 2003, **125**, 13314-13315.
31. R. Dach, J. H. J. Song, F. Roschangar, W. Samstag and C. H. Senanayake, *Organic Process Research & Development*, 2012, **16**, 1697-1706.
32. G. Lunn and E. B. Sansone, *Analytical Biochemistry*, 1985, **147**, 245-250.
33. J. D. Scollard, D. H. McConville, J. J. Vittal and N. C. Payne, *Journal of Molecular Catalysis a-Chemical*, 1998, **128**, 201-214.
34. T. Ochiai, D. Franz, E. Irran and S. Inoue, *Chemistry-a European Journal*, 2015, **21**, 6704-6707.
35. K. Yamamoto, C. P. Gordon, W. C. Liao, C. Coperet, C. Raynaud and O. Eisenstein, *Angewandte Chemie-International Edition*, 2017, **56**, 10127-10131.
36. S. Halbert, C. Coperet, C. Raynaud and O. Eisenstein, *Journal of the American Chemical Society*, 2016, **138**, 2261-2272.
37. M. F. Lappert and P. P. Power, *Journal of the Chemical Society-Dalton Transactions*, 1985, 51-57.
38. T. Ochiai, D. Franz, X. N. Wu and S. Inoue, *Dalton Transactions*, 2015, **44**, 10952-10956.
39. B. Wrackmeyer, in *Annual Reports on NMR Spectroscopy*, Academic Press, 2002, vol. 47, pp. 1-37.
40. B. Wrackmeyer and K. Horchler, in *Annual Reports on NMR Spectroscopy*, ed. G. A. Webb, Academic Press, 1990, vol. 22, pp. 249-306.
41. B. Wrackmeyer, K. Horchler, H. Zhou and M. Veith, *Zeitschrift Fur Naturforschung Section B-a Journal of Chemical Sciences*, 1989, **44**, 288-292.
42. M. J. Taylor, E. J. Coakley, M. P. Coles, H. Cox and J. R. Fulton, *Organometallics*, 2015, **34**, 2515-2521.

Chapter 6

Coordination Chemistry and Reactivity of Heavier Group 14 Element Compounds Featuring Bulky Anionic Guanidinato Ligands

---

6.1 Introduction

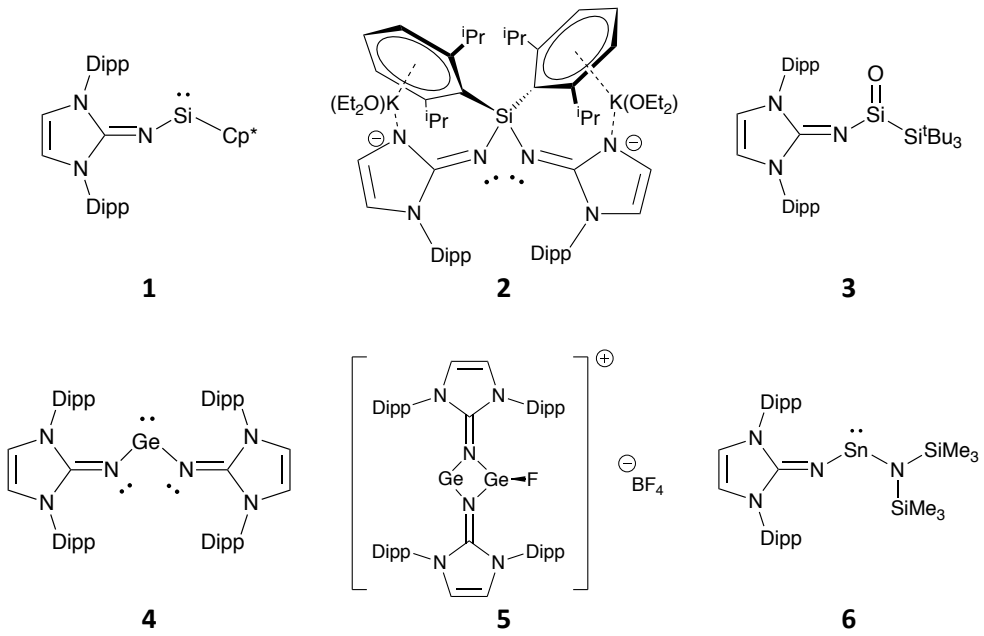


Figure 6-1: Selected complexes of group 14 elements featuring guanidinato ligands.

In recent years, research into the use of guanidinato ligands has been extended into main group chemistry, with the groups of Inoue and Rivard being major contributors. The first reported main group compound featuring a guanidinato ligand (**1**; Figure 6-1) was an acyclic silylene compound stabilized by a bulky, strongly electron donating guanidinato ligand.[1] Rivard and his co-workers mirrored the research of Inoue, attempting to support a

genuinely two-coordinate silicon centre through the use of two guanidinato ligands. However, this attempt led to reductive cleavage of the N-bound aryl groups, with accompanying transfer to the silicon centre (**2**; Figure 6-1).[2] Further applications of such guanidinato ligands in silicon systems were reported by Inoue et al. in 2017. In these reports, the π-donating guanidinato ligand has been shown to be capable of supporting a silanone (**3**; Figure 6-1)[3] and even a silicon-silicon double bond.[4] More recent research has also moved further down group 14 to germanium (e.g. **4** and **5**; Figure 6-1)[2, 5, 6] and tin (e.g. **6**; Figure 6-1)[7-9].

Despite these initial reports, the coordination chemistry of guanidinato ligands with heavier group 14 elements (especially Sn and Pb) remains relatively unexplored, with only one example for tin reported by Inoue, and none for lead. In addition, the application of expanded-ring guanidinato systems (as reported in chapter 5) in group 14 compounds would offer instructive and systematic comparison of the behaviour of this ligand family in main group chemistry. With these thoughts in mind, the work outlined in this chapter aims to explore the coordination chemistry of guanidinato ligands with tin and lead. In carrying out these studies a rare example of C-H activation at a lead centre was uncovered.

6.2 Experimental

Synthesis of ***Sn{N(SiMe$_3$)$_2$}(5g), 7:***

Sn{N(SiMe$_3$)$_2$}$_2$ (0.04 g, 0.09 mmol) and one equiv. of **5g-H** (0.04 g, 0.09 mmol) were mixed in a J. Young's NMR tube and dissolved in *d*$_6$-benzene. In situ NMR monitoring indicated that conversion was completed within 30 min at room temperature. Volatiles were

removed *in vacuo*, and the product extracted into pentane; drying *in vacuo* yielded a spectroscopically pure orange oil. Yield: 0.06 g, 92 %.

Spectroscopic data for ***Sn{N(SiMe$_3$)$_2$}(5g), 7:***

^{1}H NMR (400 MHz, benzene-d_6) δ 7.23 – 7.12 (m, 6H, *Ar-H*), 3.52 (s, 4H, *backbone CH$_2$*), 3.37 (sept, $^3J_{HH}$ = 6.9 Hz, 4H, *CHMe$_2$*), 1.41 (d, $^3J_{HH}$ = 6.8 Hz, 12H, *CH$_3$*), 1.22 (d, $^3J_{HH}$ = 6.9 Hz, 12H, *CH$_3$*), 0.15 (s, 18H, Si*(CH$_3$)$_3$*). **^{13}C NMR{^{1}H}** (101 MHz, benzene-d_6) δ 157.5 (*NCN*), 149.2 (*ipso-C*), 136.5 (*o-C*), 128.9 (*p-C*), 124.6 (*m-C*), 48.0 (*backbone CH$_2$*), 28.9 (*CHMe$_2$*), 25.5 (*CH$_3$*), 24.5 (*CH$_3$*), 5.9 (*TMS-C*). **^{119}Sn NMR** (187 MHz, benzene-d_6) δ 560. Reproducible elemental analysis could not obtained as the product is an oil.

Synthesis of ***Sn{N(SiMe$_3$)$_2$}(6g), 8:***

Sn{N(SiMe$_3$)$_2$}$_2$ (0.04 g, 0.09 mmol) and one equiv. of **6g-H** (0.038 g, 0.09 mmol) were mixed in a J. Young's NMR tube and dissolved in d_6-benzene (0.5 mL). The sample was heated for 2 h at 80°C, and volatiles then removed *in vacuo*. The product was extracted into pentane (1 mL) and the solvent then evaporated, yielding a spectroscopically pure orange oil. Yield: 0.06 g, 90 %.

Spectroscopic data for ***Sn{N(SiMe$_3$)$_2$}(6g), 8****:*

^{1}H NMR (400 MHz, benzene-d_6) δ 7.18 – 7.07 (m, 6H, *Ar-H*), 3.41 (t, $^3J_{HH}$ = 5.7 Hz, 4H, *CH$_2$N*), 3.33 (sept, $^3J_{HH}$ = 6.7 Hz, 4H, *CHMe$_2$*), 1.78 (p, $^3J_{HH}$ = 6.0 Hz, 2H, *backbone CH$_2$*), 1.42 (d, $^3J_{HH}$ = 6.9 Hz, 12H, *CH$_3$*), 1.21 (d, $^3J_{HH}$ = 6.9 Hz, 12H, *CH$_3$*), 0.06 (s, 18H, Si*(CH$_3$)$_3$*). **^{13}C NMR{^{1}H}** (101 MHz, benzene-d_6) δ 153.5 (*NCN*), 147.5 (*ipso-CH*), 141.4 (*o-CH*), 128.4 (*p-CH*), 124.8 (*m-CH*), 50.9 (*backbone CH$_2$N*), 28.9 (*CHMe$_2$*), 25.7 (*backbone CH$_2$*), 24.5 (*CH$_3$*), 23.8 (*CH$_3$*), 5.8 (*TMS-C*). **^{119}Sn NMR** (187 MHz, benzene-d_6) δ 426. Reproducible elemental analysis could not obtained as the product is an oil.

Synthesis of ***Sn{N(SiMe$_3$)$_2$}(7g), 9:***

Sn{N(SiMe$_3$)$_2$}$_2$ (0.04 g, 0.09 mmol) and one equiv. of **7g-H** (0.04 g, 0.09 mmol) were mixed in a J. Young's NMR tube and dissolved in d_6-benzene (0.5 mL). The solution was heated to 80°C for 2 d, then volatiles removed *in vacuo* and the product extracted into pentane (1 mL). **6** was obtained as single crystals suitable for X-ray crystallography by the slow evaporation of solvent from a pentane solution (yield: 0.053 g, 83 %).

Spectroscopic data for ***Sn{N(SiMe$_3$)$_2$}(7g), 9:***

^{1}H NMR (400 MHz, benzene-d_6) δ 7.20-7.10 (m, 6H, *Ar-H*), 3.63 (t, $^3J_{HH}$ = 8.5 Hz, 4H, *backbone CH$_2$N*), 3.40 (t, $^3J_{HH}$ = 6.3 Hz, 4H, *CHMe$_2$*), 1.52 (t, $^3J_{HH}$ = 5.1 Hz, 4H, *backbone CH$_2$CH$_2$*), 1.39 (d, $^3J_{HH}$ = 6.8 Hz, 12H, *CH$_3$*), 1.20 (d, $^3J_{HH}$ = 6.9 Hz, 12H, *CH$_3$*), 0.29 (s, 18H, Si*(CH$_3$)$_3$*). **^{13}C NMR{^{1}H}** (101 MHz, benzene-d_6) δ 158.6 (*NCN*), 147.3 (*o-C*), 144.5 (*ipso-C*), 128.6 (*p-C*), 125.3 (*m-C*), 55.8 (*backbone- CH$_2$N*), 28.9 (*CHMe$_2$*), 28.8 (*backbone -CH$_2$CH$_2$*), 25.6 (*CH$_3$*), 24.9 (*CH$_3$*), 5.9 (*TMS-C*), 5.8 (*TMS-C*). **^{119}Sn NMR** (187 MHz, benzene-d_6) δ 317. Elemental Analysis does not meet standard with percentage of C lower than expected after a few attempts.

Crystallographic data for ***Sn{N(SiMe$_3$)$_2$}(7g), 9:***

$C_{35}H_{60}N_4Si_2Sn$, M_r = 711.75, Monoclinic, *P 2$_1$/n*, a = 10.63900(10), b = 17.5355(2), c = 21.1814(2) Å, α = 90°, β = 103.2115(12)°, γ = 90°, V = 3847.02(7) Å^3, Z = 4, ρ_c = 1.229 Mg m^{-3}, T = 150 K, λ = 1.54184 Å, 46816 reflections collected, 8017 independent [R(int) = 0.038], which were used in all calculations. R_1 = 0.0346, wR_2 = 0.0904 for observed unique reflections [I > 2σ(I)] and R_1 = 0.0357, wR_2 = 0.0918 for all unique reflections. Max. and min. residual electron densities 0.81 and -0.62 e Å^{-3}.

Synthesis of ***[Sn{N(SiMe$_3$)$_2$}(Ig)]Mo(CO)$_5$, 10****:*

Sn{N(SiMe$_3$)$_2$}(Ig) (0.055 g, 0.08 mmol) and one equiv. of Mo(CO)$_6$ (0.021 g, 0.08 mmol) were mixed in a J. Young's NMR tube in d_6-benzene and irradiated for 1h. Evaporation of the solvent followed by extraction in pentane and crystallization by slow evaporation led to the formation of the desired product as orange, spectroscopically pure, X-ray quality crystals. Yield: 0.07 g, 91 %.

Spectroscopic data for ***[Sn{N(SiMe$_3$)$_2$}(Ig)]Mo(CO)$_5$, 10****:*

^{1}H NMR (400 MHz, benzene-d_6) δ 7.21 – 7.16 (m, 2H, *p*-C*H*), 7.12 (d, $^3J_{HH}$ = 7.2 Hz, 4H, *m*-C*H*), 6.03 (s, 2H, *backbone CH*), 3.10 (sept, $^3J_{HH}$ = 6.9 Hz, 4H, C*H*Me$_2$), 1.44 (d, $^3J_{HH}$ = 6.8 Hz, 12H, CH$_3$), 1.12 (d, $^3J_{HH}$ = 6.8 Hz, 12H, CH$_3$), 0.06 (s, 18H, Si(CH$_3$)$_3$). **^{13}C NMR{^{1}H}** (101 MHz, benzene-d_6) δ 211.7 (*CO trans to Sn*), 206.7 (*CO cis to Sn*), 150.6 (N*C*N), 147.6 (*ipso*-*C*), 133.9 (*o*-*C*), 129.9 (*p*-*C*), 124.4 (*m*-*C*), 115.5 (*backbone CH*), 28.9 (*C*HMe$_2$), 25.1 (*C*H$_3$), 23.9 (*C*H$_3$), 4.6 (*TMS*-*C*). **^{119}Sn NMR** (187 MHz, benzene-d_6) δ 508. **Elemental analysis:** Expected: C, 49.73; H, 5.93; N, 6.11 Measured: C, 47.32; H, 5.19; N, 5.78. **IR** (KBr disk/cm^{-1}): ν(CO) 2068, 1947.

Crystallographic data for ***[Sn{N(SiMe$_3$)$_2$}(Ig)]Mo(CO)$_5$, 10****:*

$C_{38}H_{54}MoN_4O_5Si_2Sn$, M_r = 917.68, Monoclinic, *P 2$_1$/n*, a = 15.1225(2), b = 17.3010(2), c = 16.5696(2) Å, α = 90°, β = 91.3619(10)°, γ = 90°, V = 4333.95(9) Å^3, Z = 4, ρ_c = 1.406 Mg m^{-3}, T = 150 K, λ = 1.54180 Å, 25390 reflections collected, 8911 independent [R(int) = 0.026], which were used in all calculations. R_1 = 0.0251, wR_2 = 0.0640 for observed unique reflections [I > 2σ(I)] and R_1 = 0.0277, wR_2 = 0.0663 for all unique reflections. Max. and min. residual electron densities 0.52 and -1.17 e Å^{-3}.

Synthesis of ***[Sn{N(SiMe$_3$)$_2$}(5g)]Mo(CO)$_5$, 11****:*

Sn{N(SiMe$_3$)$_2$}(5g) (0.06 g, 0.09 mmol) and one equiv. of Mo(CO)$_6$ (0.023 g, 0.09 mmol) were mixed together in a J. Young's NMR tube and dissolved in d_6-benzene. The sample was irradiated for 1 h, after which the solvent was removed *in vacuo* and the product into pentane. Crystallisation by slow solvent evaporation yielded spectroscopically pure orange crystals. Yield: 0.08 g, 94 %.

Spectroscopic data for ***[Sn{N(SiMe$_3$)$_2$}(5g)]Mo(CO)$_5$, 11****:*

^{1}H NMR (400 MHz, Benzene-d_6) δ 7.19 (dd, *J* = 7.0, 1.5 Hz, 2H, *p*-C<u>H</u>), 7.11 (d, *J* = 6.6 Hz, 4H, *m*-C<u>H</u>), 3.46 (s, 4H, *backbone* C<u>H</u>$_2$), 3.35 (sept, *J* = 6.8 Hz, 4H, C<u>H</u>Me$_2$), 1.48 (d, *J* = 6.8 Hz, 12H, C<u>H</u>$_3$), 1.17 (d, *J* = 6.8 Hz, 12H, C<u>H</u>$_3$), 0.03 (s, 18H, Si(C<u>H</u>$_3$)$_3$). **^{13}C NMR{^{1}H}** (101 MHz, Benzene-d_6) δ 211.8 (<u>C</u>O- *trans to Sn*), 206.7 (<u>C</u>O- *cis to Sn*), 157.5 (N<u>C</u>N), 149.3 (*ipso*-<u>C</u>), 137.6 (*o*-<u>C</u>), 129.1 (*p*-<u>C</u>), 124.6 (*m*-<u>C</u>), 48.4 (*backbone* <u>C</u>H$_2$), 28.8 (<u>C</u>H$_2$Me$_2$), 25.8 (<u>C</u>H$_3$), 24.9 (<u>C</u>H$_3$), 4.7 (*TMS*-<u>C</u>). **IR** (KBr disk / cm^{-1}): ν(CO) 1933.7, 2064.3.

Synthesis of ***Sn(Ig)$_2$, 12****:*

Sn{N(SiMe$_3$)$_2$}$_2$ (0.1 g, 0.23 mmol) and two equiv. of **Ig-H** (0.19 g, 0.46 mmol) were mixed in a J. Young's NMR tube and dissolved in d_6-benzene. The reaction mixture was then heated for 2 d at 80°C, before volatiles were removed *in vacuo.* The product was extracted into pentane and crystallised from pentane by slow diffusion, yielding orange crystals suitable for X-ray crystallography. Yield: 67 mg, 32%.

Spectroscopic data for ***Sn(Ig)$_2$, 12****:*

^{1}H NMR (400 MHz, benzene-d_6) δ 7.25 (t, $^3J_{HH}$ = 7.7 Hz, 4H, *p*-C<u>H</u>), 7.12 (d, $^3J_{HH}$ = 7.7 Hz, 8H, *m*-C<u>H</u>), 5.98 (s, 4H, *backbone* C<u>H</u>), 3.15 (sept, $^3J_{HH}$ = 6.9 Hz, 8H, C<u>H</u>Me$_2$), 1.20 (d, $^3J_{HH}$ = 4.1 Hz, 24H, C<u>H</u>$_3$), 1.18 (d, $^3J_{HH}$ = 4.5 Hz, 24H, C<u>H</u>$_3$). **^{13}C NMR{^{1}H}** (101 MHz, benzene-d_6) δ 148.5 (N<u>C</u>N), 148.2 (*ipso*-<u>C</u>), 134.9 (*o*-<u>C</u>), 128.7 (*p*-<u>C</u>), 123.9 (*m*-<u>C</u>), 113.0 (*backbone* <u>C</u>H), 28.6

(*C*HMe$_2$), 24.3 (*C*H$_3$), 23.3 (*C*H$_3$). **^{119}Sn NMR** (187 MHz, benzene-d_6) δ 459. Elemental Analysis does not meet standard with percentage of C lower than expected after a few attempts.

Crystallographic data for ***Sn(Ig)$_2$, 12****:*

$C_{54}H_{72}N_6Sn$, M_r = 923.89, Monoclinic, *P 2$_1$/c*, a = 31.2443(10), b = 12.7274(4), c = 29.4751(9) Å, α = 90°, β = 117.823(4)°, γ = 90°, V = 10366.0(7) Å^3, Z = 8, ρ_c = 1.184 Mg m^{-3}, T = 150 K, λ = 1.54180 Å, 62862 reflections collected, 21460 independent [R(int) = 0.035], which were used in all calculations. R_1 = 0.0552, *w*R_2 = 0.1251 for observed unique reflections [I > 2σ(I)] and R_1 = 0.0758, *w*R_2 = 0.1431 for all unique reflections. Max. and min. residual electron densities 0.75 and -0.99 e Å^{-3}.

In situ generation of ***Pb{N(SiMe$_3$)$_2$}(Ig), 13****:*

Pb{N(SiMe$_3$)$_2$}$_2$ (0.05 g, 0.09 mmol) and one equiv. of **Ig-H** (0.0382 g, 0.09 mmol) were mixed in a J. Young's NMR tube and dissolved in *d$_6$*-benzene. Conversion was completed within 30 min at room temperature. The product was formed quantitatively (as determined by NMR measurements) and was characterised in situ.

Spectroscopic data for ***Pb{N(SiMe$_3$)$_2$}(Ig), 13****:*

^{1}H NMR (400 MHz, benzene-d_6) δ 7.19 (dd, $^3J_{HH}$ = 8.8, 6.5 Hz, 2H, *p*-C*H*), 7.14 – 7.10 (m, 4H, *m*-C*H*), 6.19 (s, 2H, *backbone CH*), 3.19 (sept, $^3J_{HH}$ = 6.9 Hz, 4H, C*H*Me$_2$), 1.33 (d, $^3J_{HH}$ = 6.9 Hz, 12H, C*H*$_3$), 1.16 (d, $^3J_{HH}$ = 6.9 Hz, 12H, C*H*$_3$), 0.19 (s, 18H, Si(C*H*$_3$)$_3$). **^{13}C NMR** (101 MHz, benzene-d_6) δ 150.6 (N*C*N), 147.6 (*ipso*-*C*), 133.9 (*o*-*C*), 129.9 (*p*-*C*), 124.4 (*m*-*C*), 115.6 (*backbone CH*), 28.9 (*C*HMe$_2$), 25.1 (*C*H$_3$), 23.9 (*C*H$_3$), 4.6 (*TMS*-*C*). **^{207}Pb-NMR:** (104 MHz, Benzene-d_6) δ = 4710

In situ generation of ***Pb{N(SiMe$_3$)$_2$}(5g), 14****:*

Pb{N(SiMe$_3$)$_2$}$_2$ (0.05 g, 0.09 mmol) and one equiv. of **5g-H** (0.04 g, 0.09 mmol) were mixed in a J. Young's NMR tube and dissolved in d_6-benzene. Quantitative conversion occurs at room temperature overnight and the product was characterised *in situ*.

Spectroscopic data for ***Pb{N(SiMe$_3$)$_2$}(5g), 14****:*

^{1}H NMR: (400 MHz, Benzene-d_6) = δ = 7.22 – 7.17 (m, 2H, *p*-C<u>H</u>), 7.12 – 7.08 (m, 4H, *m*-C<u>H</u>), 3.58 (s, 4H, *N*-C<u>H$_2$</u>) 3.36 (sept, $^3J_{HH}$ = 6.9 Hz, 4H, C<u>H</u>Me$_2$), 1.37 (d, $^3J_{HH}$ = 6.9 Hz, 12H, C<u>H$_3$</u>), 1.27 (d, $^3J_{HH}$ = 6.9 Hz, 12H, C<u>H$_3$</u>), 0.16 (s, 12H, Si(C<u>H$_3$</u>)$_3$). **^{13}C NMR{^{1}H}** (101 MHz, benzene-d_6) δ 156.5 (N<u>C</u>N), 149.3 (*ipso*-<u>C</u>), 137.0 (*o*-<u>C</u>), 128.9 (*p*-<u>C</u>), 124.7 (*m*-<u>C</u>), 48.2 (*backbone* <u>C</u>H), 28.7 (<u>C</u>HMe$_2$), 25.3 (<u>C</u>H$_3$), 24.6 (<u>C</u>H$_3$), 6.2 (*TMS*-<u>C</u>) **^{207}Pb-NMR**: (104 MHz, Benzene-d_6) δ = 4476.

Synthesis of ***Pb$_2$(Ig)$_2${N(SiMe$_3$)$_2$Si(CH$_3$)$_2$CH$_2$}, 15****:*

Pb{N(SiMe$_3$)$_2$}$_2$ (0.05 g, 0.09 mmol) and one equiv. of **Ig-H** (0.04 g, 0.09 mmol) were mixed in a J. Young's NMR tube and dissolved in d_6-benzene (0.5 mL). The reaction mixture was then heated for 24 h at 80°C, before volatiles were removed *in vacuo.* The product was extracted into pentane (1 mL) and purified via slow solvent evaporation, yielding dark red crystals suitable for X-ray crystallography. Yield: 0.05 g, 72 %.

Spectroscopic data ***Pb$_2$(Ig)$_2${N(SiMe$_3$)$_2$Si(CH$_3$)$_2$CH$_2$}, 15****:*

^{1}H NMR (400 MHz, benzene-d_6) δ 7.16 (broad s, 4H, *p*-C<u>H</u>), 7.10 – 7.01 (m, 8H, *m*-C<u>H</u>), 5.87 (s, 4H, *backbone* C<u>H</u>), 3.34 (broad s, 4H, C<u>H</u>Me$_2$), 3.13 (sept, $^3J_{HH}$ = 6.4 Hz, 4H, C<u>H</u>Me$_2$), 1.53 – 1.44 (m, 12H, C<u>H$_3$</u>), 1.40 (d, $^3J_{HH}$ = 6.8 Hz, 12H, C<u>H$_3$</u>), 1.19 – 1.05 (m, 24H, C<u>H$_3$</u>), 0.63 (s, 6H, Si(C<u>H$_3$</u>)$_2$), 0.20 (s, 9H, *TMS*-<u>H</u>), -1.16 (s, 2H, PbC<u>H$_2$</u>). **^{13}C NMR{^{1}H}** (101 MHz, benzene-d_6) δ 161.32 (N<u>C</u>N) 147.6 (*ipso*-<u>C</u>) 143.8 (*o*-<u>C</u>H), 129.6 (*p*-<u>C</u>H), 124.6 (*m*-<u>C</u>H), 76.6 (*backbone* <u>C</u>H),

28.6 (*C*HMe$_2$), 25.8 (*C*H$_3$), 23.4 (*C*H$_3$), 22.8 (Pb*C*H$_2$), 13.1 (Si(*C*H$_3$)$_2$), 7.3 (TMS-*C*).^{207}**Pb-NMR:** (104 MHz, Benzene-d_6) δ 2790 (N*Pb*N$_2$), 3550 (C*Pb*N$_2$) . **Elemental Analysis:** calc.: C, 52.35; H, 6.72; N, 6.86; meas.: C, 52.39; H, 6.62; N, 6.95.

Crystallographic data for ***Pb$_2$(Ig)$_2${N(SiMe$_3$)$_2$Si(CH$_3$)$_2$CH$_2$}, 15****:*

$C_{65}H_{99.75}N_7Pb_2Si_2$, M_r = 1449.87, Monoclinic, *Cc*, a = 16.4104(2), b = 19.3524(2), c = 20.7030(2) Å, α = 90°, β = 95.9432(8)°, γ = 90°, V = 16539.53(12) Å^3, Z = 4, ρ_c = 1.473 Mg m^{-3}, T = 150 K, λ = 1.54180 Å, 21252 reflections collected, 7972 independent [R(int) = 0.043], which were used in all calculations. R_1 = 0.0404, wR_2 = 0.1040 for observed unique reflections [I > 2σ(I)] and R_1 = 0.0409, wR_2 = 0.1050 for all unique reflections. Max. and min. residual electron densities 4.30 and -1.38 e Å^{-3}.

Synthesis of ***Pb$_2$(5g)$_2${N(SiMe$_3$)$_2$Si(CH$_3$)$_2$CH$_2$}, 16****:*

Pb(N(SiMe$_3$)$_2$)$_2$ (0.05 g, 0.09 mmol) and one equiv. of **5g-H** (0.04 g, 0.09 mmol) were mixed in a J. Young's NMR tube and dissolved in d_6-benzene (0.5 mL). The reaction mixture was then heated for 2 h at 80°C, before volatiles were removed *in vacuo.* The product was extracted into pentane (1 mL) and volatiles were removed *in vacuo* to yield a spectroscopically pure red solid. Yield: 0.04 g, 60 %.

Spectroscopic data for ***Pb$_2$(Ig)$_2${N(SiMe$_3$)$_2$Si(CH$_3$)$_2$CH$_2$}, 16****:*

^{1}H NMR (500 MHz, benzene-d_6) δ 7.16 (broad s, 4H, *p*-C*H*), 7.11 – 7.00 (m, 8H, *m*-C*H*), 3.47 (s, 8H, *backbone* C*H*$_2$), 3.34 (broad s, 4H, C*H*Me$_2$), 3.22 (sept, $^3J_{HH}$ = 6.4 Hz, 4H, C*H*Me$_2$), 1.53 – 1.46 (m, 12H, C*H*$_3$), 1.44 (d, $^3J_{HH}$ = 6.8 Hz, 12H, C*H*$_3$), 1.20 – 1.05 (m, 24H, C*H*$_3$), 0.51 (s, 6H, Si(C*H*$_3$)$_2$), 0.25 (s, 9H, Si(C*H*$_3$)$_3$), -1.36 (s, 2H, PbC*H*$_2$). **^{13}C NMR{^{1}H}** (126 MHz, benzene-d_6) δ 159.6 (N*C*N) 148.9 (*ipso*-*C*) 138.8 (*o*-*C*H), 128.3 (*p*-*C*H), 125.2 (*m*-*C*H), 50.5 (*backbone* *C*H$_2$),

29.3 (*C*HMe$_2$), 26.6 (*C*H$_3$), 25.0 (*C*H$_3$), 24.2 (Pb*C*H$_2$), 13.36 (Si(*C*H$_3$)$_2$), 7.31 (TMS-*C*).^{207}**Pb-NMR:** (104 MHz, Benzene-d_6) δ 2800 (N*Pb*N$_2$), 3480 (C*Pb*N$_2$) .

6.3 Synthesis of Guanidinato Complexes of Tin and Germanium

6.3.1 Synthesis of systems of the type Sn{N(SiMe$_3$)$_2$}(Lg)

Using the methodology reported by Inoue we targeted analogues of **Sn{N(SiMe$_3$)$_2$}(Ig)** (**6**) by making use of our new protio-ligands, **5g-H**, **6g-H** and **7g-H** (Figure 6-2).

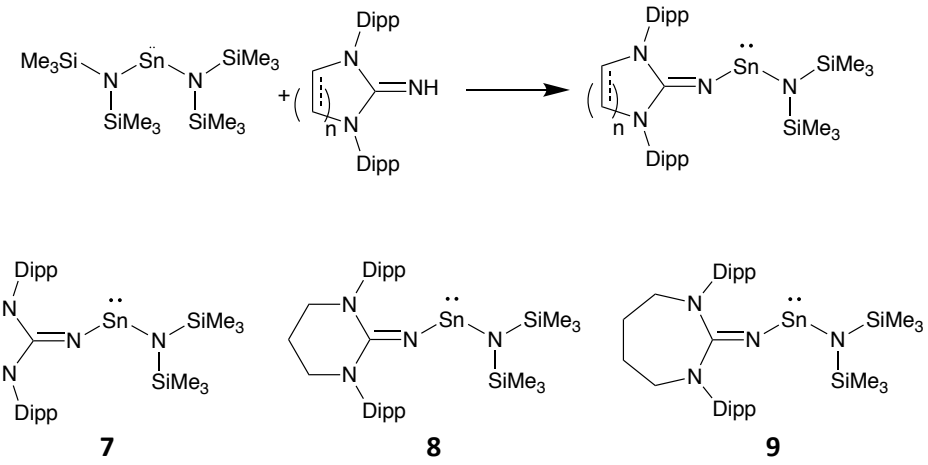


*Figure 6-2: Syntheses of **6**, **7**, **8** and **9** (upper); numbering scheme for the new compounds **7**, **8** and **9** (lower).*

The syntheses of systems of the type **Sn{N(SiMe$_3$)$_2$}(Lg)** (i.e. compounds **6**, **7**, **8** and **9**) are straightforward: Sn{N(SiMe$_3$)$_2$}$_2$ was dissolved in benzene and added to a solution containing one equivalent of ligand **Lg-H**. The reaction time strongly depends on the size of the heterocycle ring, varying from less than 1 h (for **Lg** = **Ig** or **5g**) to 2 d (for **Lg** = **7g**). Monitoring the ^{1}H NMR spectra *in situ* reveals, in each case, growth of the signal

corresponding to $HN(SiMe_3)_2$ (in benzene-d_6, δ = 0.10), together with the signal corresponding to the $SiMe_3$ group of the respective product (in benzene-d_6, **6**: δ = 0.19,[7] **7**: δ = 0.15, **8**: δ = 0.06, **9**: δ = 0.29; more details in Table 6-1); the signal corresponding to $Sn\{N(SiMe_3)_2\}_2$ (in benzene-d_6, δ = 0.30) shows a complementary decrease in intensity over the same timeframe. This observation is consistent with the substitution of $[N(SiMe_3)_2]^-$ by **[Lg]**$^-$, and the release of $HN(SiMe_3)_2$.

*Table 6-1: ^{1}H NMR comparisons between **6**, **7**, **8** and **9**, (all spectra obtained for solution in benzene-*d_6*).*

6[7]	Multiplicity	δ	Relative Intensity	**7**	Multiplicity	δ	Relative Intensity
Ar-H	multiplet	7.26-7.10	6H	Ar-H	multiplet	7.23-7.11	6H
Backbone CH	singlet	6.10	2H	Backbone CH_2	singlet	3.52	4H
$CHMe_2$	septet	3.18	4H	$CHMe_2$	septet	3.37	4H
CH_3	doublet	1.37	12H	CH_3	doublet	1.41	12H
	doublet	1.16	12H		doublet	1.22	12H
$[N(Si(CH_3)_3)_2]$	singlet	0.19	18H	$[N(Si(CH_3)_3)_2]$	singlet	0.15	18H
8	Multiplicity	δ	Relative Intensity	**9**	Multiplicity	δ	Relative Intensity
Ar-H	multiplet	7.18-7.07	6H	Ar-H	multiplet	7.20-7.10	6H
CH_2N	triplet	3.41	4H	CH_2N	triplet	3.36	4H
Backbone CH_2	quintet	1.78	2H	Backbone CH_2	triplet	1.52	4H
$CHMe_2$	septet	3.33	4H	$CHMe_2$	septet	3.40	4H
CH_3	doublet	1.42	12H	CH_3	doublet	1.39	12H
	doublet	1.21	12H		doublet	1.20	12H
$[N(Si(CH_3)_3)_2]$	singlet	0.06	18H	$[N(Si(CH_3)_3)_2]$	singlet	0.29	18H

Table 6-1 lists full details of ^{1}H NMR resonances of all four stannylenes, which show very similar patterns of signals. Compared to stannylene **6** reported by Inoue, the major differences, not surprisingly, relate to the saturated heterocycle backbone (**6**: δ = 6.10,[7] **7**: δ = 3.52, **8**: δ = 3.41 and δ = 1.78, **9**: δ = 3.36 and δ = 1.52). The similarities in their ^{1}H NMR spectra (and in their respective ^{119}Sn signals – as outlined below) are consistent with similar

structural features among the four stannylenes. That said, we were unable to obtain structural data for either **7** or **8** since they are isolated in the form of an oil. In the case of **9**, single crystals suitable for X-ray crystallography could be obtained and the crystal structure is shown in Figure 6-3. The molecular structure of **9** obtained experimentally is consistent with the results of DFT geometry optimization (Table 6-2), which gives confidence that the theoretical methodology is compatible with the stannylene systems being studied in this chapter.

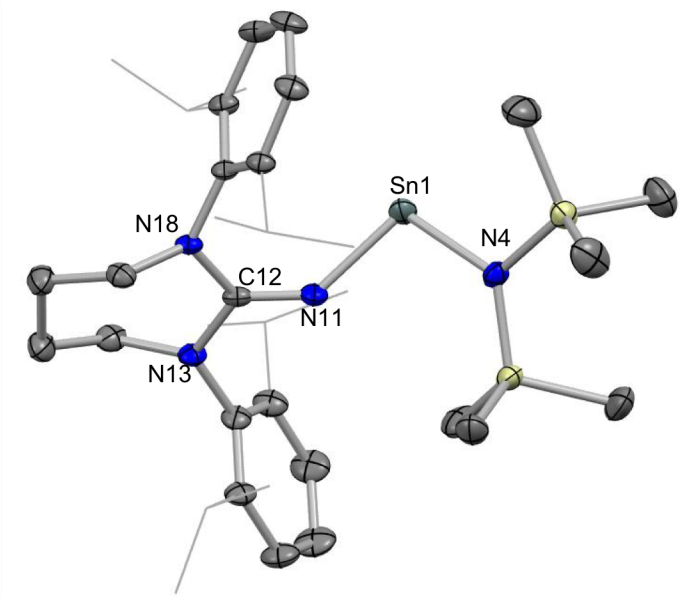


*Figure 6-3: X-ray crystal structure of **9** with H atoms omitted and Dipp groups shown in wireframe format for clarity. Thermal ellipsoids set at 50% probability level. Key bond lengths and angles: d(Sn1-N11) = 2.0237(16) Å, d(Sn1-N4) = 2.1119(16) Å, d(C12=N11) = 1.273(3) Å, ∠N11Sn1N4 = 101.58(6)°, ∠Sn1N11C12 = 138.18(13)°, ∠N18CN13 = 112.64(16)°.*

*Table 6-2: Selected geometric data of **9** (both experimental and theoretical).*

	9 (expt.)	**9** (calc.)
∠N11Sn1N4 (°)	101.58(6)	104.1
∠Sn1N11C12 (°)	138.18(13)	137.5
d(Sn1-N11) (Å)	2.0237(16)	2.060
d(Sn1-N4) (Å)	2.1119(16)	2.161
d(C12=N11) (Å)	1.273(3)	1.289

6.3.2 ^{119}Sn NMR chemical shifts of compounds of the type Sn{N(SiMe$_3$)$_2$}(Lg)

This series of stannylene compounds of the generic form **Sn{N(SiMe$_3$)$_2$}(Lg)** have similar composition, albeit featuring different guanidinato ligands, and therefore offer a convenient platform to probe the electronic properties of these ligands in main group systems through ^{119}Sn NMR spectroscopy.

*Table 6-3: ^{119}Sn NMR chemical shifts and key results from DFT calculations on compounds **6**, **7**, **8** and **9**.*

stannylene	6	7	8	9
Guanidinato ligand	[Ig]$^-$	[5g]$^-$	[6g]$^-$	[7g]$^-$
^{119}Sn δ (ppm)	580	560	426	317
HOMO-LUMO gap (kJ mol^{-1})	220	237	245	256
LUMO (kJ mol^{-1})	-193	-190	-207	-202
HOMO (kJ mol^{-1})	-413	-427	-452	-458
Sn-N(ligand) distance (Å)	2.071	2.061	2.058	2.060
Sn-N(SiMe$_3$)$_2$ distance (Å)	2.143	2.142	2.157	2.161
NSnN angle(°)	95.8	96.7	103.1	104.1
NCN angle (°)	102.8	105.6	114.7	115.3
Si-N-Sn-N torsion angle (°)	29	25	40	36
Sn-N-C-N torsion angle (°)	36	28	57	50

Table 6-3 lists the ^{119}Sn NMR chemical shifts of the four stannylenes and reveals a trend of decreasing chemical shift from **6** to **9**, which appears to run contrary to conclusions reached in chapter 5. It was concluded that the donor strength of **[6g]**$^-$ is the highest among the four systems of the type **[Lg]**$^-$. On this basis, stannylene **8** would be expected to have the highest degree of electron density donated to the Sn centre. The enhanced donor strength of **[6g]**$^-$ should therefore provide the strongest shielding of the Sn centre and stannylene **8** should therefore have the lowest ^{119}Sn NMR chemical shift. Experimentally, however, stannylene **9** has the lowest ^{119}Sn NMR chemical shift being > 100 ppm lower than that of **8**.

In fact, the shielding parameter has two main components, the diamagnetic and paramagnetic contributions (where $\sigma = \sigma_{dia} + \sigma_{para}$). The diamagnetic contribution depends on local electron density, which is affected by nearby electron donating/withdrawing groups; the paramagnetic contribution on the other hand, dominates the variation in the chemical shift of non-proton nuclei and depends strongly on the HOMO-LUMO gap of the molecule .[10, 11] A smaller HOMO-LUMO gap (e.g. between the σ and π* orbitals of a Fischer carbene) allows for better coupling between the two frontier orbitals and increases the magnitude of σ_{para}.

In the case of the stannylene systems **Sn{N(SiMe$_3$)$_2$}(Lg)**, the frontier orbitals are superficially similar to those of a carbene, and the HOMO-LUMO gap should therefore also play a significant role in influencing the ^{119}Sn NMR chemical shift. Table 6-3 summarises the results of DFT calculations carried out on **6**, **7**, **8** and **9**, and indeed shows that the HOMO-LUMO gap increases from **6** to **9**, matching the trend in the ^{119}Sn NMR chemical shifts.

The magnitude of the HOMO-LUMO gap naturally depends on the energies of both the HOMO and LUMO. By taking a closer look at Table 6-3, the most marked differences in terms of both the HOMO and LUMO energies appears to fall between stannylenes **6** and **7** (which feature a 5-membered heterocyclic ring) and compounds **8** and **9** featuring larger 'expanded' heterocycles.

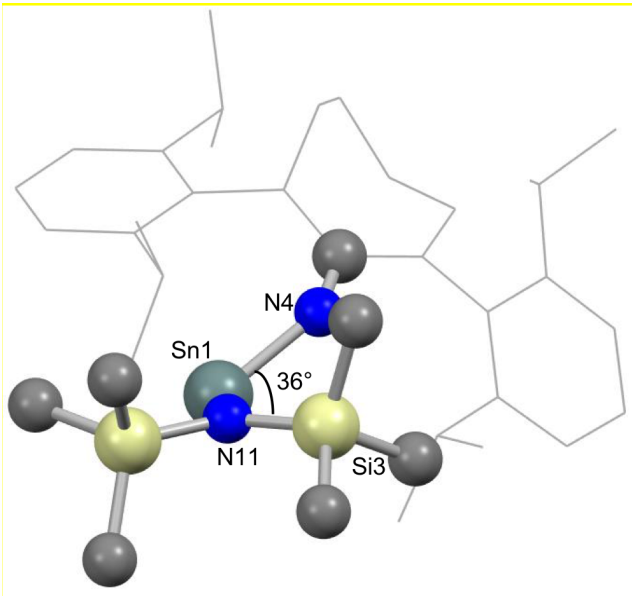


*Figure 6-4: The defined Si-N-Sn-N torsion angle, with stannylene **9** as an example.*

As detailed in Table 6-3, the LUMOs of **8**/**9** are less destabilised compared to those of **6**/**7** (by ca. 10 kJ mol^{-1}). This is largely due to differences in the Si-N-Sn-N torsion angles (as depicted in Figure 6-4), which are 29°/25°(for **6** and **7**) and 40°/36°(for **8** and **9**). As the Si-N-Sn-N torsion angle increases from 0° to 90°, the π orbital overlap between the Sn centre and the $N(SiMe_3)_2$ group become less effective. The weakening of this π interaction is also reflected in elongation of the calculated Sn-N_{Si} distance: **6**/**7**: 2.143 and 2.142 Å; **8**/**9**: 2.157 and 2.161 Å.

However, the HOMO-LUMO gap becomes bigger for **8**/**9** even though the respective LUMOs are stabilized. The main factor leading to an enlarged HOMO-LUMO gap is the (more significant) stabilisation of the HOMOs in **8**/**9**. This latter trend is counter-intuitive in two ways. Firstly, the N-Sn-N angles are wider for **8**/**9** (Table 6-3), which should lead to greater p character in the HOMO and hence to higher energies. Secondly

stannylenes **8**/**9** feature more strongly donating guanidinato ligands, which should also give to higher HOMO energies.

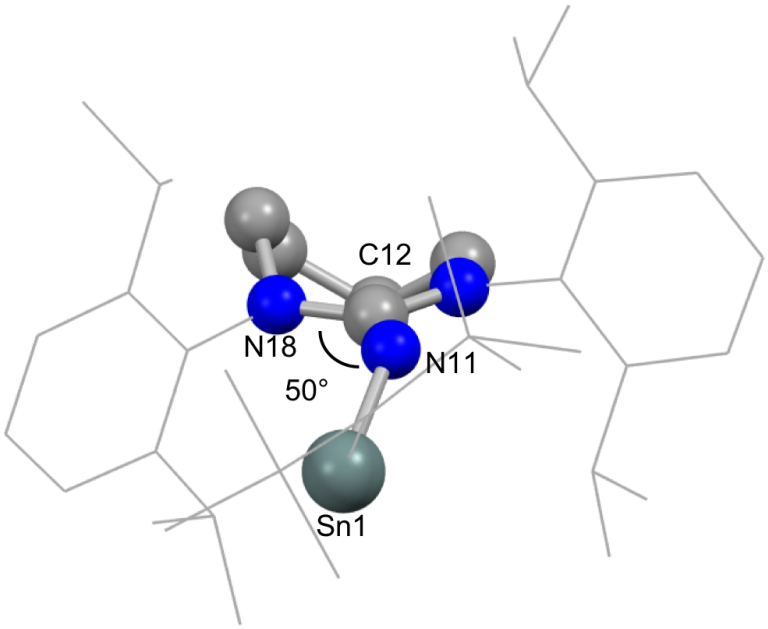
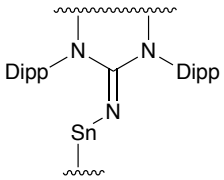
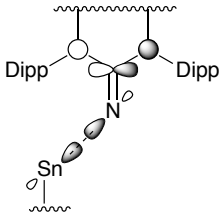
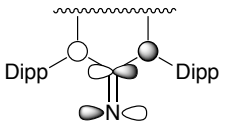
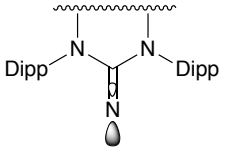
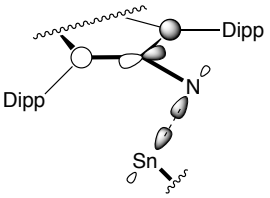
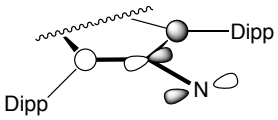
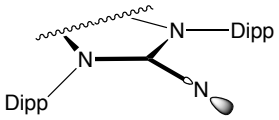
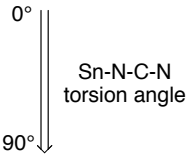
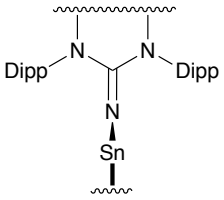
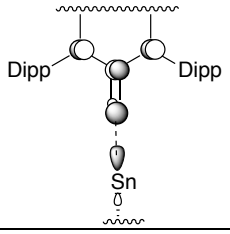
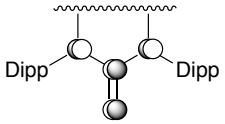
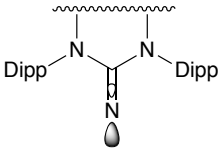
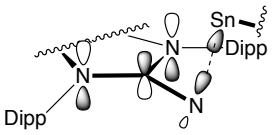
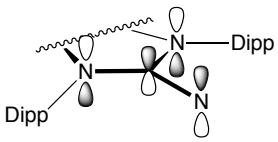
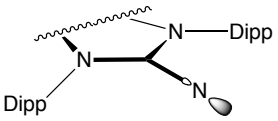


*Figure 6-5: The Sn-N-C-N torsion angle, defined using stannylene **9** as an example.*

In fact, the HOMO energies of these stannylene systems are subtly dependent on which orbital (among HOMO, HOMO-1 and HOMO-3, as described in chapter 5) from the guanidinato ligand contributes most to the σ interaction with Sn. The contribution from the guanidinato ligand to the HOMO of the stannylene is affected by the Sn-N-C-N torsion angle (as defined in Figure 6-5).

Table 6-4: The effect of Sn-N-C-N torsion angle on the guanidinato ligand orbitals contributing to the stannylene HOMO.

Orientation		Illustration of σ orbital interaction	Composition of guanidinato ligand σ orbital	
			HOMO	**HOMO-3**
	**Top-view**			
	Side-view			
				
			HOMO-1	**HOMO-3**
	**Top-view**			
	Side-view			

As illustrated in Table 6-4, at the point when Sn-N-C-N torsion angle is 0°, it is the HOMO and HOMO-3 of the guanidinato ligand which contribute to the σ interaction with the Sn centre, since the HOMO lies in the heterocycle plane. As the Sn-N-C-N torsion angle approaches 90°, the HOMO-1 of the guanidinato ligand becomes more involved in the σ interaction (and the HOMO become less involved). In all of the guanidinato ligands, the HOMO-1 is significantly lower in energy than HOMO (approx. 100 kJ mol^{-1} lower in the case of **5g**), i.e. the HOMO-1 is a more weakly donating orbital. The involvement of a guanidinato fragment orbital which is lower in energy would be expected to stabilise the

HOMO of the stannylene since it has Sn-N σ* character. The Sn-N-C-N torsion angles are wider for **8**/**9** than **6**/**7** (by 20-30°; Table 6-3), which is believed to stem from the more sterically demanding nature of the guanidinato ligands (**[6g]**$^-$ and **[7g]**$^-$). As such, the contribution from the guanidinato fragments to the σ interaction with Sn will consist of a higher ratio from the ligand HOMO-1 and will therefore lower the energy of the HOMO of the overall stannylene molecule in the case of **8** and **9**.

6.3.3 Carbonyl Stretching Frequencies of (Lg){(Me$_3$Si)$_2$N}SnMo(CO)$_5$

A further probe of the electronic/steric properties of these unsymmetrical stannylenes was targeted through complexation to the [Mo(CO)$_5$] fragment. These adducts were chosen to allow for direct comparison via infrared spectroscopy with {(Me$_3$Si)$_2$N}$_2$SnMo(CO)$_5$ (which was previously reported by Lappert *et al.*[13]). The syntheses of **(Ig){(Me$_3$Si)$_2$N}SnMo(CO)$_5$** (**10**) and **(5g){(Me$_3$Si)$_2$N}SnMo(CO)$_5$** (**11**) can readily be achieved by the photolysis of a mixture of Mo(CO)$_6$ and the respective stannylene (**6** or **7**, respectively; Figure 6-6). Due to the sterically demanding nature of stannylenes **8** and **9**, the formation of the corresponding adducts was unfortunately not successful in these cases. In each case, in situ NMR measurements show the formation of free CO, but no change in the chemical shifts of **8** and **9**. Longer irradiation times (than the synthesis of **10** and **11**) lead to the decomposition of **8** and **9**.

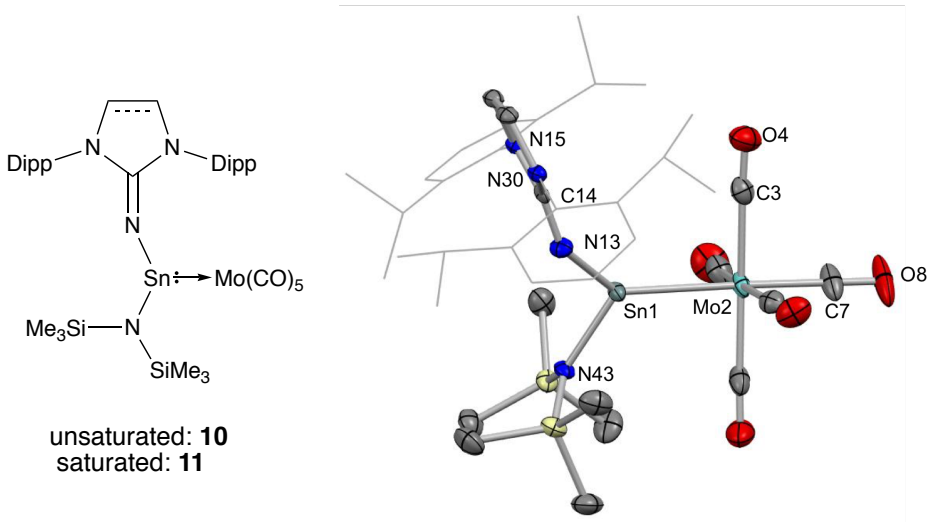


*Figure 6-6: Chemical structures of **10** and **11** (left); X-ray structure of **10** (right), H atoms omitted and Dipp groups shown in wireframe format for clarity. Thermal Ellipsoids set at 50% probability level. Key bond lengths and angles: d(Sn1-Mo2) = 2.7475(2) Å, d(Sn1-N13) = 1.954(2) Å, d(Sn1-N43) = 2.062(2) Å, d(C14=N13) = 1.279(3) Å, d(C3=O4) = 1.139(3), d(C7=O8) = 1.136(3), ∠N13SnN43 = 101.72(8)°, ∠SnN13C14 = 145.0(2)°, ∠Mo2Sn1N43 = 120.53(5)°, ∠Mo2Sn1N13 = 136.16(6)°, ∠N18C14N30 = 104.1(2)°.*

The differing donor abilities of the stannylenes **6** and **7** reflect the corresponding donor properties of the associated guanidinato substituent. Thus, more strongly σ-donating substituents are expected to lead to a more electron-rich stannylene – which in turn can be probed via the electron density at the molybdenum atom.

*Table 6-5: Infrared stretching frequencies associated with the carbonyl ligands of $Mo(CO)_6$, **10** and **11** (the strong e_u band being omitted).*

		$\{(Me_3Si)_2N\}_2SnMo(CO)_5$ [13]	**10**	**11**
$\nu_{CO}(cm^{-1})$	$A_1(1)$	2076	2068	2064
	$A_1(2)$	1928	1974	1934

In Table 6-5 two different sets of carbonyl stretching bands (ν_{CO}) for compounds **10** and **11** together with the corresponding stretches for $\{(Me_3Si)_2N\}_2SnMo(CO)_5$ are listed. The key $A_1(1)$ band, which is approximately described in terms of the stretching of the CO ligand trans to the stannylene, shows a trend of decreasing ν_{CO} from

$\{(Me_3Si)_2N\}_2SnMo(CO)_5$ to **10** to **11**, implying that the stannylene itself becomes more electron rich in the order $Sn\{N(SiMe_3)_2\}_2$ < **6** < **7**.

As such, it is apparent that on saturation of the ligand backbone, the donor abilities of the guanidinato ligands and thus the parent stannylene increase, leading to greater electron density at molybdenum, and enhanced π-back donation to the *trans* carbonyl co-ligand and a reduced stretching frequency. Unfortunately, the steric problems which apparently prevent the syntheses of the corresponding complexes of stannylenes **8** and **9** rule out further exploration of this trend in ring expanded systems.

6.3.4 Attempted Syntheses of $Sn(Ig)_2$ and $Ge(Ig)_2$

The synthesis of **$Sn(Ig)_2$** (**12**) can be achieved from $Sn\{N(SiMe_3)_2\}_2$ and two equivalents of **Ig-H**, and is readily followed by in situ ^1H NMR measurements, not least through the formation of $HN(SiMe_3)_2$. These measurements imply that conversion to the mono-iminato product **$Sn\{N(SiMe_3)_2\}(Ig)$**, is facile and occurs very rapidly at ambient temperature: characteristically, the trimethylsilyl protons of the mono-guanidinato product give rise to a sharp singlet at δ = 0.16 ppm. Upon heating, a depletion of intensity is observed for the mono-guanidinato product, while the intensity of free $HN(SiMe_3)_2$ increases (Table 6-7).

Beyond two days at 80°C, the relative intensities of these two peaks remain constant: the reaction apparently stops at ca. 85% conversion. However, the low-yielding nature of the crystallisation protocol results in a low overall yield for the reaction. Stannylene **12** can be crystallised by the slow evaporation of solvent from a pentane solution to yield crystals suitable for X-ray crystallography (Figure 6-8). The structure of

stannylene **12** is found to be consistent with DFT calculations, with the NSnN bond angle [95.8(1)°], being very similar to the angle calculated by DFT methods (96.4°).

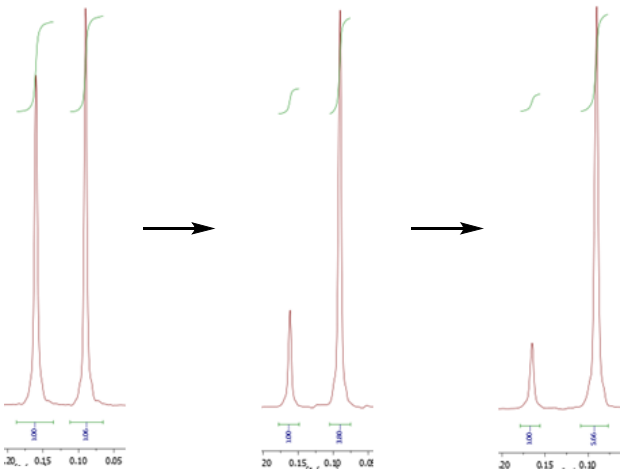


*Figure 6-7: Change in intensity of selected signals in the ^{1}H NMR spectrum of the reaction mixture derived from $Sn\{N(SiMe_3)_2\}_2$ and **Ig-H** (2.0 equiv): (left to right) room temperature, 80°C for 1 d, 80°C for 2 days.*

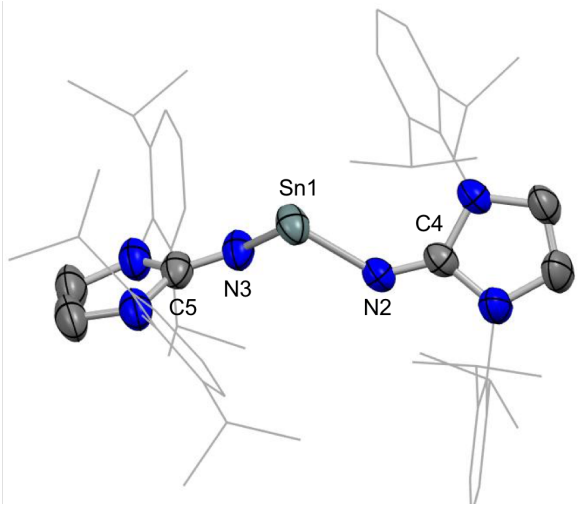


*Figure 6-8: X-ray structure of **12**, H atoms omitted and Dipp groups shown in wireframe format for clarity. Thermal Ellipsoids set at 50% probability level. Key bond lengths and angles: d(Sn-N2) = 2.030(4) Å, d(Sn1-N3) = 2.039(3) Å, d(N3-C5) = 1.270(7) Å, d(N2-C4) = 1.260(7) Å, ∠N3Sn1N2 = 95.4(1)°, ∠C5N3Sn1 = 130.9(3)°, ∠Sn1N2C4 = 133.2(3)°.*

The analogous reaction between $Ge\{N(SiMe_3)_2\}_2$ and **Ig-H** shows full conversion to the previously reported mono-substituted product[5] after heating at 80°C for two days, while no conversion to the **$Ge(Ig)_2$** is observed under any conditions examined. This can be attributed to two factors: the sterically demanding nature of the ligand and the shorter/stronger nature of the Ge-N bond, compared to that to Sn. Both of these factors presumably lead to a higher activation barrier for substitution, which, in the case of germanium, are kinetically prohibitive.

6.3.5 Attempted Syntheses of $Sn(5g)_2$ and $Ge(5g)_2$

Treatment of $Sn\{N(SiMe_3)_2\}_2$ with two equivalents of **5g-H**, leads to an unidentified mixture of products. At room temperature, the ^1H NMR spectrum shows a mixture of **5g-H**, **$Sn\{N(SiMe_3)_2\}(5g)$** and free $HN(SiMe_3)_2$, in a 1:1:1 ratio. However, upon heating the reaction mixture the ^1H NMR spectrum changes such that **5g-H** and **$Sn\{N(SiMe_3)_2\}(5g)$** no longer appear to be present in the solution. Unfortunately, attempts to crystallise the products from the reaction mixture, e.g. by the slow evaporation of pentane, led only to the formation of crystals of **5g-H**.

In the case of germanium, after heating for two days at 80°C and entirely analogous ^1H NMR spectrum is observed to that of the reaction with $Sn\{N(SiMe_3)_2\}_2$. In this case attempts were made to trap the product in solution, via the addition and irradiation of molybdenum hexacarbonyl in situ. This led to a colour change from a bright orange solution to brown. Crystallisation by the slow evaporation of pentane led to the formation of X-ray quality crystals, but unfortunately these were of the guanidinate complex **$(5g)Mo(CO)_5$**.

6.4 Intramolecular C-H Activation at Lead

6.4.1 The Preparation and C-H Activation of Pb{N(SiMe$_3$)$_2$}(Lg)

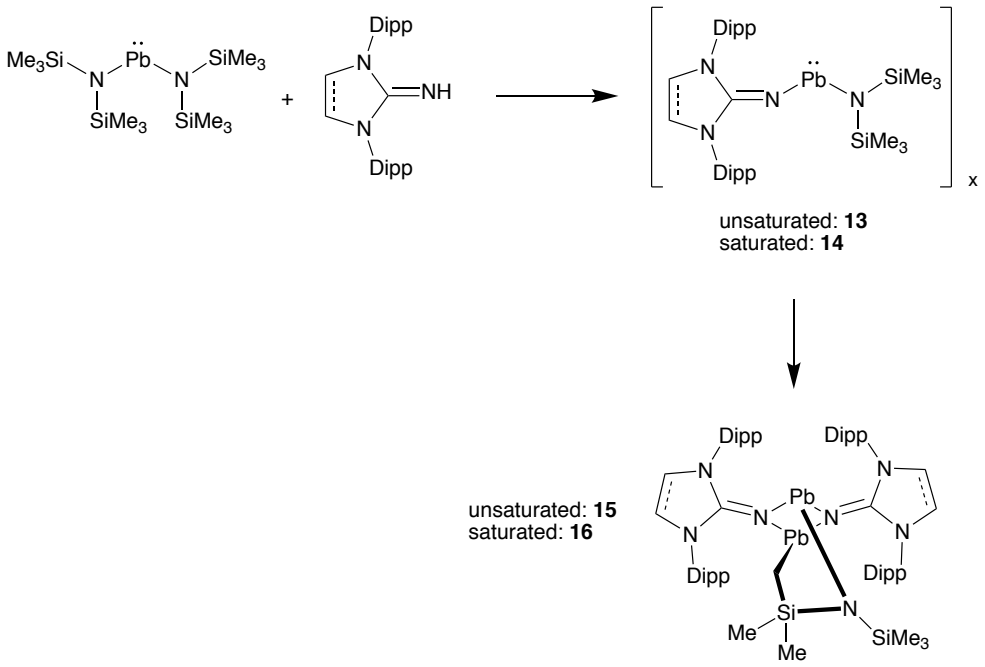


*Figure 6-9: Syntheses of plumbylenes **13** and **14**, and their activation to give plumbylenoids **15** and **16**.*

On the basis of the observations made for germanium and tin, it was hypothesized that as group 14 is descended more gentle reaction conditions are required for formation of the di-iminato metallylene, reflecting the increasing covalent radii of the group 14 element and the decreasing M-N bond strength (M = Ge, Sn, Pb). In order to support this notion, the analogous chemistry with the lead analogue, Pb{N(SiMe$_3$)$_2$}$_2$, was examined.

As expected, the 1:1 reaction between Pb{N(SiMe$_3$)$_2$}$_2$ and **Ig-H**, is facile at room temperature, and leads initially to the formation of one product, **[Pb{N(SiMe$_3$)$_2$}(Ig)]$_x$** (**13**; Figure 6-9). However, under these conditions the bright red colour of this compound begins to darken over time in solution. At room temperature, the ^{1}H NMR spectrum changes slowly, but the process can be accelerated (and driven to completion) by heating

to 80°C. Moreover, it is apparent from the ^{1}H NMR spectrum that more than one equivalent of $HN(SiMe_3)_2$ is liberated over time. Crystallisation of the product formed after heating shows that it is a plumbylenoid, **15**, featuring two metal centres linked via a bridging $N(SiMe_3)SiMe_2CH_2$ moiety formed by C-H activation of one of the trimethylsilyl substituents (Figure 6-9). In fact, crystallisation from either the heated reaction mixture or the room temperature reaction mixture via slow evaporation of pentane leads to the formation of plumbylenoid **15** as dark red crystals suitable for X-ray diffraction (Figure 6-10).

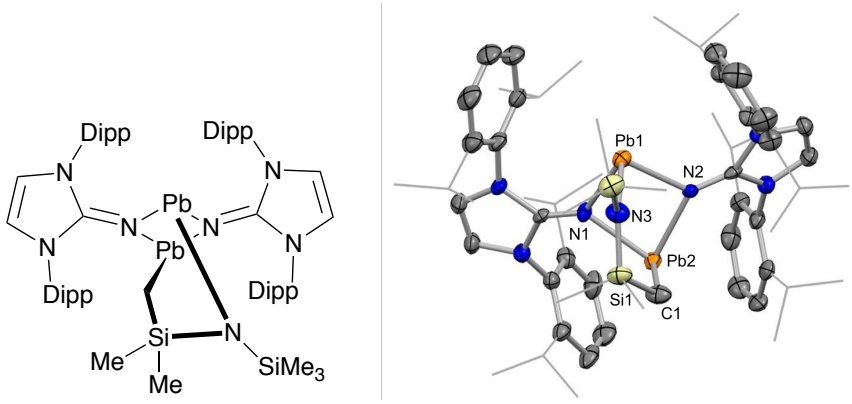


*Figure 6-10: (left) The structure of **15**; (right) X-ray crystal structure of **15** (right); H atoms omitted and isopropyl groups shown in wireframe format for clarity. Thermal ellipsoids set at 50% probability level. Key bond lengths and angles: d(N1-Pb1) = 2.324(6) Å, d(Pb1-N2) = 2.358(7) Å, d(N2-Pb2) = 2.334(7) Å, d(Pb2-N1) = 2.347(7) Å, d(Pb1-N3) = 2.260(9) Å, d(N3-Si1) = 1.72(1) Å, d(Si1-C1) = 1.85(1) Å, d(C1-Pb2) = 2.31(1) Å, ∠N1Pb1N2 = 78.1(2)°, ∠Pb1N2Pb2 = 98.6(3)°, ∠N2Pb2N1 = 78.2(2)°, ∠N2Pb2N1 = 99.2(3)°, ∠N1Pb2C1 = 92.7(3)°, ∠N1Pb1N3 = 94.6(3)° ∠Pb2C1Si1 = 124.4(5)°, ∠C1Si1N3 = 114.3(5)°, ∠Si1N3Pb1 = 120.7(5)°.*

Monitoring the ^{1}H NMR spectrum *in situ* at 80°C allows the activation of plumbylene **13** to plumbylenoid **15** to be examined in more detail; key ^{1}H NMR data are summarised in Table 6-6. In general, **15** has lower symmetry than **13** resulting in a greater

number of chemical environments for the isopropyl groups. For example, there is only one C<u>H</u>$(CH_3)_2$ septet with relative intensity of 4H for **13**, while **15** gives rise to two signals of equal intensity (both 4H): a broad resonance and δ_H = 3.34 and a sharper septet at δ_H = 3.13 ppm. The case of the CH(C<u>H</u>$_3)_2$ protons is similar: for **13** the methyl groups give rise to two sets of doublets (each of relative intensity 12H), while for **15** the groups are indicated by two sets of multiplets and one doublet, which together account for a relative intensity of 48H. (From the perspective of reaction stoichiometry, two equivalents of **13** are apparently activated to yield one equivalent of **15**, and in the process release one equivalent of $HN(SiMe_3)_2$, hence the relative intensity has been set to double in the ^{1}H NMR spectra of **15**)

*Table 6-6: Key ^{1}H NMR data relevant to the conversion of **13** to **15**.*

13	multiplicity	δ	Relative Intensity	**15**	multiplicity	δ	Relative Intensity
Backbone C<u>H</u>	singlet	6.19	2H	Backbone-C<u>H</u>	singlet	5.85	4H
C<u>H</u>Me_2	septet	3.19	4H	C<u>H</u>Me_2	broad	3.34	4H
					septet	3.13	4H
C<u>H</u>$_3$	doublet	1.33	12H	C<u>H</u>$_3$	multiplet	1.53-1.44	48H
					doublet	1.40	
	doublet	1.16	12H		multiplet	1.19-1.05	
[N(Si(C<u>H</u>$_3)_3)_2$]	singlet	0.19	18H	Si(C<u>H</u>$_3)_2$	singlet	0.63	6H
				Si(C<u>H</u>$_3)_3$	singlet	0.20	9H
				HN(Si(C<u>H</u>$_3)_3$)	singlet	0.10	18H
				PbC<u>H</u>$_2$	Singlet	-1.16	2H

The activation from plumbylene **13** to plumbylenoid **15** also gives rise to an unsymmetrical -$N(SiMe_3)SiMe_2CH_2$- bridging unit between the two Pb centres. During the activation process, one equivalent of the [N(Si(C<u>H</u>$_3)_3)_2]^-$ ligand is protonated and released as free H[N(Si(C<u>H</u>$_3)_3)_2$] another equivalent of [N(Si(C<u>H</u>$_3)_3)_2]^-$ loses a proton in the bridge

formation process and gives rise to three signals that correspond to two different silyl methyl groups and a $PbC\underline{H}_2$ unit. Notably, the appearance of the high field resonance of the $PbC\underline{H}_2$ group stems from the shielding brought about by proximity to the electropositive Pb centre (Table 6-6).

*Table 6-7: ^{1}H NMR comparison between plumbylene **13** and **14**.*

13	**multiplicity**	**δ**	**Relative Internsity**	**14**	**multiplicity**	**δ**	**Relative Internsity**
p-C<u>H</u>	doublet of doublet	7.19	2H	p-C<u>H</u>	multiplet	7.22-7.17	2H
m-C<u>H</u>	multiplet	7.14-7.10	4H	m-C<u>H</u>	multiplet	7.12-7.08	4H
Backbone C<u>H</u>	singlet	6.19	2H	Backbone C<u>H</u>$_2$	singlet	3.58	4H
C<u>H</u>Me$_2$	septet	3.19	4H	C<u>H</u>Me$_2$	septet	3.36	4H
C<u>H</u>$_3$	doublet	1.33	12H	C<u>H</u>$_3$	doublet	1.37	12H
	doublet	1.16	12H		doublet	1.27	12H
[N(Si(C<u>H</u>$_3$)$_3$)$_2$]	singlet	0.19	18H	[N(Si(C<u>H</u>$_3$)$_3$)$_2$]	singlet	0.16	18H

*Table 6-8: ^{1}H NMR comparison between plumbylenoid **15** and **16**.*

15	multiplicity	δ	Relative Internsity	16	multiplicity	δ	Relative Internsity
p-C<u>H</u>	broad	7.16	4H	p-C<u>H</u>	broad	7.16	4H
m-C<u>H</u>	multiplet	7.10-7.01	8H	m-C<u>H</u>	multiplet	7.11-7.00	8H
Backbone C<u>H</u>	singlet	5.87	4H	Backbone C<u>H</u>$_2$	singlet	3.47	8H
C<u>H</u>Me$_2$	broad	3.34	4H	C<u>H</u>Me$_2$	broad	3.34	4H
	septet	3.13	4H		septet	3.22	4H
C<u>H</u>$_3$	multiplet	1.53-1.44	48H	C<u>H</u>$_3$	multiplet	1.53-1.46	48H
	doublet	1.40			doublet	1.44	
	multiplet	1.19-1.05			multiplet	1.20-1.05	
Si(C<u>H</u>$_3$)$_2$	singlet	0.63	6H	Si(C<u>H</u>$_3$)$_2$	singlet	0.51	6H
Si(C<u>H</u>$_3$)$_3$	singlet	0.20	9H	Si(C<u>H</u>$_3$)$_3$	singlet	0.25	9H
PbC<u>H</u>$_2$	singlet	-1.16	2H	PbC<u>H</u>$_2$	singlet	-1.36	2H

Repeating the reaction using the saturated backbone system **5g-H** instead of **Ig-H** yields the analogous compounds, plumbylene **14** and plumbylenoid **16** respectively, as

deduced from the very similar ^{1}H NMR chemical shift patterns determined for these species compared to plumbylene **13** and plumbylenoid **15** (Table 6-7 and Table 6-8). The reaction was also repeated with **6g-H** and **7g-H**; however, a black precipitate started to form immediately after mixing of the starting materials, implying that the lead starting material was reduced to the form of the elemental metal; no compounds analogous to plumbylene **13** were obtained.

The ^{1}H NMR chemical shifts can be compared between each pair of analogues featuring the two different guanidinato ligands (**Ig-H** and **5g-H**). Not surprisingly, in comparing between plumbylenes **13** and **14** (Table 6-7), the signals corresponding to the respective backbones (C<u>H</u> vs. C<u>H$_2$</u>) are only the major difference. As **13** has an unsaturated backbone, the respective signal has higher chemical shift (δ = 6.19 ppm), with relative intensity of 2H; saturated backbone system **14** however, gives rise to a signal at lower chemical shift (δ = 3.58 ppm) with a relative intensity of 4H. All of the other ^{1}H NMR signals of **13** and **14** including those corresponding to the isopropyl groups, aromatic rings and the silyl groups fall in very similar chemical shift windows (< 0.1 ppm).

Similar conclusions can be also drawn from a comparison between plumbylenoids **15** and **16** – most of the ^{1}H NMR signals have same relative intensity and fall in the same part of the spectrum, with the signals corresponding to the heterocycle backbones being the major difference (**15**: δ = 5.87 ppm, 4H; **16**: δ = 3.47 ppm, 8H). Notably, both **15** and **16** feature a pattern of signals corresponding to the -N(SiMe$_3$)SiMe$_2$CH$_2$- bridge in their ^{1}H NMR spectra, with both PbC<u>H$_2$</u> signals falling in the high field region. Unlike **15**, however, the isolation of a single crystal of **16** was unsuccessful and no X-ray crystal structure of **16** could be obtained.

In the absence of structural characterization by X-ray crystallography, we were keen to determine by spectroscopic means, the state of aggregation (and by implication the coordination number of the lead centre(s)) in the plumbylenes **13** and **14**. While related tin systems are known to be monomeric, the dimeric nature of the subsequent plumbylenoid C-H activation products **15** and **16** caused us to consider both monomer and dimer species (Figure 6-11) - since both possibilities are compatible with the measured ^{1}H NMR spectra (Table 6-7). Initial studies began with computational evaluation of the relative energies of various possible oligomeric structures.

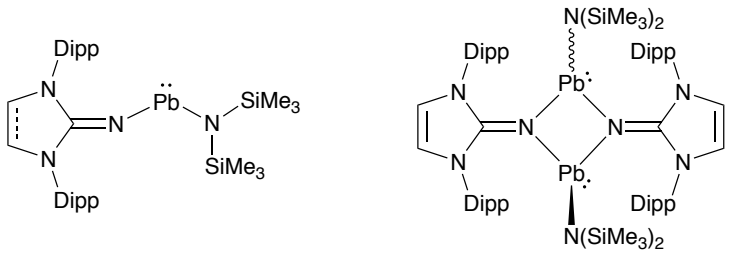


*Figure 6-11: Possible monomeric and dimeric forms of **13**.*

*Table 6-9: Energies – relative to two equivalents of the monomeric form – of potential dimeric forms of **13** together with the C-H activated product **15**. Comparative data are also given for the hypothetical compounds in which the Dipp groups have been replaced by Ph or o-Xyl.*

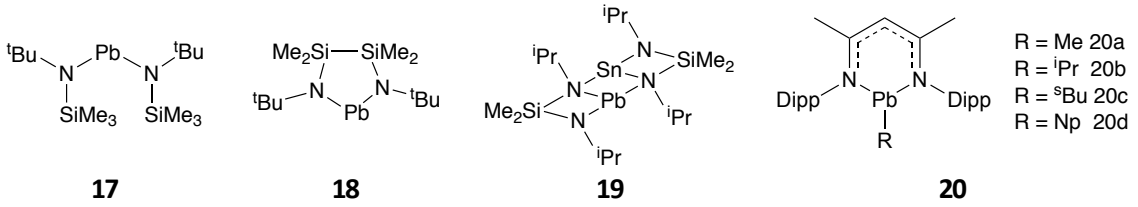
Ar	Energy relative to monomeric form (kJ mol^{-1})		
	Dimer (*cis*)	Dimer (*trans*)	C-H activation product
Ph	-50	-80	-268
o-Xyl	-4	a	-318
Dipp	+96	+88	-240

a. Geometry optimisation not converged.

Table 6-9 shows the relative energies of monomeric and dimeric forms (together with the C-H activated product) for different guanidinato N-substituents (Ar). When Ar is

the experimentally used Dipp group, the monomer form is favoured over either the *cis* or *trans* dimeric species by ~90 kJ mol^{-1}. Steric factors are clearly important: as Ar changes from Dipp to Xyl and then Ph, the dimer form (especially when the two -N(Si(C$\underline{H}_3$)$_3$)$_2$ are in a *trans* configuration) becomes more energetically favourable. These data do suggest – in the case of the systems employed experimentally – that **13** should be in the form of monomer as the Dipp groups strongly hinder the two plumbylene molecules from interacting with each other.

From an experimental perspective, we sought to discriminate between these possible states of aggregation by using ^{207}Pb NMR spectroscopy, since the chemical shifts of organolead species are known to be strongly dependent on coordination number. Thus, solutions of **13** and **14** in benzene are characterized by ^{207}Pb NMR chemical shifts of δ_{Pb} = 4710 and 4476 ppm, respectively, which are in the range expected for systems of the type Pb(NR$_2$)$_2$ (Figure 6-12 and Table 6-10).[14, 15]



17 **18** **19** **20**

Figure 6-12: The structures of previous reported two and three coordinate Pb(II) compounds.

*Table 6-10: ^{207}Pb NMR chemical shift of Pb{N(SiMe$_3$)$_2$}$_2$ and compounds **13** – **20**.*

	^{207}Pb NMR		^{207}Pb NMR		^{207}Pb NMR
13	4710	**15**-Pb(1)	2790	**15**-Pb(2)	3550
14	4476	**16**-Pb(1)	2800	**16**-Pb(2)	3480
Pb(N(SiMe$_3$)$_2$)$_2$[14,15]	4916	**19**[16]	2930	**20a**[17]	3002
17[14]	5371			**20b**[17]	3145
				20c[17]	3262
18[14]	4900			**20d**[17]	3506

Table 6-10 lists the ^{207}Pb NMR chemical shifts for compounds **13** - **16**, as well as those for selected plumbylene and related complexes for reference (Figure 6-12). In the case of **13** and **14**, the ^{207}Pb NMR chemical shifts in benzene are very close to the precursor Pb{N(SiMe$_3$)$_2$}$_2$ and to the related two-coordinate (diamido)plumbylenes **17** and **18**, implying that both plumbylenes **13** and **14** are monomeric in benzene. The activated product **15**, by contrast, features two three-coordinate Pb centres (as determined crystallographically) and gives rise to two ^{207}Pb NMR signals at higher field (δ_{Pb} = 3550 and 2790 ppm). The related compound **16**, also features two signals at very similar chemical shifts (δ_{Pb} = 3480 and 2800 ppm) consistent with the proposal of a very similar structure to that of **15**.

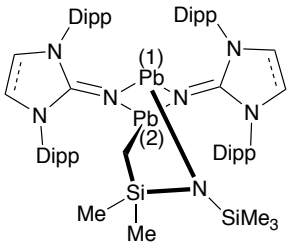


*Figure 6-13: The two different lead chemical environments assigned on plumbylenoid **15** and **16**. (Pb(1) and Pb(2))*

To assign the ^{207}Pb NMR chemical shifts to the two Pb centres, we have distinguished one Pb from the other as illustrated in Figure 6-13. Pb(1) atom is coordinated by three N-donors (analogous to **19** in Figure 6-12) while Pb(2) atom is coordinated by two N-donors and one alkyl group (analogous to **20a**-**d** in Figure 6-12). By comparing to the ^{207}Pb NMR chemical shifts of **19** and **20a**-**d** in Table 6-10, it is reasonable to believe that Pb(1) gives rise to the ^{207}Pb chemical shift at 2790 and 2800 ppm for compound **15** and **16**, respectively, while Pb(2) has a chemical shift at 3550 and 3480 ppm. Given the implication from both computational and NMR studies of a two-coordinate geometry for the lead centre in plumbylene **13**, we were interested to probe the reaction mechanism leading to the formation of plumbylenoid **15** – both by experimental and theoretical means.

6.4.2 Mechanistic studies of the conversion of 13 to 15

A kinetic study of the activation of compound **13** was undertaken by *in situ* ^{1}H NMR measurements; Pb{N(SiMe$_3$)$_2$}$_2$ and one equivalent of **Ig-H** were allowed to mix in a J. Young's NMR tube (in toluene-d$_8$) over a period of 30 min. A ^{1}H NMR spectrum measured at this point was used to confirm complete conversion to compound **13**. The sample was then heated at 90°C over a period of 24 h in the NMR spectrometer, with a ^{1}H NMR spectrum being measured every 15 min. Integration of the signals of both the starting material, **13**, and product, **15**, allowed the temporal plot shown in Figure 6-14 to be constructed. From these data a (straight line) logarithmic plot can be derived, implying that the rate-determining step is first order in **13** (and that dimerization is therefore not likely to be mechanistically relevant, in line with DFT calculations on the relative energies of different oligomeric forms).

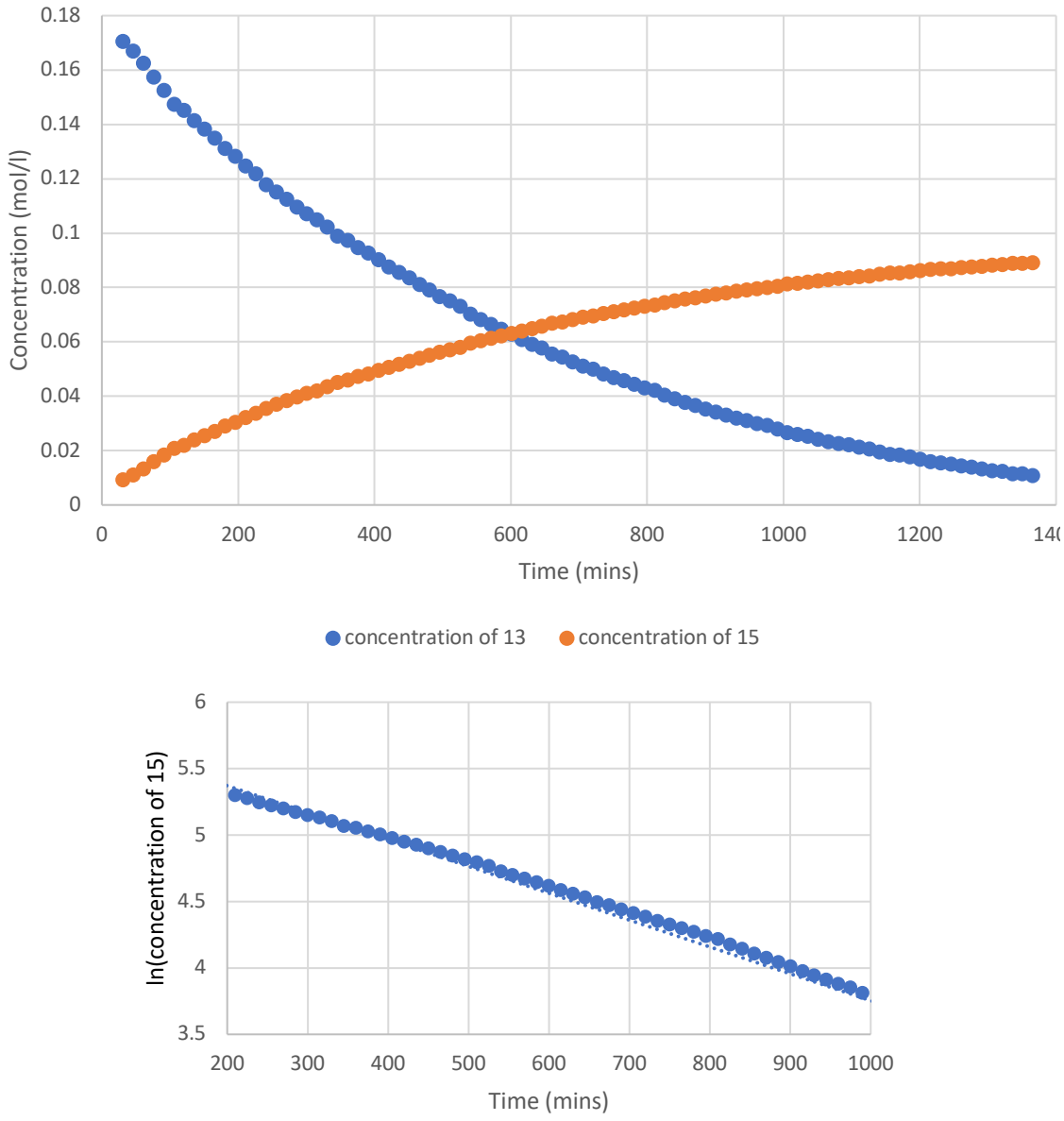


*Figure 6-14: Kinetic studies of the conversion of **13** to **15**. R^2 = 0.994 for the linear fit*

On this basis, we postulate that the activation pathway (Figure 6-15) begins with an intra-molecular step, involving activation of one of the C-H bonds of the $N(SiMe_3)_2$ group across the Pb-N_{guan} bond to give a four-membered cyclic plumbylene fragment (**13-1**) stabilized by coordination of the **Ig-H** protio-ligand. This system can then ring open in the opposite sense to generate a two coordinate plumbylene system featuring a pendant amido N-H bond (**13-2**). The thermodynamics of this isomerization process are very close

to neutral (Figure 6-16), and the highest activation barrier (that associated with the initial formation of the four-membered ring) is calculated to be 111.7 kJ mol^{-1}. At this transition state (**13-1-1**), one of the C-H bonds within the N(SiMe$_3$)$_2$ group is significantly lengthened, with the H atom in question also interacting with N$_{guan}$, and the carbon atom moving towards the Pb centre. At this transition state, the N---H distance is 1.32 Å (c.f. 1.01 Å for N-H single bond), the C---H distance 1.43 Å (c.f. 1.09 Å for C-H single bond), and the Pb---C distance 2.77 Å (c.f. 2.22 Å for Pb-C single bond).

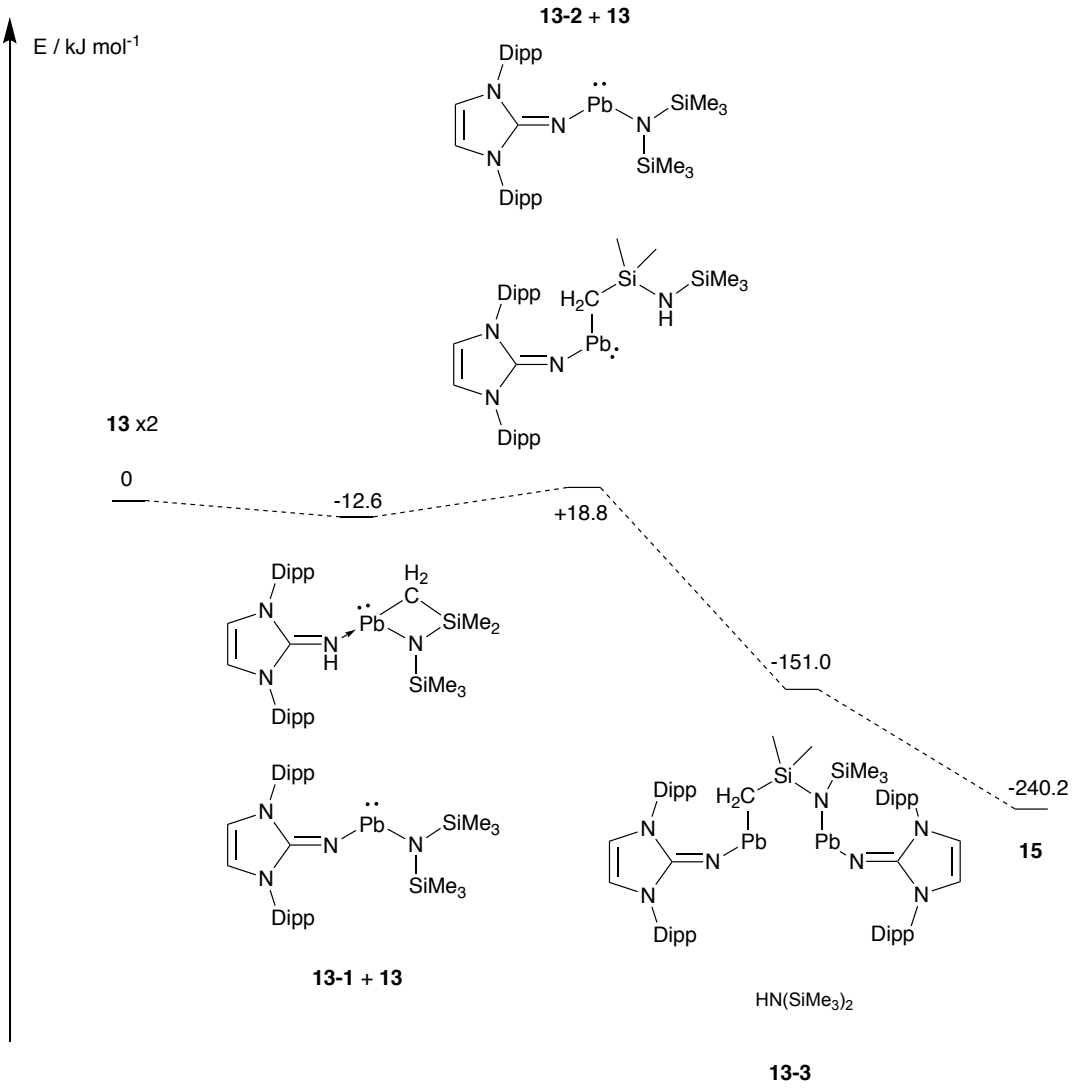


Figure 6-15: P*otential mechanism of* C-H *activation* at Pb showing local minima (energies *in kJ mol^{-1}*).

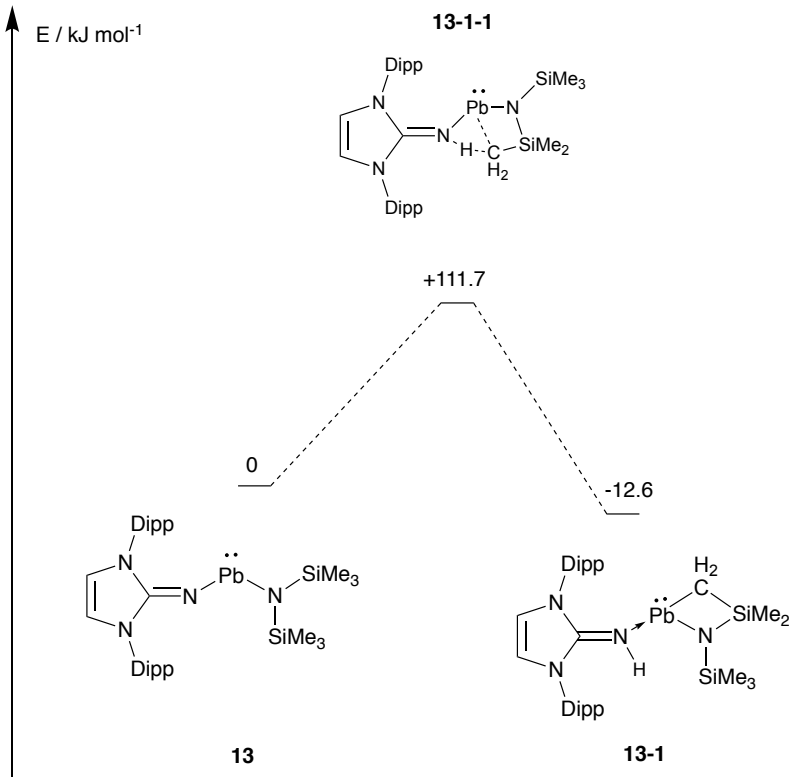


Figure 6-16: Calculation of the highest activation barrier for the C-H activation process (energies in kJ mol^{-1}).

In the next step, the intermediate (**13-2**) reacts with another molecule of **13** to form $HN(SiMe_3)_2$ and a dinuclear molecule (**13-3**) at which two **[Pb(Ig)]** units are linked via an unsymmetrical (N,C) bridging ligand. This intermediate (**13-3**) then generates the final product (**15**) by forming additional bridging interactions between Pb and N_{guan}. The overall activation process is thermodynamically favourable being downhill by more than 240 kJ mol^{-1}.

6.5 Summary

In summary, we have successfully introduced each of the guanidinato ligands developed in chapter 5 into stannylene systems, by synthesizing a series of compounds of

the type **(Lg)Sn{N(SiMe$_3$)}$_2$**. These stannylenes in turn have been used as experimental probes of the donor strength of each **[(L)g]** ligand, via the infrared spectra of the respective [Mo(CO)$_5$] adducts. This leads to the conclusion that as the size of ring increases, the donor strength tends to increase. The donor strength may also contribute to the decrease in the ^{119}Sn NMR chemical shift from **Sn{N(SiMe$_3$)}$_2$(Ig)** to **Sn{N(SiMe$_3$)$_2$}(7g)**, although a better rationale for this trend revolves around variation in the HOMO-LUMO gap. Theoretical studies of the **Sn{N(SiMe$_3$)$_2$}(Lg)** systems show an increase in the HOMO-LUMO gap from **Ig** to **7g**, which is driven by the stabilisation of the HOMO energy level across the group of stannylene (from **6** to **9**). The change in the HOMO energy level may ultimately stem from the change of Sn-N-C-N torsion angle brought about on steric grounds. We have attempted to synthesise the related homoleptic compounds **Sn(Lg)$_2$** and **Ge(Lg)$_2$**; however, **Sn(Ig)$_2$** was the only compound of this type successfully synthesised, possibly due to steric factors with the other ligand backbones.

In the course of the attempted synthesis of related plumbylene compounds, C-H activation by the Pb centre of compounds **13** and **14** has been uncovered. Although we were not able to isolate **13** and **14** in pure form (due to their lability to onward C-H activation), in situ ^{207}Pb NMR measurements imply that they are monomeric in solution, in line with the related stannylene system. Kinetic studies carried out on **13** reveal that the activation process is first order in **13**, and a mechanism including intramolecular C-H activation as first step is therefore proposed. The energy barrier associated with this process is 111.7 kJ mol^{-1} and the overall stabilisation energy 240.2 kJ mol^{-1}.

6.6 References

1. S. Inoue and K. Leszczynska, *Angewandte Chemie-International Edition*, 2012, **51**, 8589-8593.
2. M. W. Lui, C. Merten, M. J. Ferguson, R. McDonald, Y. J. Xu and E. Rivard, *Inorganic Chemistry*, 2015, **54**, 2040-2049.
3. D. Wendel, D. Reiter, A. Porzelt, P. J. Altmann, S. Inoue and B. Rieger, *Journal of the American Chemical Society*, 2017, **139**, 17193-17198.
4. D. Wendel, T. Szilvasi, C. Jandl, S. Inoue and B. Rieger, *Journal of the American Chemical Society*, 2017, **139**, 9156-9159.
5. T. Ochiai, D. Franz, X. N. Wu and S. Inoue, *Dalton Transactions*, 2015, **44**, 10952-10956.
6. T. Ochiai, T. Szilvasi, D. Franz, E. Irran and S. Inoue, *Angewandte Chemie-International Edition*, 2016, **55**, 11619-11624.
7. T. Ochiai, D. Franz, E. Irran and S. Inoue, *Chemistry-a European Journal*, 2015, **21**, 6704-6707.
8. T. Ochiai, D. Franz, X. N. Wu, E. Irran and S. Inoue, *Angewandte Chemie-International Edition*, 2016, **55**, 6983-6987.
9. T. Ochiai and S. Inoue, *Rsc Advances*, 2017, **7**, 801-804.
10. K. Yamamoto, C. P. Gordon, W. C. Liao, C. Coperet, C. Raynaud and O. Eisenstein, *Angewandte Chemie-International Edition*, 2017, **56**, 10127-10131.
11. S. Halbert, C. Coperet, C. Raynaud and O. Eisenstein, *Journal of the American Chemical Society*, 2016, **138**, 2261-2272.
12. M. Usher, A. V. Protchenko, A. Rit, J. Campos, E. L. Kolychev, R. Tirfoin and S. Aldridge, *Chemistry-a European Journal*, 2016, **22**, 11685-11698.
13. M. F. Lappert and P. P. Power, *Journal of the Chemical Society-Dalton Transactions*, 1985, 51-57.
14. B. Wrackmeyer, in *Annual Reports on NMR Spectroscopy*, Academic Press, 2002, vol. 47, pp. 1-37.
15. B. Wrackmeyer and K. Horchler, in *Annual Reports on NMR Spectroscopy*, ed. G. A. Webb, Academic Press, 1990, vol. 22, pp. 249-306.
16. B. Wrackmeyer, K. Horchler, H. Zhou and M. Veith, *Zeitschrift Fur Naturforschung Section B-a Journal of Chemical Sciences*, 1989, **44**, 288-292.
17. M. J. Taylor, E. J. Coakley, M. P. Coles, H. Cox and J. R. Fulton, *Organometallics*, 2015, **34**, 2515-2521.